MBE Growth, Processing and Stability of Zinc blende MgS based Heterostructures

Akhil Rajan

Submitted for the degree of Doctor of Philosophy

Heriot-Watt University

Institute of Photonics and Quantum Sciences

School of Engineering and Physical Sciences

July 2013

Abstract

This thesis investigates the MBE growth, stability and processing of zinc blende (ZB) MgS based structures. Although MgS has already proven effective in several applications, its growth in the ZB phase is still restricted due to a variety of reasons. Therefore, the main emphasis of this thesis is on probing the growth related problems and developing new growth techniques. A new method to control the formation of surface defects which causes the rapid oxidation of MgS layers has been developed first. In contrast to theoretical predictions, the growth of ZB MgS has been successfully demonstrated on GaP, together with GaAs and InP. The Epitaxial Lift-off (ELO) of deposited layers was successfully demonstrated on all three substrates. A new modification to the existing ELO technique, by using polyurethane based flexible carriers, which eliminates the use of wax and thus avoids many associated problems, has been demonstrated and a simple sample passivation method based on amorphous selenium is also explained. An effective method to reduce the number of quantum dots by introducing time delays at various stages of the growth is developed. Finally, the first experimental demonstration of the direct growth of ZB MgS on GaAs substrate is followed by the application of this result in reusable substrates. A single GaAs substrate has been reused five times while still maintaining the epilayer quality, by performing ELO.

Acknowledgements

To the Creator and Engineer of the entire universe and the One who made this all possible, God, I give You thanks. Thanking Him for being my strength and guide in the writing of this thesis. Without Him, I would not have had the wisdom or the physical ability to do so.

I would like to take this opportunity to offer my sincerest gratitude to my supervisor, Dr Kevin Prior, who has supported and encouraged me throughout my thesis with his patience and knowledge whilst allowing me the room to work in my own way. I would also like to thank my second supervisor, Prof. John Wilson.

I am honoured to have this thesis examined by Prof. David Ritchie and Prof. Ajoy Kar.

I would like to thank Ian Davidson for the initial training and for providing the spectroscopic data. A special thanks to Richard Moug for all those thought provoking conversations and ideas. A year working with him was very productive.

I am thankful to my office mates, Adetunmise, Chaitanya, Frauke and Silvia for sharing a wonderful time with me. Thanks for their efforts to convert me from Word to LaTeX.

I am eternally grateful to my family, especially my Mum for the constant support, both moral and financial. Thanks to Aju, Chethan, Lallu and Ponnu for all the support and love. Thanks to Paru for the support and being a special part of my life.

ACADEMIC REGISTRY
Research Thesis Submission

Name*:*			
School/PGI:			
Version: *(i.e. First, Resubmission, Final)*		Degree Sought (Award **and** Subject area)	

Declaration

In accordance with the appropriate regulations I hereby submit my thesis and I declare that:

1) the thesis embodies the results of my own work and has been composed by myself
2) where appropriate, I have made acknowledgement of the work of others and have made reference to work carried out in collaboration with other persons
3) the thesis is the correct version of the thesis for submission and is the same version as any electronic versions submitted*.
4) my thesis for the award referred to, deposited in the Heriot-Watt University Library, should be made available for loan or photocopying and be available via the Institutional Repository, subject to such conditions as the Librarian may require
5) I understand that as a student of the University I am required to abide by the Regulations of the University and to conform to its discipline.

* *Please note that it is the responsibility of the candidate to ensure that the correct version of the thesis is submitted.*

Signature of Candidate*:*		Date:	

Submission

Submitted By *(name in capitals):*	
Signature of Individual Submitting:	
Date Submitted:	

For Completion in the Student Service Centre (SSC)

Received in the SSC by *(name in capitals):*			
Method of Submission *(Handed in to SSC; posted through internal/external mail):*			
*E-thesis Submitted (**mandatory for final theses)***			
Signature:		Date:	

Contents

Abstract ii

Acknowledgements iii

Contents x

List of Tables xi

List of Figures xv

List of Abbreviations xvi

List of Publications xviii

1 Introduction **1**

1.1 Historical Overview of Semiconductor growth technology 1

1.2 III-V Semiconductors 2

1.3 II-VI Semiconductors 2

1.4 Growth technologies 3

1.5 II-VI materials research at Heriot-Watt 5

1.6 Overview of thesis 6

1.7 References 8

2 MBE Growth, technology and characterisation techniques **12**

2.1 Introduction 12

2.2 MBE system design 13

2.3 Ultra high vacuum environment 14

2.3.1 Pressure measurement 14

2.4 MBE Growth Chamber 15

2.4.1 Cell fluxes 17

2.5 Substrate temperature measurement 17

2.5.1 Thermocouple Measurements 17

2.5.2 Pyrometer Measurements 18

2.6 RHEED . . . 21
2.6.1 Electron Diffraction . . . 22
2.6.2 Surface Reconstruction . . . 25
2.7 Heteroepitaxial Growth . . . 26
2.7.1 Frank-van der Merwe (FM) . . . 27
2.7.2 Volmer-Weber (VW) . . . 28
2.7.3 Stranski-Krastanow (SK) . . . 28
2.8 Growth techniques . . . 29
2.9 Zinc Blende (ZB) crystal structure . . . 30
2.10 Characterisation techniques . . . 32
2.11 X-ray Diffraction . . . 32
2.11.1 Rocking curves . . . 33
2.11.2 Bragg's Law . . . 35
2.11.3 Reflections . . . 36
2.12 Atomic Force microscopy (AFM) . . . 37
2.12.1 Contact mode . . . 38
2.12.2 Tapping Mode . . . 39
2.13 Photoluminescence Spectroscopy . . . 40
2.13.1 PL experimental setup . . . 42
2.14 Spectroscopic Ellipsometry . . . 43
2.15 Summary . . . 46
2.16 References . . . 47

3 Density control of CdSe quantum dots deposited on MgS 50

3.1 Introduction . . . 50
3.2 Quantum Dots . . . 52
3.3 Quantum Dot Fabrication Techniques . . . 53
3.3.1 Lithography . . . 53
3.3.2 Colloidal Synthesis . . . 54
3.3.3 Epitaxy: Self-Assembling . . . 55
3.4 Stranski-Krastanov (SK) Growth . . . 55
3.4.1 Energetics . . . 56
3.4.2 Dot formation . . . 58

3.5 Limitations of Stranski-Krastanov growth . . . 59
3.5.1 Control of size . . . 59
3.5.2 Coherence . . . 60
3.5.3 Control of QD density . . . 60
3.6 Growth of self assembling II-VI quantum dots . . . 60
3.7 Growth of MgS/CdSe QDs . . . 64
3.8 Selenium clusters vs QDs . . . 65
3.9 Density control of CdSe QDs grown on MgS . . . 67
3.10 Effects of growth delay after CdSe layer deposition, t_0 . . . 69
3.11 Effects of annealing time, t_2 . . . 75
3.12 Summary . . . 77
3.13 Future Work . . . 78
3.14 References . . . 79

4 Control of surface morphology in zinc blende MgS 85
4.1 Introduction . . . 85
4.2 Growth of Magnesium Sulphide . . . 88
4.2.1 Flux stability . . . 88
4.2.2 GaAs substrate preparation . . . 89
4.2.3 ZB MgS growth mechanism . . . 90
4.2.4 Additional notes . . . 90
4.3 Challenges in initial MgS growth . . . 90
4.3.1 Changes in growth environment after lab relocation . . . 91
4.3.2 Issues faced during initial growths . . . 93
4.3.3 Sample degradation . . . 99
4.4 MgS growth improvement as a function of Mg flux . . . 100
4.5 Growth rate and layer composition calibration . . . 106
4.6 Epitaxial Lift Off on MgS . . . 108
4.7 Effect of a smoothing layer on thick MgS layers . . . 109
4.8 Observation of surface pits . . . 113
4.9 Growth of the thickest ZB MgS . . . 115
4.10 AFM Topology of the rock salt MgS surface . . . 117
4.11 Summary . . . 119
4.12 Future Work . . . 120

4.13 References 121

5 Growth and stability of ZB MgS grown on GaAs, GaP and InP substrates 124

5.1 Introduction 124
5.2 Growth on different substrates 125
5.3 Predictions of the Froyen-Wei-Zunger (FWZ) model 126
5.4 Substrate cleaning 128
5.4.1 GaAs and GaP substrate cleaning 129
5.4.2 InP substrate cleaning 129
5.4.3 One-step chemical etching previously used at HWU 130
5.4.4 A two-step chemical etching process 133
5.5 Growth 134
5.5.1 Growth on GaAs 136
5.5.2 Growth on GaP 136
5.5.3 Growth of thicker MgS on GaP 137
5.5.4 Growth on InP 138
5.6 Dislocation density calculations 138
5.7 Experimental results vs. FWZ prediction 143
5.8 Summary 145
5.9 Future Work 146
5.10 References 147

6 Epitaxial lift-off of II-VI heterostructures from III-V substrates 152

6.1 Introduction 152
6.1.1 ELO alternatives 153
6.2 Epitaxial Lift-off (ELO): An overview 154
6.3 Epitaxial Lift-off: II-VI materials 156
6.3.1 Release layer thickness 156
6.4 Epitaxial Lift-off: MgS based method 157
6.4.1 MgS chemical etch mechanism 159
6.5 Growth of MgS based liftoff structures 160
6.6 X-Ray Diffraction of structures before ELO 161
6.7 Epitaxial Lift-off on GaP, GaAs and InP substrates based structures 163

6.8 Optical analysis of the structures . . . 166
6.8.1 Analysis of absorption spectra . . . 167
6.8.2 Analysis of PL spectra . . . 168
6.9 Summary . . . 173
6.10 Future Work . . . 174
6.11 References . . . 175

7 Epitaxial Lift-off and Surface passivation; A new perspective 180
7.1 Introduction . . . 180
7.2 Limitations of existing II-VI ELO technique . . . 180
7.2.1 Application of wax cap . . . 181
7.2.2 Use of solvents and solvent-related contamination . . . 182
7.2.3 Curling of epilayer . . . 183
7.2.4 Scalable area . . . 184
7.2.5 Damage to substrate . . . 185
7.2.6 Inability to control and monitor the etch process . . . 185
7.3 Recent developments in III-V ELO . . . 186
7.3.1 Weight Induced Epitaxial Lift-Off (WIELO) . . . 186
7.4 Polyurethane based carriers for II-VI ELO . . . 187
7.4.1 Steps of the improved ELO process . . . 188
7.4.2 Advantages of polyurethane based ELO . . . 190
7.4.3 Observation of the etch process . . . 191
7.5 Stabilisation of semiconductor surfaces . . . 194
7.5.1 Surface reactions . . . 195
7.5.2 Case study: MgS . . . 195
7.5.3 Case study: ZnSe . . . 196
7.5.4 Case study: CdSe quantum dots deposited on MgS . . . 197
7.6 Existing surface passivation techniques . . . 198
7.6.1 Vacuum desiccators . . . 198
7.6.2 Vacuum transfer devices . . . 198
7.6.3 Arsenic passivation layer in III-V semiconductors . . . 198
7.7 Selenium protection layer in II-VI materials . . . 199
7.7.1 Deposition method . . . 199
7.7.2 Selenium on ZnSe surface . . . 200

7.7.3 Selenium on MgS surface . . . 202
7.7.4 Transportation and surface characterisation . . . 205
7.8 Summary . . . 206
7.9 Future Work . . . 207
7.10 References . . . 209

8 Direct epitaxial growth of zinc blende MgS on GaAs and the development of reusable substrates 211

8.1 Introduction . . . 211
8.2 Direct growth of ZB MgS on GaAs . . . 212
8.2.1 History of direct MgS growth . . . 212
8.2.2 Growth procedures . . . 213
8.3 Direct growth of ZB MgS . . . 213
8.3.1 Analysis of MgS layers . . . 215
8.3.2 Growth rate calibration . . . 218
8.3.3 Re-evaluation of the Mg sticking coefficient . . . 219
8.3.4 Stability of the growth range . . . 221
8.3.5 Comparison of dislocation densities . . . 221
8.4 Reusable substrates . . . 223
8.4.1 Initial attempts on ZnSe buffer layers . . . 224
8.4.2 Surface preparation of ZnSe . . . 225
8.4.3 Regrowth on ZnSe . . . 226
8.5 First successful demonstration of reusable substrates . . . 228
8.5.1 Advantages compared to III-V ELO system . . . 232
8.6 Summary . . . 233
8.7 Future Work . . . 234
8.8 References . . . 236

9 Conclusions and outlook 240

List of Tables

2.1 Table for determining temperature errors due to emissivity errors 20

3.1 Effect of various growth delays on QD areal density 70
3.2 Effect of varying annealing time on QD areal density. 75

4.1 Applications of MgS in both ZB and RS phase 86
4.2 Past growths of MgS in ZB phase 87
4.3 MgS thickness and growth rate determined by XRI (Batch B) 93
4.4 MgS growth rate determined by 004 XRI from Batch A samples 96
4.5 MgS growth rate determined by 004 XRI from Batch B samples 98
4.6 AFM and RHEED observations from samples. 104
4.7 MgS growth rate determined by 004 XRI from Batch C samples 106
4.8 MgS growth rate determined by 115 XRI from Batch C samples 107
4.9 Epitaxial Lift off on MgS samples 108
4.10 AFM and RHEED observations from samples 111
4.11 RMS roughness from samples grown with varying smoothing layers . . . 113
4.12 AFM surface anaysis data obtained from the three thickest MgS samples . 116

5.1 Strains of MgS on different substrates and buffer layer combinations. . . . 135
5.2 Dislocation densities calculated from two azimuths 142

6.1 Lattice constants of three substrates and lattice mismatch of ZnSe 163
6.2 PL peak positions and FWHM for ZnSe layers before and after ELO . . . 169
6.3 Relaxations in ZnSe epilayers determined from strains and mismatches . . 170

8.1 Comparison of dislocation densities calculated from 300nm ZnSe 223
8.2 Comparison of dislocation densities calculated from 300nm ZnSe (2) . . . 228
8.3 Comparison of dislocation densities calculated from 300nm ZnSe (3) . . . 232

List of Figures

2.1 Top elevation of the Heriot-Watt MBE system 13
2.2 Schematic of the side elevation of the V80H MBE system 16
2.3 Schematic of the geometry of RHEED setup 22
2.4 Schematic of various RHEED patterns 24
2.5 Cross-section views of the MBE thin film growth modes 27
2.6 Schematic of the zincblende structure of ZnSe 31
2.7 Schematic of ZB ZnSe showing the bonding between atoms 31
2.8 A typical 004 XRD rocking curve 34
2.9 Schematic of $\theta/2\theta$ scan and degrees of freedom of sample stage. 35
2.10 Schematic of symmetric and asymmetric planes 36
2.11 Graph of AFM tip-to-sample separation versus van der Waals forces . . . 38
2.12 Schematic of the optical setup used for PL measurements 42
2.13 Schematic of a rotating analyser ellipsometer. 44

3.1 Schematic of density of states functions 52
3.2 Schematic of Stranski-Krastanow growth mode. 56
3.3 Energy vs. time schematic for 2D to 3D transformation 57
3.4 Schematic of Surface cross section of a quantum dot 58
3.5 Conduction band and Valence band offsets for MgS/CdSe structures. . . . 63
3.6 Typical MgS/CdSe quantum dot structure for AFM and PL 64
3.7 AFM images of Se cluster removal 66
3.8 Schematic representation of the different time delays 68
3.9 AFM images showing density controlled QDs 69
3.10 Graph of QD areal density vs. growth delay 71
3.11 PL spectra showing the reduction in number of dots 72
3.12 Plot of Log pump power vs Log intensity (PL) from sample HWC416 . . 73
3.13 AFM images of density controlled QDs 74

3.14 Graph of QD areal density vs. annealing time 76

4.1 004 XRI scans of HWC273, HWC271 and HWC272 93
4.2 Graph of ZnS cell temperature vs. number of growths 95
4.3 004 XRI scans of HWA1158, HWA1159 and HWA1162 96
4.4 004 XRI scans from HWA304, HWA303 and HWA310 98
4.5 UVM images of various surface formations and microscopic pores 99
4.6 XRI scans from HWC304 over several weeks 100
4.7 AFM images showing the reduction of surface pits with Mg flux 102
4.8 Mg BEP versus the pit density observed using AFM. 103
4.9 AFM images from samples grown with 15nA and 13nA Mg flux 105
4.10 004 XRI scans from HWC397, HWC396 and HWC400 106
4.11 115 XRI scans from HWC397, HWC396 and HWC400 107
4.12 AFM section analysis of HWC393 and HWC394 110
4.13 AFM images from samples HWC403, HWC405 and HWC406 112
4.14 AFM cross sectional analysis Type A and Type B pits 114
4.15 AFM images from samples HWC403, HWC407 and HWC409 116
4.16 004 XRD scans from HWC403, HWC407 and HWC409 117
4.17 AFM of HWC395 showing crack formation at the point of RS formation . 118

5.1 Lattice parameter vs. band gap of ZB MgS, GaP, GaAs and InP. 125
5.2 Schematic diagram explaining FWZ prediction 127
5.3 UVM images showing InP surfaces improperly vacuum annealed 130
5.4 UVM images showing In droplets as a result annealing at 400^{o}C 131
5.5 UVM images showing surface formations from improper etching 132
5.6 Schematic of the MgS structures grown on GaAs, GaP and InP 134
5.7 004 XRD scans shows ZB and RS MgS structures grown on GaP 137
5.8 004 XRD scans of MgS based structures grown on GaAs, GaP and InP . . 139
5.9 004 XRD scan from GaP/ZnS/MgS/ZnS with Gaussian fit 140
5.10 004 XRD scans along two azimuths showing difference in FWHM 141

6.1 Photographs of various stages involved in wax based ELO 157
6.2 UVM images showing crack formations on lifted epilayers 158
6.3 UVM images showing the effect of dust on deposited epilayer 159
6.4 004 XRD rocking curves from the first set of samples 161

6.5 004 XRD rocking curves from the second set of samples 162
6.6 Absorption spectra of ZnSe epilayers lifted from GaP, GaAs and InP . . . 166
6.7 Absorption spectra of ZnSe and ZnCdSe epitaxial layers after ELO 167
6.8 PL from GaP/ZnS/MgS/ZnSe before and after (from ZnSe) ELO 168
6.9 PL from ZnSe grown on GaP, GaAs and InP before and after ELO 171
6.10 Plot of the shift of epilayer peak emission energy before and after ELO . . 172

7.1 UVM images showing substrate damage after ELO 182
7.2 Photograph showing residual deposit on lifted epilayer 183
7.3 Photographs showing curling of epilayers during ELO 184
7.4 UVM images of scratches on substrate after ELO 185
7.5 Schematic of WIELO 187
7.6 Various stages involved in polyurethane based ELO 189
7.7 UVM images of various stages of polyurethane based ELO 192
7.8 UVM images showing progression of etch channels 193
7.9 UVM images showing an unetched substrate edge 194
7.10 UVM images of MgS layer with thin cap shows surface degradation . . . 196
7.11 Schematic of Se capped structures 200
7.12 Comparison of 004 XRD scans from growth after Se capping 201
7.13 AFM images from samples HWC462, HWC486 and HWC467 202
7.14 AFM images from HWC462 on Day 1, Day 3, Day 5 and Day 10 203
7.15 004 XRD scans from HWC467 showing initial and regrown structures . . 204
7.16 Photographic representation of various stages of Se desorption 206
7.17 UVM images showing surface formations on lifted epilayers 208

8.1 ZB MgS growth regions in a phase diagram of Mg flux *vs* growth temp. . 214
8.2 004 XRD scan showing the ZB MgS peak, grown directly on GaAs 216
8.3 004 XRD scan of the structure GaAs(sub)/MgS(12nm)/ZnSe(300nm) . . 217
8.4 77K PL from the structure MgS(20nm)/ZnCdSe(4.5nm)/MgS(20nm) . . . 218
8.5 SIMS analysis of structure GaAs(sub)/MgS(12nm)/ZnSe(300nm) 219
8.6 SEM image of structure GaAs(sub)/MgS(12nm)/ZnSe(300nm) 220
8.7 Comparison of 004 XRD scans 222
8.8 Structure of GaAs/ZnSe based reusable substrate 224
8.9 004 XRD scans from HWC485 and HWC512 227
8.10 Structure of the directly deposited MgS based reusable substrate 229

8.11 XRD scans of GaAs/MgS/ZnSe after 1^{st}, 3^{rd} and 5^{th} regrowth 230
8.12 004 XRD scans of GaAs substrate after 1^{st}, 3^{rd} and 5^{th} ELO 231

List of Abbreviations

AFM	Atomic Force Microscopy
ALE	Atomic Layer Epitaxy
BEP	Beam Equivalent Pressure
CCD	Charge Coupled Device
DCXRD	Double Crystal X-ray Diffraction
DI	Deionized (water)
DMS	Dilute Magnetic Semiconductors
EBL	Electron Beam Lithography
ELO	Epitaxial Lift-Off
FCC	Face Centred Cubic
FIBL	Focused Ion Beam Lithography
FM	Frank-van der Merwe
FWHM	Full Width at Half Maximum
FWZ	Froyen, Wei and Zunger
GOF	Goodness Of Fit
HH	Heavy-hole exciton
HWA	Heriot-Watt A chamber (where sample was grown)
HWC	Heriot-Watt C chamber (where sample was grown)
HWU	Heriot-Watt University
IR	Infra Red
LCAO	Linear Combination of Atomic Orbitals
LED	Light Emitting Diode
LH	Light-Hole Exciton
LN_2	Liquid Nitrogen
MBE	Molecular Beam Epitaxy
MEE	Migration Enhanced Epitaxy
MESFET	Metal Semiconductor Field Effect Transistor

ML	Monolayer
$MOVPE$	Metalorganic Vapour Phase Epitaxy
NA	Numerical Aperture
ODS	Ozone-Depleting Substances
OFN	Oxygen Free Nitrogen
PBN	Pyrolytic Boron Nitride
PES	Photoemission Electron Spectroscopy
PID	Proportional-Integral-Derivative
PL	Photoluminescence
QD	Quantum Dot
QW	Quantum Well
$RADS$	Rocking Curve Analysis by Dynamical Simulation
$RHEED$	Reflection High Energy Electron Diffraction
RMS	Root Mean Square
RS	Rocksalt (crystal structure)
SEM	Scanning Electron Microscopy
$SERS$	Surface Enhanced Raman Spectroscopy
$SIMS$	Secondary Ion Mass Spectroscopy
SK	Stranski-Krastanov mode
SM	Strain-Modified
$STEM$	Scanning Transmission Electron Microscopy
TEM	Transmission Electron Microscopy
UHV	Ultra High Vacuum
UVM	Ultra Violet Microscopy
VW	Volmer-Weber
$WIELO$	Weight Induced Epitaxial Lift-Off
XRD	X-ray Diffraction
XRI	X-ray Interference
ZB	Zinc Blende (crystal structure)
$\mu - PL$	Micro Photoluminescence
$2D, 3D$	Two Dimensional, Three Dimensional
$6N$	99.9999% (material purity)

List of Publications

The work carried out in this thesis resulted in the following publications:

1. A. Rajan, R. T. Moug and K. A. Prior: Growth and stability of zinc blende MgS on GaAs, GaP, and InP substrates, *Applied Physics Letters* **102**, 032102 (2013).

2. A. Rajan, R. T. Moug and K. A. Prior: Control of surface defects in zinc blende MgS grown by MBE, *Journal of Crystal Growth* **368**, 62 (2013).

3. A. Rajan, R. T. Moug and K. A. Prior: Density control of MBE grown CdSe quantum dots, *(Submitted to: The 16th International Conference on II-VI Compounds and Related Materials, Nagahama, Japan)*

4. A. Rajan, I. A. Davidson, R. T. Moug and K. A. Prior: Epitaxial lift-off of II-VI semiconductors from III-V substrates using a MgS release layer, *(In preparation)*

5. A. Rajan, R. T. Moug and K. A. Prior: Direct epitaxial growth of zinc blende MgS on GaAs, *(In preparation)*

6. A. Rajan, R. T. Moug and K. A. Prior: III-V substrate reuse for II-VI semiconductor growth using MgS based epitaxial lift-off, *(In preparation)*

Chapter 1

Introduction

1.1 Historical Overview of Semiconductor growth technology

The discovery of semiconductors and their applications is one of the most important scientific breakthroughs of twentieth century. Modern electronic devices including lasers, solar cells, transistors and integrated circuits are all based on various semiconductor materials. For over fifty years, semiconductor technology developments have been based on silicon (Si). Availability of large, high purity substrates and high device densities were among the main advantages associated with the use of Si. Si is also an excellent heat conductor and combines with oxygen to form SiO_2, a stable oxide, which acts as a protective layer during processing and also shields against diffusion of dopants [1]. However Si has some drawbacks including the indirect band gap and hence cannot be used for optical devices like LEDs and laser diodes. The slower response time of Si makes it unsuitable for high performance applications such as high speed large scale signal processing [2].

The demand for high performance semiconductor devices that can be used for advanced technology applications lead researchers to investigate alternatives for Si, leading to the development of compound semiconductors including II-VI and III-V semiconductors. These two semiconductor groups have the advantages of having many compounds with direct bandgaps covering a wide spectral range which have high quantum efficiency.

1.2 III-V Semiconductors

Some of the criteria missing in the Si technology have been fulfilled by the advances in the material research based on III-V semiconductors. The majority of MBE research is focused on the development of III-V materials and structures with the successful, commercial production of visible-Infra Red, Light Emitting Diodes (LEDs) and Laser Diodes (LDs). The emission wavelength of these devices is however limited to 600-2000 nm due to the band gaps of the III-V materials. Compounds such as GaAs and InP have properties that make them ideal candidates for high speed, analogue and mixed signal applications. Generally, III-V devices operate faster and consume less power than Si based devices. GaAs is a typical example, where it has a low-field electron velocity greater than Si and a lower saturation electric field. However they are comparatively difficult to grow epitaxially and their material properties are more difficult to control [1].

The development of the blue laser diode using GaN was a major break through in III-V semiconductor research [3, 4]. These laser diodes allowed a four fold increase in optical data storage capacity over IR based technology. The main advantages of GaN devices come from high output power coupled with small volume, whereas the main setback is the cost. The growing demand on larger bandwidth for wireless communications has stimulated the quest for transistors that can be operated at fastest possible frequencies. Besides the conventional silicon metal oxide semiconductor field-effect transistors (MOSFETs), III-V nanowires have been heavily explored for radio frequency (RF) applications. The III-V high electron mobility transistors (HEMTs) are the latest in this range with the record-high cut-off frequency (f_t) for InAs-based HEMTs, reaching 644 GHz for 30 nm long devices on InP substrates [5].

1.3 II-VI Semiconductors

II-VI semiconductors have a wide range of band gap energies ranging from BeSe (6eV) to HgTe (0eV). The large band gap II-VI materials give transitions corresponding to wavelengths in the visible and ultra violet region of the electromagnetic spectrum. De-

velopments in solar cells [6] and electroluminescent phosphors [7] have initially created interest in these materials. Attempts to fabricate long wavelength IR sensors based on HgCdTe [8] and during the 1990s, ZnSe based blue laser diodes [9] has also driven research in these materials. Even though the outstanding success of the GaN based devices has almost stopped research in optoelectronic devices based on ZnSe, research in the field of IR detectors and solar cells still continues.

The study of dilute magnetic semiconductors (DMS) is another active area of interest for II-VI materials [10]. ZnSe, CdSe, CdTe and CdS can be used as hosts for transition metal ions such as Fe, Mn and Co, substituting their original cations to form the alloys ZnxSe, CdxSe etc., where x = Fe, Mn and Co are the most common DMSs. The electronic properties and the structure of the host crystals are well known and so they are ideal for studying the dynamical interplay between carrier transport, electron spin-scattering and magnetic dimensionality [10].

The main limitation in the II-VI semiconductor material development is the need to grow on III-V substrates [11], mainly caused by the poor quality and the high cost of the commercially available II-VI substrates. The lattice mismatch between the substrate and epitaxial layers leads to strain between the two materials. Dislocations are formed as a result of the strain relief in the growing layers, thus resulting in the degradation of the material quality [12]. The life time of active devices like LEDs and lasers will be reduced as a consequence. The use of II-VI semiconductors as base materials for optoelectronic devices also depends on the realisation of p- and n- type doping in the same material [13], and the ability to form ohmic contacts to large band gap semiconductors [14], both of which have proved problematic in the past.

1.4 Growth technologies

Growth techniques have a significant role in the development of any semiconductor materials. Both molecular beam epitaxy (MBE) and metal-organic vapour phase epitaxy (MOVPE) offer a precise level of control over the growth process of compound semiconductors. The use of non invasive *in situ* process sensors that precisely control the film

thickness, composition, interface quality and uniformity during growth is one of the main reasons for the success of these fabrication technologies. The successful development of the devices mentioned in the previous sections has resulted from the atomic resolution of the growth thickness and composition offered by MBE and MOVPE techniques. These fabrication techniques allow the use of band gap engineering to alter the band gap by spatially varying the composition and doping concentrations of the semiconductor materials [15]. Quantum well and quantum dot structures, whose properties have been tailored by this method and incorporated in devices have resulted in the development of a series of new electronic and optoelectronic devices [16, 17].

For II-VI semiconductor growth, MOVPE has a number of problems which have hindered its development. The crucial problems are first, the lack of clean organometallic sources with low impurity levels and second, the presence of gas phase reaction between the group II and group VI containing molecules.

MBE is a versatile technique for the epitaxial growth of semiconductor, metal and insulator thin films. In MBE, thin films crystallise via reactions between thermal-energy molecular beams of the constituent elements and a substrate surface which is maintained at an elevated temperature under ultra-high vacuum conditions. The absence of carrier gases as well as the ultra high vacuum environment result in the highest achievable purity of the grown films. The composition of the grown epilayer and its doping level depend on the relative arrival rates of the constituent elements and dopants, which in turn depend on the evaporation rates of the appropriate sources. The growth rate can be precisely controlled, and is low enough that surface migration of the impinging species on the growing surface is ensured.

There were many attempts to grow compound semiconductors in vacuum before the development of MBE technology. Fabrication techniques for epitaxial GaAs on GaAs and single crystalline Ge substrates by a modified three-temperature vacuum evaporation was initially demonstrated [18]. The term MBE was first used in 1970 after several years of extensive studies of molecular beams interacting with solid surfaces. A theoretical paper published in 1970 on superlattices and negative differential conductivity in semiconductors opened a whole new dimension for MBE growth for the study of quantum mechanical effects on a new physical scale [19]. Further, addition of computer control to the MBE

system and the observation of the negative differential conductivity in superlattice structures were significant developments [20]. By the mid 1970s, MBE became more common after reports of the first varactor [21], IMPATT diode [22], room temperature CW semiconductor laser [23] and microwave FETs [24]. MBE continued to develop and became a high volume production technology in the late 1980s. More recently, a series of developments enabling larger substrates, high uniformity, faster turnaround and real-time sample monitoring were designed into the MBE system. MBE is broadly used today for advanced multilayer crystal growth and has led to radically new devices including high-speed transistors, microwave devices, laser diodes and detectors [25].

1.5 II-VI materials research at Heriot-Watt

The MBE group at Heriot-Watt University was established in 1988 and the first high quality ZnSe epitaxial layers were grown in May 1989 [26]. The Group was the first to demonstrate ZnSe/ $Zn_{0.8}Cd_{0.2}Se$ quantum well blue lasers in Europe and has a long record of doping studies in these materials and provided the first standard CV profiling methods for these materials [27]. Following the world-wide shift away from blue laser development, the group has concentrated on a number of different topics related to the structural properties and fundamental spectroscopy of II-VI semiconductors [28]. Using X-ray topography, the Heriot-Watt MBE group made the first observations of the onset of dislocation formation in ZnSe [12, 29].

Later, the group developed ZnS based layers on both GaAs and GaP [30]. At the same time, the group has also focused on novel II-VI semiconductor systems and for the first time, demonstrated the growth of the compound MgS in the ZB crystal structure in layers up to 130nm thick [31]. This material has an extremely wide band gap ($\sim$5eV) and has opened up the possibility of producing many novel devices. The group has also grown transition metal sulphides such as MnS, MnCrS, and CrS and investigated the ferromagnetic and anti-ferromagnetic properties [32]. Intense photoluminescence (PL) emission has been demonstrated in both MgS/ZnSe and MgS/CdSe low dimensional structures [33, 34]. Experimental studies on MgS have led to new II-VI technologies being developed such as a novel lift-off technique in order to investigate room temperature polari-

tons [35].

1.6 Overview of thesis

This thesis presents the details of the growth of zinc blende magnesium sulphide based materials and devices. Both the structural and optical characterisation of the materials are also described along with the developments in some of the key processing techniques.

The Heriot-Watt MBE system is described in Chapter 2. The *in situ* monitoring technique, RHEED which is essential to the precision control of the MBE device fabrication is also detailed in this chapter, together with various characterisation techniques used during this project, including: X-ray Diffraction, Atomic Force Microscopy, Photoluminescence & spectroscopic ellipsometry, etc. The experimental setup along with some background theory of the techniques are also explained.

Chapter 3 gives details of a new method to effectively control the areal density of MgS based CdSe quantum dots. The dots are mainly counted using AFM with the back up of PL spectroscopy. Details of the procedures used and the results obtained are presented. An effective method to eliminate the Se containing clusters from the surface is also demonstrated.

The control of surface defects during the growth of ZB MgS using a range of Mg fluxes and a low growth temperature is presented in Chapter 4. XRD rocking curves were used to determine the growth rate and Zn incorporation. Topography of the MgS surface measured by AFM will also be included in this chapter along with the observation of two different types of growth defects. By optimising growth parameters, the growth of the thickest ZB MgS layer grown to date is also demonstrated.

Chapter 5 compares the growth of ZB MgS on three substrates, GaAs, GaP, and InP where the growth is investigated by XRD and RHEED. MgS layer strain on these substrates varied between 3.1% compressive strain (GaP) and 4.4% tensile strain (InP). Results are compared with predictions that stable growth on GaP is unlikely and relaxed ZB MgS

should not grow in layers over a few Å thick. The calculated dislocation densities are also compared.

The use of thin ZB MgS epitaxial layers as an effective release layer for epitaxial lift off for layers deposited on GaP, GaAs and InP substrates is demonstrated in Chapter 6. The lifted epilayers have been examined using PL and absorption spectroscopy as well as XRD. The changes in the strain states of the epilayers after lift-off are also studied.

Chapter 7 details the application of two of the post growth processing techniques in II-VI materials. A modification to the existing ELO technique, offering many advantages and increasing the range of applications for the technique is demonstrated first. An easy to apply, sample passivation technique is investigated next.

Chapter 8 gives the details of the first direct epitaxial growth of ZB MgS on a substrate. Layers up to 40 nm thick have been grown directly on GaAs substrates and this is subsequently used to demonstrate for the first time, the reuse of substrates for II-VI materials regrowth. Regrowth has been performed up to 5 times on a single substrate without increasing the dislocations on epilayers.

Finally, Chapter 9 includes a summary of the results presented in this thesis along with the conclusions drawn from the collated data.

1.7 References

[1] S. M. Sze. *Semiconductor devices, physics and technology*. Wiley, 1985 (cited on pages: 1, 2).

[2] C. K. Maiti and G. A. Armstrong. *Applications of Silicon-Germanium Heterostructure Devices*. Series in Optics and Optoelectronics Series. Taylor & Francis Group, 2001 (cited on page: 1).

[3] S. Nakamura, M. Senoh, S.-i. Nagahama, N. Iwasa, T. Yamada, T. Matsushita, H. Kiyoku and Y. Sugimoto. "InGaN-Based Multi-Quantum-Well-Structure Laser Diodes". *Japanese Journal of Applied Physics* Vol. 35 (1996), pp. L74–L76 (cited on page: 2).

[4] S. Nakamura, M. Senoh, N. Iwasa and S.-i. Nagahama. "High-Brightness InGaN Blue, Green and Yellow Light-Emitting Diodes with Quantum Well Structures". *Japanese Journal of Applied Physics* Vol. 34 (1995), pp. L797–L799 (cited on page: 2).

[5] D.-H. Kim and J. A. del Alamo. "30-nm InAs PHEMTs With f(T)=644 GHz and f(max)=681 GHz". *IEEE Electron Device Letters* Vol. 31 (2010), 806–808 (cited on page: 2).

[6] M. Yamaguchi. "Present status and prospects of photovoltaic technologies in Japan". *Renewable and Sustainable Energy Reviews* Vol. 5 (2001), pp. 113–135 (cited on page: 3).

[7] P. D. Rack and P. H. Holloway. "The structure, device physics, and material properties of thin film electroluminescent displays". *Materials Science and Engineering: R: Reports* Vol. 21 (1998), pp. 171–219 (cited on page: 3).

[8] R. K. Willardson. *Semiconductors and Semimetals*. Semiconductors and semimetals. Elsevier Science, 1970 (cited on page: 3).

[9] K. A. Prior. "The development of II-VI semiconductors for blue diode lasers". *Contemporary Physics* Vol. 37 (1996), 345–358 (cited on page: 3).

[10] T. S. Moss, P. T. Landsberg, C. Hilsum and S. Mahajan. *Handbook on Semiconductors: Basic properties of semiconductors*. Handbook on Semiconductors. North-Holland, 1992 (cited on page: 3).

[11] H. H. Farrell, M. C. Tamargo and J. L. de Miguel. “Optimal GaAs(100) substrate terminations for heteroepitaxy”. *Applied Physics Letters* Vol. 58 (1991), pp. 355–357 (cited on page: 3).

[12] G. Horsburgh, K. A. Prior, W. Meredith, I. Galbraith, B. C. Cavenett, C. R. Whitehouse, G. Lacey, A. G. Cullis, P. J. Parbrook, P. Möck and K. Mizuno. “Topography measurements of the critical thickness of ZnSe grown on GaAs”. *Applied Physics Letters* Vol. 72 (1998), pp. 3148–3150 (cited on pages: 3, 5).

[13] R. N. Bhargava. “Compact blue lasers in the near future”. *Journal of Crystal Growth* Vol. 117 (1992), pp. 894–901 (cited on page: 3).

[14] Y. Fan, J. Han, L. He, J. Saraie, R. L. Gunshor, M. Hagerott, H. Jeon, A. V. Nurmikko, G. C. Hua and N. Otsuka. “Graded band gap ohmic contact to p-ZnSe”. *Applied Physics Letters* Vol. 61 (1992), pp. 3160–3162 (cited on page: 3).

[15] S. Mahajan and K. S. SreeHarsha. *Principles of growth and processing of semiconductors*. McGraw-Hill international editions. WCB/McGraw-Hill, 1999 (cited on page: 4).

[16] W. T. Wenckebach. *Essentials of semiconductor physics*. J. Wiley, 1999 (cited on page: 4).

[17] D. Bimberg, M. Grundmann and N. N. Ledentsov. *Quantum Dot Heterostructures*. Wiley, 1999 (cited on page: 4).

[18] J. E. Davey and T. Pankey. “Epitaxial GaAs Films Deposited by Vacuum Evaporation”. *Journal of Applied Physics* Vol. 39 (1968), pp. 1941–1948 (cited on page: 4).

[19] L. Esaki and R. Tsu. “Superlattice and Negative Differential Conductivity in Semiconductors”. *IBM Journal of Research and Development* Vol. 14 (1970), pp. 61–65 (cited on page: 4).

[20] L. L. Chang, L. Esaki, W. E. Howard and R. Ludeke. “The Growth of a GaAs–GaAlAs Superlattice”. *Journal of Vacuum Science and Technology* Vol. 10 (1973), pp. 11–16 (cited on page: 5).

[21] A. Y. Cho and F. K. Reinhart. “Interface and doping profile characteristics with molecular-beam epitaxy of GaAs: GaAs voltage varactor”. *Journal of Applied Physics* Vol. 45 (1974), pp. 1812–1817 (cited on page: 5).

[22] A. Y. Cho, C. N. Dunn, R. L. Kuvas and W. E. Schroeder. “GaAs IMPATT diodes prepared by molecular beam epitaxy”. *Applied Physics Letters* Vol. 25 (1974), pp. 224–226 (cited on page: 5).

[23] A. Y. Cho, R. W. Dixon, J. H. C. Casey and R. L. Hartman. “Continuous room-temperature operation of GaAs-$Al_xGa_{1-x}As$ double-heterostructure lasers prepared by molecular-beam epitaxy”. *Applied Physics Letters* Vol. 28 (1976), pp. 501–503 (cited on page: 5).

[24] A. Y. Cho, J. V. DiLorenzo, B. S. Hewitt, W. C. Niehaus, W. O. Schlosser and C. Radice. “Low-noise and high-power GaAs microwave field-effect transistors prepared by molecular beam epitaxy”. *Journal of Applied Physics* Vol. 48 (1977), pp. 346–349 (cited on page: 5).

[25] A. Y. Cho. “How molecular beam epitaxy (MBE) began and its projection into the future”. *Journal of Crystal Growth* Vol. 201–202 (1999), pp. 1–7 (cited on page: 5).

[26] K. A. Prior, J. M. Wallace, J. J. Hunter, S. J. A. Adams, M. J. L. S. Haines, M. Saoudi and B. C. Cavenett. “Growth of MBE ZnS_xSe_{1-x} using a novel electrochemical sulphur source”. *Journal of Crystal Growth* Vol. 101 (1990), pp. 176–179 (cited on page: 5).

[27] I. S. Hauksson, S. Y. Wang, J. Simpson, M. R. Taghizadeh, K. A. Prior and B. C. Cavenett. “Development and characterization of II–VI blue-green diode lasers”. *Physica B: Condensed Matter* Vol. 191 (1993), pp. 124–129 (cited on page: 5).

[28] J. S. Milnes, C. Morhain, S. A. Telfer, W. Meridith, T. A. Steele, K. A. Prior and B. C. Cavenett. “A spectroscopic study of the piezoelectric effect in ZnSe/ZnCdSe single quantum wells grown on (2 1 1)B GaAs”. *Journal of Crystal Growth* Vol. 184–185 (1998), pp. 714–717 (cited on page: 5).

[29] C. B. O’Donnell, G. Lacey, G. Horsburgh, A. G. Cullis, C. R. Whitehouse, P. J. Parbrook, W. Meredith, I. Galbraith, P. Möck, K. A. Prior and B. C. Cavenett. “Measurements by X-ray topography of the critical thickness of ZnSe grown on GaAs”. *Journal of Crystal Growth* Vol. 184–185 (1998), pp. 95–99 (cited on page: 5).

[30] S. A. Telfer, C. Morhain, B. Urbaszek, C. O’Donnell, P. Tomasini, A. Balocchi, K. A. Prior and B. C. Cavenett. “MBE growth of ZnS and ZnCdS layers on GaP”. *Journal of Crystal Growth* Vol. 214–215 (2000), pp. 197–201 (cited on page: 5).

[31] C. Bradford, C. B. O'Donnell, B. Urbaszek, A. Balocchi, C. Morhain, K. A. Prior and B. C. Cavenett. "Growth of zinc blende MgS/ZnSe single quantum wells by molecular-beam epitaxy using ZnS as a sulphur source". *Applied Physics Letters* Vol. 76 (2000), pp. 3929–3931 (cited on page: 5).

[32] L. David and K. A. Prior. "Determination of the lattice constant of CrS from $Mn_{1-x}Cr_xS$ MBE epitaxial layers". *Physica Status Solidi (b)* Vol. 243 (2006), pp. 778–781 (cited on page: 5).

[33] C. Bradford, C. B. O'Donnell, B. Urbaszek, A. Balocchi, C. Morhain, K. Prior and B. Cavenett. "Growth of zinc blende MgS and MgS/ZnSe quantum wells by MBE using ZnS as a sulphur source". *Journal of Crystal Growth* Vol. 227–228 (2001). Proceeding of the Eleventh International Conference on Molecular Beam Epitaxy, pp. 634–638 (cited on page: 5).

[34] C. Bradford, B. Urbaszek, M. Funato, A. Balocchi, T. C. M. Graham, E. J. McGhee, R. J. Warburton, K. A. Prior and B. Cavenett. "Growth and characterization of MgS/CdSe self-assembled quantum dots". *Journal of Crystal Growth* Vol. 251 (2003), pp. 581–585 (cited on page: 5).

[35] A. Curran, J. K. Morrod, K. A. Prior, A. K. Kar and R. J. Warburton. "Exciton–photon coupling in a ZnSe-based microcavity fabricated using epitaxial liftoff". *Semiconductor Science and Technology* Vol. 22 (2007), p. 1189 (cited on page: 6).

Chapter 2

MBE Growth, technology and characterisation techniques

2.1 Introduction

Molecular beam epitaxy (MBE) is an ultra-high vacuum technique for the growth of semiconductor materials of high chemical purity and structural perfection. The technique typically uses solid elemental or compound sources of high purity, normally $\geq$ 6N i.e. better than 99.9999 % pure.

MBE was developed in the early 1970s in order to accommodate the increasing demand for a crystal growth technique that could artificially structure layers of high quality compound semiconductors [1]. Its introduction has enabled major advances in the development of III-V, II-VI and group IV semiconductor materials.

In this chapter, the operation and structure of MBE systems and the Heriot-Watt MBE systems in particular are described together with the standard procedure for sample growth. The main characterisation techniques used in the determination of the structure, composition and properties of the samples grown in thesis are also outlined in this chapter.

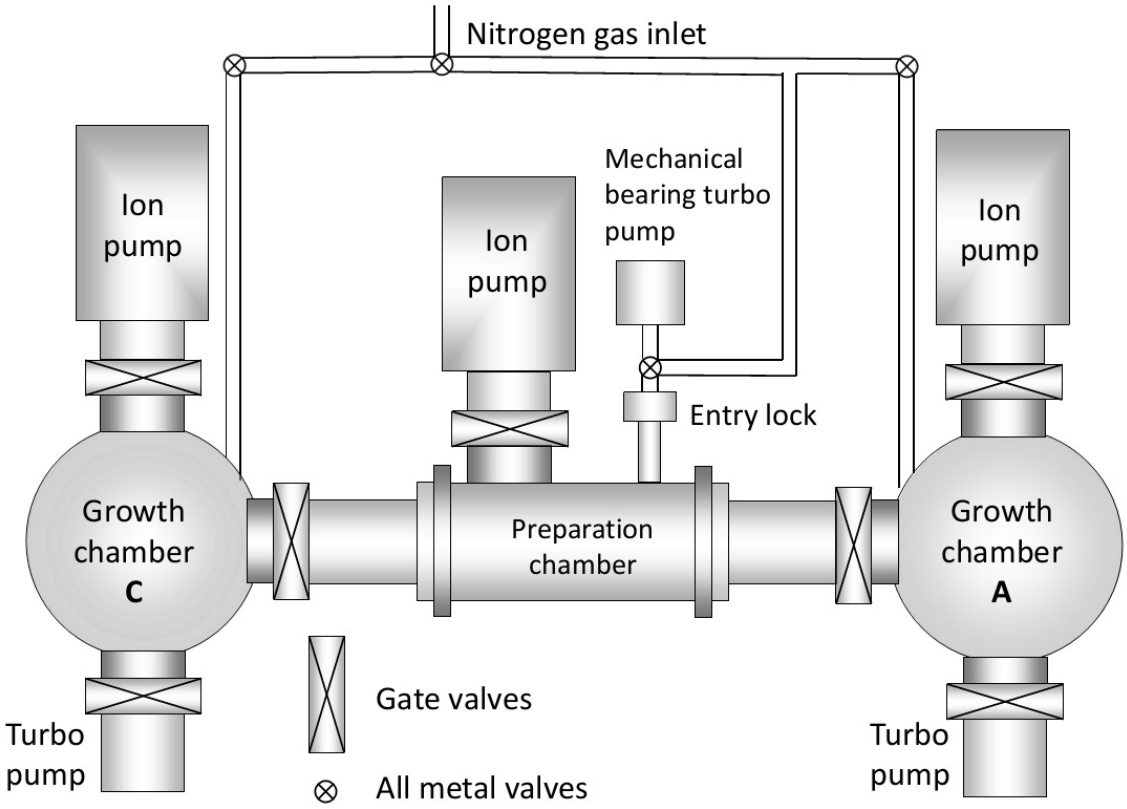

Figure 2.1: *Top elevation of the Heriot-Watt MBE system highlighting the external components*

2.2 MBE system design

The MBE system used at Heriot-Watt is a Vacuum Generators V80H machine, which is constructed from stainless steel. It consists of four vacuum chambers, separated by gate valves. It has two growth chambers on either ends which are connected by a preparation chamber, used for sample storage and the pregrowth outgassing of the substrate. A pulley driven railway system in the preparation chamber enables the transport of samples via a trolley to and from the growth chambers. In order to maintain the vacuum integrity of these chambers, samples are transferred to and from the MBE system via an entry lock, which can be evacuated to a pressure of $\sim 10^{-6}$ mbar in approximately 30 minutes by means of a rotary pump and a small turbo molecular pump. The growth chambers are named HWA and HWC, where HWC is the newest one, purchased in 2005 and almost all of the samples grown for this project were grown in chamber C. Samples from C chamber are numbered sequentially and given the prefix HWC. Both chambers are used for the growth of II-VI compounds. They each contain sources of Zn, Se, Cd, Mg and ZnS enabling the growth of a variety of binary, ternary and quaternary compounds. In addition, the A chamber contains sources for the growth of transition metal compounds.

To maintain system cleanliness, transition metal sources are not used in the C chamber.

2.3 Ultra high vacuum environment

Although pressures of $\sim 10^{-10}$ mbar are maintained during growth, pressures in the beam are $\sim 10^{-8}$ to 10^{-6}. These pressures ensure that the mean free path of the atoms effusing from the Knudsen cells is much larger than the size of the chamber and hence intermolecular collisions are negligible.

2.3.1 Pressure measurement

Pressure measurement is very important in a UHV environment. A pressure gauge capable of measuring pressures from atmosphere to UHV has not yet been developed. To monitor pressures in Heriot-Watt MBE system, two types of gauges are used. The choice of gauge used is dependent on both the residual gases in the vacuum and pressure range. Accurate pressure measurement of gas mixtures is a difficult process due to the difference in ionisation potential and cross section. Gauge errors and drift may also contribute to the accumulated inaccuracy of the measurement.

The ultra high vacuum in both the growth chambers and preparation chamber is measured by Bayard-Alpert ionisation gauges. In ion gauges, electrons are emitted by a cathode or filament and accelerated towards an anode grid. These ions may collide with and ionise molecules in this journey. A collector held at the earth potential attracts the ions. The collector current depends on the number of ions reaching it, which is dependent on the pressure. Ion gauges operate in the range of 10^{-4} mbar to 10^{-11} mbar and so is ideal for pressure measurement in the UHV chambers. The upper limit is reached when pressure is high enough for an electron to ionise more than one molecule after emission by the filament. The lower limit comes from photoelectrons leaving collector due to the X-rays emitted when electrons strike the anode grid. During growth, the normal operating pressure is $\sim 10^{-10}$ mbar.

2.4 MBE Growth Chamber

The crystal growth technology of molecular beam epitaxy involves generating fluxes of molecules which react at a substrate to form a layered deposit in a UHV environment such that the molecules do not undergo any collisions between source and substrate. The growth sources are contained in Knudsen cells (K-cells), which are aligned in line of sight of the substrate. Heating the source causes material at the surface to evaporate in all directions and some material travel towards the substrate. As previously mentioned, the mean free path of the molecules are $\sim$ 50m with respect to the growth chamber diameter of $\sim$ 1m and is in the molecular flow regime, giving the term molecular beam. This ensures that the molecules travel uninterrupted to the substrate.

When reaching the substrate surface, various elements and compounds react each other and form compounds bonded to the surface below them. This way the materials grow epitaxially and hence the process is called Molecular Beam Epitaxy. In MBE, the composition of the surface can be changed in under a monolayer (2.8 Å for ZnSe based structures) for, enabling the growth of high quality multilayers and quantum confined structures. Surface migration is one of the key aspects of MBE growth, where the incident atoms move around the surface to find suitable bonding locations. This ensures the formation of a homogeneous surface as the growth progresses. The surface migration of atoms is influenced by various growth parameters including growth temperature, growth interruptions and material fluxes. A typical atom can move around the growth surface for up to several tens of nanometers.

A schematic of the HWC growth chamber, which was used for all the growths described in this thesis, is shown in Figure 2.2. The source flange of the chamber has eight ports, which house the K-cells. The HWC chamber uses the II-VI elemental sources of zinc (6N), selenium (6N), cadmium (6N), Magnesium (5N8) and a compound source of ZnS (6N). Other ports accommodate the high and low pyrometers, quadruple mass spectrometer and RHEED gun. A viewing port is used to enable the alignment of the pyrometers on the substrate surface. Another viewing port is used to facilitate the sample loading/unloading on the manipulator. The substrate arm provides heating and rotation of the wafer during the growth.

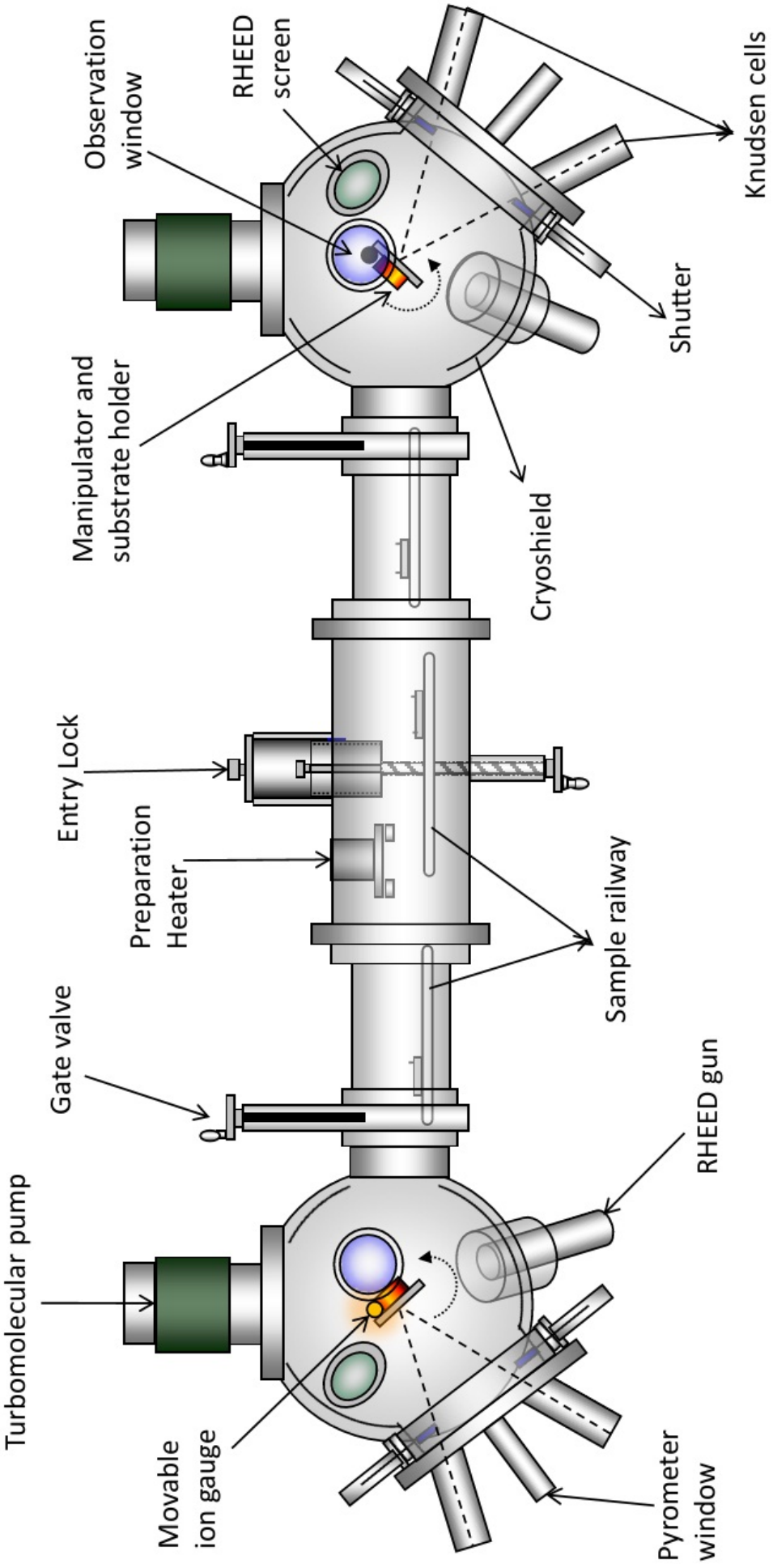

Figure 2.2: *Schematic of the side elevation of the V80H MBE system at Heriot-Watt MBE facility.*

2.4.1 Cell fluxes

Shutters placed in front of the cells provide means of flux control. The rates of growth and the compositions of the epitaxial layers are determined by the amount of material reaching the substrate surface and by the substrate temperature. The source cell temperature determines the rate of thermal effusion of the material and is proportional to the vapour pressure for the element or compound in respective cells. By taking a reading of the flux from a cell, the amount of material effused can be measured. A Bayard-Alpert type ion gauge fixed behind the manipulator is turned towards the growth position to measure the fluxes in Beam Equivalent Pressures (BEP). The material flux is proportional to the current at the collector of ion gauge. A pico ammeter is connected to the ion gauge on the other end, which reads the flux in nano ampere (nA).

2.5 Substrate temperature measurement

The temperature of the substrate is crucial to the effectiveness of the chemical reactions taking place on its surface. The atomic processes effective during the growth including adsorption, desorption, migration and reaction are sensitive to temperature fluctuations. Therefore it is very important to achieve accurate temperature control of the substrate to maintain a constant growth rate and ensure superior crystalline quality of the material produced. Thermocouples and pyrometers are used to control the substrate temperature at Heriot-Watt MBE system.

2.5.1 Thermocouple Measurements

A thermocouple is formed at the junction of two dissimilar metals, which produce a voltage in the vicinity of the point where the two conductors are in contact. A small voltage is produced, typically in the mV range and is highly dependent on, but not necessarily proportional to, the difference of temperature of the junction to other parts of those conductors. Therefore by choosing the correct thermocouple type to reflect the

temperature range over which control is required, a very effective means of temperature measurement is obtained. As the thermocouple is made from two strands of wire, connected only at the junction, it can be designed into the UHV component to provide the best position for temperature control.

For the substrate temperature control, a C type thermocouple is used, which is made of a tungsten/rhenium (W/Re) alloy. This material is used in order to withstand the high temperatures and corrosive environment found in an MBE system. The thermoelectric emf generated by the thermocouple is measured by the PID temperature controller which can remotely control the heater power supply to provide a stable measurement-control loop. Such a control circuit is used to enable active control of the heater temperature through the means of a feedback loop. Individual PID parameters are fine tuned to ensure temperature overshoots and oscillations are minimised.

Correct positioning of the thermocouple is imperative in obtaining an accurate temperature measurement. The substrate needs to be rotated during the growth and so positioning the thermocouple in direct contact with the substrate is not practical. Hence it is necessary to position the thermocouple directly behind the substrate heater. This result in a temperature offset with respect to the substrate surface and thus introduces a systematic error to the measurement. This offset can also be strongly affected by other factors, including the thickness and finish of the molybdenum transfer block and the emissivity of the surface/deposited layer.

There were problems associated with the thermocouple based temperature measurement during the growths carried out in the beginning of this project, because of an improperly connected thermocouple head in the substrate manipulator. Due to the difficulties in fixing this problem, the entire manipulator has been replaced. This is detailed in Chapter 4.

2.5.2 Pyrometer Measurements

The problems described above, associated with the thermocouple based temperature measurements are largely resolved by the use of infrared pyrometry. Optical pyrometry provides

a valuable means of indirectly measuring the substrate temperature, and it is a non-contact form of measurement. This is necessary as the sample is mounted on a solid molybdenum block with the thermocouple behind the block and in front of the heaters with no thermal contact with both. Due to this reason, a temperature offset is apparent between the thermocouple and pyrometer temperature readings.

Two Ircon Mirage optical pyrometers were used for the temperature measurements of the substrate at Heriot-Watt. The low temperature pyrometer covers the range from $120^{o}C - 310^{o}C$ and is used to measure the growth temperature of the samples. The high temperature pyrometer has a range of $250^{o}C - 700^{o}C$ and is used to monitor the temperature during the oxide desorption of the respective substrates used.

An optical pyrometer works on the principal that the intensity of radiation emitted from a body is dependent on the temperature of the body as described by Stefan's law:

$$\mathrm{H} = Ae\sigma T^4 \tag{2.1}$$

where, H is the heat current due to radiation, A is the surface area, e is the emissivity, σ is Stefans constant = $5.6699 \times 10^{-8} Wm^{-2}K^{-4}$, and T is the absolute temperature of the body [2]. In this way a temperature measurement can be made without direct contact to the substrate. The pyrometer sensors detect the incident photon flux from the substrate and convert it into an electrical signal. This signal is coupled through the signal cable to the detector, where it is linearised and scaled to the temperature range of the system.

The temperature measured may not be the true temperature reading of the sample surface. A combination of various components can contribute to the total measurement error in the system (ΔT_{system}), represented by:

$$\Delta \mathrm{T}_{\mathrm{system}} = \left[\Delta \mathrm{T}_{\mathrm{emissivity}} + \Delta \mathrm{T}_{\mathrm{transmission}} + \Delta \mathrm{T}_{\mathrm{background}}\right] + \Delta \mathrm{T}_{\mathrm{instrument}} \tag{2.2}$$

In the above equation, parts within the square bracket represent application errors that can be controlled manually and are the main contributors to the total error. Precautions must

Target Temperature (^oC)	$\Delta T_{table}(^oC)$
0	0.12
100	0.22
200	0.36
300	0.53
400	0.73
500	0.96
600	1.2
700	1.41

Table 2.1: *Table used to determine temperature errors due to emissivity errors.*

therefore to be taken to keep these errors at minimum. The substrates used for the growth of samples mentioned in this thesis are transparent to the operating wavelength of the pyrometers, $\sim 2.3\mu m$. Hence measurement is made of the indium solder used for mounting through the substrate. The use of these long wavelength pyrometers helps to eliminate the errors due to reflections of evaporation sources and hot filaments ($\Delta T_{background}$).

Although the substrates are largely transparent in the measurement regime of the pyrometer, there still is some free carrier absorption of long wavelength radiation. The pyrometer will only indicate the real temperature when their emissivity setting corresponds to that of the target. This necessitates the adjustment of the pyrometer emissivity setting for the substrate used ($\Delta T_{emissivity}$). The magnitude of a temperature error produced by the uncertainty of a given emissivity error depends on the spectral range of the pyrometer and the target temperature.

The Mirage pyrometer will indicate a temperature error of a magnitude shown in table corresponding to 1% emissivity errors [3], ΔT_{table}. Temperatures can be determined for emissivity errors greater than 1% by using the following equation:

$$\Delta T = -100 \times \frac{\varepsilon_{dial} - \varepsilon_{true}}{\varepsilon_{true}} \times \Delta T_{table} \tag{2.3}$$

where ε_{dial} is the emissivity setting on the instrument dial and ε_{true} is the true target

emissivity.

It is very important to have a clear optical path between the pyrometer and the sample. One of the most common errors is caused by the build-up of material on the pyrometer port window ($\Delta T_{transmission}$). To reduce this effect a shuttered UHV window was installed on the pyrometer port flange, facing substrate. The shutter was necessary to minimise the material deposited on the pyro window to ensure reproducible measurements, which were taken at intervals throughout the growth. The build-up is caused by the deposition from the background pressure of sulphur or from other sublimation of material from the substrate. By using the ion gauge filament as a reference point for temperature calibration, it is possible to compensate for this error. The emissivity settings can be adjusted until the same filament temperature is measured at the beginning of each growth. The pyrometer window was cleaned whenever the machine was brought up to atmosphere as an additional precaution against the deposition related effects.

2.6 RHEED

Reflection High-Energy Electron Diffraction (RHEED) is one of the most useful analytical tool for characterizing thin films during growth by molecular beam epitaxy, since it is very sensitive to surface structure and morphology. This technique is only available to UHV growth systems as it requires a collimated beam of electrons to impinge on the surface of the sample at a glancing angle producing a diffraction pattern which can be imaged. RHEED is particularly suited to MBE as the apparatus does not use the direction vertical to the surface of the crystal which is required for the arriving fluxes. It is also very sensitive to surface roughness, down to monolayer sensitivity. This allows the growth rate of layers of atoms on the surface to be monitored, by analysing the periodic variations of the RHEED intensity during growth, the so-called RHEED oscillations. By knowing both the distance from the sample to the screen or recording medium and the energy of the electron source, it is possible to calculate the lattice spacings of the sample grown.

RHEED can provide valuable information including, observation of the removal of oxide layers from the substrate surface, calibration of the surface temperature and monitoring

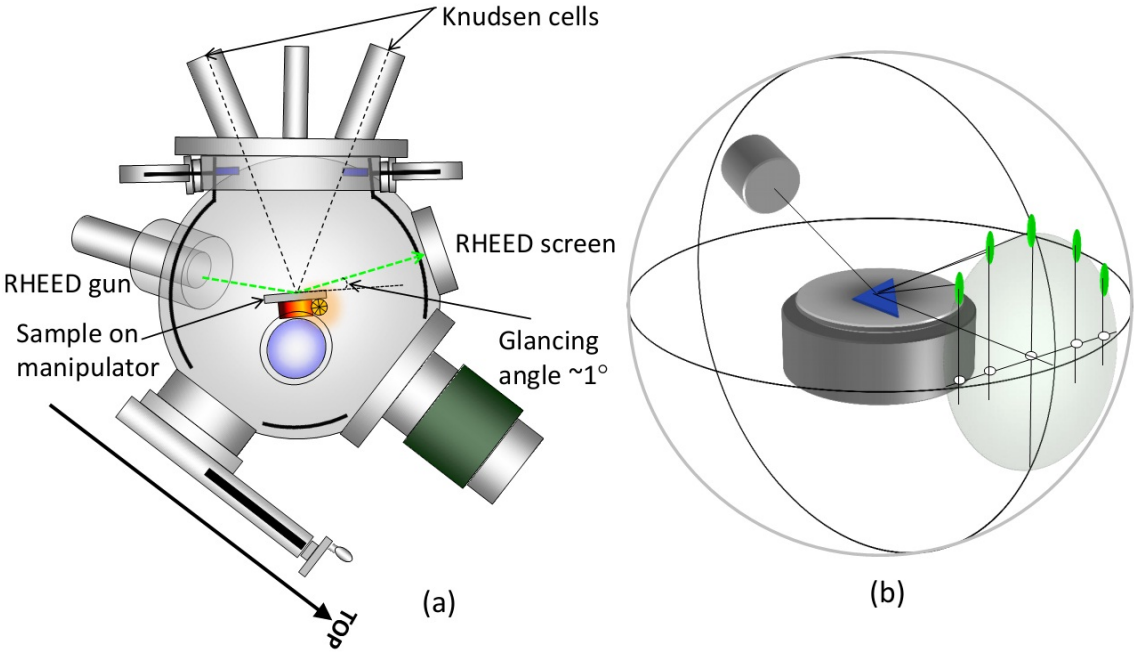

Figure 2.3: *Schematic of (a) the geometry of RHEED setup inside an MBE growth chamber and (b) interaction of the RHEED beam with a sample.*

the surface reconstruction of the material flux ratio. Information on the growth kinetics can also be obtained from RHEED patterns.

A RHEED system consists of an electron gun unit and a phosphor screen. In the C chamber, a RHEED gun from STAIB Instruments, which emits high energy electrons in the range of 0-15 keV was used. The inelastic scattering mean free paths of the beams are relatively long ($\sim 100 - 1000$Å) and hence the elastic scattering is strongly peaked in the forward direction with very little back scattering. At glancing angles of incidence, total external reflection of the beam occurs and thus the beam is diffracted out of the sample after penetrating only a few atomic layers. This results in a diffraction pattern that is determined by the periodicity of the sample surface.

2.6.1 Electron Diffraction

The reciprocal lattice of the surface of a flat semiconductor is an array of rods. These rods are perpendicular to the real surface because in reciprocal space the real lattice spacing is effectively zero in this direction [4]. Thus the electrons impinging the surface generate a diffraction pattern which depends on the coherency and lattice spacing of the surface. When the electron beam is reflected by the substrate, a strong interaction takes place with

the periodic electric potential of the surface. This incident electron wave is scattered by each atom in the periodic crystal which generates spherical scattering waves. The waves generated interfere and cancel each other in almost all directions.

Constructive interference will occur only where the Ewald sphere intersects with the reciprocal lattice rods. In practice the intersection occurs over an extended distance and a streaked pattern is obtained because of the following reasons:

1. The Ewald sphere is of finite thickness, because the incident electrons are never exactly monochromatic.

2. lattice vibrations and structural imperfections cause the reciprocal lattice rods to be of finite thickness.

3. diameter of the Ewald sphere is considerably larger than the spacing of the lattice rods.

RHEED is a very surface sensitive technique, which penetrates only the topmost layer of the crystal surface. Both the incident and reflected electron beams travel almost parallel to the sample surface. The very small glancing angle to the sample surface, $\sim 1^{o}$, causes the component of the electron momentum normal to the surface to be small (Figure 2.3). This limits the penetration depth of the primary electrons to the top few monolayers of the surface under investigation. The crystal periodicity perpendicular to the surface is absent and we are dealing with a 2D layer, rather than a 3D volume. The resulting RHEED pattern gives detailed information about the surface morphology of the surface layer during growth. As the layer grows layer by layer, RHEED intensity oscillations can be monitored to give detailed information on the surface migration kinetics [5].

Typical RHEED patterns observed during the growth of II-VI semiconductors are given schematically in Figure 2.4. The diffraction pattern of an amorphous surface is a series of concentric semicircles. These amorphous rings are observed in two different situations. First, they are produced during the coating of grown sample surfaces with amorphous selenium. The RHEED pattern transitions to and from the amorphous rings are vital for ensuring the deposition/evaporation of the selenium from the surface. Second, this pattern

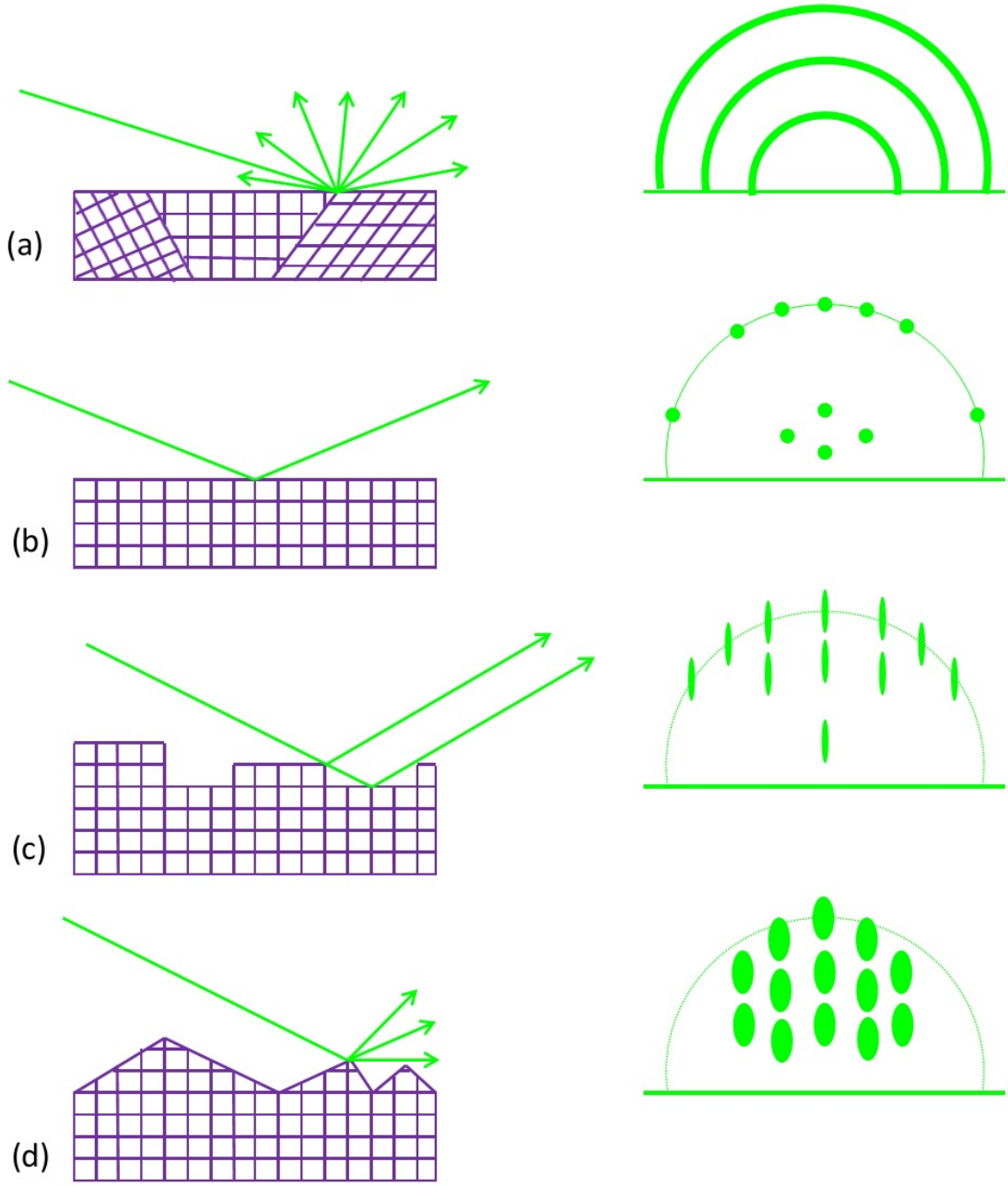

Figure 2.4: *Schematic of RHEED patterns for various surfaces; (a) amorphous surface (b) flat surface, (c) stepped surface and (d) rough surface with 3D features.*

is also observed during the heat clean procedure prior to the desorption of the oxide layer from the surface. During thermal desorption of the oxide layer, the RHEED patterns change from an initial diffuse glow to a sharply reconstructed surface pattern consisting of narrow streaks.

Once the oxide layer is removed a perfectly flat substrate surface is indicated by a circular pattern of diffracted spots which shows high contrast and low background intensity, indicating an ideal diffraction situation, referred to as a Laue circle. During growth, these spots typically become elongated, forming streaks. This elongation may be due to the

surface irregularities arising from a number of factors including, surface defects such as a stepped surface and the energy and angular spread of the incident electron beam.

The occurrence of significant surface roughening causes the incident electron beam to be diffracted into a series of discrete spots rather than the streaks obtained from a flat surface. However a streaked pattern can still be obtained if the epilayer surface undulates over distances appreciably greater than the electron beam coherence length [6] which is $\sim$ 150nm.

2.6.2 Surface Reconstruction

Surface reconstruction is a reordering of the outermost atomic layer(s) of a crystal to reduce the energy of the free surface [7]. Surface reconstruction of the semiconductor surfaces is one reason for, RHEED being such a useful tool for MBE *in situ* characterisation. This surface reconstruction is dependent on factors such as flux ratios, growth rate, temperature and surface species termination. Therefore, unique surface reconstruction patterns for different conditions are obtained and can be used as a system-independent monitor of the growth conditions [8]. Hence, RHEED is routinely used for the monitoring of many of the most important aspects of MBE growth such as:

1. thermal cleaning of the substrate prior to the growth.
2. selection of the correct flux ratios.
3. structural purity of the growing layer.
4. growth rate measurement.
5. deposition/evaporation of amorphous Se or As for sample preservation.

While initiating a II-VI semiconductor growth on a III-V substrate, a reconstruction of the surface is required to minimise the surface energy and maintain an average charge neutrality. [9]. As a result, termination of the lattice may lead to the modification of periodicity and loss of symmetry on the surface when compared to the bulk. Even though

the lateral periodicity may not necessarily be the same as the bulk, it is in close contact with it and therefore there is typically a multiple or submultiple of it.

The structure and composition of the ZnSe (100) surface has been studied during Atomic Layer epitaxy (ALE) growth using RHEED [10]. Two different surface reconstructions are observed: the Se terminated (2×1) dimer reconstruction when the Se beam is applied and the Zn terminated $c(2 \times 2)$ when the Zn beam is applied. This second pattern is a Se vacancy structure.

The ALE growth results in a growth rate of 0.5 ML per ALE cycle, which is expected from the alternate formation of the (2×1) Se dimer and $c(2 \times 2)$ Se vacant dimer.

2.7 Heteroepitaxial Growth

The process of the deposition of a single crystalline semiconductor layers on a single crystalline semiconductor substrate is epitaxy. To occur, there must be one or more preferred orientations of the epitaxial layer with respect to the substrate for this to be termed epitaxial growth.

In heteroepitaxy, an epitaxial layer grows on a crystalline substrate or film of a different material. Lattice mismatch has a noticeable effect on film morphology. The strain resulting from lattice mismatch contributes to the interface energy, a crucial parameter in determining the growth mode. However, the surface free energies for the substrate and epilayer materials also influence the mode of growth. Essentially it is a result of the competition between the kinetic energy of adatoms and the free energies of the bulk surfaces and interfaces.

Heteroepitaxy is regularly used to grow semiconductor epilayers of materials for which crystals cannot otherwise be obtained and to fabricate integrated crystalline layers of different materials. The heteroepitaxial growths of thin films in general has been placed in one of the three primary modes, depending on the resulting epilayer morphology, described below (Schematically shown in Figure 2.5).

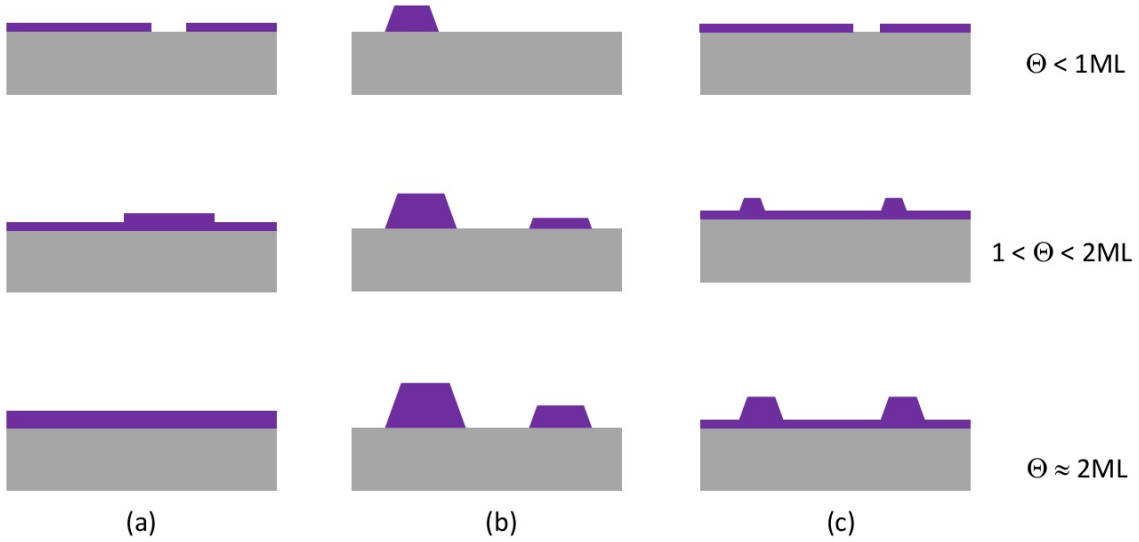

Figure 2.5: *Cross-section views of the three MBE thin film growth modes; (a) Frank-van der Merwe (FM: layer-by-layer), (b) Volmer-Weber (VW: island formation), and (c) Stranski-Krastanov (SK: layer-plus-island). Each mode is shown for several different amounts of surface coverage,* Θ.

2.7.1 Frank-van der Merwe (FM)

This is a layer by layer growth mode, mostly found in lattice matched combinations of material systems. The interatomic interactions between substrate and epilayer materials are stronger and more attractive than those in between the different atomic species within the epilayer material in FM growth mode. Here, adatoms attach preferentially to surface sites resulting in atomically smooth, fully formed layers. This layer-by-layer growth is two dimensional; indicating that complete films form prior to growth of subsequent layers [11, 12].

Bauer and Frank-van der Merwe expressed the energetics of film growth in a very simple form under the assumption of equilibrium between the layer components in the gas phase and those in the layer surface [13]. In this formalism, layer-by-layer growth of epilayer on substrate requires,

$$\Delta\gamma = \gamma_{\text{epi}} + \gamma_{\text{int}} - \gamma_{\text{sub}} \leq 0 \tag{2.4}$$

Where, γ_{epi} and γ_{sub} are the surface free energies of the epilayer and substrate, respectively, and γ_{int}, the interfacial free energy. The free energy of interface depends on the strain and the strength of chemical interactions between the epilayer and substrate at the interface. Therefore FM growth mode takes place when the sum of the epilayer surface

energy and the interface energy is lower than the energy of the substrate, resulting in the deposited layer wetting the substrate:

$$\gamma_{\text{epi}} + \gamma_{\text{int}} < \gamma_{\text{sub}} \tag{2.5}$$

Alternatively, it becomes easier for layer-by-layer growth to occur as the surface energy of the substrate increases. Thus, FM growth is expected if Equation 2.4 is obeyed.

2.7.2 Volmer-Weber (VW)

In Volmer-Weber growth, adatom-adatom interactions are stronger than those of the adatom with the surface, leading to the formation of three-dimensional adatom clusters or islands [12]. Growth of these clusters, along with coarsening, will cause rough multilayer films to grow on the substrate surface. This growth mode is characteristic of highly mismatched combinations of semiconductors.

When γ_{epi} is sufficiently in excess of γ_{sub}, Equation 2.4 will never be fulfilled even for a strong attractive interaction between the epilayer and substrate and little strain ($\gamma_{int} < 0$). In this case, three dimensional islands nucleate from the onset resulting in VW growth. In other words, VW growth takes place when the sum of the epilayer surface energy and the interface energy is greater than the surface energy of the substrate:

$$\gamma_{\text{epi}} + \gamma_{\text{int}} > \gamma_{\text{sub}} \tag{2.6}$$

2.7.3 Stranski-Krastanow (SK)

Stranski-Krastanov growth is a transitional process categorized by both 2D layer and 3D island growth. Also known as 'layer-plus-island growth', the SK mode follows a two-step process: initially, complete films of adsorbates, up to several monolayers thick, grow in a layer-by-layer fashion on a substrate. Transition from the layer-by-layer to island-based growth occurs at a critical layer thickness which is highly dependent on the chemical and physical properties, such as surface energies and lattice parameters, of the substrate and

epilayer [11, 12, 14].

The strain energy, which is a term in γ_{int} , increases linearly with the number of strained layers. At a critical thickness, $\gamma_{epi} + \gamma_{int}$ exceeds γ_{sub} and the growth mode transforms from FM to SK resulting in 3D islands on the 2D wetting layer.

This is a very important mode of heteroepitaxial growth and is discussed in detail in section 3.4.

2.8 Growth techniques

The epitaxial layers in each sample grown at Heriot-Watt are typically fabricated using one of the three MBE growth variants namely, normal MBE growth, atomic layer epitaxy and migration enhanced epitaxy.

1. MBE: This is the standard growth technique used for the growth of majority of the samples. Here, shutters for all the cells necessary for a particular epitaxial layer are open simultaneously and the thickness of the layer increases linearly with time.

2. Atomic Layer Epitaxy (ALE): This is a modified version of the normal MBE growth mode, where instead of opening the all the shutters together, they are instead opened one at a time so that half a monolayer of each material (metal or non-metal) are sequentially deposited. This growth works best for binary compounds, whereas it would be necessary to open either all the metallic or non-metallic shutters together for ternary and quaternary alloys.

3. Migration Enhanced Epitaxy (MEE): This is a further modified version of ALE, where a growth delay is introduced between closing one shutter and opening another shutter to enhance the deposited material to migrate around the surface so as to produce a smoother layer surface.

Both ALE and MEE are primarily used during deposition of the quantum dot materials as these techniques enable precise control of thickness. Furthermore sometimes these techniques are also used to provide a smoother finish to the MBE as-grown epitaxial layer surfaces before depositing another layer.

2.9 Zinc Blende (ZB) crystal structure

ZnSe based semiconductor alloys, in common with many II-VI and III-V compounds have the zinc blende (ZB) structure. While the stable crystal structure of MgS is rock salt (RS), the focus of the work in this thesis was on the ZB structure of MgS. Similarly CdSe can exist in hexagonal wurtzite form, but only the ZB structure is produced in this thesis.

In the case of ZnSe, the ZB structure can be demonstrated in two ways. First, it can be seen as two interlaced face centred cubic (FCC) lattices, one of zinc atoms and one of selenium atoms. If a zinc atom is placed at the origin of a 3D Cartesian graph, then the corresponding origin of the selenium lattice would be at $(1/4, 1/4, 1/4)$, as shown in Figure 2.6.

In terms of bonding, each atom is bonded to four of the other type arranged tetrahedrally. The bonding between the Zn and Se atoms and some of the important planes are shown in Figure 2.7 [15].

It can be seen from this figure that if the zinc blende structure is cut along the (111) plane, then one side will terminate in A-atoms triple bonded to the crystal (known as the (111)A surface) and the other side will terminate in B-atoms triple bonded to the surface (known as (111)B surface). A-atoms are defined as the lower valence element (zinc) and B-atoms as the higher valance element (selenium) [16]. All of the samples mentioned in this thesis were grown on a (100) plane.

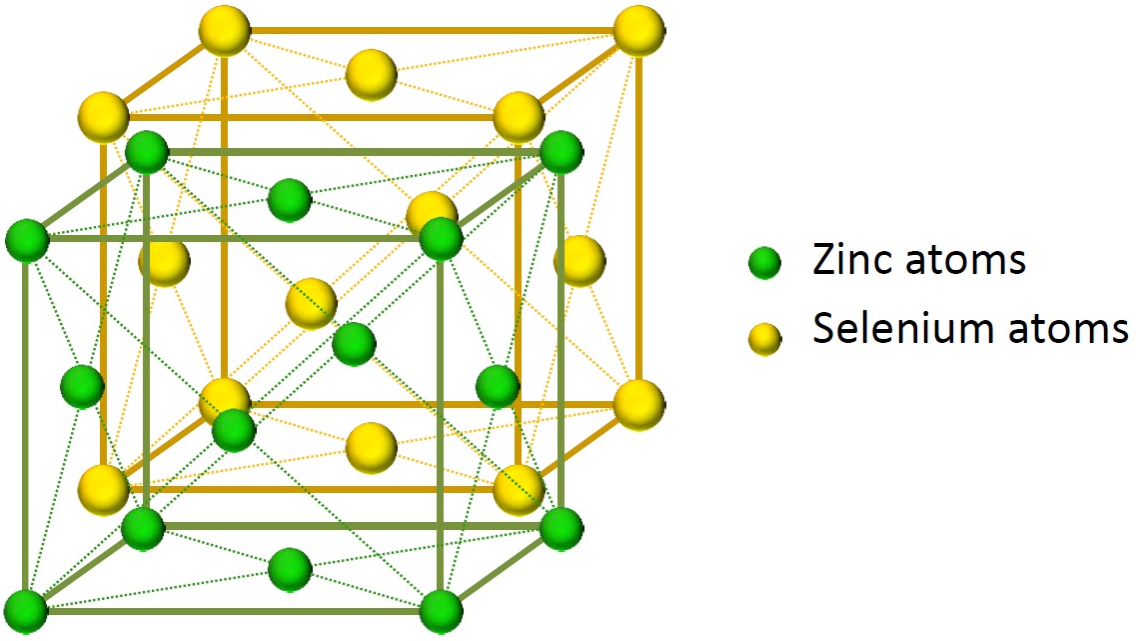

Figure 2.6: *Schematic of zincblende structure for ZnSe displayed as two interlaced face-centred-cubic lattices.*

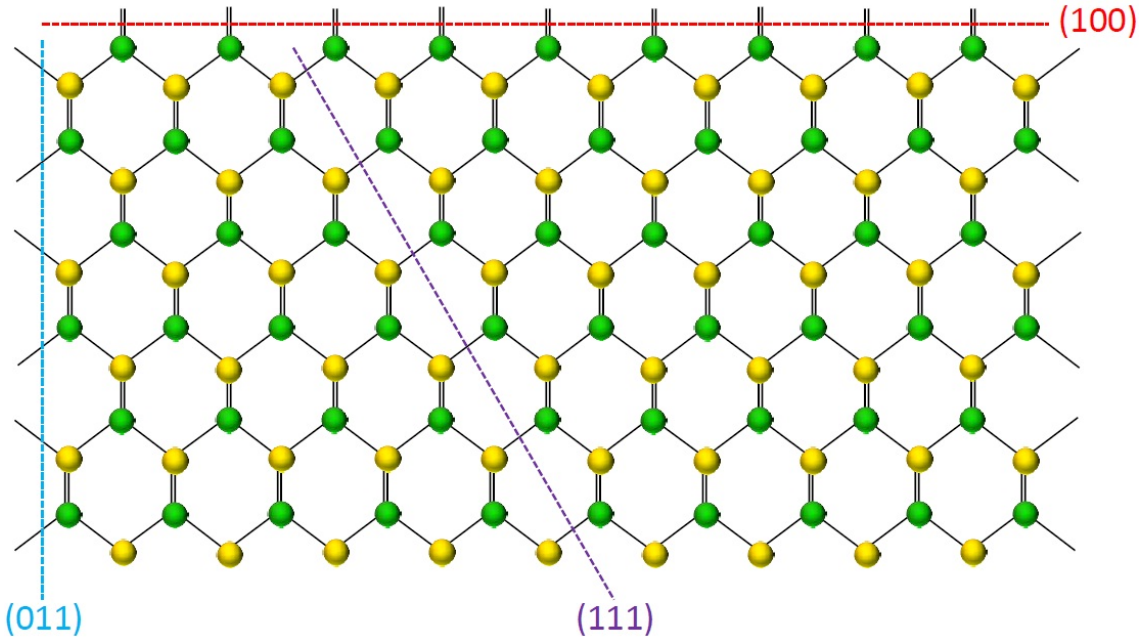

Figure 2.7: *Schematic of zincblende structure for ZnSe showing the bonding between the atoms. Each single line is a bond on the surface of the page $(00\bar{1})$. Each double line represents two bonds, one going diagonally up and one going diagonally down to two different atoms, either of which could be represented by the atom on the figure. The traces of three common planes are marked.*

2.10 Characterisation techniques

Characterisation techniques are used in order to gain knowledge on the structural, optical, and electrical properties of semiconductor materials. Two types of contactless, non-invasive procedures are used here extensively. X-ray techniques can reveal information about the composition, thickness and quality of the materials examined. Optical spectroscopy techniques are sensitive enough to reveal some details of the electronic structure of low dimensional semiconductor materials. These characterisation techniques are instrumental in understanding the most important properties of various semiconductors as building blocks of many useful electronic and optoelectronic devices and also an invaluable aid to improving the structural quality of materials and devices.

2.11 X-ray Diffraction

The completely non-destructive X-ray diffraction (XRD) method has long provided a reliable means to evaluate crystalline materials parameters where modest material volumes are available, but the increasing reduction in size of devices and the increasing importance of thin film structures has brought the need for microstructural characterization methods with high strain sensitivity. Double Crystal X-Ray Diffraction (DCXRD), utilizes the inherent narrowness of X-ray rocking curves ($\sim$ 1 arc sec) to offer strain sensitivities of 10^{-4} to 10^{-8}. DCXRD methods rely on the sharpness of the rocking curve and the precision with which its width, shape and position can be deduced independently of instrumental broadening. This method is particularly applicable to the characterization of multiple epitaxial layers fabricated by MBE growth.

X-ray diffraction employs electromagnetic waves with a wavelength of the order of one angstrom. Diffraction of x-rays occurs when a plane wave front of x-ray photons collides with matter. Electrons in the material interact with the x-rays, re-emitting an electromagnetic photon which travels outwards with a spherical wave front. This process normally takes place without any energy losses and is known as coherent scattering. Since, wave diffraction occurs when the dimensions of the diffracting object are of the same order

of magnitude as the wavelength of the incident wave, x-rays are ideally suited to probe crystal lattice structures [17].

X-ray measurements on semiconductor materials can obtain information such as:

1. Lattice constants: Lattice mismatch between the epilayer and the substrate perpendicular to the growth plane can be determined from the separation of the peaks. Lattice mismatch is also indicative of stress and strain.

2. Dislocation density: The Full Width at Half Maximum (FWHM) of the x-ray rocking curve, is inversely related to the number of dislocations in the epilayer.

3. Layer thickness: Obtained from the ratio of layer peak area to substrate peak area, or layer peak fine structure (Pendellösung fringes).

4. Thickness and quality of super lattices: The thickness is determined from the angular distance between the satellite peaks appearing on the sides of the main peak, while the intensity and number of satellite peaks is a measure of the film quality.

5. Variation of composition with thickness: From changes in rocking curve shape.

6. Strain components perpendicular and parallel to the interface: using reflecting planes either parallel or at some angle to the interface plane.

2.11.1 Rocking curves

A Rocking curve is a plot of diffracted intensity versus angular position, θ of the sample [18] (see Figure 2.8). By rotating the sample through small angles about both the vertical rotation axis and the tilt axis of the sample stage, rocking curves can be obtained. The x-ray data used in this thesis were collected by using the $\theta - 2\theta$ scan, where the sample and detector are scanned through angles with a 1:2 ratio, while the detector aperture is restricted with a slit in order to reduce the scattered and background radiation. (Figure

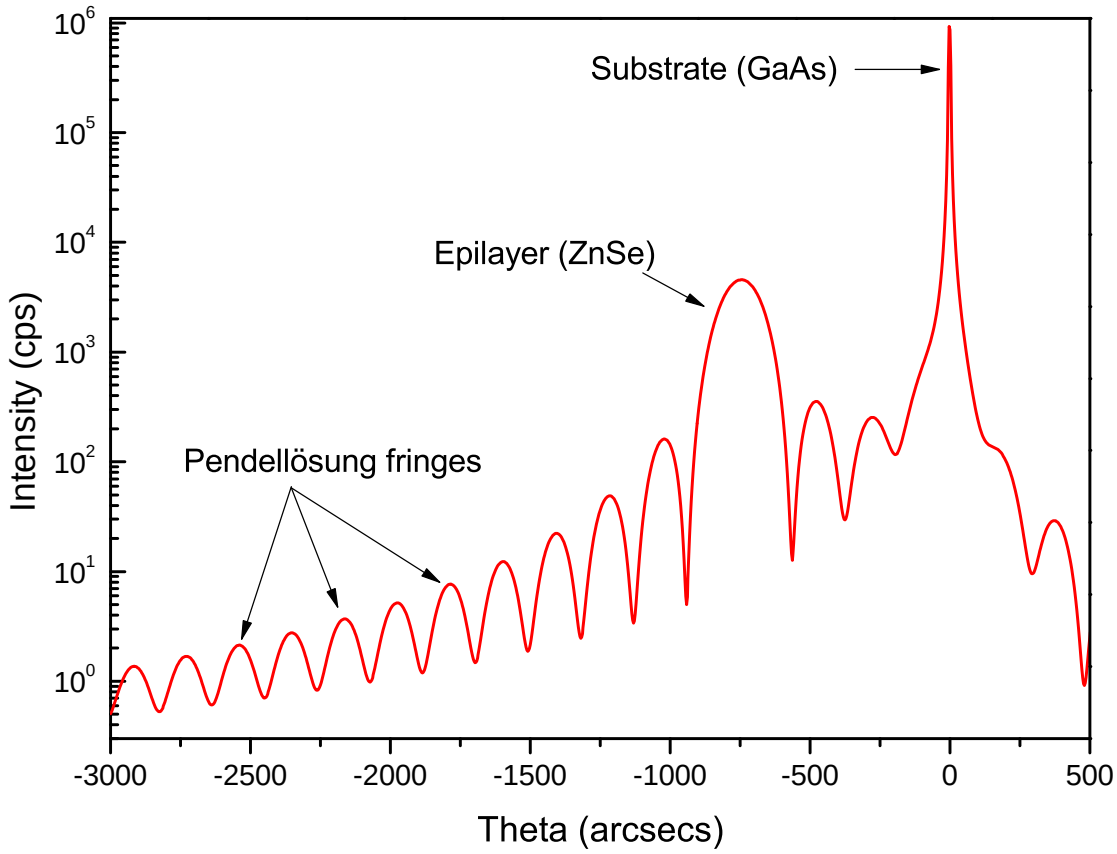

Figure 2.8: *Typical 004 X-ray simulated rocking curve for a 100 nm fully strained ZnSe epilayer on GaAs substrate showing the main features.*

2.9)

The Bragg angle, θ_{epi} of the epilayer can be found from:

$$\theta_{\text{epi}} = \theta_{\text{sub}} + \Delta\theta_{\text{epi}} \tag{2.7}$$

Where $\Delta\theta_{epi}$ is the angular splitting given by the separation of the layer peak from the substrate and θ_{sub} is the Bragg angle for the lattice spacing of the substrate.

The analysis of the rocking curves can be simplified by using simulation software such as Jordan Valley RADS (Rocking Curve Analysis by Dynamical Simulation). This software package uses the Takagi-Taupin equations to simulate the diffraction of X-rays through a crystal [19]. These simulations can then be compared to the experimental data using a Goodness of Fit (GOF) merit figure and information about strain, thickness and composition can be calculated. The GOF is a chi squared statistic which ranges from 0 to 1 where

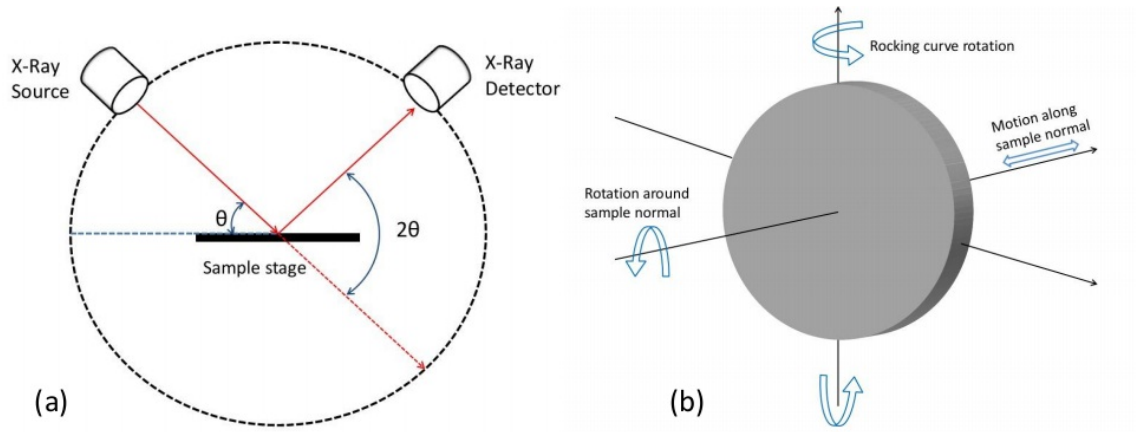

Figure 2.9: *Schematic of (a) $\theta - 2\theta$ scan and (b) Degrees of freedom of sample stage.*

0 represents a perfect match (Equation 2.8).

$$\chi^2 = \sum_{i=j}^{k} [\log(y_i^{ref}) - \log(y_i^{comp})]^2 \tag{2.8}$$

where, y_i^{ref} is the ordinate of the reference data and y_i^{comp} is the ordinate of the comparison, and j and k are the indices of the first and last points defining the overlapping of the two data sets. If the two data sets become more alike, the GOF value reduces.

2.11.2 Bragg's Law

Bragg's law gives the angles for coherent and incoherent scattering from a crystal lattice and forms the foundation of X-ray diffraction [20]. When a crystal plane is bombarded with X-rays of a fixed wavelength and at a glancing angle θ, intense reflected X-rays are produced when the wavelengths of the scattered X-rays interfere constructively. Constructive interference will occur when the travel path length difference between the rays diffracting from consecutive parallel planes is equal to integer multiples of the wavelength. When this constructive interference occurs, a diffracted beam of X-rays will leave the crystal plane at an angle equal to that of the incident beam, θ.

The general relationship between the wavelength of the incident X-rays, angle of incidence and spacing between the crystal lattice planes of atoms is known as Bragg's Law, expressed as:

$$\lambda = 2d_{hkl}\sin\theta \tag{2.9}$$

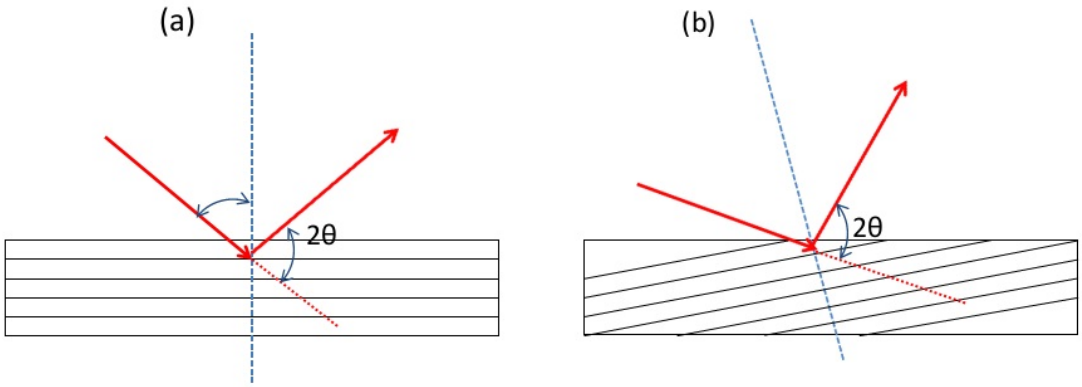

Figure 2.10: *Schematic of (a) symmetric (e.g. 004) and (b) asymmetric (e.g. 115) planes*

Where, λ is the wavelength of the incident X-ray photons, d is the inter-planar spacing of the crystal plane and θ is the angle of incidence.

2.11.3 Reflections

Reflections from the samples fall into two categories, symmetric and asymmetric. The set of planes undergoing diffraction are parallel to the surface in symmetric reflection. Whereas in asymmetric reflection, there is a non-zero angle between the planes and the surface (see Figure 2.10). There are two possible angle of entry for asymmetric reflections as an X-ray can travel the reverse path just as easily. Entry angles less than the Bragg angle for the reflection are known as glancing incidence reflections, ω_-, while exit angles less than the Bragg angle are known as glancing exit reflections, ω_+, given by:

$$\omega_- = \theta - \phi \tag{2.10}$$

$$\omega_+ = \theta + \phi \tag{2.11}$$

The interplanar angle, ϕ between two planes, the diffracting plane (hkl) and the sample surface $(h'k'l')$ in a cubic crystal can be derived using Equation 2.12 [21]:

$$\cos\phi = \frac{hh' + kk' + ll'}{\sqrt{h^2 + k^2 + l^2}\sqrt{h'^2 + k'^2 + l'^2}} \tag{2.12}$$

For a (001) surface, Equation 2.12 reduces to:

$$\cos\phi = \frac{l}{\sqrt{h^2 + k^2 + l^2}} \tag{2.13}$$

In a symmetric scan, strain and compositional changes produce similar peak shifts in rocking curves and hence cannot distinguish between strain and compositional changes. Thus, in order to quantify both strain and composition, a symmetric scan must be combined with an asymmetric scan.

2.12 Atomic Force microscopy (AFM)

Atomic force microscopy (AFM) is a high-resolution type of scanning probe microscopy, which can be used to measure the three-dimensional topography of a sample surface with demonstrated subnanometer resolution, more than 1000 times better than the optical diffraction limit. The size of the features imaged with the AFM is typically less than the visible wavelength of electromagnetic spectrum and hence the information obtained from the sample surface is processed electronically.

The AFM consists of a cantilever with a sharp tip which is used to scan the sample surface. The cantilever is typically made of silicon with a tip radius of curvature on the order of nanometres. When the tip is brought into proximity of the sample surface, forces between the tip and the sample surface lead to a deflection of the cantilever according to Hooke's law. Depending on the tip and sample used, forces that are measured in AFM include mechanical contact force, van der Waals forces, capillary forces, chemical bonding, electrostatic forces, magnetic forces (if using magnetic tips), Casimir forces, solvation forces, etc. This deflection in motion is monitored with a split photodiode detector using a laser spot reflected from the top surface of the cantilever. Scanning the tip at a constant height risks the possibility of the tip colliding with the surface, causing damage. Therefore, a feedback mechanism which works using the signal obtained by the photodetector is employed to adjust the tip to sample distance to maintain a constant force between the tip and the sample.

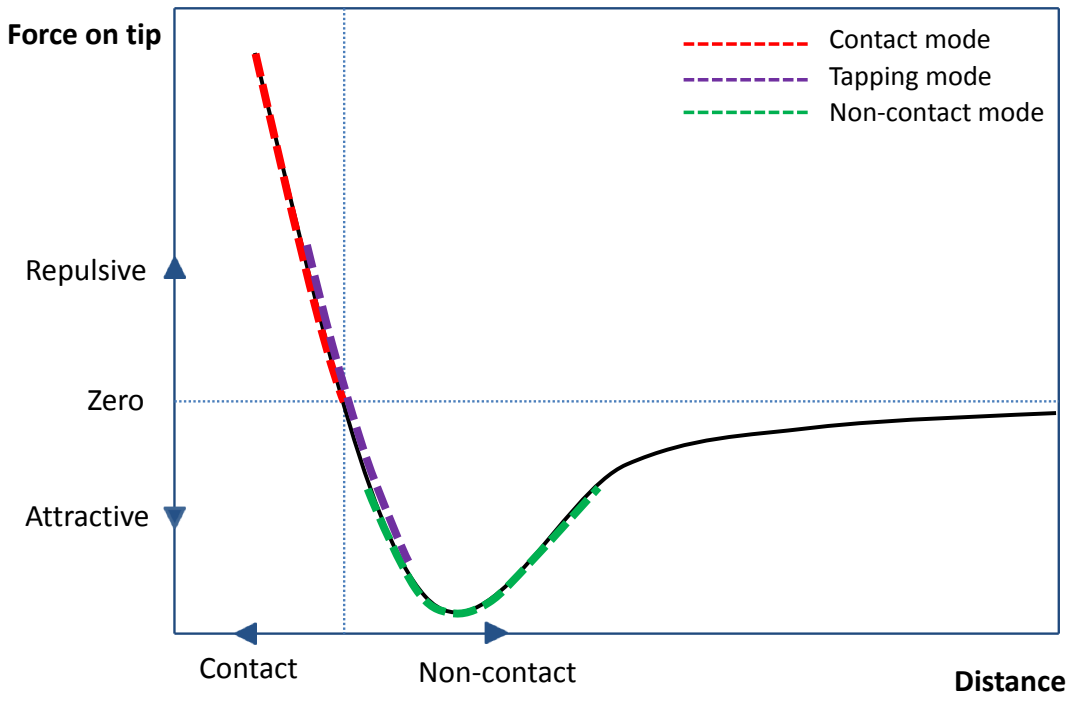

Figure 2.11: *Graph of AFM tip-to-sample separation versus van der Waals forces*

Various modes of operation can be adopted and although the feedback mechanism performs in effect the same function, the signal processing will change depending on the mode used. Contact mode and tapping mode were used for characterising samples grown for the works described in this thesis.

2.12.1 Contact mode

In contact mode AFM, the tip scans the sample in close contact with the surface. The force on the tip is repulsive with a mean value of $\sim 10^{-9}$ N. This force is set by pushing the cantilever against the sample surface with a piezoelectric positioning element. Here the deflection of the cantilever and the laser beam is sensed and compared in a DC feedback amplifier to some desired value of deflection. If the measured deflection varies from the desired value, the feedback amplifier applies a voltage to a piezo crystal on which the cantilever is mounted, to raise or lower the cantilever height relative to the sample surface to restore the desired value of deflection. The voltage that the feedback amplifier applies to the piezo in order to achieve this is a measure of the height of features on the sample

surface. This information is displayed as a function of the lateral position of the sample by the computer to form a topographic image of the sample surface.

2.12.2 Tapping Mode

Tapping mode is a rather new advance in AFM technology which allows high resolution topographic imaging of sample surfaces that may be easily damaged, loosely held to their substrate, or difficult to image by other AFM techniques. Tapping mode helps to overcome the problems, associated with friction, adhesion, electrostatic forces, and other difficulties typical to conventional AFM scanning methods by alternately placing the tip in contact with the surface to provide high resolution and then lifting the tip off the surface to prevent dragging the tip across the surface.

Tapping mode imaging is executed by oscillating the cantilever assembly at or near the cantilever's resonant frequency by means of the piezoelectric crystal. The piezo motion results in the cantilever to oscillate with high amplitude ranging typically from 20 to 200 nm, when the tip is not in contact with the surface. The oscillating tip is then moved toward the surface until it begins to lightly touch surface. While scanning, the vertically oscillating tip intermittently contacts the surface and lifts off at a frequency of $\sim$ 50 to 500 kHz per second. As the cantilever begins to intermittently contact the surface, the oscillation is necessarily reduced due to energy loss caused by the tip contacting the surface and this reduction in oscillation amplitude is used to measure the surface features. A schematic of the van der Waals forces acting on the tip with respect to the tip-to-sample separation is given in Figure 2.11. In tapping mode operation, the cantilever oscillation amplitude is maintained constant by a feedback loop.

Majority of the AFM images used for this thesis were produced using tapping mode of AFM.

2.13 Photoluminescence Spectroscopy

Photoluminescence spectroscopy (PL) is a characterisation method provides sensitive analysis of material quality. It is a non-contact, non-destructive technique used for probing the electronic structure of semiconductors. Any impurities or defects which provide optical traps produce transitions at specific energies which will show up on the spectra.

Photoluminescence occurs when a semiconductor is subjected to above band gap radiation. Light with photon energy greater than that of the band gap of the sample is directed onto the surface. Photo-excitation causes the light to be absorbed resulting in electrons being excited from the valence band to the higher energy states in conduction band [22]. Simultaneously holes with a positive charge are created in the valance band. The electron-hole pairs may be bound by coulombic attraction, forming excitons. This coulombic interaction is responsible for the exciton binding energy and for a given state n given by:

$$\mathrm{E_x^n} = -13.6\frac{\mu}{\varepsilon_\mathrm{r}^2}\frac{1}{\mathrm{n}^2}\mathrm{eV} \tag{2.14}$$

where, ε_r^2 is the bulk dielectric constant and μ is the equivalent mass. In II-VI materials, exciton binding energies are $\sim$25 meV (up to 40 meV, if confined) so dominate at low temperatures.

The excited electrons will dissipate energy in a process known as thermalisation before dropping down to the lower energy states at the conduction band edge, due to the interactions with crystal lattice [23]. These non radiative interactions take place within a few picoseconds. The process of photon excitation followed by photon emission is called photoluminescence. The radiative recombination process or photoluminescence involves the emission of photons, which takes place within a few nano seconds of excitation. The intensity and energy of the emitted photon gives an indication of the crystalline quality of the material. Direct band to band transitions will dominate in high quality material and the energy of the emitted photon is given by:

$$hv = E_g - E_x \tag{2.15}$$

Where E_x is the binding energy of the exciton. Radiative transitions may also involve localised defect and impurity levels resulting in photon emission with a reduced energy. Emission associated with these energy levels can be used to identify specific defects in a material [24, 25].

The intensity and spectral content of the emitted photoluminescence is a direct measure of important material properties, including:

- *Bandgap Determination :* The spectral distribution of photoluminescence from a semiconductor material can be examined to non-destructively calculate the electronic band gap. This provides a means to quantify the elemental composition of a compound semiconductor.

- *Impurity Levels and Defect Detection :* The photoluminescence spectrum at low temperatures often reveals spectral peaks associated with impurities contained within the material. The high sensitivity of this method delivers the potential to recognise extremely low concentrations of intentional and unintentional impurities that can strongly affect material quality and device performance.

- *Recombination Mechanisms :* The quantity of photoluminescence emitted from a semiconductor material is directly related to the relative amount of radiative and non-radiative recombination rates. The latter is typically associated with impurities and thus, this technique can qualitatively monitor changes in material quality as a function of growth and processing conditions.

- *Surface structure and excited states :* The widely used characterisation techniques such as XRD, infra-red and Raman spectroscopy, are very often not sensitive enough for supported oxide catalysts with low metal oxide concentrations. However, photoluminescence is very sensitive to surface effects or adsorbed species of semiconductor particles and thus can be used as a probe of electron-hole surface processes.

Strong photoluminescence signals will be observed only in relatively thick bulk material ($\sim 1\mu m$) but when the excitons are confined in low dimensional structures, the process

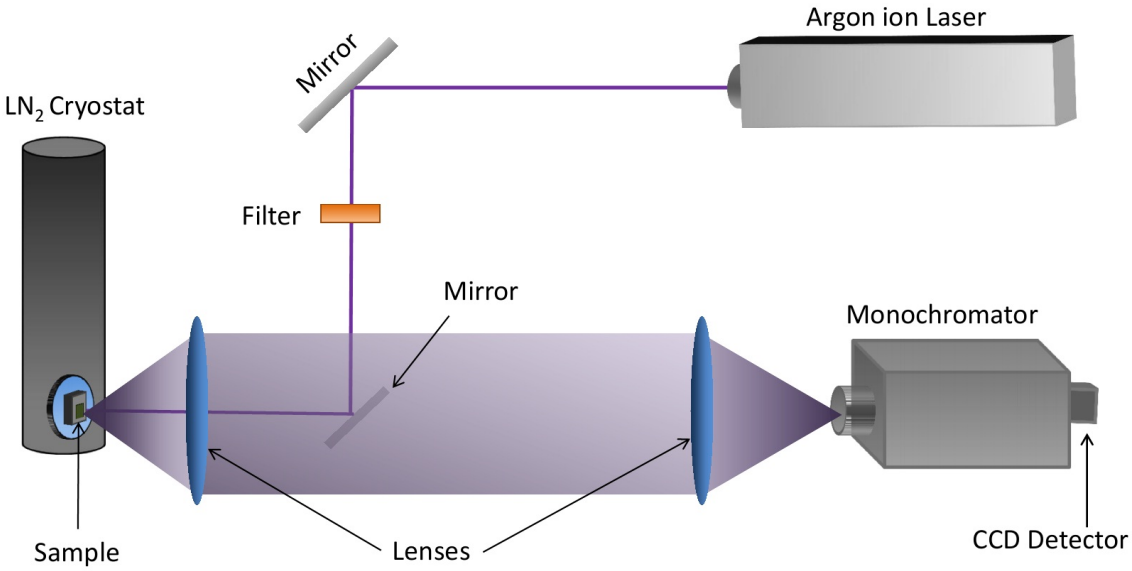

Figure 2.12: *Schematic of the optical setup used for photoluminescence measurements.*

becomes much more efficient. In order to observe emission from these structures, excitons excited in the barrier region travel by drift or diffusion before being captured by the quantum well. Since the band gap of a two-dimensional quantum well is smaller than that of the surrounding material, excitons encountering the well will dissipate energy by thermalisation in order to drop to the energy of the smaller band gap. These excitons are now trapped by the surrounding potential barriers and results in a higher exciton binding energy due to the additional quantum confinement. An increase in the recombination rate will occur due to the increased localisation and an enhancement in the PL emission intensity will be observed. Variations in the width of the band gap material and fluctuations in the interface composition will cause energy shifts in the PL spectrum and also broadening of the PL peaks.

Very low concentrations of optical centres can be probed using photoluminescence, but it is not generally a quantitative method. The main limitation of photoluminescence is that many optical centres may have multiple excited states, which are not populated at low temperature.

2.13.1 PL experimental setup

A schematic of the experimental setup used at Heriot-Watt to obtain the data presented in this thesis is shown in figure 2.12. Initially a 351nm (3.53eV) line of an argon ion laser

(Ar^+) is used as the excitation source. The samples were placed in a liquid nitrogen (LN_2) cryostat at a temperature of 77 K to prevent thermal dissociation and broadening of the excitonic transitions. The laser source is coupled into the LN_2 cryostat using a 0.36 NA lens, producing a pump spot ∼975nm in diameter and imaging an area 1-2μm in diameter. Luminescence from the samples was dispersed in a 0.75m double monochromator and recorded with a cooled GaAs photomultiplier tube and a lock in amplifier.

Later into this project, the monochromator and photomultiplier tube were replaced with a 100mm focal length fibre coupled monochromator and CCD detector as older equipment became unserviceable. Subsequently the Ar^+ source was replaced with a 405nm GaN diode laser. This new arrangement has a much lower resolution of ∼1.5meV and lower signal-to-noise ratio, but is capable of measuring continuous readings across the entire wavelength range typically measured, 405-800nm.

2.14 Spectroscopic Ellipsometry

Spectroscopic ellipsometry is a non destructive optical characterisation technique for the examination of the dielectric properties of thin films. It measures both the intensity and polarisation of light incident on a thin film. After analysing the change of polarisation of light, which is reflected off a sample, ellipsometry can produce information about layers that are thinner than the wavelength of the probing light itself, even down to a single atomic layer. Ellipsometry is sensitive to a wide range of material properties and can probe the complex refractive index or dielectric function tensor. It gives information about a range of sample properties including crystal quality, thickness, chemical composition, surface and interface roughness and electrical conductivity. It is frequently used to characterise film thickness for single layers or complex multilayer stacks ranging from a few angstroms to several micrometers thick with an excellent accuracy.

Figure 2.13 shows the schematic representation of an ellipsometer. Light emitted from a source is passed through, and linearly polarised by a half wave plate polariser. The light is then focussed on a sample at a variable angle of incidence, normally around 70^o. The incident light is reflected and passes through a half wave plate analyser into the detector.

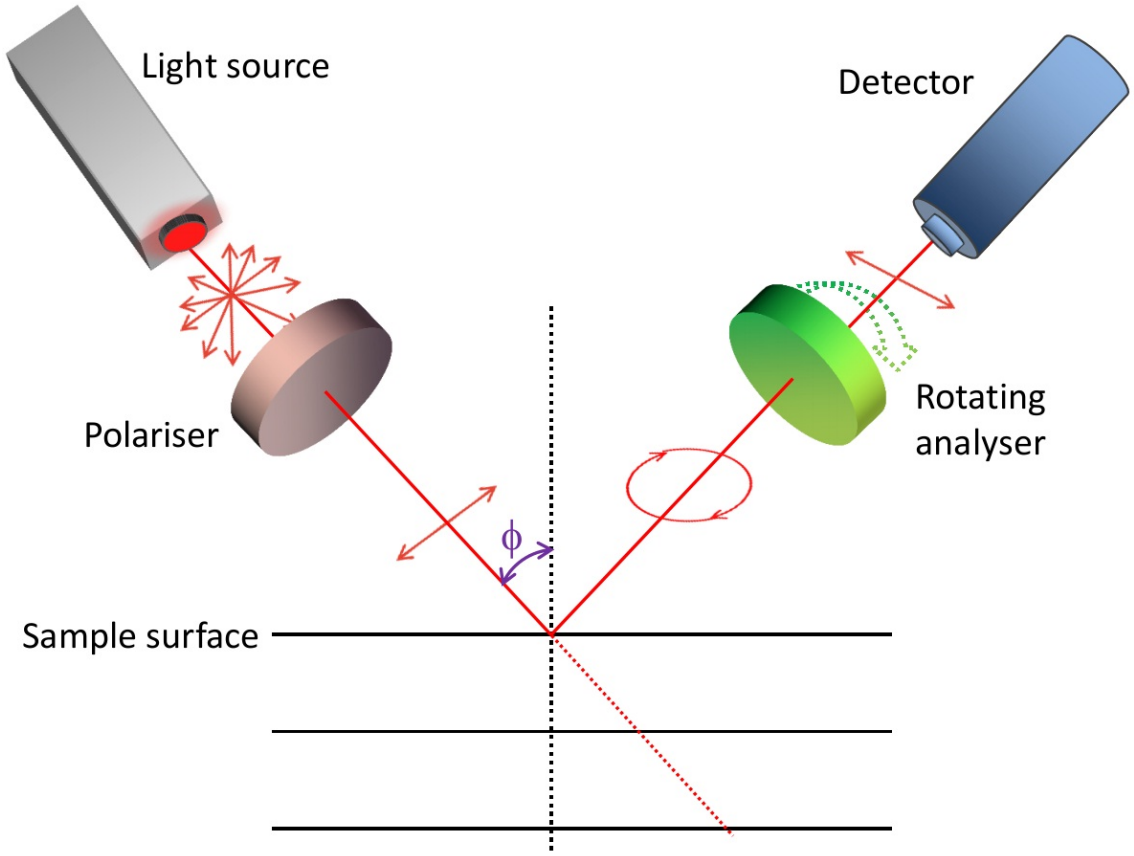

Figure 2.13: *Schematic of a rotating analyser ellipsometer.*

Ellipsometry is a specular optical technique where the angle of incidence equals the angle of reflection. The incident and the reflected light beam span the plane of incidence. Light which is polarised parallel to this plane is called *p* polarisation whereas the light polarised in the perpendicular direction is called *s* polarisation.

Ellipsometry measures the complex reflectance ratio, ρ, of a system, which may be parameterised by the amplitude component, Ψ and the phase difference, Δ. The amplitudes of the *s* and *p* polarisations, after reflection and normalised to their initial value, are denoted by r_s and r_p. The complex reflectance ratio, ρ, which is the ratio of r_p over r_s can be calculated from Equation 2.16.

$$\rho = \frac{r_p}{r_s} = \tan(\Psi)e^{i\Delta} \tag{2.16}$$

For bulk materials, ρ is simply the product of the materials refractive indices and therefore it is possible to calculate the refractive index using Equation 2.17.

$$\widetilde{N} = \sin^2(\phi)\left[1+\tan^2(\phi)\left(\frac{1-\rho}{1+\rho}\right)^2\right] \tag{2.17}$$

where, $\widetilde{N} = n + ik$ and ϕ is the angle of incidence. However, it is only for samples that are isotropic, homogeneous and infinitely thick that, n and k can be determined directly from ρ. Equation 2.17 assumes there are no surface layers of any type. However, in any bulk material, there is typically a surface oxide or some roughness, and the direct inversion of Equation 2.17 would include these as part of the bulk optical constants.

The modelling and analysis of the spectroscopic ellipsometry data was undertaken using a number of computer modelling packages; J. A. Woollams CompleteEASE and WVASE as well as the open source RegressPRO. All of these programs operate in a similar way, where the user first uploads an experimental ellipsometric spectrum and then creates a layer by layer model of the sample. The software then calculates the Ψ and Δ for each wavelength and angle of incidence (ϕ) from the spectrum.

The calculated values can then be compared to the measured values and an error value calculated. The software use the mean squared error, χ^2, as a figure of merit calculated using Equation 2.18.

$$\chi^2 = \frac{1}{N.M - m - 1} \sum_{j=1}^{M} \sum_{i=1}^{N} \frac{[\rho_{j.exp}(\lambda_i) - \rho_{j.calc}(\lambda_i)]^2}{\rho_j(\lambda_i)^2} \tag{2.18}$$

where $\rho_{j.exp}, \rho_{j.calc}$ and ρ_j represent the experimental, calculated and error quantities respectively at wavelength λ_i and data set j while N is the total number of data points, m the number of fitted parameters and M is the number of data sets.

Multilayer samples have a large number of independent parameters which means the choice of initial model is very important as if it differs significantly from the actual structure, the optimisation process can find a local minimum instead of the true minimum. Therefore it is necessary to examine the structure of such samples using other characterisation methods such as X-ray or PL before it is modelled.

All of the transmission spectra used in this thesis were obtained using a J.A. Woollam vertical-VASE (Variable Angle Spectroscopic Ellipsometer). A schematic of the working of a basic ellipsometer is given in Figure 2.13.

2.15 Summary

A detailed account on the working and structure of the MBE machine as well as the growth mechanism is given in this chapter. Similarly an overview of the most important characterization process used throughout this thesis is also presented, with emphasis on the X-ray, RHEED and AFM methods as they are the prominent techniques used and provide the most comprehensive data for growth development. It can be seen that individually each technique has its merits but together they provide a more detailed description of the materials. PL and ellipsometry measurements are used to obtain optical spectra . SIMS (Loughborough surface analysis) and SEM (nano optics group, Heriot-Watt University) techniques are also used occasionally.

2.16 References

[1] A. Y. Cho, M. B. Panish and I. Hayashi. “3rd Int. Symp. on Gallium Arsenide and Related Compounds”. *The Institute of Physics, Conference Series* (1970), pp. 18–29 (cited on page: 12).

[2] F. W. Sears, M. W. Zemansky and H. D. Young. *University Physics, 7th Edition*. Addison-Wesley, 1987, p. 381 (cited on page: 19).

[3] `http://www.ircon.com/pdf/irhandbo.pdf`. Accessed: 19/09/2012 (cited on page: 20).

[4] M. Prutton. *Surface Physics, 2nd Edition*. Clarendon Press, Oxford, 1983 (cited on page: 22).

[5] D. J. O’Connor, B. A. Sexton and R. S. C. Smart. *Surface Analysis Methods in Material Science*. Springer-Verlag, 1992 (cited on page: 23).

[6] J. H. Neave and B. A. Joyce. “Structure and stoichiometry of 100 GaAs surfaces during molecular beam epitaxy”. *Journal of Crystal Growth* Vol. 44 (1978), pp. 387–397 (cited on page: 25).

[7] A. Y. Cho. “Growth of III–V semiconductors by molecular beam epitaxy and their properties”. *Thin Solid Films* Vol. 100 (1983), pp. 291–317 (cited on page: 25).

[8] S. M. Newstead, R. A. A. Kubiak and E. H. C. Parker. “On the practical applications of MBE surface phase diagrams”. *Journal of Crystal Growth* Vol. 81 (1987), pp. 49–54 (cited on page: 25).

[9] E. A. Wood. “Vocabulary of Surface Crystallography”. *Journal of Applied Physics* Vol. 35 (1964), pp. 1306–1312 (cited on page: 25).

[10] A. Ohtake, T. Hanada, T. Yasuda, K. Arai and T. Yao. “Structure and composition of the ZnSe(001) surface during atomic-layer epitaxy”. *Phys. Rev. B* Vol. 60 (1999), pp. 8326–8332 (cited on page: 26).

[11] A. Pimpinelli and J. Villain. *Physics of Crystal Growth*. Collection Aléa-Saclay. Cambridge University Press, 1998 (cited on pages: 27, 29).

[12] K. Oura, V. G. Lifshits, A. A. Saranin and A. V. Zotov. *Surface Science: An Introduction*. Advanced Texts in Physics. Springer, 2003 (cited on pages: 27–29).

[13] E. Bauer and J. H. van der Merwe. “Structure and growth of crystalline superlattices: From monolayer to superlattice”. *Phys. Rev. B* Vol. 33 (1986), pp. 3657–3671 (cited on page: 27).

[14] J. A. Venables. *Introduction to Surface and Thin Film Processes*. Cambridge University Press, 2000 (cited on page: 29).

[15] M. Henini. “High index surfaces grow novel devices”. *III-Vs Review* Vol. 11 (1998), pp. 48–52 (cited on page: 30).

[16] D. Holt. “Polarity reversal and symmetry in semiconducting compounds with the sphalerite and wurtzite structures”. *Journal of Materials Science* Vol. 19 (1984). 10.1007/BF02403230, pp. 439–446 (cited on page: 30).

[17] M. Razeghi. *Fundamentals of Solid State Engineering*. Springer, 2009 (cited on page: 33).

[18] D. K. Bowen and B. K. Tanner. *High Resolution X-Ray Diffractometry And Topography*. Taylor & Francis, 1998 (cited on page: 33).

[19] *Reference Guide*. Jordan Valley Semiconductors Ltd., 2011 (cited on page: 34).

[20] W. H. Bragg. “The Reflection of X-rays by Crystals. (II.)” *Proceedings of the Royal Society of London. Series A, Containing Papers of a Mathematical and Physical Character* Vol. 89 (1913), pages (cited on page: 35).

[21] A. Kelly, G. W. Groves and P. Kidd. *Crystallography and Crystal Defects*. John Wiley & Sons, 2000 (cited on page: 36).

[22] A. Gustafsson, M.-E. Pistol, L. Montelius and L. Samuelson. “Local probe techniques for luminescence studies of low-dimensional semiconductor structures”. *Journal of Applied Physics* Vol. 84 (1998), pp. 1715–1775 (cited on page: 40).

[23] R. A. Stradling and P. C. Klipstein. *Growth and Characterisation of Semiconductors*. Taylor & Francis, 1990 (cited on page: 40).

[24] T. Yao, M. Ogura, S. Matsuoka and T. Morishita. “Electrical and Photo-luminescence Properties of ZnSe Thin Films Grown by Molecular Beam Epitaxy: Substrate Temperature Effect”. *Japanese Journal of Applied Physics* Vol. 22 (1983), pp. L144–L146 (cited on page: 41).

[25] T. Yao. “Characterization of ZnSe grown by molecular-beam epitaxy”. *Journal of Crystal Growth* Vol. 72 (1985), pp. 31–40 (cited on page: 41).

Chapter 3

Density control of CdSe quantum dots deposited on MgS

3.1 Introduction

The growth of new types of Quantum Dots (QDs) for various applications is still an active field. The main driving force behind this research is the development of innovative devices based on the unique electronic properties of QDs. Novel device applications are possible in the fields such as optics, optoelectronics, quantum computing and quantum cryptography. Research also allows an insight into the fundamental physics of confinement in 0D QD structures.

In III-V compound semiconductor systems, devices with InAs/GaAs QD structures have been successfully demonstrated [1]. Successful examples were also subsequently found in II-VI compound semiconductor based QD structures, such as laser diodes and bright light-emitting diodes. CdSe QDs grown on the ZnSe buffer layer constitute one of the most well-studied systems among the II-VI compound semiconductors. The lattice constant of ZnSe is almost matched to that of the GaAs substrate and the lattice constant of CdSe has a mismatch of ~ 7.2 % to that of ZnSe buffer layer. This lattice mismatch is nearly identical to the InAs/GaAs system, which has a mismatch of 7.1 %. However, the interdiffusion between ZnSe and CdSe layers is significant. Also wide bandgap II-VI semiconductors are normally grown on commercially available III-V substrates, which have far smaller bandgaps than the II-VI epitaxial layers. This is not ideal for many ap-

plications where absorption by the substrate prohibits the transmission of light through the epitaxial layers.

ZB MgS has a very large band gap of ∼5eV and hence shows excellent potential as a barrier material for wide bandgap II-VI QDs. The lattice parameter of ZB MgS is similar to that of ZnSe and GaAs and so the strain in MgS/CdSe is almost identical to that in ZnSe/CdSe system and a similar transition from two dimensional to three dimensional growth, resulting in self formation of QDs is expected with increasing CdSe deposition. However, the MgS/CdSe interface is not a simple replica of ZnSe/CdSe because of the much larger exciton confinement. On the basis of linear combination of atomic orbital theory [2], the conduction and valence band offsets at the MgS/CdSe interface were evaluated to be 2.16 and 0.87 eV, respectively, which are much larger than those in the ZnSe/CdSe system (0.84 and 0.23 eV). The large band discontinuities and almost complete immiscibility of the MgS barrier with CdSe is very beneficial in enhancing the confinement.

Successful growth of MgS based CdSe quantum structures has already been demonstrated by Heriot-Watt MBE group [3, 4] and the ability to grow good crystalline quality, thick ZB MgS has enabled the group to investigate the low dimensional MgS based quantum structures even further [5, 6].

The control of QD density is of particular interest. Some QD devices such as high efficient QD lasers require a large number of QDs in the active region with a high density ($\sim 10^{11} cm^{-2}$). On the other hand, for some QD based devices and applications such as single photon emitters and micro cavity quantum electro-dynamics devices, low density ($\sim 10^{8} cm^{-2}$) QDs are required. The density range from 2×10^{10} to $1 \times 10^{11} cm^{-2}$ with a size distribution of $\sim 10\%$ is typical for Stranski-Krastanov (SK) mode QD ensembles. SK growth outside this range is certainly difficult. Low density QDs are particularly difficult by the self-assembly process [7]. Currently, lower density II-VI QDs are fabricated mainly using lithography techniques which has several disadvantages such as contamination, defect formation, etc.

This chapter details attempts to control the density of the MgS based CdSe QDs. Uncapped QDs were examined using AFM for calculating the dot density and investigating the island formation mechanism.

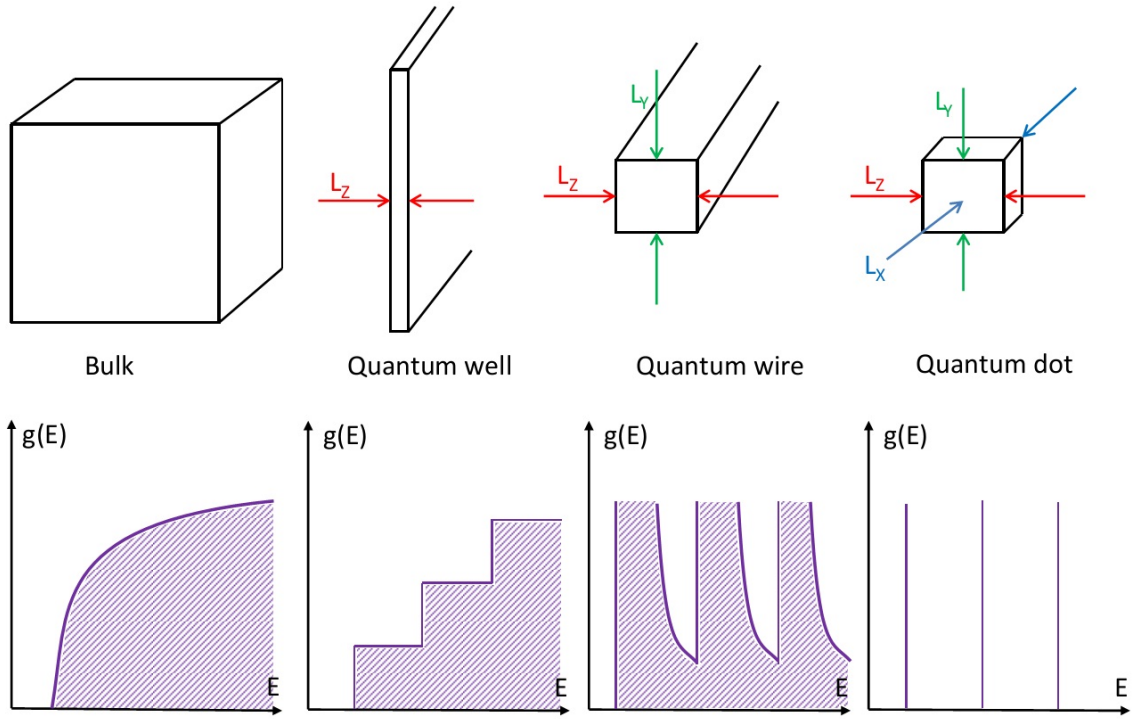

Figure 3.1: *Density of states functions for bulk material, quantum well, quantum wire and quantum dot.*

3.2 Quantum Dots

Quantum dots are coherent nanometre sized semiconductor structures whose carriers are confined in all three spatial dimensions in a semiconductor matrix of larger band gap. Simply, when a narrow band gap material is completely surrounded by a larger band gap material, the electrons and holes are confined into discrete quantum states and their movement is restricted in all three dimensions. Therefore, such materials have electronic properties intermediate between those of bulk semiconductors and those of discrete molecules. As in atoms, the allowed energies in such a confined volume are quantised, forming a discrete spectrum of energy levels. The quantisation of allowable electron energies can however provide a variety of advantages for electronics, including increased radiative efficiency, reduced power requirements and increased speed of operation.

The density of states of QDs compared to those of bulk materials, quantum wells and quantum wires are given in Figure 3.1. Energy spectra of multi-electron QDs (a dot may contain $\sim 10^5$ to 10^6 atoms) differ from that of the ordered shell structure of atoms, in that they are generally more complex due to quantum chaos associated with irregular shape or disorder and electron-electron interactions [8]. Unlike electrons in a single atom, carriers

in QDs will interact strongly with lattice vibrations and may be strongly influenced by defect, surface or interface states.

3.3 Quantum Dot Fabrication Techniques

Defining the smaller dimensions of nanostructures is one of the main stumbling blocks for advancement in the field of nanostructure technology. By the end of the 1980s, techniques like lithographic patterning [9] and etching of quantum well structures [10] were developed for QD fabrication. Several new and advanced processing methods have been developed in recent years, both prior to and after the growth that allowed the fabrication of novel structures and devices.

3.3.1 Lithography

Patterning of quantum wells using lithography was considered to be the most straightforward way of QD fabrication in the 1990s. Followed by etching, lithographic patterning is still one of the most widely used techniques for producing conventional integrated circuits. Lithography can be used successfully to fabricate QD structures, due to the high level of control in this process. Unlike in epitaxy, in lithographically defined QDs a quantum well provides a confining potential along the growth direction, while the lateral confinement is provided by an electrostatically induced potential barrier.

The most commonly used lithographic techniques are photolithography [1], X-ray lithography [11], electron beam lithography (EBL) [12], and focused ion beam lithography (FIBL) [13]. The first three techniques typically use a high energy source to selectively expose and pattern a resist film. This pattern in the film is later transferred to the underlying substrate by etching. The resolution of photolithography is limited by the wavelength of the laser source used in the exposure and generally is in the range of $\sim 0.15\ \mu$m. X-ray lithography has the advantage of a much better resolution, due to the shorter X-ray wavelength, but an additional process is required to fabricate the mask for using this method. For direct lateral patterning, the most advanced methods are EBL and FIBL.

Resolution in the 10-20 nm range has already been established by the early 1980s [14]. However the spatial resolution of EBL and FBIL is limited by problems including charging and proximity effects. Process induced defects and contamination that typically deteriorate the structure quality of the QDs are inevitable in lithography techniques. The technological requirements of constructing nano scale features that are defect free and exhibit an abrupt carrier confining potential has evidently limited the success of using lithography for QD fabrication.

3.3.2 Colloidal Synthesis

Colloidal II-VI semiconductor crystallites are synthesized from precursor compounds dissolved in solutions based on organometallic and polymer chemistry [15]. The synthesis of colloidal QDs is based on a three component system composed of precursors, organic surfactants, and solvents. When heating at a low precipitation temperature of $\sim 200^{o}$C, the precursors chemically transform into monomers. Once the monomers reach a high enough supersaturation level, the growth of crystals starts with a nucleation process. Isolated clusters can be obtained under certain conditions with very low size distributions or dispersed in a very thin film.

The temperature during the growth is critical in determining optimum conditions for the crystal growth. It must be high enough to allow for rearrangement and annealing of atoms during the synthesis process while being low enough to promote crystal growth. Monomer concentration is another important factor which has to be strictly controlled, as at high monomer concentrations, the critical size, i.e. the size where crystals neither grow nor shrink, is relatively small, resulting in growth of nearly all particles. In this regime, smaller particles grow faster than large ones, as larger crystals need more atoms to grow than small crystals. The nanocrystal growth is optimal when the monomer concentration is kept such that the average crystal size present is always slightly larger than the critical size. In order to prevent a rapid agglomeration of particles resulting from Ostwald ripening, it is essential to use a stabilising agent.

Typical dots like Cadmium Selenide (CdSe) are fabricated using binary compounds, here

CdSe. The size of these crystallites is controlled by various factors including temperature, mixing rate of reagents and the concentration of stabilizer. Generally these quantum dots can contain as few as $\sim$ 100 to 100,000 atoms within the volume of the dot, with a diameter of $\sim$ 10 to 50 atoms. This corresponds to $\sim$ 2 to 10 nanometers in diameter.

Large quantities of QDs can be synthesised using colloidal synthesis. Low defect concentration is another advantage of this method.

3.3.3 Epitaxy: Self-Assembling

The self-assembling method has the greatest potential for fabrication of semiconductor nanostructures. Self-assembly occurs for strained heteroepitaxial growth where the lattice mismatch between the buffer layer and the overlayer is several per cent. Initially the growth mode is two dimensional, but due to the large strain energy stored within the layer, it is a metastable growth mode. When the overlayer reaches a critical thickness, strain relief is achieved by the formation of islands. It is possible to fabricate arrays and stacks of small quantum dots of $\sim <$10 nm in diameter, ordered in size and shape with high area density and high optical quality, using self-assembly with suitable growth conditions in MBE.

3.4 Stranski-Krastanov (SK) Growth

Stranski-Krastanov (SK) growth is one of the three primary modes by which thin films grow epitaxially at a crystal surface or interface. Also known as 'layer-plus-island growth', the SK mode is initially a 2D layer by layer growth, but beyond a critical layer thickness, which depends on strain and the chemical potential of the deposited film, growth continues through the nucleation and coalescence of 3D islands [16–18]. Figure 3.2 shows a schematic of the SK growth.

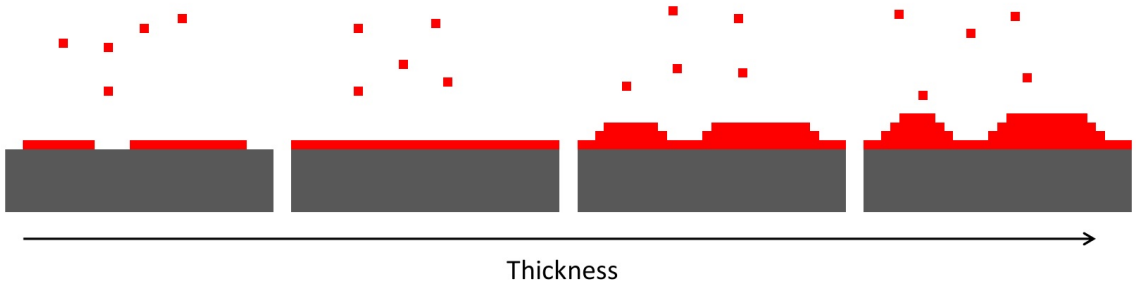

Figure 3.2: *Schematic of Stranski-Krastanow growth mode.*

3.4.1 Energetics

For dot formation, dot material layer (e.g. here CdSe) must have a lower band gap energy and a larger lattice parameter than the buffer layer material (e.g. MgS) on which the growth is initiated. The mismatch in lattice parameter generates a strain energy in the epitaxial layer. The energy of the system decreases until the substrate surface is covered with a monolayer of deposited material. A uniform strain layer is formed as the deposition continues and the elastic strain energy, E_{strain} will increase linearly with the layer thickness, t [19].

$$E_{strain} = \lambda \varepsilon^2 A t \tag{3.1}$$

Where, λ is the elastic modulus, $\varepsilon = \frac{\Delta a}{a}$ is the misfit, a is the lattice constant, A is the surface area and t is the thickness. Deposition then continues by either of the following processes.

- FM growth is maintained until the activation energy for the creation of dislocations reaches the critical thickness, t_{cd}.

- The strain energy in SK growth can be lowered by the nucleation of 3D islands at a lower critical thickness, t_{cw} (critical thickness of the wetting layer)

The metastable, supercritical, 2D wetting layer in SK growth mode undergoes a phase transition resulting in the more stable SK island plus thin 2D wetting layer configuration. No further material deposition is needed at this stage as the dots are formed by collecting material from the wetting layer.

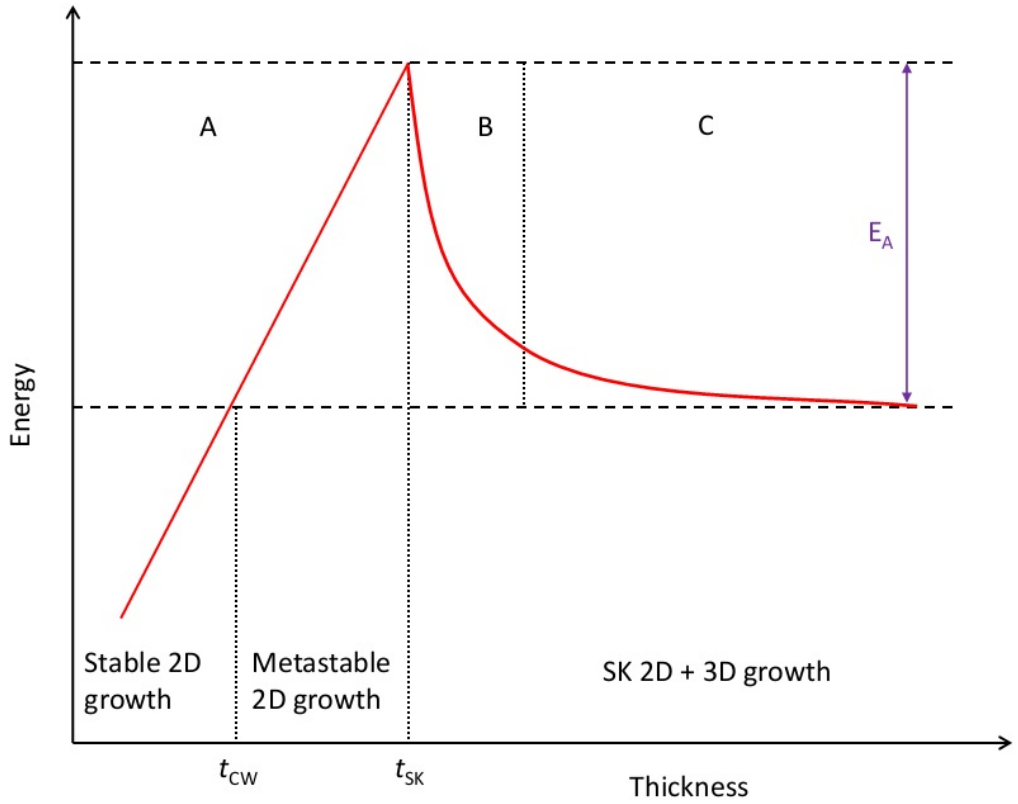

Figure 3.3: *Schematic of Energy vs. time for the transformation from 2D to 3D morphology.*

The self-assembly process can be qualitatively described based on the following conditions [19].

1. Perfect wetting of the surface.

2. The driving force for island nucleation is the increase in the elastic misfit strain, with increasing wetting layer thickness.

3. Once island formation starts, there is inhomogeneous elastic strain within each island as well as induced strain in the substrate.

The QD formation process is shown in Figure 3.3 and can be divided into the following three main steps (A, B and C in figure). t_{cw} is the critical thickness of wetting layer, where 2D growth starts to become 3D growth and t_{sk} is the thickness where the excess strain energy induces dot formation.

1. The 2D growth phase. (A)

2. The 2D to 3D transition phase.(B)

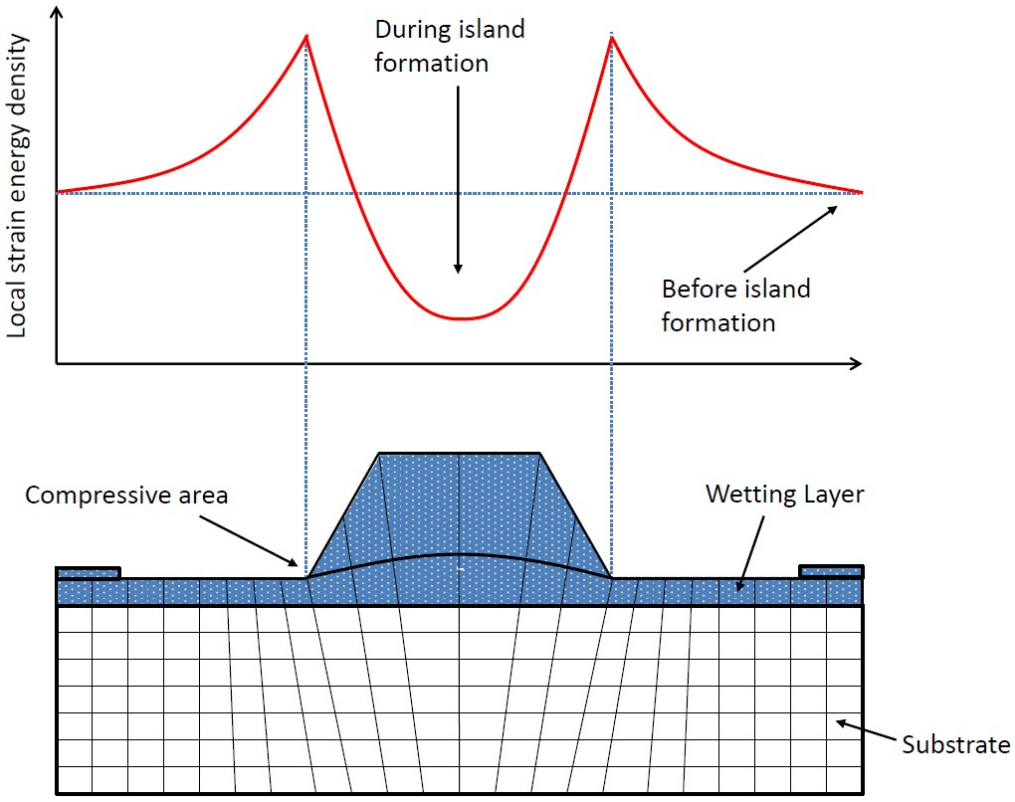

Figure 3.4: *Schematic of Surface cross section of a quantum dot showing strain distribution around the nucleation.*

3. The ripening of dots phase.(C)

3.4.2 Dot formation

Thickness fluctuations in the wetting layer lead to the formation of critical nuclei and the rate of nucleation is given by,

$$\frac{dN}{dt} = const.\sigma e^{[-\frac{(E_A - E_E)}{k_B T}]} \tag{3.2}$$

Where, $\frac{dN}{dt}$ is the number of critical nuclei created per unit time and σ is the supersaturation (the concentration of the mobile excess material on the surface) and E_A is the activation energy barrier for 2D to 3D transition. After the onset of nucleation the nucleation rate will decrease rapidly as the excess energy, E_E is reduced due to strain relaxation and the excess material is consumed by the islands, decreasing σ.

SK growth is a self-limiting process, resulting in dots which exhibit a fairly uniform size and shape distribution. Different theories were proposed to explain this growth mode, but there is still uncertainty about the interplay between thermodynamic factors such as adsorption, heat of formation, etc. and kinetic factors such as islanding, nucleation, etc. involved in this process [20]. However it is known that QD formation alters the strain distribution in the wetting layer. The strain before and after the nucleation of the dot is shown in Figure 3.4. It can be seen that the strain relaxation in the island causes an energy minimum on the surface. The strain is at maximum around the edge of the island, due to the higher compressive strain in this area. This higher strain tends to act as a barrier for surface diffusion towards the island and material is forced away from this region resulting in a dot surrounded by a thinner wetting layer.

3.5 Limitations of Stranski-Krastanov growth

SK growth method is still not considered as a practical QD fabrication technique for certain device applications because of the inability to control the distribution and fluctuation in size of the dots. In order to incorporate this technique into devices operating at room temperature, the following issues have to be addressed.

3.5.1 Control of size

The size of a QD is very important as the required properties will be obtained only if the size of the QD is within a specific range [1]. The lower size limit of a QD is determined by the condition that one energy level of an electron, hole or both is present. The maximum dot size must limit the thermal population of higher lying energy levels to 5% [1]. The energy level spacing may become too small for large dots, leading to thermal smearing and evaporation of carriers from the dots and thus destroying the required quantum properties. The dot material determines the upper size limit and for CdSe based II-VI structures, this limit should be 5-6 nm. Size uniformity is essential in order to reduce the variation in the energy positions of the electronic levels, which results in the inhomogeneous broadening. It has been shown earlier that the dot diameter is exponentially dependent on temperature

and only weakly dependent on monolayer coverage [21].

3.5.2 Coherence

QDs are formed by strain relaxation during SK growth. This method has in the past been associated with the formation of defects, however dislocation free QD growth has been reported [22]. The elastic relaxation during QD formation depends strongly on the dot dimensions [19] and for a given shape is proportional to volume. Unfortunately this relaxation process is a mechanism which competes with the formation of dislocations, which are known to occur when the amount of deposited material exceeds the critical thickness, h_{crit}. These defects provide sites for non-radiative recombination, leading to degradation of the material quality.

3.5.3 Control of QD density

The density and size of QDs forming on a material surface is a function of various factors, including flux ratio, substrate temperature, layer thickness and growth rate. For III-V systems, it has been shown that QD density decreases as the growth rate and V/III ratio increases [21]. Control of density may therefore be achieved by careful manipulation of these variables.

However as detailed in the introduction section, it has been found to be particularly difficult to control the density of the II-VI quantum dots using the above mentioned variables [7]. In this chapter, the use of a new set of variables to successfully control the density of QDs grown using SK method is demonstrated.

3.6 Growth of self assembling II-VI quantum dots

The formation of defect free QDs in strained heterostructures by SK growth method has been reported for a number of II-VI material systems which include CdSe/ZnSe [23–26],

CdSe/CdS [27], CdTe/ZnSe [28] and ZnSe/ZnS [29, 30]. Out of these material combinations, CdSe on (001) ZnSe is the most extensively investigated and is similar to the InAs/GaAs material system in terms of a lattice mismatch of $\sim$7 % and band gap difference of $\sim$1 eV. The MBE growth of CdSe dots in a ZnSe matrix was first reported in 1996 [23], where the dot profile determining by AFM was observed to be very similar to that of III-V dots.

Various studies have shown that the transition of 2D to 3D occurs gradually in CdSe/ZnSe system and is more complex than the spontaneous and abrupt change implied by the SK growth mode [31–35]. Evidence has been obtained which strongly suggests that when CdSe is grown on ZnSe, QDs begin to form well before the critical thickness of the deposited layer. The SK growth mechanism is therefore inadequate to describe fully the 2D to 3D transition. PL and μ-PL studies carried out on these structures have shown strongly confined 0D excitons for coverages of only 1.1 ML, which is far below the critical thickness for CdSe on ZnSe [32, 36]. These results suggest that ZnCdSe 2D islands with some graded composition containing local maxima of Cd concentration form as the CdSe is deposited, providing localisation for 0D excitons.

Strassburg et al. have shown the presence of two well distinguishable classes of nanoscale islands in CdSe/ZnSe structures, which were identified by optical spectroscopy and cross-section high-resolution TEM [31]. For 2.1 to 3.1 ML CdSe deposition, coherent 3D islands, formed in SK mode, were found with typical diameters of $\sim$16nm and a coverage dependent density of up to $3 \times 10^{10}\text{cm}^{-2}$. Simultaneously, small islands with lateral extensions below 10nm and a density of $5 \times 10^{11}\text{cm}^{-2}$ were formed by strain-modified (SM) island growth. Interdiffusion processes at the ZnSe/CdSe interfaces and segregation lead to the formation of a ZnCdSe-alloy layer. The investigation by cross-sectional scanning transmission electron microscopy (STEM) clearly indicated a coexistence of 2D ZnCdSe platelets within the wetting layer and 3D islands, showing clearly that the platelets act as precursors for the formation of the final 3D dots [33].

High-resolution TEM studies have also revealed the coexistence of two different classes of islands during the formation of CdSe QDs, the islands of an average size about of 16nm and the smaller clusters with an average size less than 10nm [34]. The kinetic reasons for the formation of the different size class islands was investigated. The density of

the large islands was found to be strongly dependent on the CdSe coverage, showing a steep increase when the critical thickness is exceeded and characteristic of SK growth. By contrast, it was found that the density of the small clusters was almost invariant with respect to CdSe coverage, and that they were formed during the growth of wetting layer on top of large, flat 2D islands most probably due to strain-driven surface kinetics near the island edges. These small islands have been referred to as fractional-monolayers formed by SM island growth [35]. It was also shown that the QD structure is significantly modified during the growth of the ZnSe cap due to interdiffusion processes at the CdSe/ZnSe interface.

A bimodal distribution of QD sizes has also been observed, where plan-view TEM images show the coexistence of two classes of QDs with an average lateral size of $<$10nm (area density $100\mu m^2$) and 10-50 nm ($20\mu m^2$), respectively [37]. The shape of the larger entities is pyramidlike. These dots were formed during reorganization of an initially uniform film by thermal activation from an almost uniform CdSe layer which resembles the wetting layer of the SK mechanism. The TEM findings were consistent with optical data and x-ray diffraction measurements which indicated that roughly 1 of the 3MLs condenses into QDs.

Concerns about post growth stability and origin of islands are another important issue regarding QD formation. Many groups have reported the instability of the self organised CdSe dots [23, 38], which is uncharacteristic of the self-regulating SK growth regime. Similarly in some cases, the size of the uncapped islands measured using AFM does not correlate with the blue shift of the PL observed for capped dots which has been shown to be strongly dependent on the shape of the dots [39]. Dot like structures have also been observed on pure ZnSe surfaces [24, 26], which are thought to consist of Selenium oxide clusters and have been observed to undergo Ostwald ripening [40]. This observation has led to doubt about the origin and chemical composition of II-VI QDs.

Further investigations based on the equilibrium properties of strained heteroepitaxial systems, incorporating the growth of wetting layer, dislocation-free island formation, and ripening predicted that the stability of dots is very sensitive to the amount of material deposited and Ostwald ripening can be avoided by carefully controlling this [22]. Although the theory of Ostwald ripening is fairly well understood much less is known about

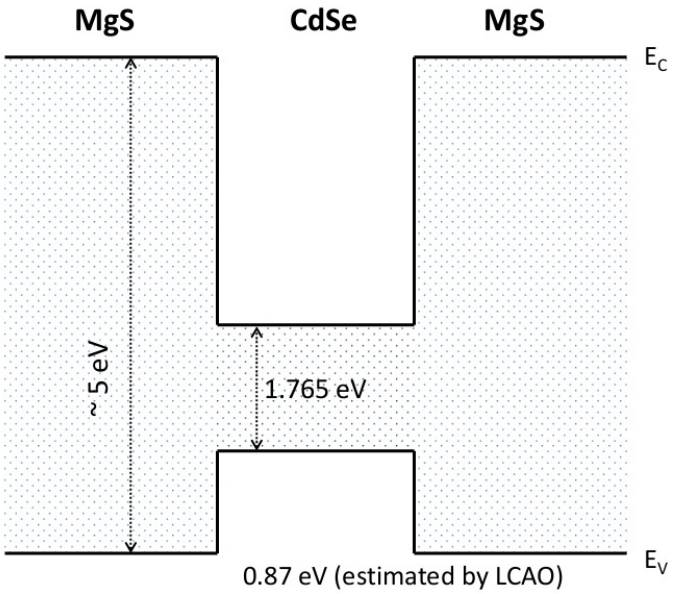

Figure 3.5: *Conduction band and Valence band offsets for MgS/CdSe structures.*

the influence of strain [41], not only on the island stability but also on size and spatial distributions.

A systematic investigation of the surface morphology of CdSe QDs as a function of time, using AFM measurements in air reported that Ostwald ripening was observed and was an intrinsic material property of the CdSe based II-VI heterosystems [42]. Conversely, another group has demonstrated that the Ostwald ripening does not occur on laboratory time scales [43]. Their *in situ* AFM measurements were carried out once the sample had cooled down to room temperature. After scanning the same area over a 5 day period, no change in the surface topography of the sample was observed. However, new larger structures appeared after the sample was exposed to atmosphere for some time. These new structures were not statistically correlated with existing features on the CdSe surface. Investigations carried out using lateral force and force modulation microscopy on CdSe/CdS QDs have shown material contrast indicating that the observed islands may not be composed of CdSe but instead consist of selenium clusters [27].

An examination of these islands is given in Section 3.8.

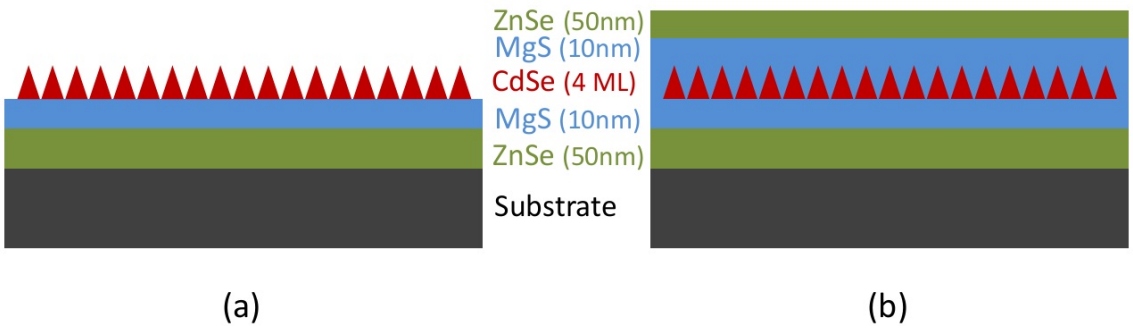

Figure 3.6: *Schematic of typical MgS/CdSe quantum dot structure for (a) AFM and (b) PL characterisation.*

3.7 Growth of MgS/CdSe QDs

The lattice parameter of ZB MgS is similar to that of ZnSe and GaAs and so the strain in MgS/CdSe is almost identical to that in ZnSe/CdSe system. Therefore a similar transition from two dimensional to three dimensional growth, resulting in self formation of QDs is expected with increasing CdSe deposition. As a result, the strain driven Stranski-Krastanov growth method used to fabricate ZnSe/CdSe QDs can be used successfully in the MgS/CdSe material system.

The growth method used to fabricate the self-assembled QD structures presented in this chapter is a surface reorganisation process that occurs during the growth interruption with thermal activation [44]. A 50nm ZnSe buffer layer was deposited on to a (100) GaAs substrate at a growth temperature of 240^{o}C. Soon after ZnSe growth commences, a (2×1) reconstruction along with a weaker c(2×2) reconstruction are observed by RHEED, indicating slightly selenium rich growth conditions. ZnSe layer is followed by the deposition of a 10nm MgS barrier. A streaky c(2×2) RHEED pattern is maintained during MgS growth. A 4 ML thick CdSe layer is then deposited on the MgS barrier layer using migration enhanced epitaxy (MEE). The structure of a typical MgS based CdSe QD device is shown in Figure 3.6.

MEE is a modification of the MBE growth technique, where the growth proceeds layer by layer, which leads to improvements in the structural quality of the material produced [45, 46]. During normal MBE growth, the migration distance of adatoms is limited, resulting in surface roughness that may be more than a ML thick. The MEE technique, however, leads to an enhancement of the adatom migration, by alternatively exposing the growing

surface to the constituent elements. A short time delay between each exposure not only enhances surface atom migration but also eliminates background interaction between the fluxes at the surface of the growing film. For MEE growth of CdSe, the Cd incorporation kinetics are governed by various factors, including the Cd flux intensity, deposition time and substrate temperature. During PL and TEM studies of CdSe/ZnSe QDs formation, it was found that the nominal thickness deposited per cycle linearly increases with the amount of Cd supplied up to $\sim$ 0.5 ML before saturating, showing that the growth rate for MEE is self-limiting at 0.5ML per cycle [47].

During the MEE growth of the samples presented in this chapter, each cycle consisted of 10s deposition of Cd plus 5s growth interruption, followed by 10s deposition of Se plus 5s growth interruption. After the CdSe deposition, samples were subsequently annealed at a higher temperature, before being cooled to the growth temperature under Se flux. The surface was continuously observed using RHEED. During the CdSe deposition, the RHEED became diffuse and long streaks appeared. During annealing, these streaks become very spotty, indicating a transition from 2D to 3D. However this transition was also observed during the CdSe deposition, while growing thicker samples. Once the structure is cooled down to the original growth temperature, a monolayer or two of ZnSe is grown over the quantum dots to protect the underlying MgS layers from oxidation.

3.8 Selenium clusters vs QDs

The observation of nanometer scale surface clusters 40-200 nm in diameter and 10-40 nm in height, which form as a result of the initial exposure of the Se contained surface layer to atmosphere has always caused confusion when it comes to the surface study of QD containing structures. These clusters exhibit Ostwald ripening at room temperature over a period of days and weeks. Due to the small size and sensitivity to electron beams, direct chemical analysis of cluster composition has proved difficult. However experimental observations combined with existing literature suggested that the cluster composition was not pure Se, but instead SeO_2 [40]. Due to the striking similarity in surface morphology of these nanometer scale clusters to quantum dot structures, many research groups have reported room temperature ripening or 'Ripening mode' quantum dots based on AFM

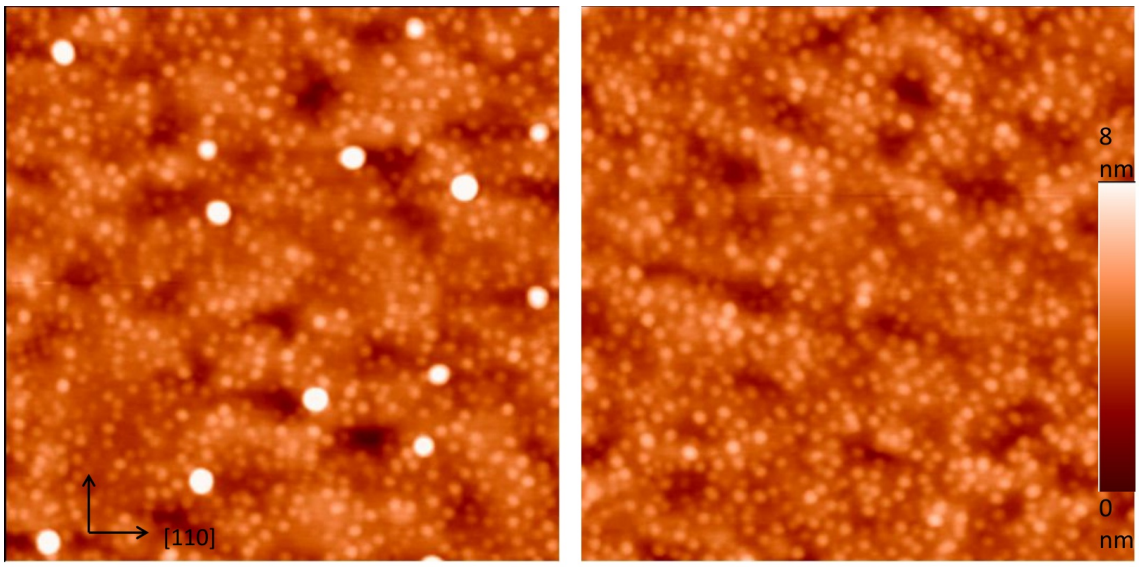

Figure 3.7: *$2\mu m \times 2\mu m$ AFM images showing a 4 ML CdSe surface (a) after the growth, outside growth chamber and (b) after subsequent ex situ annealing in room temperature at 200 ^oC for 2 min. Both Se clusters (bright dots) and CdSe QDs (smaller, less bright dots) can be seen in (a).*

studies, which were in fact SeO_2 clusters [23, 48, 49].

The main challenge in surface morphological study was in differentiating these clusters from actual QDs. 3D islands may not necessarily appear as a distinct dot on an uncapped AFM sample and the apparent Se cluster formation, on the other hand can be easily mistaken for a QD. Smathers *et. al.* have demonstrated the formation of these clusters and their ripening over time at room temperature on ZnSe epilayers and proved that following growth in air, the clusters were volatile in vacuum and disappeared if left under vacuum for approximately 6 hours [40]. However there have been no reports yet on eliminating selenium clusters from real QD structures. For such an experiment it is important to visualize both QDs and Se clusters on sample surface and removing the latter without compromising the QDs.

Uncapped QD samples were grown for AFM surface analysis with the structure GaAs/ ZnSe(50nm)/ MgS (10nm)/ CdSe(4 ML). Two distinct types of dots were observed on AFM images: QDs with $\sim$2nm height, $\sim$20nm diameter were observed along with selenium clusters with $\sim$30nm height and $\sim$150nm diameter. The areal densities of these dots were approximately 10^{11} cm^{-2} and 10^{8} cm^{-2} respectively. The CdSe dots may not appear on AFM scans all the time, due to a variety of reasons. In such instances it is very

easy to mistakenly count the visible selenium containing clusters for QDs.

Ripening of selenium clusters has been observed on all the samples. QDs remain unaffected throughout several weeks while selenium clusters have undergone Ostwald ripening. Several attempts were made to eliminate the Se clusters including vacuum treatments [40] which proved to be ineffective in this case. Se clusters were present on sample surfaces left under vacuum for up to 24 hours.

Figure 3.7 shows the results of a simple procedure, in which Se clusters were evaporated by heating the sample in atmosphere at 200 ^{o}C for 2 minutes. The bigger, brighter dots are Se clusters while the smaller ones are QDs. This experiment was first tried under vacuum but the atmospheric version proved to be as effective and more convenient. No changes in the QD size or density were noted. Samples were examined further under AFM over a two weeks period and no further Se cluster formations were found. From observing several QD structures grown under various conditions for several weeks, no ripening of the QDs was found after this simple heat treatment.

3.9 Density control of CdSe QDs grown on MgS

There is much interest in using the CdSe QDs for applications such as in single photon emitters/detectors. In order to achieve this, low density QDs are needed because at low density ($<10^{9}$cm^{-2}), only a few QDs are pumped by a laser spot and thus single photons can be ejected from single QDs. However, reproducible procedures necessary for a controlled formation of CdSe quantum dot structures are not available presently.

Controlling the areal density and distribution of QDs is the main challenge in SK growth mode. Various factors affecting the growth and structure of QDs include CdSe thickness, Cd/Se flux ratio, annealing temperature, annealing time, substrate temperature and growth delays. However, by using the MEE growth method, Cd/Se flux ratio is not significant as long as sufficient flux is maintained from each cell.

In this chapter, the areal density control of CdSe quantum dots is achieved by introducing

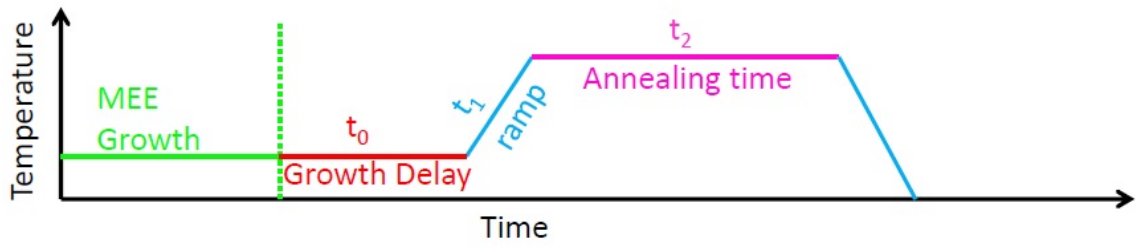

Figure 3.8: *Schematic representation of the three different time delays, t_0, t_1 and t_2. t_0 is the initial growth delay after after the CdSe deposition, t_1 is the temperature ramp up time and t_2 is the annealing time.*

appropriate growth delays at various stages of the CdSe growth. All other parameters are left constant. A 4 ML thick layer of CdSe has been grown for all the samples. All of the AFM samples mentioned in this chapter have the same structure described below, whereas samples intended for PL have an additional cap . This is primarily a surface study using AFM, whereas ensemble 77 K PL is used to back up the conclusions, by optically confirming the presence of dots.

The AFM sample structure is, GaAs(substrate)/ ZnSe(50nm)/ MgS(10nm)/ CdSe(4ML)/ ZnSe(2ML). This additional 2ML ZnSe cap on AFM samples is to prevent the oxidation of the underlying MgS layers. Samples grown for the PL characterisation have the structure, GaAs(substrate)/ ZnSe(50nm)/ MgS(10nm)/ CdSe(4ML)/ MgS(10nm)/ ZnSe(12nm), as seen in Figure 3.6.

All of the samples were grown at a growth temperature of 240^{o}C. Samples were further annealed at a high temperature of 320^{o}C, followed by cooling down to the initial growth temperature 240^{o}C, and succeeding growth of capping layers. A constant Se flux is applied throughout the annealing and subsequent cooling.

This study is focussed only on varying the times t_0 and t_2 while keeping all other growth parameters unchanged. These times are schematically shown in Figure 3.8. Initially a combination of three time delays t_0, t_1 and t_2 were examined extensively. Variations in t_1 produced no significant changes in the QD growth rate kinetics and hence a fixed value was used afterwards. On the other hand, changing t_0 and t_2 proved to be very influential in controlling the areal density of QDs. Two set of samples were grown and examined for each combination to confirm the changes and average out any random fluctuations in QD density during SK growth mode.

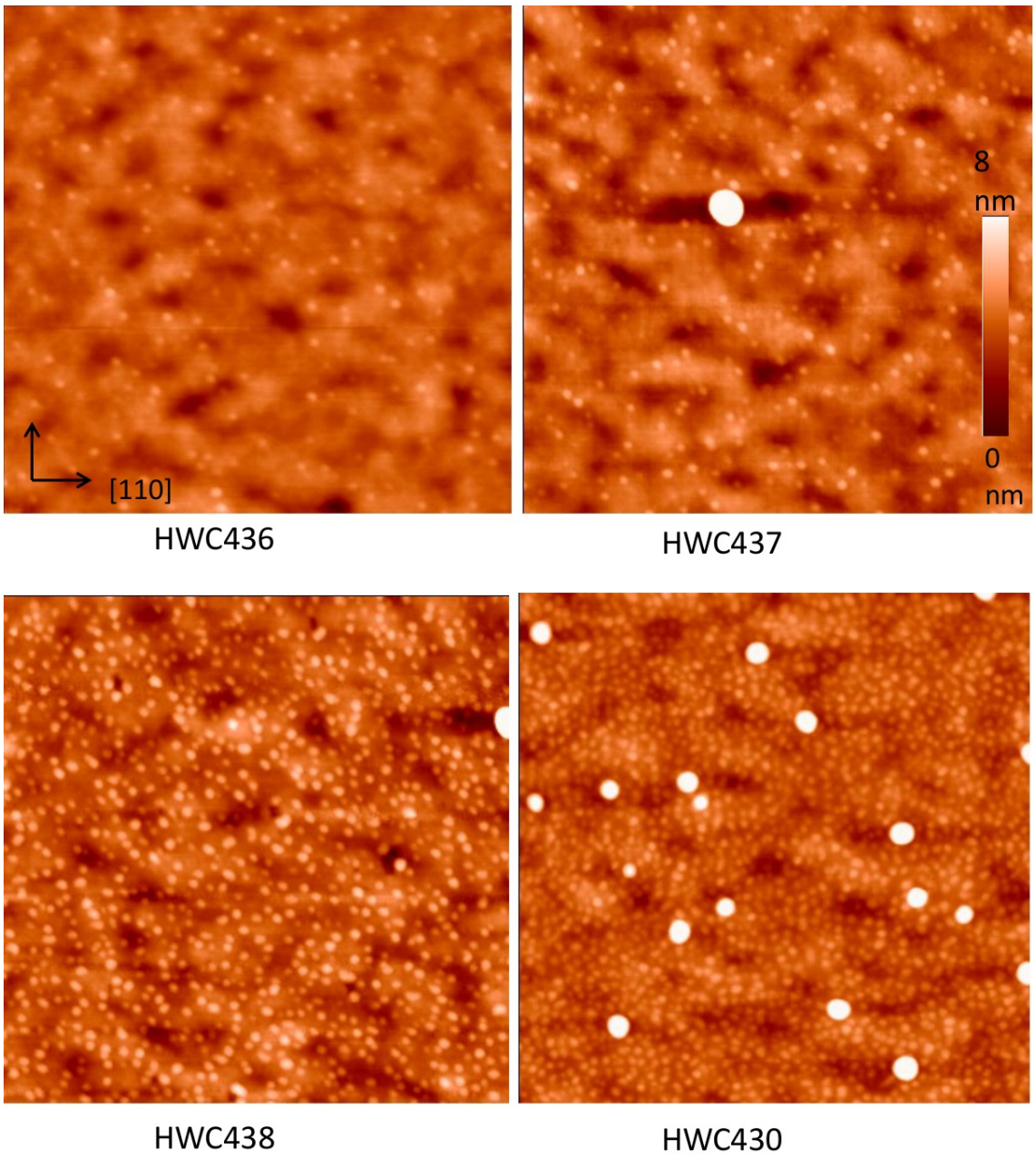

Figure 3.9: *2$\mu m \times 2\mu m$ AFM images of samples HWC436, HWC437, HWC438 and HWC430. The data obtained from these scans are given in Table 3.1. (The brighter dots on HWC430 and the single bright dot on HWC437 are selenium clusters.)*

3.10 Effects of growth delay after CdSe layer deposition, t_0

t_0 is the growth delay introduced after the final monolayer of CdSe was deposited, while the samples were still at the growth temperature and was varied from 0 to 100 minutes. Samples were then heated to the annealing temperature in 2 minutes(t_1) and annealed (t_2). For all the samples grown for this part of the study, t_2 was fixed at 15 minutes. Table 3.1 shows the results obtained from introducing the growth delay, also shown graphically in Figure 3.10.

Sample No.	Growth Delay, t_0 (min)	Annealing Time, t_2 (min)	QD Areal Density ($\times 10^8 cm^{-2}$)
HWC430	0	15	360
HWC436	1	15	40
HWC433	5	15	55
HWC437	10	15	64
HWC438	20	15	160
HWC439	40	15	184
HWC442	100	15	200

Table 3.1: *Effect of introducing various growth delays on quantum dot areal density for a fixed annealing time.*

Seven sets of samples, with each set containing at least two samples were grown with different growth delays t_0. The first set of samples were grown with t_0=0, i.e. samples were heated to the annealing temperature straight after the CdSe deposition. This was the usual way of QD growth at Heriot-Watt. The AFM images showed a large density of quantum dots in the range of $\sim$ 350-400 $\times 10^8 \text{cm}^{-2}$. The next set of samples was grown with t_0=1 min. Samples were then heated to the annealing temperature after 1 min. Surprisingly all three samples show a very low density of surface dots in AFM, varying from 38 - 44 $\times 10^8 \text{cm}^{-2}$. The change in the areal density of surface dots by introducing a 60 sec delay was dramatic. (See HWC436 in Figure 3.9)

This led to the growth of five more sets of samples, with increasing t_0 of 5, 10, 20, 40 and 100 minutes. Detailed results from all the seven sets of samples are given in Table 3.1. Scans were obtained from at least three different regions of every sample surface to ensure the uniformity of dot formation. No variations in the number of dots were observed from scans obtained from the center of a sample and its edges.

These samples can be easily assigned into three groups, depending on the areal density of dots. In the first group, samples grown with t_0=0 have shown the highest number of dots, whereas in the second group, samples grown with t_0= 1, 5 and 10 min have produced the lowest number of dots. Finally in the last group, samples grown with t_0= 20 min to 100 min have shown an almost saturation in the number of dots. No samples were grown further to investigate the effects of a prolonged (>100 min) growth delay in the areal

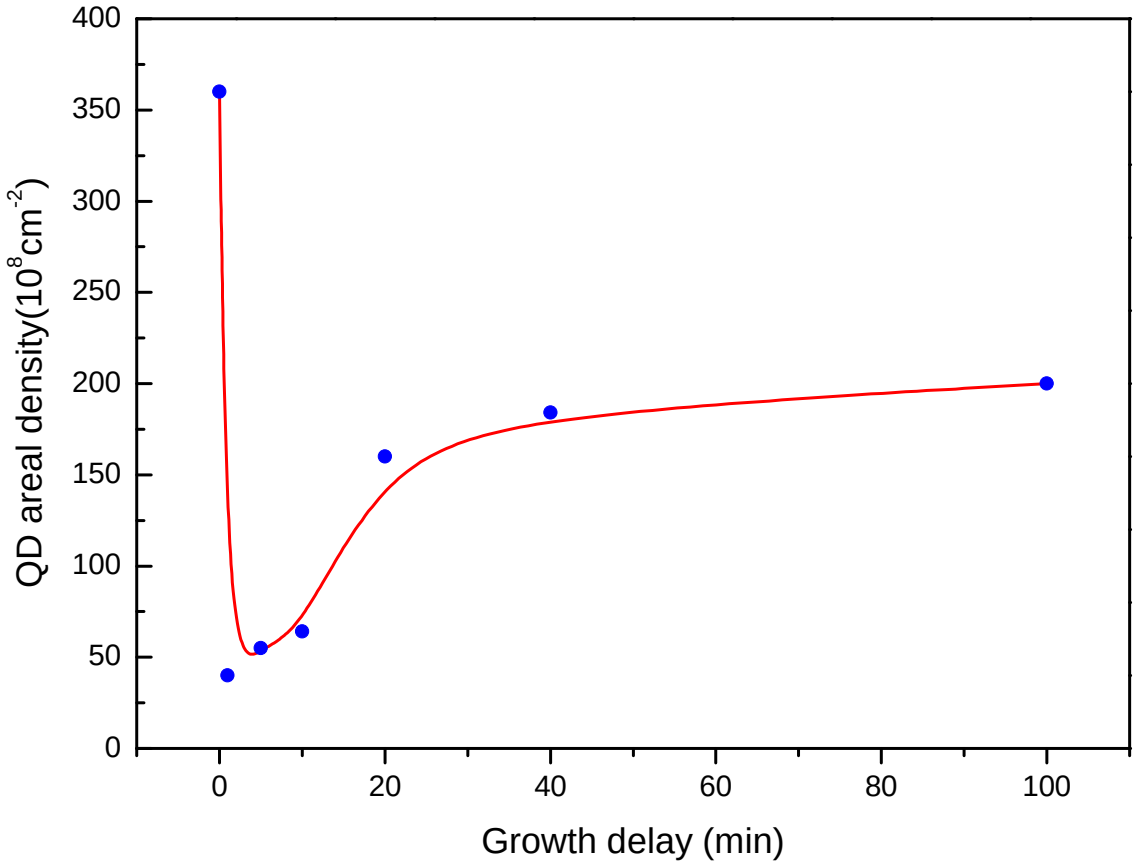

Figure 3.10: *Graph of QD areal density vs. growth delay, obtained from Table 3.1. (An effective error bar cannot be plotted alongside as the errors differ with density range. The lower dot denity (50-100 dots) samples had no errors whereas the high dot density (200-400 dots) samples had an error of ± 8 dots.)*

density of dots.

In terms of growth delay, a sudden drop in the areal density has been observed within the first minute. The density has slightly increased with time thereafter and from 1 min to 20 min, there was a gradual but slow increase. From 20 min onwards up to 100 min the dot formation has appeared to be saturated as the rate of increase in density has become negligible and by the 40-100 min range it was almost constant.

Figure 3.11 shows the PL emission spectra from three samples, HWC416, 417 and 418. The only difference among these three samples were the varying t_0. HWC416 has been annealed straight away after the CdSe deposition. Whereas t_0 of 20 min and 1 min were introduced during the growth of HWC417 and 418 respectively. From the shape and intensity of the PL emission, HWC416 has most dots and HWC418 the least.

The dots appear to be in the same size range as well. The ZnSe and QD features both show

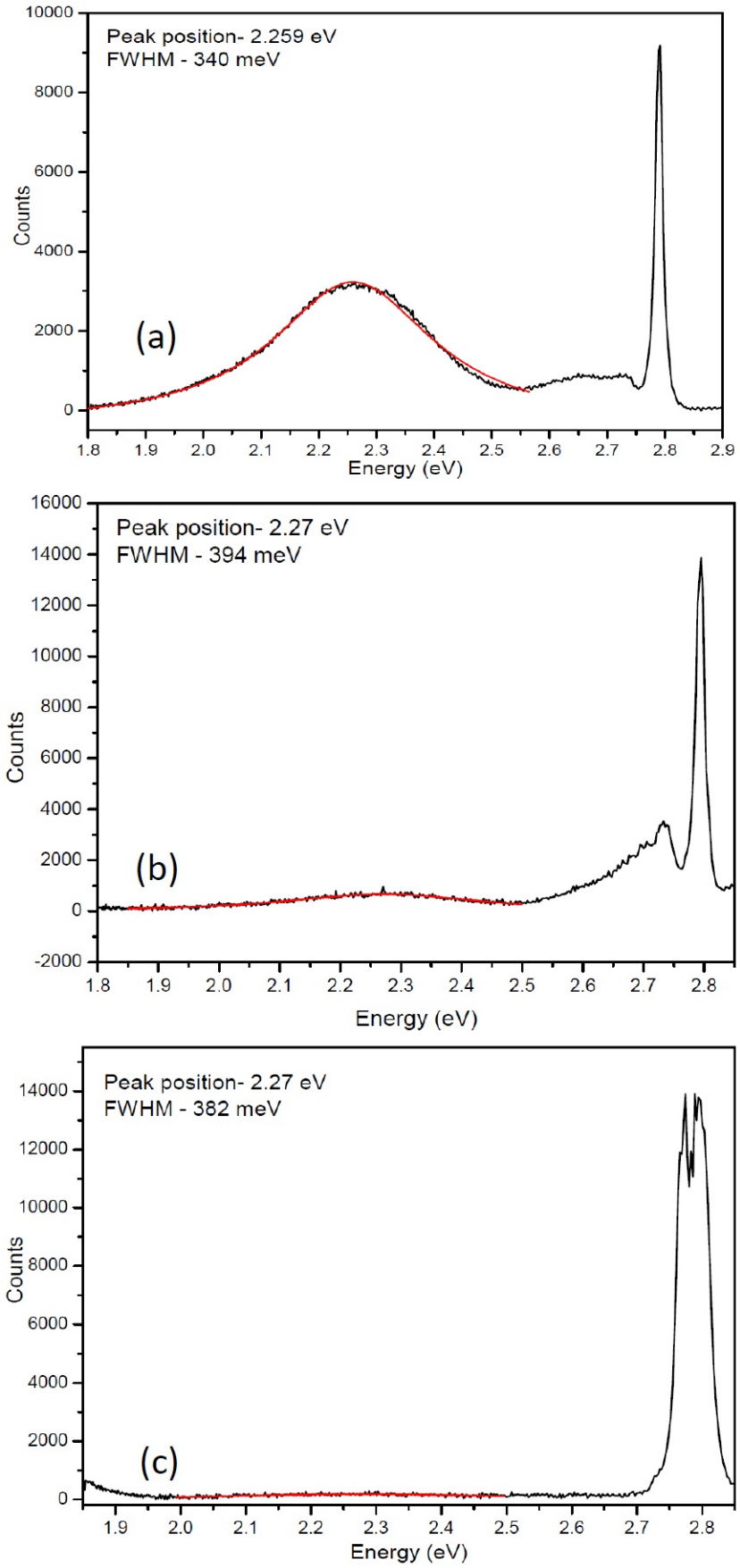

Figure 3.11: *77K PL spectra from samples (a) HWC416, (b) HWC417 and (c) HWC418, where the peak from the CdSe QDs is outlined in red. The corresponding t_0 are (a) 0 min, (b) 20 min and (c) 1 min.*

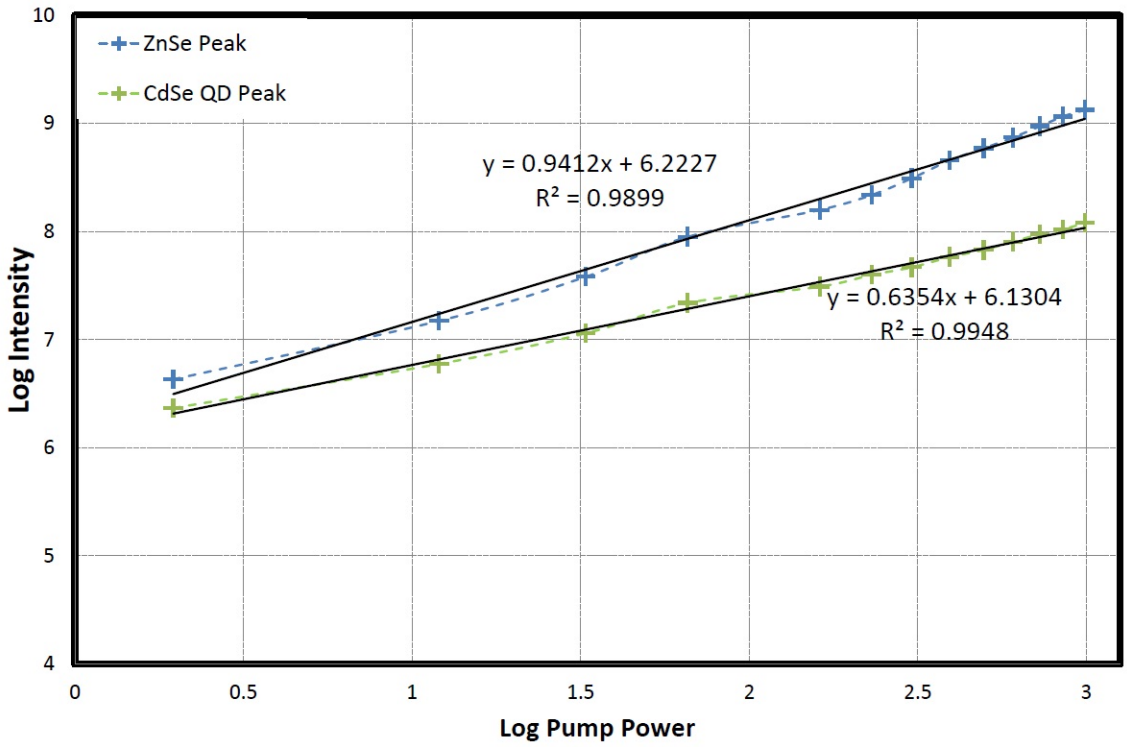

Figure 3.12: *The plot of Log pump power vs Log intensity from sample HWC416, where both the QD peak and ZnSe peaks show linear power scaling.*

roughly linear curves on a log/log intensity plot with gradient at least >0.5, so appear to be excitonic. See Figure 3.12. The reason for the plot to be not exactly linear is possibly due to not all photons being collected by the spectrometer. This is a drawback of the PL setup used currently at Heriot-Watt.

It is not practical to estimate the actual number of dots from PL at 77K. However similar samples were later grown uncapped and AFM characterisation agrees on the range of number of dots present. HWC416 has the highest number of dots, 400 $\times 10^8 \mathrm{cm}^{-2}$ while samples HWC417 and 418 have QD areal densities of 160 $\times 10^8 \mathrm{cm}^{-2}$ and 40 $\times 10^8 \mathrm{cm}^{-2}$ respectively. These PL spectra are thus in good agreement with the changes in the QD areal density with respect to growth delay.

All the QDs grown by varying growth delay, were of the same height measured using AFM, between 1.52 nm and 1.61 nm, except sample HWC438 which showed slightly taller dots at $\sim$ 1.78 nm. Diameter of a QD this small cannot be accurately measured using an AFM cantilever with tip radius in the range of $\sim$ 10 nm. This ultimately prevented calculating the total amount of material used for the QD formation and wetting layer. All the samples have shown randomly distributed QDs and the average dot seperation varied

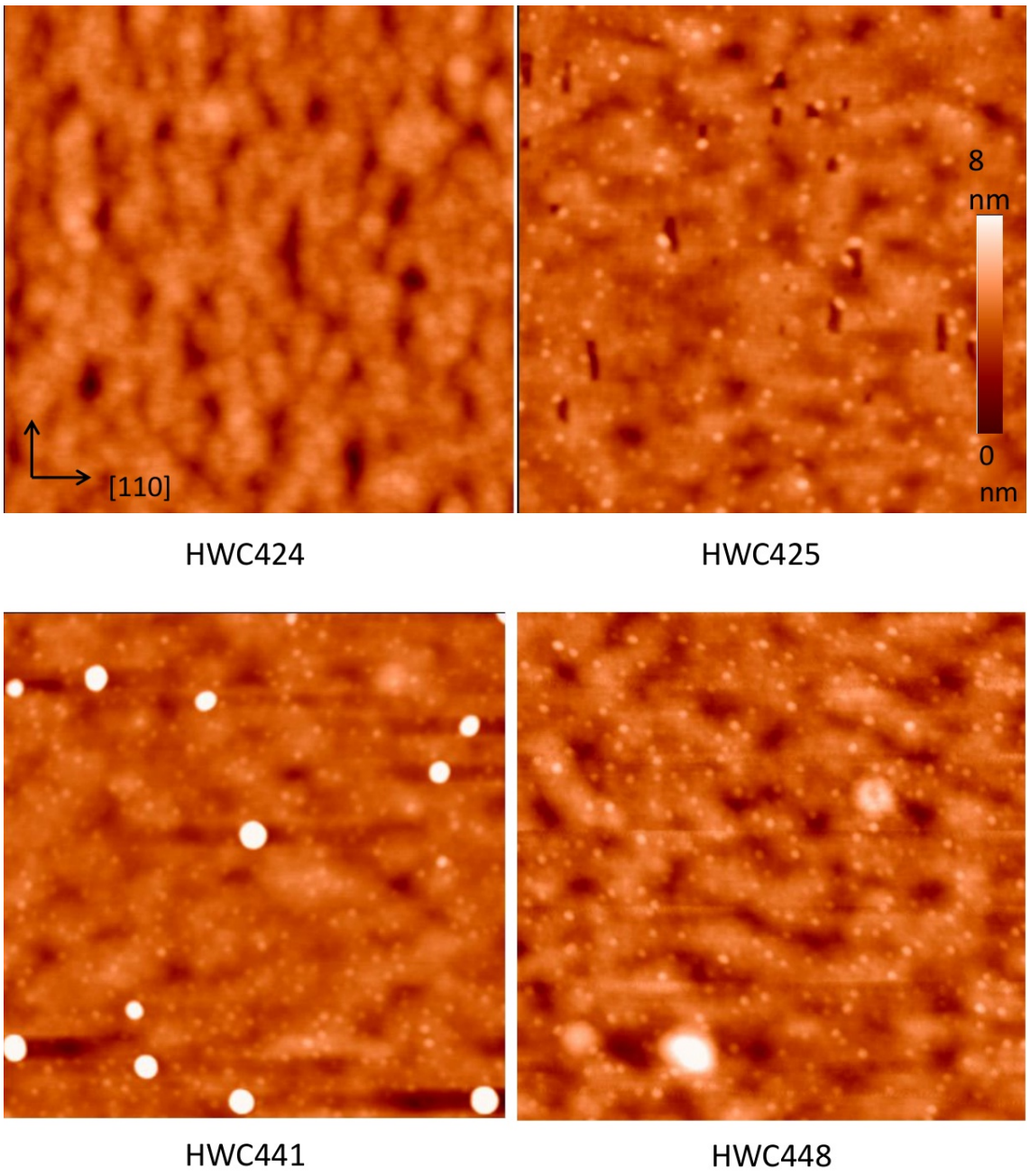

Figure 3.13: $2\mu m \times 2\mu m$ *AFM images of samples HWC424, HWC425, HWC441 and HWC448 with* t_2*=1, 5, 30 and 45 min respectively. The data obtained from these scans are given in Table 3.2. (The brighter dots on HWC441 and HWC448 are selenium containing clusters.)*

from $\sim$ 20 nm on HWC430 to $\sim$ 200 nm in HWC436.

These results have shown that the as grown CdSe initially prefers to smoothen and stabilize against islanding when a growth delay is introduced. This could be due to the loss of mobile adatoms initially available for the 3D island formation during the growth delay. These adatoms may then be incorporated at the edges of existing 2D precursor islands. The loss of adatoms is most important in the first minute with a slower nucleation rate

Sample No.	Growth Delay, t_0 (min)	Annealing Time, t_2 (min)	QD Areal Density ($\times 10^8 cm^{-2}$)
HWC428	1	0	0
HWC424	1	1	0
HWC425	1	5	42
HWC426	1	10	38
HWC436	1	15	40
HWC441	1	30	60
HWC448	1	45	72

Table 3.2: *Effect of varying annealing time on quantum dot areal density for a fixed growth delay time.*

becoming important at longer t_0. Material transport between islands is believed to be high during the initial growth delay. Exchange of atoms across the surface takes place during this time. This could explain why there were fewer dots initially and increasing with t_0. The highest number of 3D islands possible after any finite growth delay is still only less than half the number, in samples grown with t_0=0. This indicates that at least half of these adatoms are lost by introducing the initial growth delay. Even further high temperature annealing over extended period can recover only half the adatoms initially available and eventually it leads to 3D island formations.

3.11 Effects of annealing time, t_2

The second time delay examined during this study was the annealing time, t_2, which varied from 0 to 45 min. Seven sets of samples with each set containing at least two samples were grown. This time, the growth delay t_0 was set constant at 1 min, as this provided earlier the lowest areal density of dots. Again all other growth parameters were left unchanged within experimental error.

The first set consisted of samples grown with no annealing (t_2=0). Here, after the CdSe deposition, 1 min growth delay (t_0=1 min) was introduced and samples were immediately capped, without any high temperature annealing. AFM images of these samples (See Figure 3.13)have shown no 3D islands as expected. The next set of samples were annealed

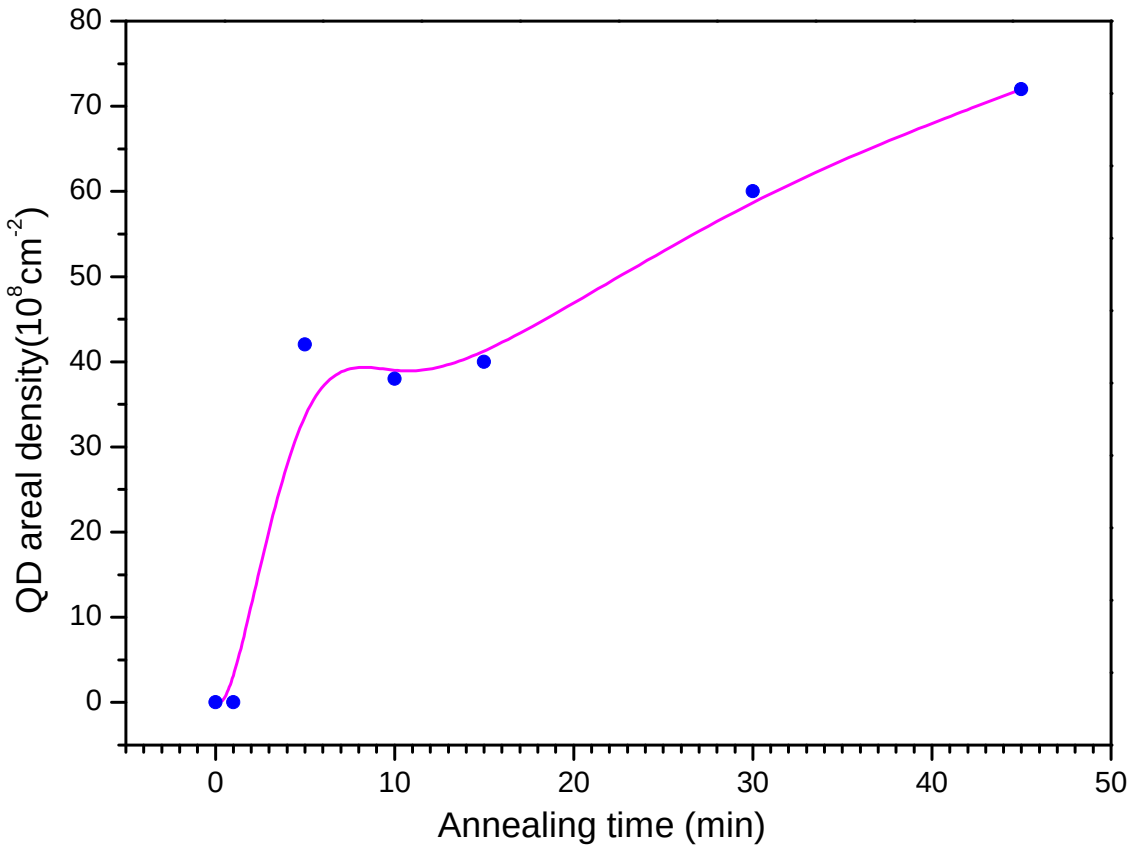

Figure 3.14: *Graph of QD areal density vs. annealing time, obtained from Table 3.2*

for 1 min and again the AFM showed no surface dots. However t_2=2 min produced some island like structures, but due to the long period surface undulations, it was not possible to count the 3D islands from an AFM image.

The corresponding RHEED pattern during growth supported the AFM data. For samples grown with t_2=0 or 1 min, the RHEED pattern was streaky and slightly diffuse without any presence of spots, which could indicate the start of the surface nucleation. The streaky patterns could be due to the continuous Se exposure throughout. However for t_2=2 min, the RHEED patterns showed elongated spots starting to form along the streaks, indicating the onset of formation of islands.

The next set of samples was grown with t_2= 5 min. AFM images showed clear surface islands in the density range of $\sim 40 \times 10^8 \text{cm}^{-2}$. The gradual transformation of the RHEED pattern from slightly diffused streaks to completely elongated spots was observed during the growth. Further growths with increased t_2 of 10 and 15 min produced similar results. The areal density of the dots was constant throughout this annealing time window of 5-15 min, and with similarly sized dots in the range of 38 - 42 $\times 10^8 \text{cm}^{-2}$. This is the lowest

II-VI QD density reported to date on non patterned substrates.

Further increasing t_2 has shown a gradual increase in the number of dots. For t_2=45 min, the dot density was $\sim 70 \times 10^8 \text{cm}^{-2}$. No attempts were made to anneal the sample beyond t_2=45 min. The results from varying annealing time are shown in Figure 3.13. It is also schematically represented in Figure 3.14, where the numbers of dots are plotted against t_2. It can be seen that within a time window of 5-10 min the dot density is stable. Beyond this range, the density can be effectively tuned upwards by changing t_2.

3.12 Summary

An easy and effective method for eliminating SeO_2 clusters from the surface of QD structures by annealing to above the evaporation temperature of Se has been demonstrated. This technique prevents any future ripening of SeO_2 and the QDs are not affected. No significant difference has been noticed between performing the annealing in atmosphere and under vacuum.

The areal density of CdSe QDs grown on MgS barriers has been examined. Introducing a growth delay soon after the CdSe deposition, before annealing has proved to be very effective in significantly reducing the number of QDs. A one minute delay has reduced the number of dots by a tenth. Further growth interruptions have helped to gradually increase the number of dots, to get to a saturation point, beyond which any further growth delay seems to be not affecting the number of dots. The number of dots have been confirmed through repeated growths.

The effect of annealing time on the number of dots has also been studied. Samples grown with different annealing time have shown varying number of dots. At least two minutes of annealing was required for any quantum dot formation. An increased number of dots with increased annealing time was noticed. Three ranges of saturation in number of dots formed with respect to the annealing time has been observed.

RHEED has also been used to monitor the QD formation *in situ*. AFM was extensively

used to count the surface dots, whereas 77K PL was primarily used to ensure the presence of QDs. Majority of the dots were of the same height range, $\sim$ 1.52 to 1.61 nm. By controlling just the growth delay and annealing time, the number of dots can be effectively reduced to as low as $\sim 3.8 \times 10^9 \text{cm}^{-2}$. This is the lowest, reproducible II-VI dot density reported to date using MBE/MEE on non-patterned substrates.

3.13 Future Work

By combining various growth delays (t_0) and annealing temperatures (t_2), it has been demonstrated that the QD areal density can be tuned effectively, over the range 3.8 - 40 $\times 10^9 \text{cm}^{-2}$. With the help of changes in other important parameters, this method could lead to a more precise control of areal density. The number of QDs can also be controlled by varying other important parameters such as the CdSe layer thickness, metal/non-metal flux ratio (only in MBE growth mode), substrate temperature, annealing temperature, etc.

By properly measuring the dimensions of a dot using a characterisation technique such as TEM, the amount of material transformed to QDs can be studied. Any difference in the structure of dots grown with t_0= 0 and 1 minute is of particular interest as it is possible to get a more convincing explanation for the significant drop in the number of dots within such a short time.

One of the major difficulties associated with this study was the lack of an appropriate optical characterisation technique. The 77K PL presented in this chapter is not adequate to study the optical properties of the QDs. All counting of the dot densities were performed using an AFM on tapping mode. A μ-PL setup is necessary to compliment the AFM results as well as to provide even more details on the grown dots.

The effects of strain on QD formation can possibly be studied by growing a series of samples on relaxed off-lattice ZnCdSe, ZnSSe, ZnMgSSe, ZnCdSSe or ZnCdMgSe of different thickness deposited on MgS. Growth of both PL and AFM samples would be beneficial.

3.14 References

[1] D. Bimberg, M. Grundmann and N. N. Ledentsov. *Quantum Dot Heterostructures*. Wiley, 1999 (cited on pages: 50, 53, 59).

[2] W. A. Harrison. "Elementary theory of heterojunctions". *Journal of Vacuum Science and Technology* Vol. 14 (1977), pp. 1016–1021 (cited on page: 51).

[3] C. Bradford, B. Urbaszek, M. Funato, A. Balocchi, T. C. M. Graham, E. J. McGhee, R. J. Warburton, K. A. Prior and B. Cavenett. "Growth and characterization of MgS/CdSe self-assembled quantum dots". *Journal of Crystal Growth* Vol. 251 (2003), pp. 581–585 (cited on page: 51).

[4] C. Bradford, C. B. O'Donnell, B. Urbaszek, A. Balocchi, C. Morhain, K. A. Prior and B. C. Cavenett. "Growth of zinc blende MgS/ZnSe single quantum wells by molecular-beam epitaxy using ZnS as a sulphur source". *Applied Physics Letters* Vol. 76 (2000), pp. 3929–3931 (cited on page: 51).

[5] M. Funato, A. Balocchi, C. Bradford, K. A. Prior and B. C. Cavenett. "Photoluminescence properties of MgS/CdSe quantum wells and quantum dots". *Applied Physics Letters* Vol. 80 (2002), pp. 443–445 (cited on page: 51).

[6] C. Bradford, C. B. O'Donnell, B. Urbaszek, C. Morhain, A. Balocchi, K. A. Prior and B. C. Cavenett. "Highly confined excitons in MgS/ZnSe quantum wells grown by molecular beam epitaxy". *Phys. Rev. B* Vol. 64 (2001), pages (cited on page: 51).

[7] H. Lan and Y. Ding. "Ordering, positioning and uniformity of quantum dot arrays". *Nano Today* Vol. 7 (2012), pp. 94–123 (cited on pages: 51, 60).

[8] C. M. Marcus, S. R. Patel, A. G. Huibers, S. M. Cronenwett, M. Switkes, I. H. Chan, R. M. Clarke, J. A. Folk, S. F. Godijn, K. Campman and A. C. Gossard. "Quantum chaos in open versus closed quantum dots: Signatures of interacting particles". *Chaos, Solitons & Fractals* Vol. 8 (1997), pp. 1261–1279 (cited on page: 52).

[9] C. R. K. Marrian, E. A. Dobisz and M. C. Peckerar. "Nanostructure patterning". *Proceedings of the IEEE* Vol. 79 (1991), pp. 1149–1158 (cited on page: 53).

[10] S. P. Beaumount. *Low-dimensional Structures in Semiconductors*. Plenum Press, New York, 1991 (cited on page: 53).

[11] A. C. Warren, I. Plotnik, E. H. Anderson, M. L. Schattenburg, D. A. Antoniadis and H. I. Smith. “Fabrication of sub-100-nm linewidth periodic structures for study of quantum effects from interference and confinement in Si inversion layers”. *Journal of Vacuum Science Technology B: Microelectronics and Nanometer Structures* Vol. 4 (1986), pp. 365–368 (cited on page: 53).

[12] R. E. Howard, L. D. Jackel and W. J. Skocpol. “Nanostructures: Fabrication and Applications”. *Microelectronic Engineering* Vol. 3 (1985), pp. 3–16 (cited on page: 53).

[13] T. Kanayama, M. Komuro, H. Hiroshima, J. Itoh, N. Atoda, H. Tanoue and T. Tsurushima. “Fine pattern definition with atomic intermixing induced by focused ion beam and its application to x-ray mask fabrication”. *Journal of Vacuum Science Technology B: Microelectronics and Nanometer Structures* Vol. 9 (1991), pp. 295–301 (cited on page: 53).

[14] H. G. Craighead, R. E. Howard, L. D. Jackel and P. M. Mankiewich. “10-nm linewidth electron beam lithography on GaAs”. *Applied Physics Letters* Vol. 42 (1983), pp. 38–40 (cited on page: 54).

[15] S. V. Gaponenko. *Optical Properties of Semiconductor Nanocrystals*. Cambridge Studies in Modern Optics. Cambridge University Press, 1998 (cited on page: 54).

[16] A. Pimpinelli and J. Villain. *Physics of Crystal Growth*. Collection Aléa-Saclay. Cambridge University Press, 1998 (cited on page: 55).

[17] K. Oura, V. G. Lifshits, A. A. Saranin and A. V. Zotov. *Surface Science: An Introduction*. Advanced Texts in Physics. Springer, 2003 (cited on page: 55).

[18] J. A. Venables. *Introduction to Surface and Thin Film Processes*. Cambridge University Press, 2000 (cited on page: 55).

[19] W. Seifert, N. Carlsson, M. Miller, M.-E. Pistol, L. Samuelson and L. R. Wallenberg. “In-situ growth of quantum dot structures by the Stranski-Krastanow growth mode”. *Progress in Crystal Growth and Characterization of Materials* Vol. 33 (1996), pp. 423–471 (cited on pages: 56, 57, 60).

[20] M. Meixner, E. Schöll, V. A. Shchukin and D. Bimberg. “Self-Assembled Quantum Dots: Crossover from Kinetically Controlled to Thermodynamically Limited Growth”. *Phys. Rev. Lett.* Vol. 87 (2001), p. 236101 (cited on page: 59).

[21] G. S. Solomon, J. A. Trezza and J. J. S. Harris. “Effects of monolayer coverage, flux ratio, and growth rate on the island density of InAs islands on GaAs”. *Applied Physics Letters* Vol. 66 (1995), pp. 3161–3163 (cited on page: 60).

[22] I. Daruka and A.-L. Barabási. “Dislocation-Free Island Formation in Heteroepitaxial Growth: A Study at Equilibrium”. *Phys. Rev. Lett.* Vol. 79 (1997), pp. 3708–3711 (cited on pages: 60, 62).

[23] S. H. Xin, P. D. Wang, A. Yin, C. Kim, M. Dobrowolska, J. L. Merz and J. K. Furdyna. “Formation of self-assembling CdSe quantum dots on ZnSe by molecular beam epitaxy”. *Applied Physics Letters* Vol. 69 (1996), pp. 3884–3886 (cited on pages: 60–62, 66).

[24] M. Rabe, M. Lowisch, F. Kreller and F. Henneberger. “Self-Assembled Visible-Bandgap II–VI Quantum Dots”. *physica status solidi (b)* Vol. 202 (1997), pp. 817–826 (cited on pages: 60, 62).

[25] E. Kurtz, H. D. Jung, T. Hanada, Z. Zhu and T. Yao. “Properties of self-organized CdSe quantum dots on an atomically flat (111)A ZnSe surface”. *Applied Surface Science* Vol. 130 - 132 (1998), pp. 755–759 (cited on page: 60).

[26] D. Hommel, K. Leonardi, H. Heinke, H. Selke, K. Ohkawa, F. Gindele and U. Woggon. “CdSe/ZnSe Quantum Dot Structures: Structural and Optical Investigations”. *physica status solidi (b)* Vol. 202 (1997), pp. 835–843 (cited on pages: 60, 62).

[27] M. Grün, F. Funfrock, P. Schunk, T. Schimmel, M. Hetterich and C. Klingshirn. “On the nature of nanometer-scale islands formed by cadmium selenide deposition on hexagonal cadmium sulfide (0001)A”. *Applied Physics Letters* Vol. 73 (1998), pp. 1343–1345 (cited on pages: 61, 63).

[28] N. Matsumura, Y. Kimura, H. Endo and J. Saraie. “Self-assembling CdTe quantum dots on ZnSe by alternate supplying and molecular beam epitaxial method”. *Journal of Crystal Growth* Vol. 214 - 215 (2000), pp. 694–697 (cited on page: 61).

[29] Z. H. Ma, W. D. Sun, I. K. Sou and G. K. L. Wong. “Atomic force microscopy studies of ZnSe self-organized dots fabricated on ZnS/GaP”. *Applied Physics Letters* Vol. 73 (1998), pp. 1340–1342 (cited on page: 61).

[30] K. Arai, Z. Q. Zhu, T. Sekiguchi, T. Yasuda, F. Lu, N. Kuroda, Y. Segawa and T. Yao. “Photoluminescence and cathodoluminescence studies of ZnSe quantum

structures embedded in ZnS". *Journal of Crystal Growth* Vol. 184 - 185 (1998), pp. 254–258 (cited on page: 61).

[31] M. Strassburg, T. Deniozou, A. Hoffmann, R. Heitz, U. W. Pohl, D. Bimberg, D. Litvinov, A. Rosenauer, D. Gerthsen, S. Schwedhelm, K. Lischka and D. Schikora. "Coexistence of planar and three-dimensional quantum dots in CdSe/ZnSe structures". *Applied Physics Letters* Vol. 76 (2000), pp. 685–687 (cited on page: 61).

[32] C. S. Kim, M. Kim, S. Lee, J. K. Furdyna, M. Dobrowolska, H. Rho, L. M. Smith and H. E. Jackson. "Optical observation of quantum-dot formation in sub-critical CdSe layers grown on ZnSe". *Journal of Crystal Growth* Vol. 214 - 215 (2000), pp. 761–764 (cited on page: 61).

[33] C. S. Kim, M. Kim, J. K. Furdyna, M. Dobrowolska, S. Lee, H. Rho, L. M. Smith, H. E. Jackson, E. M. James, Y. Xin and N. D. Browning. "Evidence for 2D Precursors and Interdiffusion in the Evolution of Self-Assembled CdSe Quantum Dots on ZnSe". *Phys. Rev. Lett.* Vol. 85 (2000), pp. 1124–1127 (cited on page: 61).

[34] D. Schikora, S. Schwedhelm, I. Kudryashov, K. Lischka, D. Litvinov, A. Rosenauer, D. Gerthsen, M. Strassburg, A. Hoffmann and D. Bimberg. "Investigations on the formation kinetics of CdSe quantum dots". *Journal of Crystal Growth* Vol. 214 - 215 (2000), pp. 698–702 (cited on page: 61).

[35] S. V. Ivanov, A. A. Toropov, S. V. Sorokin, T. V. Shubina, I. V. Sedova, A. A. Sitnikova, P. S. Kop'ev, Z. I. Alferov, H.-J. Lugauer, G. Reuscher, M. Keim, F. Fischer, A. Waag and G. Landwehr. "CdSe fractional-monolayer active region of molecular beam epitaxy grown green ZnSe-based lasers". *Applied Physics Letters* Vol. 74 (1999), pp. 498–500 (cited on pages: 61, 62).

[36] J. C. Kim, H. Rho, L. M. Smith, H. E. Jackson, S. Lee, M. Dobrowolska, J. L. Merz and J. K. Furdyna. "Spectroscopic characterization of the evolution of self-assembled CdSe quantum dots". *Applied Physics Letters* Vol. 73 (1998), pp. 3399–3401 (cited on page: 61).

[37] H. Kirmse, R. Schneider, M. Rabe, W. Neumann and F. Henneberger. "Transmission electron microscopy investigation of structural properties of self-assembled CdSe/ZnSe quantum dots". *Applied Physics Letters* Vol. 72 (1998), pp. 1329–1331 (cited on page: 62).

[38] I. Suemune, K. Uesugi, H. Suzuki, H. Nahiki and M. Arita. “Low-Dimensional II–VI Semiconductor Structures: ZnSe/MgS Superlattices and CdSe Self-Organized Dots”. *physica status solidi (b)* Vol. 202 (1997), pp. 845–856 (cited on page: 62).

[39] M. Grundmann, O. Stier and D. Bimberg. “InAs/GaAs pyramidal quantum dots: Strain distribution, optical phonons, and electronic structure”. *Phys. Rev. B* Vol. 52 (1995), pp. 11969–11981 (cited on page: 62).

[40] J. B. Smathers, E. Kneedler, B. R. Bennett and B. T. Jonker. “Nanometer scale surface clustering on ZnSe epilayers”. *Applied Physics Letters* Vol. 72 (1998), pp. 1238–1240 (cited on pages: 62, 65–67).

[41] F. Liu, A. H. Li and M. G. Lagally. “Self-Assembly of Two-Dimensional Islands via Strain-Mediated Coarsening”. *Phys. Rev. Lett.* Vol. 87 (2001), p. 126103 (cited on page: 63).

[42] S. Lee, I. Daruka, C. S. Kim, A. L. Barabási, J. L. Merz and J. K. Furdyna. “Dynamics of Ripening of Self-Assembled II-VI Semiconductor Quantum Dots”. *Phys. Rev. Lett.* Vol. 81 (1998), pp. 3479–3482 (cited on page: 63).

[43] P. R. Kratzert, M. Rabe and F. Henneberger. “Formation and stability of II - VI self-assembled quantum dots revealed by in situ atomic force microscopy”. *Applied Surface Science* Vol. 166 (2000), pp. 332–335 (cited on page: 63).

[44] M. Rabe, M. Lowisch and F. Henneberger. “Self-assembled CdSe quantum dots Formation by thermally activated surface reorganization”. *Journal of Crystal Growth* Vol. 184 - 185 (1998), pp. 248–253 (cited on page: 64).

[45] A. Ohtake, T. Hanada, T. Yasuda, K. Arai and T. Yao. “Structure and composition of the ZnSe(001) surface during atomic-layer epitaxy”. *Phys. Rev. B* Vol. 60 (1999), pp. 8326–8332 (cited on page: 64).

[46] Y. Horikoshi. “Advanced epitaxial growth techniques: atomic layer epitaxy and migration-enhanced epitaxy”. *Journal of Crystal Growth* Vol. 201- 202 (1999), pp. 150–158 (cited on page: 64).

[47] S. Sorokin, T. Shubina, A. Toropov, I. Sedova, A. Sitnikova, R. Zolotareva, S. Ivanov and P. Kopev. “Peculiarities of migration-enhanced-epitaxy (MEE) versus molecular beam epitaxy (MBE) growth kinetics of CdSe fractional monolayers in

ZnSe". *Journal of Crystal Growth* Vol. 201 - 202 (1999), pp. 461–464 (cited on page: 65).

[48] Y. J. Lai, Y. C. Lin, C. P. Fu, C. S. Yang, C. H. Chia, D. S. Chuu, W. K. Chen, M. C. Lee, W. C. Chou, M. C. Kuo and J. S. Wang. "Growth mode transfer of self-assembled CdSe quantum dots grown by molecular beam epitaxy". *Journal of Crystal Growth* Vol. 286 (2006), pp. 338–344 (cited on page: 66).

[49] J. L. Merz, S. Lee and J. K. Furdyna. "Self-organized growth, ripening, and optical properties of wide-bandgap II–VI quantum dots". *Journal of Crystal Growth* Vol. 184–185 (1998), pp. 228–236 (cited on page: 66).

Chapter 4

Control of surface morphology in zinc blende MgS

4.1 Introduction

MgS is an unusual II-VI semiconductor with a number of interesting properties, in particular, its huge bandgap, $\sim$ 5eV. As a result, thin ($<$20 nm) layers of ZB MgS have found a number of uses. A few of the important applications of MgS in both the ZB and RS phase is given in Table 4.1.

Although stable bulk crystal structure of MgS is RS, the Phillips' ionicity of MgS is 0.786, which is close to the boundary between the regions of stability for the ZB and RS phases. Navrotsky and Philips [1] have proved that the free energy for the transformation between the ZB and RS phases is close to zero. Using a thin film growth technique like MBE, it is possible to grow compounds and alloys in the ZB phase when it is not their stable crystal structure. MgS can be grown epitaxially in the metastable ZB structure if grown on a (001) ZnSe layer, and is lattice matched to both ZnSe and GaAs. When grown on GaAs substrate in ZB crystal structure, MgS has a tensile strain of only 0.55% whereas ZnSe has a compressive strain of -0.27%. Hence strain symmetrised structures are possible with ZnSe/MgS multilayers.

Growth of metastable rocksalt compounds such as MgS on ZB substrates is not straightforward. Prior to the attempts to grow MgS epitaxially, the material was grown as a low purity polycrystalline powder using different methods based on the reduction of Magnesium sulphate [8]. A number of groups have also attempted to grow ZB MgS by both

Structure	Application	Grower	Year	Reference
(ZB)MgS/ZnSe/(ZB)MgS	Barrier for ZnSe QWs	Heriot-Watt University	2000	[2]
ZnSe/(ZB)MgS superlattice	DBR stacks	University of Bremen	2002	[3]
(ZB)MgS/CdSe/(ZB)MgS	Barrier for CdSe QWs and QDs	Heriot-Watt University	2002	[4]
ZnSe/(ZB)MgS/ZnSe	Epitaxial Lift-off	Heriot-Watt University	2005	[5]
CdSe/ZnSSe/(ZB)MgS	Barrier in room temperature CdSe single photon emitters	University of Duisburg-Essen and University of Bremen	2012	[6]
(RS)MgS/Au	Solar blind UV detectors	The Hong Kong University of Science and Technology	2012	[7]

Table 4.1: *Applications of MgS in both ZB and RS phase*

Grower	Method	Year	Thickness (nm)
Sharp Labs [9]	MBE	1995	0.96
Suemune et. al. [11]	MOVPE	1996	10
Konczewicz et. al. [10]	MOVPE	1996	2000 (ZB & RS phases)
C. Bradford et. al [2]	MBE	2000	134

Table 4.2: *Past growths of MgS in ZB phase*

Metalorganic Vapour Phase Epitaxy (MOVPE) and MBE and the results are given in Table 4.2. Initial attempts to grow ZB MgS by MBE directly on GaAs produced layers of only 0.96 nm thick before changes in the RHEED patterns indicated a phase transition back to RS [9] and recently, it has been confirmed that MgS only grows in the RS structure when deposited directly on GaAs, possibly as a result of interaction with the substrate forming coumpounds such as Ga_2S_3 [7]. Layers of MgS up to approximately 2μm thick have also been grown on GaAs (100) substrates using MOVPE, but both the ZB and rocksalt phases were detected by X-ray diffraction [10].

Previous work at Heriot-Watt has however shown that thick ZB MgS layers can be deposited on ZnSe buffer layers using Mg and ZnS as sources [2]. Above a certain critical thickness the layer always reverts to the stable RS structure. The thickest ZB Mgs layer reported before this study was 134 nm thick, which was produced with the aid of an added MgS/ZnSe smoothing layer [12].

It was not obvious if the critical thickness value obtained was an upper limit, determined primarily by thermodynamic constraints, or merely a product of the normal operating conditions. This chapter is an investigation into the factors affecting the growth of thicker ZB MgS layers. By varying different growth parameters such as material fluxes, growth temperature, etc the effect of MgS growth dynamics has been studied here. A brief account on the difficulties faced while attempting the MgS growth in the beginning of this project is followed by the demonstration of successful growth. RHEED was used to study the surface morphology, *in situ* during growth. Post growth examinations were carried out using AFM, XRI and XRD.

4.2 Growth of Magnesium Sulphide

4.2.1 Flux stability

All of the samples mentioned in this study were grown in the HWC chamber using 6N elemental sources of Zn, Se and Mg and a 6N compound source of ZnS. A liquid nitrogen cooled shutter was fitted between the ZnS cell and the shutter in order to help reduce the amount of sulphur leaking around the shutter when the cell is at its normal operating temperature [13]. Previous work showed that this approach has helped considerably to reduce the low partial pressure of sulphur containing species in the chamber during growth.

However there were other issues related to the long term stability of the ZnS flux, where it was noted that the flux began to drop considerably after approximately 25-30 growths. Examining the ZnS cell and shutter revealed that there were chunks of ZnS built up around the liquid nitrogen cooled shutter, effectively reducing the exit area and thus causing a reduction of the material effusing from the cell.

Although at this point there was enough source material left in the cell, big crystals of ZnS on the top of the cell were intact and thought to be acting as a plug and restricting the evaporation of material from behind. This phenomenon has been noted earlier in this group and measures were taken to use only small crystals of ZnS during refill. But this tends to happen if extra care has not been taken in selecting the ZnS pieces used to fill the cell.

Another problem with the ZnS shutter is associated with the built up of material on the shutter itself. This prevents the shutter from opening sometimes. This is a real challenge as there is no visual aid on the actual position of ZnS shutter and the external shutter mechanism is not mechanically connected to the internal shutter but uses magnetic coupling. During growth, while opening the shutter, the outer magnet moves and will be in the shutter open position with the indicator ON regardless of the real position of the internal shutter. If the shutter gets stuck inside during growth, the only way to find out is from the changes in RHEED pattern.

Later it was found that Se cell was also developing a similar issue when excess material was left on the shutter. But this is a rather rare event compared to ZnS.

4.2.2 GaAs substrate preparation

GaAs(100) substrates from American Crystal Technology (ATX) were used for the growth of MgS epitaxial layers. Prior to entry into the growth chamber, substrates were etched in a 2:2:20 solution of H_2O_2:H_2O:H_2SO_4 for 90s. The substrates were then rinsed in 18 MΩ deionised water and quickly dried with a jet of dry oxygen free nitrogen (OFN) gas. The substrates were then bonded to a molybdenum block using indium as a bonding agent. Massies et al. [14] has shown that this bonding process leaves a substrate surface oxidised. Depending on the temperature and time taken during bonding, oxide layer thickness typically varies to 2-3 nm.

The sample is then transferred to the prep chamber via the fast entry lock and placed under the prep heater and heated to $\sim$ 120 °C for 10 minutes to remove any water left on the sample. In the growth chamber the oxide layer is removed from the sample surface by rapidly heating to $\sim$ 580 °C. The sample is then cooled down to the growth temperature below 280 °C under a Zn flux [15]. After oxide layer removal, a sharp (4x2) RHEED pattern was observed on the (001) GaAs surface, indicating a clean surface with no sulphur contamination.

All MgS growths were initiated on thin ZnSe buffer layers (typically $\sim$ 50nm) grown on the GaAs substrate. These buffer layers helps prevent the sulphur from reacting with the GaAs substrate. A 3D RHEED pattern will be visible for the first 20-30 seconds into the growth, which subsequently transforms into a streaky (2x1) pattern indicating flat surface within the next 10 sec.

No changes were made to this preparation process during this study.

4.2.3 ZB MgS growth mechanism

The development of ZB MgS crystal structure and the growth occurs when at least, part of the impinging Zn flux become bonded at the surface, with the favoured tetrahedral bonding. But before the next layer is formed, these Zn atoms are replaced by Mg atoms which are then forced into a four fold coordination.

The ZnS growth rate in the region 240-270 °C was calculated in calibration 'Batch A' samples to be 0.09 μm/hr, while that of the MgS was 0.15 μm/hr because the incorporation rate of sulphur on a growing ZnS growth is considerably lower than unity while Mg is known to increase the incorporation of sulphur in quaternary alloy ZnMgSSe [16].

4.2.4 Additional notes

Three different batches of samples were investigated in this chapter. The first batch of samples belong to a set, grown at Heriot-Watt in the year 2000 and called in this chapter as 'Batch A'. 'Batch B' is the set of defective samples initially grown after the lab relocation for the works mentioned in this chapter whereas 'Batch C' samples were the final set, grown by optimising all the growth parameters.

All the material fluxes were measured using a Keithley picoammeter, which shows the beam equivalent pressure (BEP) in nA.

XRI structures used in this chapter typically have a structure ZnSe (50nm)/ MgS (varying thickness)/ ZnSe (50nm), unless otherwise specified.

4.3 Challenges in initial MgS growth

Initially MgS samples were grown by keeping the Mg cell temperature constant at 375 °C and adjusting the ZnS cell temperature so that to get a ZnS BEP of $\sim$ 500 nA. This was

based on the previous successful growths performed at Heriot-Watt MBE group. It was thought that prolonged exposure to Mg flux results in the background current of an ion gauge to rise rapidly and hence routine measurement of Mg flux was avoided to prevent contamination. Occasional Mg flux measurements have shown a steady BEP of ∼45 nA, giving a BEP ratio of ∼ 1:11 Mg:ZnS.

4.3.1 Changes in growth environment after lab relocation

There were a number of unavoidable changes in the growth environment compared to the previous growths in this group. Because of the small range of growth conditions which produces ZB MgS, any small alterations could lead to dramatic changes in the sample morphology. This section briefly discusses about the changes in the MBE growth situation.

Shifting of the MBE laboratory was a massive step at the beginning of this project. The entire MBE system has been moved to a new lab in another building. The whole process of decommissioning and assembling back took several months. All of the shutters and cells from both the chambers have been securely removed and valves were closed tightly with flanges. The reassembly followed a careful leak detection of several sections and a comprehensive baking. After restarting growth in the new lab, there were signs of roughening substrate surface during growth, as evidenced from RHEED. However the sample morphology began to improve over the next few growths and was judged acceptable after approximately 10 growths.

Another problem arising was from the substrate temperature reading. The thermocouple attached to the rear of the substrate heater in manipulator was the primary temperature measuring point. Soon after the growth resumed in the lab, the thermocouple reading began to fluctuate by over tens of degrees during growth. A few times, the thermocouple has registered no temperatures for approximately 20-30 seconds during growth. This started to happen at regular intervals and jeopardised an ongoing growth. The substrate manipulator had to be brought out for inspection. It was found that the thermocouple junction at the back of the substrate heater became loose causing a separation when the

substrate arm rotates during growth.

This temperature uncertainty lead to the re-evaluation of the use of pyrometers. While thermocouple measurements always have a certain temperature offset, pyrometer readings can give a more accurate temperature (See Section 2.5.2 for more details on the pyrometers used here). Both the high temperature and low temperature pyrometers needed calibration. The melting point of indium at 156 °C was used as a reference for calibrating the low temperature pyrometer, while the GaAs oxide desorption temperature was used for the high temperature pyrometer. In the latter case, the progress was monitored using RHEED. It was already proven that the oxide layer on a GaAs substrate will be removed at $\sim$ 582 °C by rapidly heating in vacuum chamber [17].

Difficulty in loading samples into the substrate manipulator was next to address. The horse shoe shaped sample holder in front of the substrate heater has a spacing of around one centimetre to enable easy transfer of the samples. Over time this spacing became narrower causing difficulties in the sample transfer. It was found that the molybdenum screws which hold the heater in place became loose over time and as a result it slipped down to the horse shoe, virtually leaving a few millimetres which was inadequate for the sample transfer. It was not possible to easily repair the unit without breaking the molybdenum screw. Subsequently the whole manipulator was replaced with an identical unit from another system. The new manipulator has been thoroughly outgassed and the cleanliness of the chamber was examined using mass spectrometer and growth resumed. This replacement manipulator had a very stable thermocouple connection, ultimately eliminating all the thermocouple related problems.

Another important change in this study, compared to the previous research in this group is the change in Mg flux. Since the beginning of the MgS growth research in 1999, the Mg cell temperature in this group was kept constant at 375 °C, while the BEP was $\sim$ 45 nA. But from the beginning of this project there were issues in MgS growth such as the higher Zn incorporation, lower growth rates and poor reproducibility resulting in the degradation of the sample after few months exposure to air. Several problems encountered are discussed in the next section.

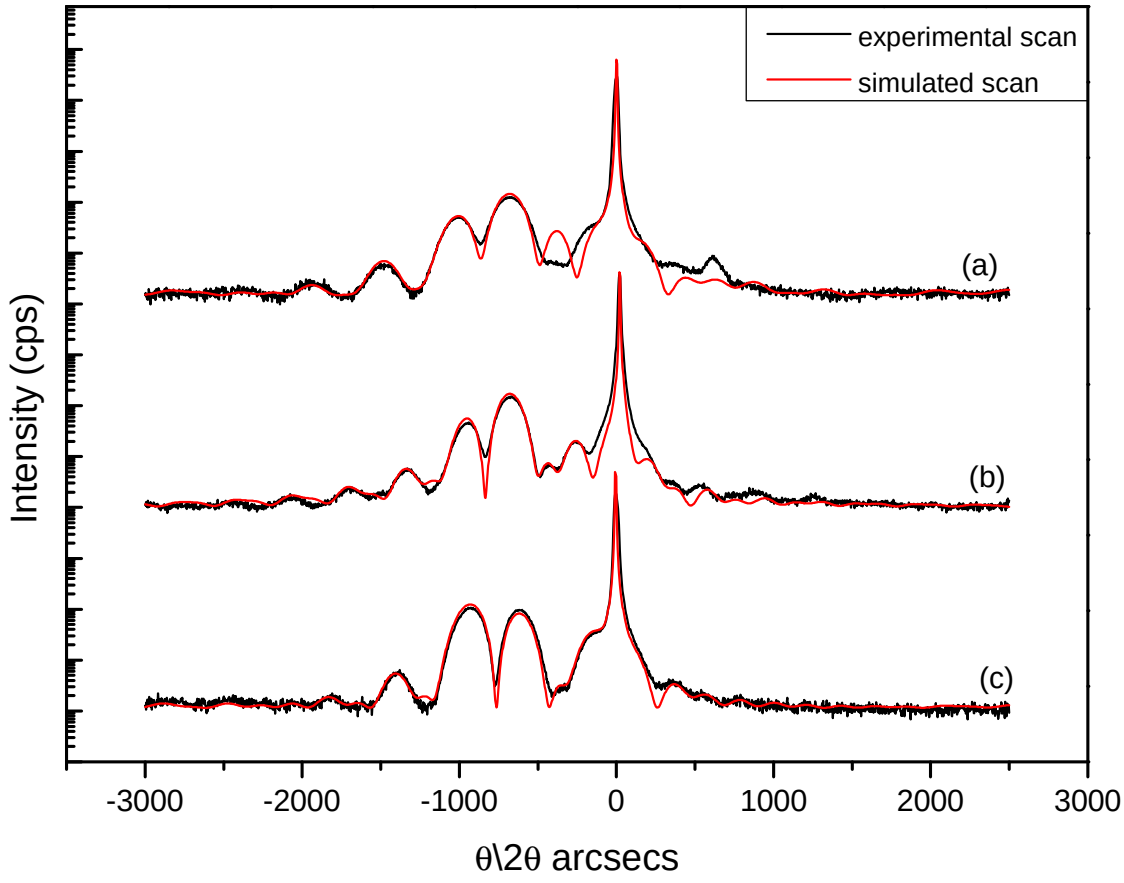

Figure 4.1: *004 reflection experimental and simulation scans of (a) HWC273, (b) HWC271 and (c) HWC272, with a structure GaAs(substrate)/ZnSe(60nm)/MgS(x)/ZnSe(60nm), where x, the growth time was 1, 2 and 3 minutes respectively.(Batch B)*

Sample No.	MgS Growth Time (sec)	MgS Thickness (nm)	Zn mole fraction (%)	Growth Rate (Å/s)
HWC273	60	1.08	11	0.18
HWC271	120	2.39	10	0.19
HWC272	180	3.62	12	0.20

Table 4.3: *MgS thickness and growth rate determined by XRI (Batch B)*

4.3.2 Issues faced during initial growths

Due to the above mentioned changes in the growth system, it was necessary to start with recalibrating the MgS growth rate. Three 'Batch B' samples, HWC271, HWC272 and HWC273 were grown with the structure GaAs(substrate)/ ZnSe(50nm)/ MgS(x)/ ZnSe(50nm) where x, the growth time was 2mins, 3mins and 1min respectively. These samples were grown at 270 °C. Samples were characterised using XRI on both the 004 and 115 planes. Figure 4.1 shows the 004 simulation on all three samples. Table 4.3

contains the data obtained from this scan. XRI analysis of these samples revealed higher residual Zn content in MgS than expected. All three samples have the best Goodness of Fit (GOF) when the zinc content was around 10 %. Furthemore, the growth rate was found to be $\sim$ 0.2 Å/s, which was half the previous growth rate.

The 'Batch A' samples had a smaller residual Zn incorporation when analysed using XRI and these values were confirmed by Secondary Ion Mass Spectrometry (SIMS) and Auger spectroscopy at Loughborough Surface Analysis. The results had shown that the residual zinc content lies in the range of 0.5 to 3.0 %. The growth rate of MgS was found to be $\sim$ 0.45 Å/s.

The primary factors affecting the higher Zn incorporation and lower growth rate were the growth temperature, ZnS flux and Mg flux. Since any changes in the simulation program could also lead to miscalculations, this was also examined.

The growth temperature used for the samples grown for this study was 270 °C. It has been proved already in this group that a growth temperature range of 240-270 °C was ideal for good quality MgS growth and at 270 °C, up to 12 nm of ZB MgS can be grown.

ZnS flux data were constantly monitored before and after growth. The 'Batch A' XRI samples were grown using a ZnS BEP of $\sim$ 500nA at a cell temperature of $\sim$ 850 °C. The same flux was used for the growth of 'Batch B' samples mentioned above, but the cell temperature had to be raised to 915 °C. This is due to the fact that there were some deposit build up on the shutter and the liquid nitrogen cooled ring, effectively restricting material effusion. Raising the cell temperature would not affect the growth rate if the same flux is used. The drop in ZnS BEP with respect to the number of growths can be seen in Figure 4.2

As regular measurement of Mg flux was avoided, it was difficult in identifying problems with the Mg flux. Over 300 samples had been grown thus far on growth chamber C, and the Mg flux had been measured only 12 times. Out of these 12 flux measurements, seven readings were taken during low Mg quaternary alloy growths, using a lower Mg cell temperature and cannot be used to compare the flux taken at the normal cell temperature of around 375 °C. However for all the 'Batch A' MgS growths, the cell temperature was

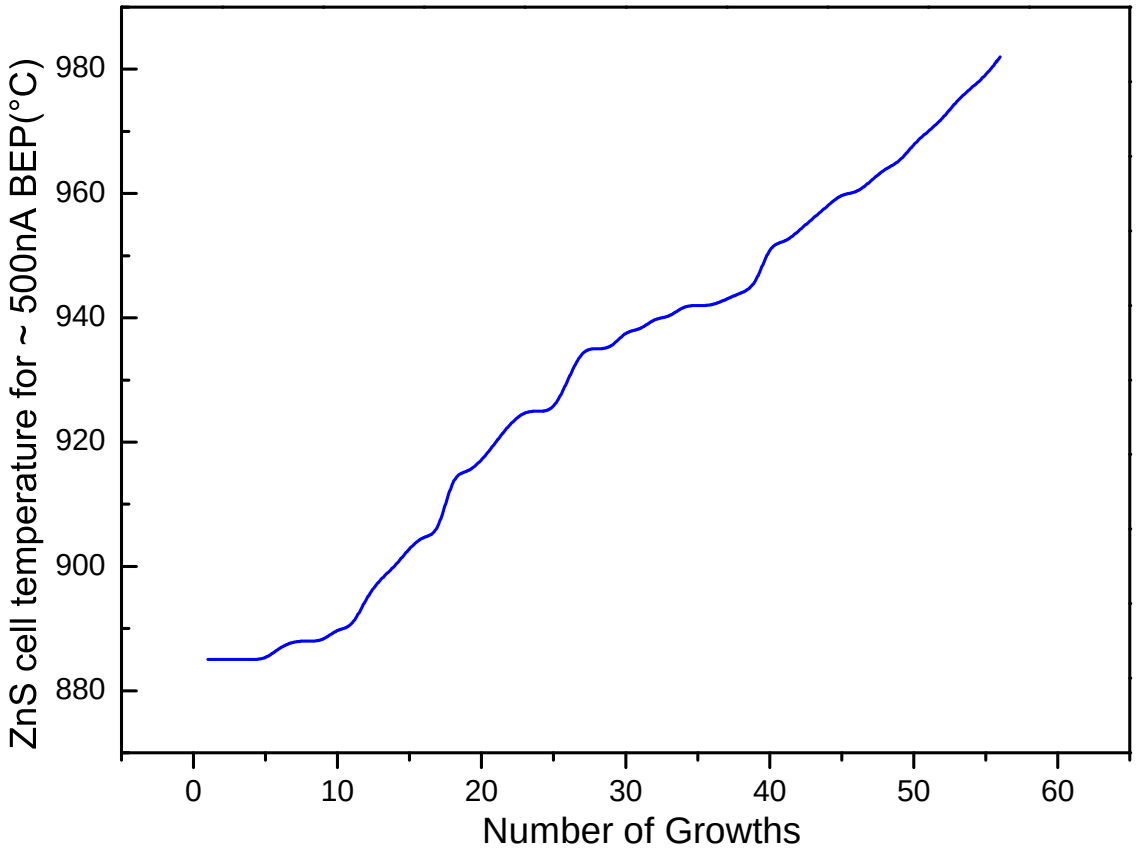

Figure 4.2: *Graph of ZnS cell temperature for a BEP of 500 nA versus number of growths.*

fixed at 375 °C and the measured flux was always ∼ 45 nA. Mg flux was found to be the same during the 'Batch B' growths as well. Since the Mg cell was refilled during assembling the MBE machine in the new lab, it was sure that the cell is not running low.

The next step was to examine the results from the simulation program. Recently the JV RADS program was reinstalled and an incorrect value in the materials parameter database might give the wrong Zn incorporation. The lattice constant (5.619 Å) and Poissons ratio (0.425) of MgS were checked and verified. At this point it was decided to re-simulate x-ray data from 'Batch A' samples and compare this with the values obtained previously. 'Batch A' samples HWA1158, HWA1159 and HWA1162 were measured, which were used previously for the growth rate measurement of MgS. All of these samples were grown with the XRI structure, where the thickness of MgS spacer layer was 3, 5 and 6 nm respectively [12].

All three samples were simulated using JV RADS, on both the 004 and 115 reflections. Figure 4.3 shows the XRI simulation results from the samples on 004 reflection. Cor-

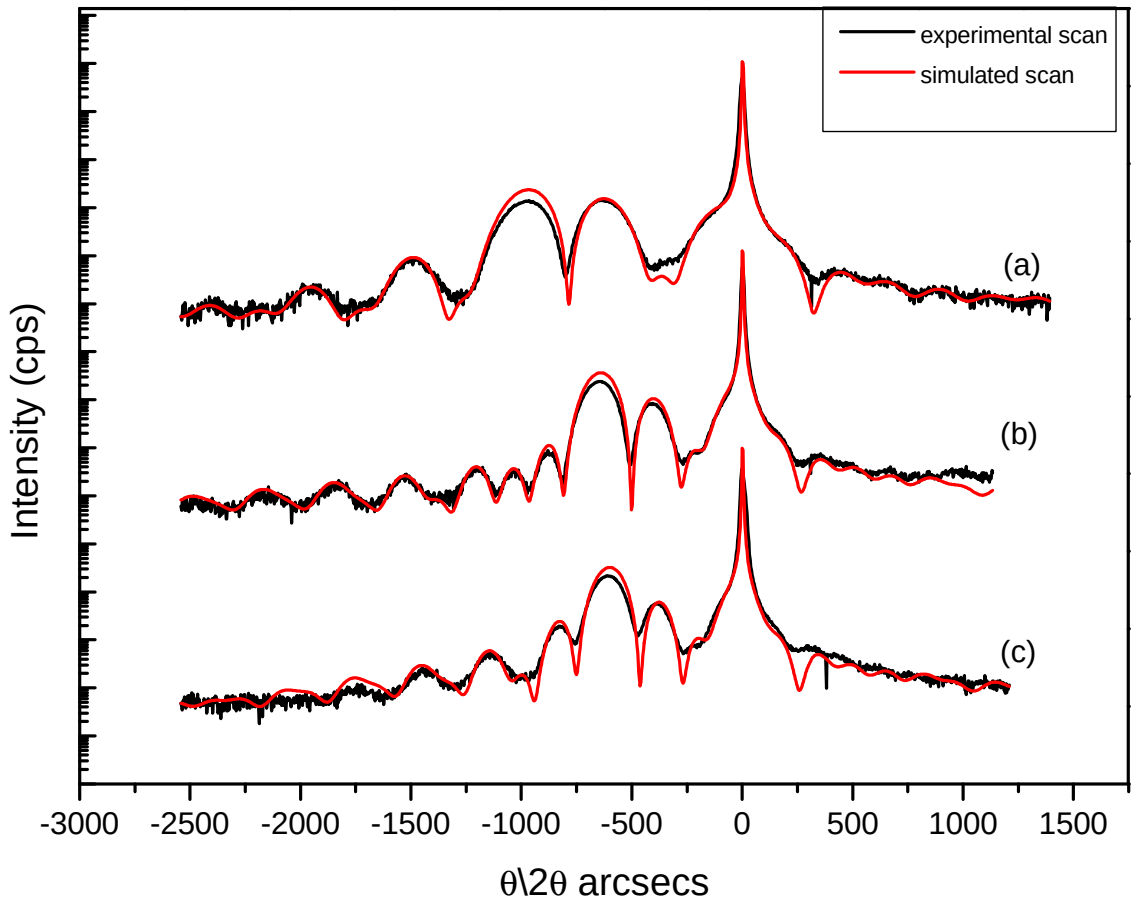

Figure 4.3: *004 reflection experimental and simulation scans of (a) HWA1158, (b) HWA1159 and (c) HWA1162, with a structure GaAs(substrate)/ZnSe(60nm)/MgS(x)/ZnSe(60nm), where x, the growth time was 80, 120 and 150 seconds respectively. (Batch A)*

Sample No.	MgS Growth Time (sec)	MgS Thickness (nm)	Zn incorporation (%)	Growth Rate (Å/s)
HWA1158	80	3.20	2.2	0.41
HWA1159	120	5.21	1.4	0.43
HWA1162	150	6.73	1.7	0.45

Table 4.4: *MgS thickness and growth rate determined by XRI from batch A samples.*

responding data obtained from these scans are on Table 4.4. The simulations were then repeated adding thin mixing layers of the quaternary alloy, $Zn_{(0.5)}Mg_{(0.5)}S_{(0.5)}Se_{(0.5)}$in between ZnSe and MgS. The results obtained matched with the previous findings in terms of growth rate and Zn incorporation. A growth rate of approximately 0.45 Å/s and a Zn content of <2 % were confirmed, showing the simulation program was working normally.

Based on these results, alterations were made in growth temperature and ZnS and Mg

fluxes to examine the effects on MgS growth. Seven samples (Batch B) were grown by varying the growth temperatures from 250 °C to 300 °C to study the changes in Zn incorporation with respect to the calibration samples. These XRI samples all had an MgS spacer layer, grown for 3 minutes. The main difference from the previous growths was that during the MgS growth, RHEED began to show signs of spots from surface roughening as early as 2 minutes into growth when the growth temperature was above 280 °C whereas the samples grown below this temperature showed a flatter surface with a c(2x2) pattern visible throughout the 3 minutes growth time. The best RHEED patterns were observed at 250 °C. XRI analysis on these samples has shown little difference in terms of Zn incorporation and growth rate, regardless of the temperatures they were grown.

From the ZnS flux measurements during 'Batch A' growths, it was clear that any ZnS BEP between 450 to 550 nA was sufficient for a good MgS growth. This variation of $\sim$ 100 nA gave enough room to accommodate any temporary flux instability during growth. Since ZnS flux had such a wide range, and all the present growths were using a flux well within this range, no further adjustments were necessary. However two further samples were grown using the same structure as above while keeping the growth temperature constant at 250 °C, but using two different ZnS fluxes, one each from both the lower (400 nA) and upper end (700 nA) of the ZnS flux range. The XRI results were slightly different. The sample grown with 700 nA of ZnS did not show any variations in Zn incorporation and growth rate. But the second sample grown using a ZnS flux of 400 nA was very difficult to simulate. The best GOF was $\sim$ 0.18 and the MgS thickness was still the same. RHEED was also showing a spotty pattern during the growth, which denotes a rough surface. So at this stage the ZnS flux was fixed at $\sim$ 500 nA or above for all the growths followed.

Another three 'Batch B' XRI calibration samples, HWC303, HWC304 and HWC310 were grown with varying MgS growth times of 2m, 1m and 3m respectively. A growth temperature of 250 °C and ZnS flux of $\sim$ 500 nA were used. The aim was to see if any changes had occurred as the first batch B structures were among the first samples grown in the HWC chamber after the refit. Figure 4.4 shows the simulated XRI curves from these three samples. The results obtained were identical to the three samples HWC271, HWC272 and HWC273. A growth rate of $\sim$ 0.2 Å/s was obtained. The Zn incorporation was found to be $\sim$ 10 %. Corresponding data obtained from these scans are on Table 4.5.

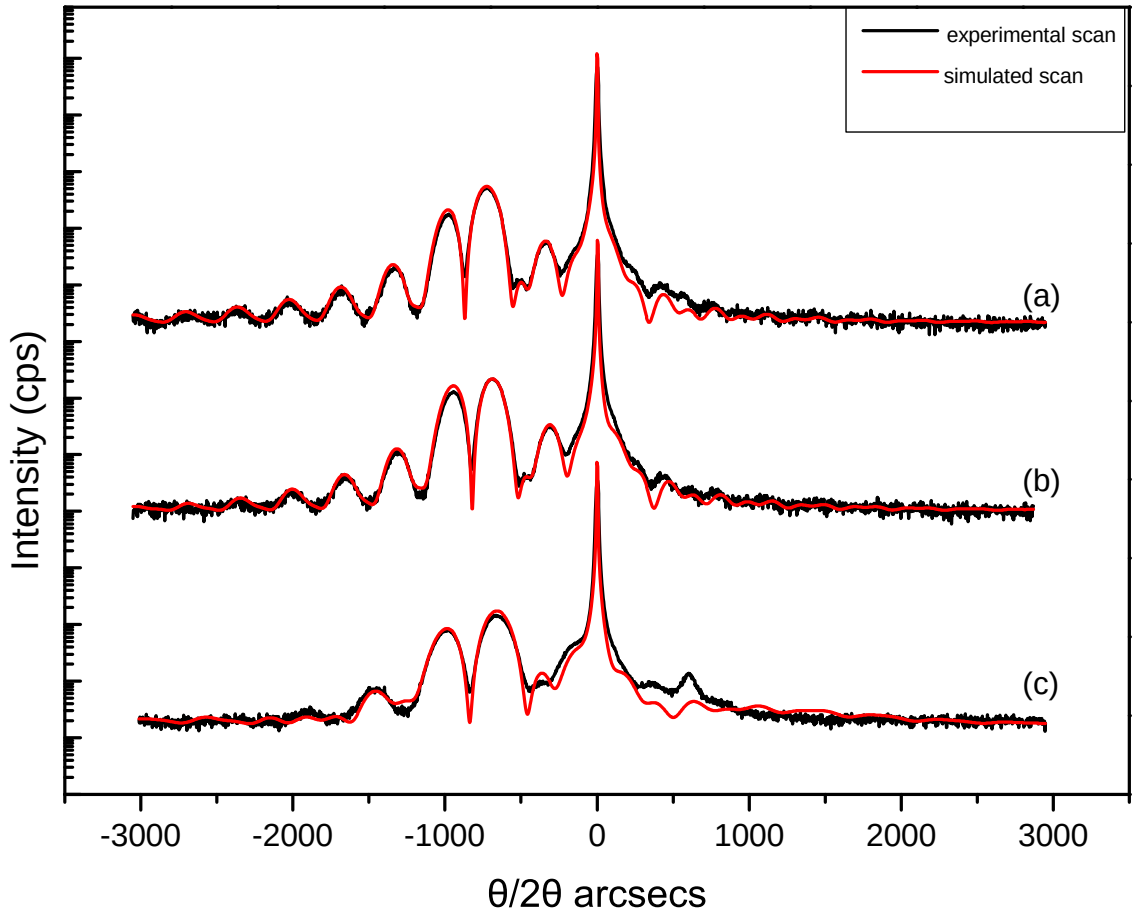

Figure 4.4: *004 reflection experimental and simulation scans from batch B samples. (a) HWA304, (b) HWA303 and (c) HWA310, with a structure GaAs(substrate)/ZnSe(50nm)/MgS(x)/ZnSe(50nm), where x, the growth time was 60, 120 and 180 seconds respectively.*

Sample No.	MgS Growth Time (sec)	MgS Thickness (nm)	Zn incorporation (%)	Growth Rate (Å/s)
HWC304	60	1.31	8.7	0.22
HWC303	120	2.86	9.1	0.23
HWC310	180	4.47	8.3	0.24

Table 4.5: *MgS thickness and growth rate determined by XRI from the batch B samples.*

At this point the only parameter left unchanged was the Mg flux. It was left untouched, as during the previous growths at Heriot-Watt, for a cell temperature of 375 °C, Mg flux was constant at 45 nA, and this has been used to successfully grow the first thicker ZB MgS layers (including Batch A samples examined here). Results of changing the Mg cell temperature/flux are detailed in Section 4.4.

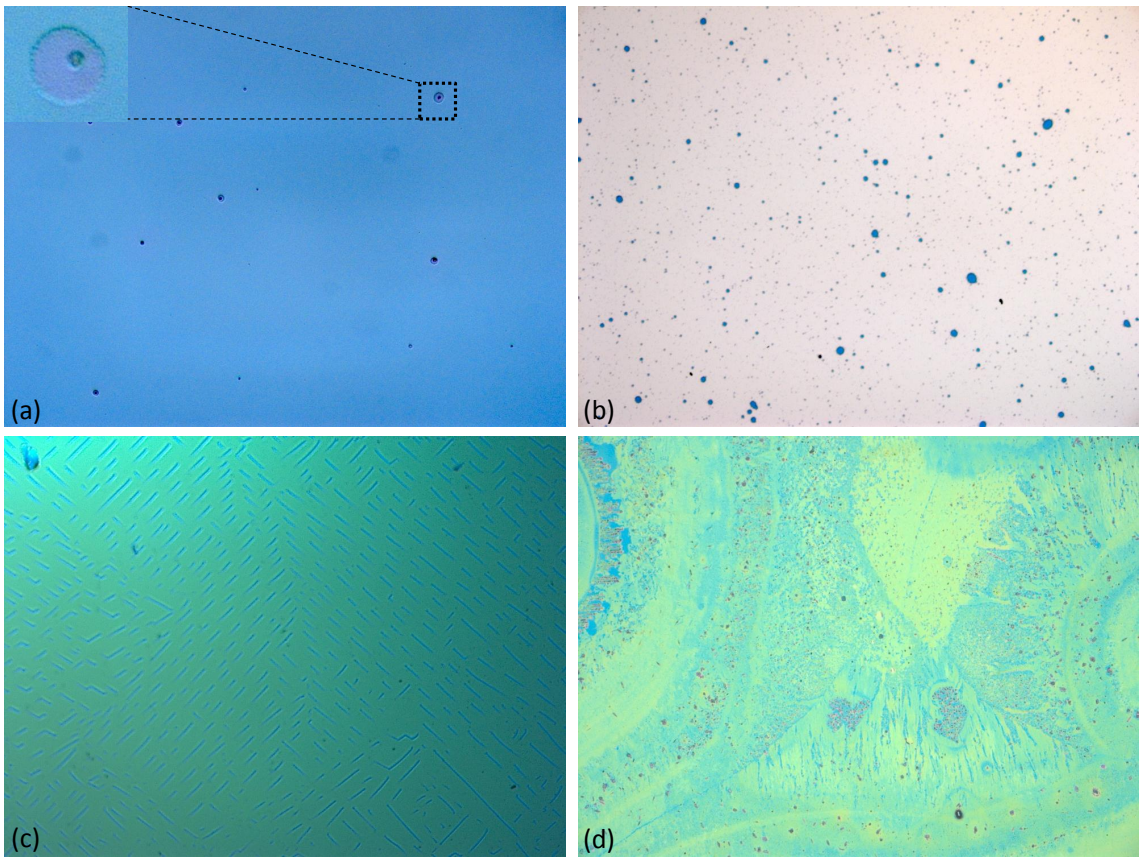

Figure 4.5: *200× UV microscope images of samples (a) HWC304, (b) HWC311, (c) HWC310 and (d) HWC303 showing developments of various surface formations and microscopic pores. (Note: Samples were exposed to atmosphere for varying times)*

4.3.3 Sample degradation

Some samples from the growths so far have also been used for Epitaxial Lift Off (ELO) (see Chapter 6 for more about ELO). From the beginning it was noticed that while some of the samples were likely to etch, some do not. It was also noted that different pieces of substrates cleaved from the same sample behaved differently in the etching solution. The etching time varied from several hours to a day for 'Batch B' samples compared to 30-60 minutes required for older samples. This pointed towards growth defects induced in MgS layer. Examining some of these samples under a UV microscope showed small openings or holes on sample surface (See Figure 4.5). Various surface formations were observed here, possibly due to the rapid oxidation of MgS through the openings or pores at the surface.

Samples HWC303 and HWC304 were analysed using XRI again after three months, to examine if these defects were evident on an X-ray scan. Figure 4.6 compares the 004

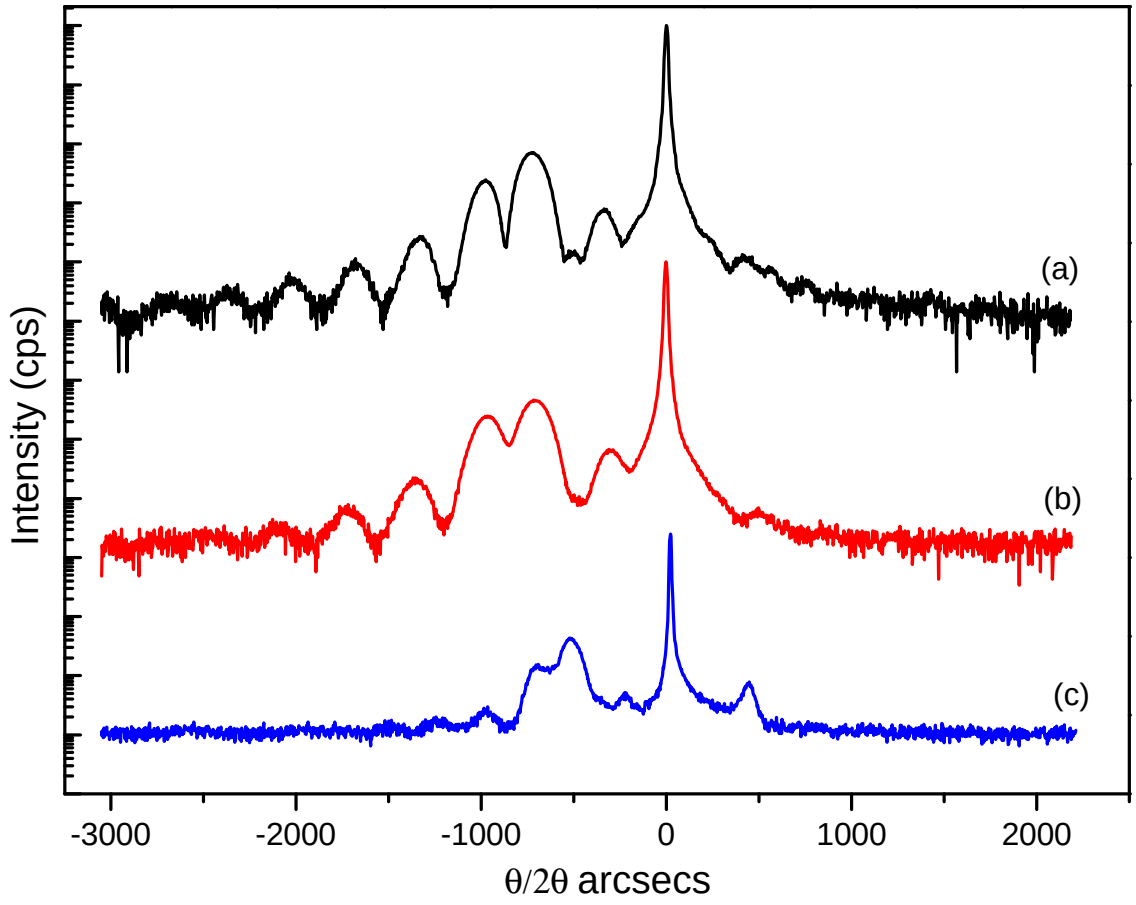

Figure 4.6: *XRI experimental scans from HWC304 over several weeks interval. (a) one day after growth, (b) eight weeks after growth, (c) 12 weeks after growth.*

reflection experimental scans from the sample HWC304, between immediately after the growth and after 3 months. Newer scans from both the samples were entirely different from the older ones. The epilayer separation from older scans has almost disappeared, with a broad ZnSe peak instead. The degradation of MgS spacer layer is obvious from the XRI scans and this explains why the ELO was not successful on these samples.

4.4 MgS growth improvement as a function of Mg flux

At this point, the only parameter left unchanged was Mg flux. As stated earlier, the steady flux of $\sim$ 45nA obtained from Mg cell at a constant cell temperature of 375 °C was used for all the previous successful MgS growths performed in this group. Finally it was decided to study the changes in MgS growth with respect to the varying Mg flux.

Initially few samples were grown by raising the Mg cell temperature by increments of

5 °C. HWC314 and HWC328 were AFM samples grown with a structure ZnSe(90nm)/ MgS(x m)/ ZnSe(4nm), where x, the MgS growth was terminated when RHEED started to show spots and diffusion. These two samples were grown at Mg BEP of 53nA and 60nA where the corresponding cells temperatures were 385 °C and 390 °C. When a BEP of 53 nA was used, the RHEED pattern went spotty just after five minutes into MgS growth whereas at 60nA of Mg, the RHEED went spotty and diffuse after two minutes. This, when compared to the regularly used flux of 45nA where the spots began to appear only after 7-8 minutes into the growth has shown that raising the Mg flux was not a solution. AFM scans of these two samples have shown a very rough surface with $\sim$ 15 nm wide ridges running along the [110] orientation and no flat areas in between.

The growth temperature used for these two samples was 250 °C. Before commencing further growths it was decided to study if lowering the growth temperature further was of any help. Increasing the growth temperature was previously found to be reducing the MgS thickness. Two more samples were grown at a temperature of 245°C and 240°C and slight improvements were found. At 240 °C the MgS growth time increased to 8 minutes before the RHEED spots started to appear. Hence the growth temperature of 240 °C was fixed for all the growths followed.

All of the samples in this section had a structure ZnSe(60nm)/ MgS(18 mins of growth)/ ZnSe(2nm) and were grown at a constant growth temperature of 240 °C, ZnS BEP of $\sim$ 500nA and with the Mg flux varied. The AFM samples had a 2 nm ZnSe capping layer to prevent the MgS layer from oxidation. This very thin layer does not alter the surface morphology of the sample during AFM analysis. HWC383 was grown with a Mg BEP of 45nA to study the surface morphology changes. Sharp and streaky c(2x2) patterns were observed from the beginning of MgS growth. The RHEED started to show spots and become slightly diffuse after 8 minutes MgS growth. These spots slowly increased in intensity and size over time. The growth was continued until an MgS growth time of 18 minutes and by this time the RHEED had lost all diffraction features and was diffuse. The AFM scan (Figure 4.7a) shows large pits up to 2 μm wide. There were flatter areas between pits with RMS roughness of $\sim$ 0.8 nm denoting a near atomically flat surface. From calculated thickness and XRI growth rate measurements, it was evident that these pits originate at the interface, passing through the MgS over layer and reaching the ZnSe capping layer surface.

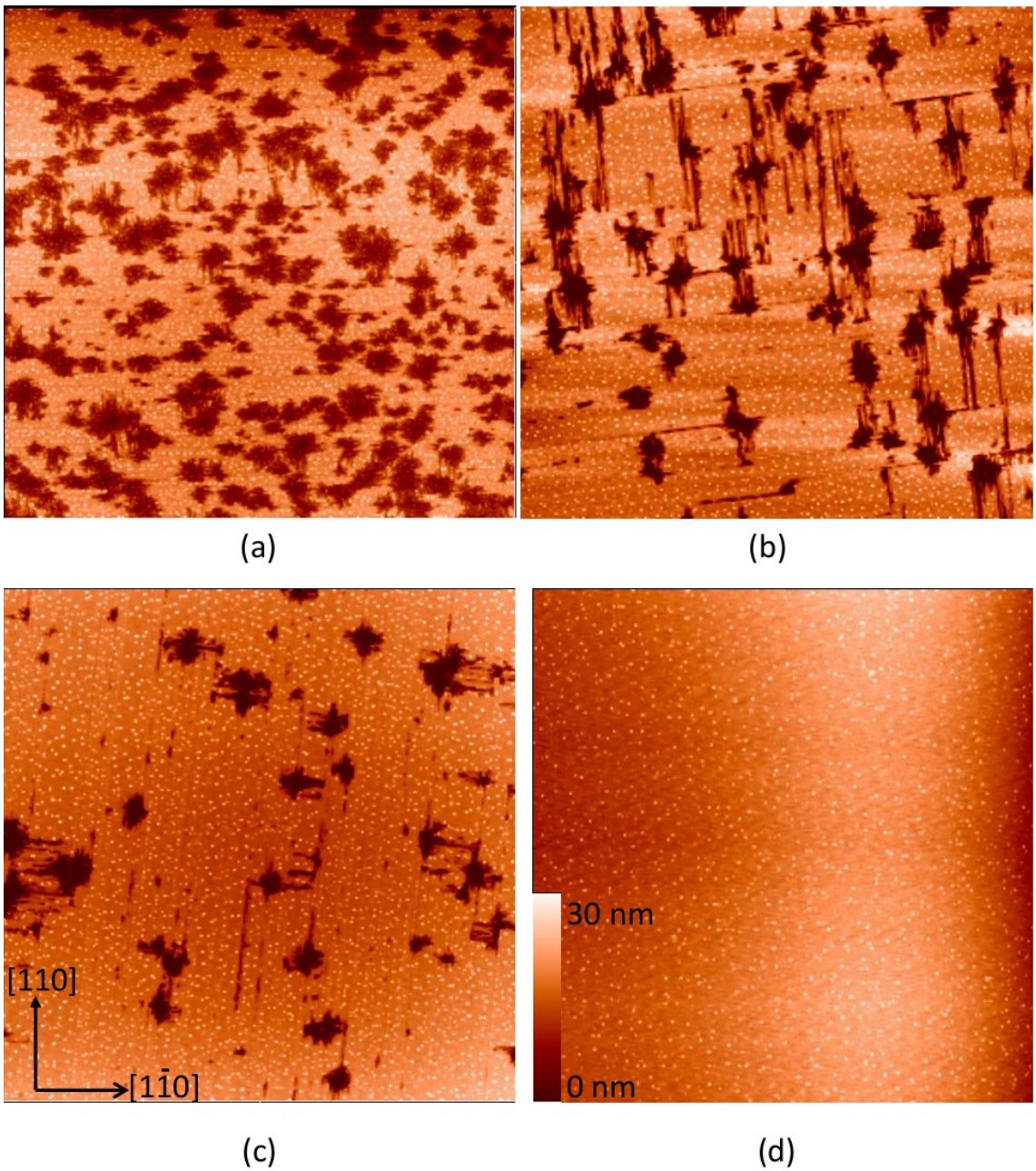

Figure 4.7: $20\mu m \times 20\mu m$ *AFM images from samples (a) HWC383, (b) HWC382, (c) HWC390 and (d) HWC391 grown with Mg BEP of 45 nA, 22 nA, 17 nA and 15 nA respectively. HWC392 grown with 13 nA Mg BEP shows similar features to (d).*

Immediate improvements were noticed from the beginning of the next growth, HWC382. Mg flux was reduced to a BEP of 22 nA for this sample, where the corresponding Mg cell temperature was 370 °C. A strong and streaky c(2x2) pattern was visible from the beginning of MgS growth and it began to fade after 12 minutes into growth. By the end of the growth, the half order diffraction features had almost disappeared, but the RHEED was still streaky. Upon examining the sample with AFM, improvements were visible. The pit density has reduced compared to the first sample. The pit size was reduced to a maximum of $\sim$ 1.3 μm and were clearly oriented along [110] (Figure 4.7b). Mean

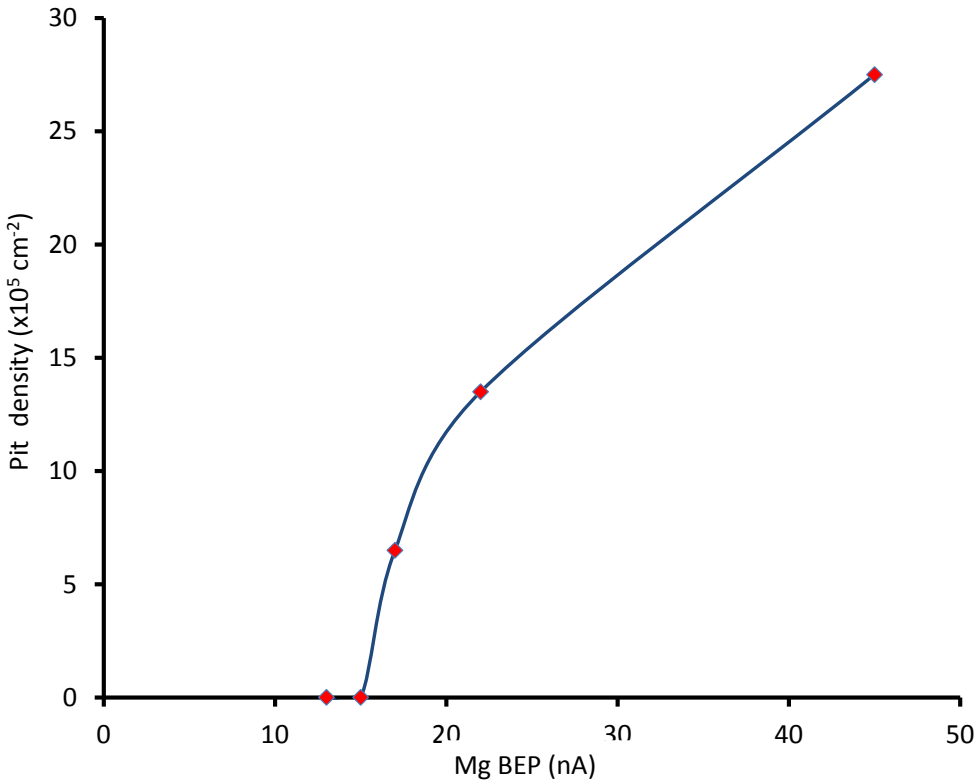

Figure 4.8: *Mg BEP versus the pit density observed using AFM.*

roughness was reduced to 3.91nm. From this analysis it was in no doubt that decreasing the Mg flux was the key in improving the ZB MgS growth conditions.

Three samples, HWC390, HWC391 and HWC392 were then grown with gradually reducing the Mg flux to 17 nA, 15 nA and 13 nA respectively. Improvement in the RHEED pattern was visible where the c(2x2) pattern was observed throughout the growth of MgS on all these three samples. RHEED spots were not noticeable for the samples grown with the Mg BEP of 15 nA and 13 nA. AFM surface analysis on these three samples has shown clear enhancement in smoothness and a reduction in the number and size of pits. HWC390 had very few pits while HWC391 and HWC392 had no pits at all (See Figure 4.7). RMS surface roughnesses for these samples were 2.57 nm, 1.8 nm and 0.89 nm respectively.

An increase in the pit density with increasing Mg flux can be seen from Figure 4.8. AFM and RHEED observations from all the five samples mentioned in this section are given in Table 4.6.

Sample No.	Mg BEP (nA)	Mg Cell Temperature (°C)	Pit Density (x10^5cm^{-2})	Average Pit Diameter (μm)	Average Pit Depth (nm)	RMS Roughness (nm)	RHEED observations
HWC383	45	375	27.5	2	37	4.33	Spotty after 8 min growth and completly lost patterns at the end.
HWC382	22	370	13.5	1.6	38	3.91	Spotty after 12 min growth but streaky pattern even at the end
HWC390	17	367	6.5	1.1	32	2.57	c(2x2) throughout the growth, bits of spots
HWC391	15	364	na	na	na	1.8	c(2x2) throughout the growth
HWC392	13	361	na	na	na	0.89	c(2x2) throughout the growth

Table 4.6: *AFM and RHEED observations from samples.*

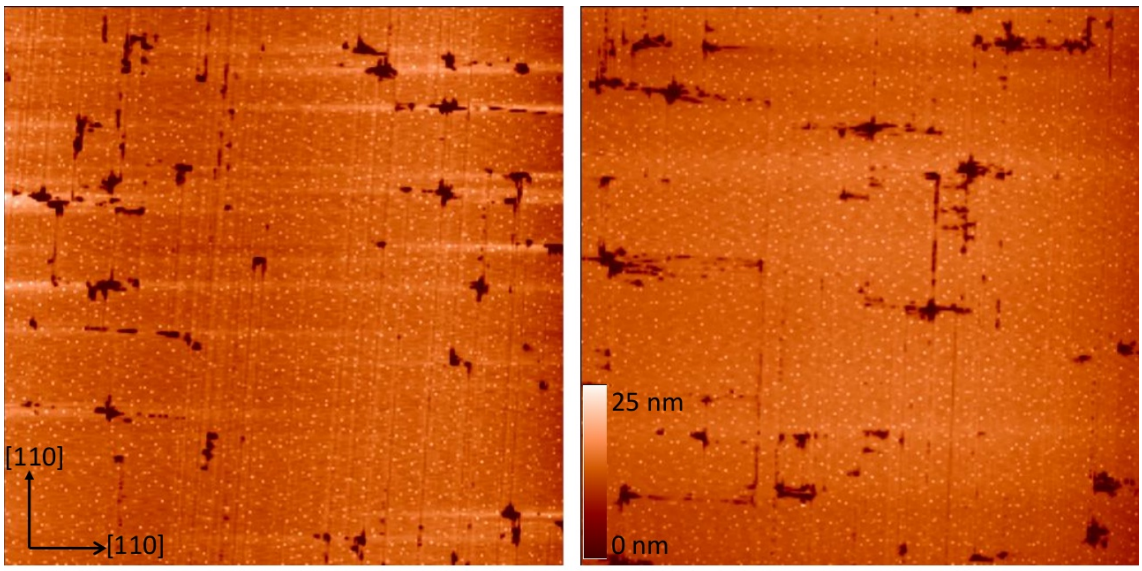

Figure 4.9: $20\mu m \times 20\mu m$ *AFM scans of samples with the structure ZnSe(60nm)/ MgS(64nm)/ ZnSe(2nm), where the Mg BEP was (a) 15nA and (b) 13nA.*

Since the last two samples in this set had identical, smooth surface with no pits, two additional samples were grown with larger MgS thicknesses using 15nA and 13 nA Mg BEP in order to determine if the good surface morphology was maintained or alternatively could generate a measurable density of surface pits. During the growth of these thicker samples, the RHEED pattern became slightly diffuse and weak spots began to appear at 30 minutes into MgS growth. Growth was halted at this stage to study the surface. AFM scans showed very similar surfaces for the two samples (see Figure 4.9). These showed a very small number of much shallower pits $\sim$ 25nm deep along with the signs of beginning of ridge formation along [110] direction . These [110] oriented ridges are a prominent surface feature on thicker MgS layers [18]. The sample grown with 13 nA BEP had a slightly better surface with fewer pits and ridges. As a result the Mg BEP was fixed at 13 nA for all subsequent samples. After thickness calibrations (in next section) the MgS thickness in these two samples were found to be 64 nm thick. From AFM measurements average pit depth for these samples were found to be $\sim$ 25 nm, which was less than half the thickness of the MgS layer. This was different from the samples grown with higher Mg flux, where the pit depth was the same as the layer thickness of MgS, means the pits originated at the surface.

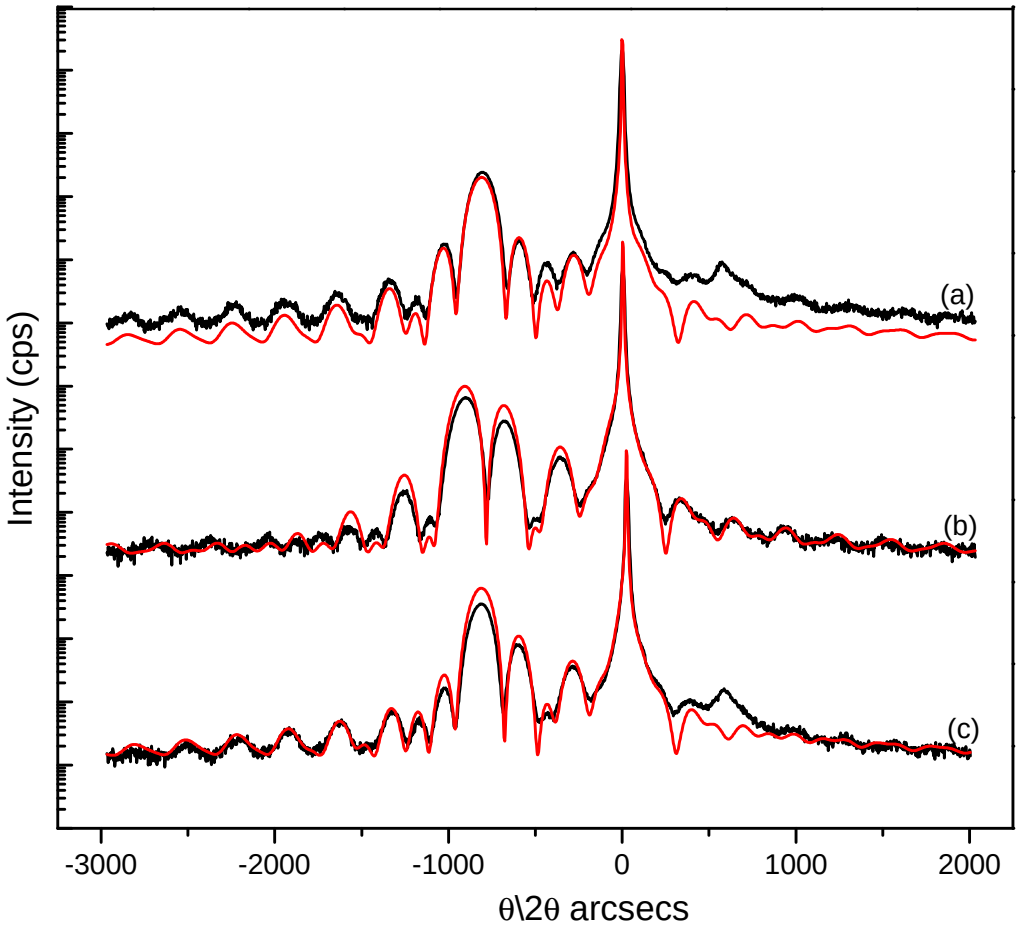

Figure 4.10: *004 reflection experimental (black) and simulation (red) scans from the 'Batch C' samples. (a) HWC397, (b) HWC396 and (c) HWC400, with a structure GaAs(substrate)/ZnSe(60nm)/MgS(x)/ZnSe(60nm), where x, the growth time was 60, 120 and 180 seconds respectively.*

Sample No.	MgS Growth Time (sec)	MgS Thickness (nm)	Zn mole fraction (%)	Growth Rate (Å/s)
HWC397	60	2.04	0.9	0.34
HWC396	120	4.32	1.2	0.36
HWC400	180	6.99	0.3	0.39

Table 4.7: *MgS thickness and growth rate determined by 004 XRI from the 'Batch C' samples.*

4.5 Growth rate and layer composition calibration

As the smallest Mg BEP is only a third of that previously used, it was necessary to re-calibrate the growth rate. Calibration samples were grown to examine if the changes compromised the layer composition, growth rate and crystalline quality of the MgS layer. Three XRI samples HWC397, HWC396 and HWC400 with an MgS spacer grown for 1

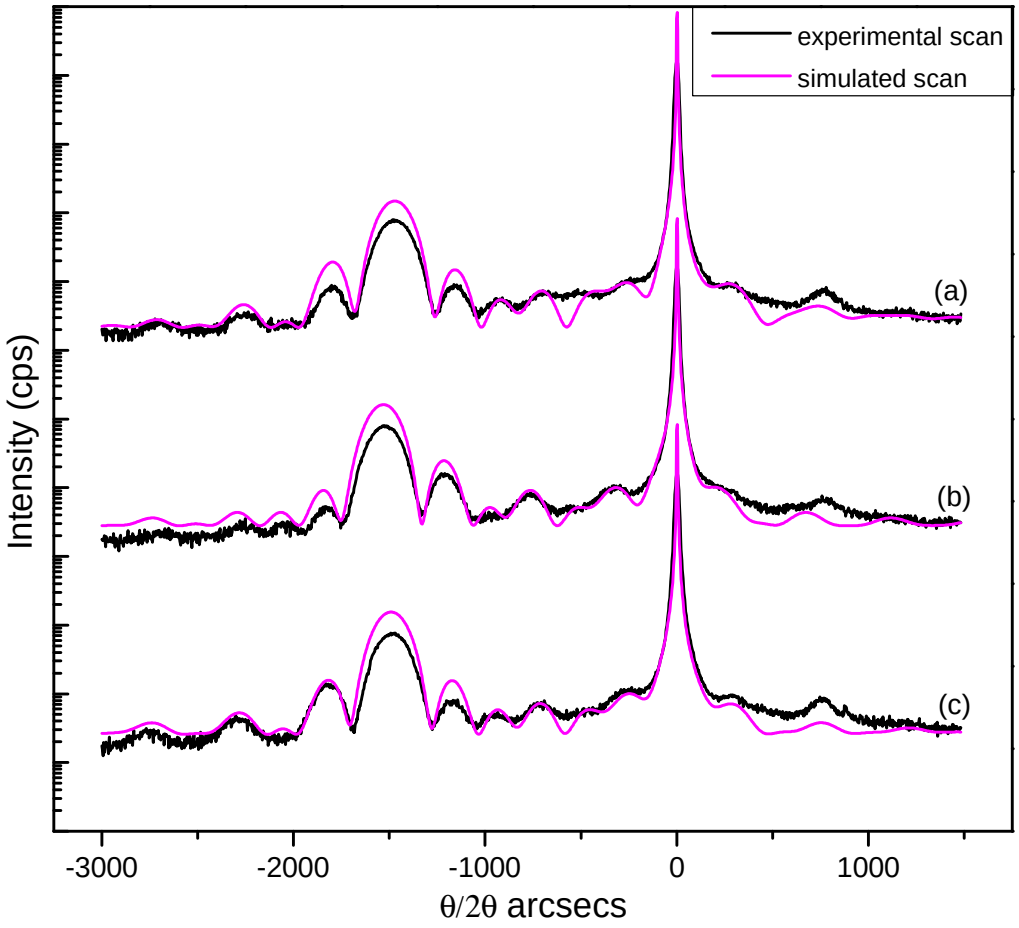

Figure 4.11: *115 reflection experimental and simulation scans from the 'Batch C' samples. (a) HWC397, (b) HWC396 and (c) HWC400, with a structure GaAs(substrate)/ZnSe(60nm)/MgS(x)/ZnSe(60nm), where x, the growth time was 60, 120 and 180 seconds respectively.*

Sample No.	MgS Growth Time (sec)	MgS Thickness (nm)	Zn mole fraction (%)	Growth Rate (Å/s)
HWC397	60	2.11	1.1	0.35
HWC396	120	4.27	0	0.35
HWC400	180	6.82	0.4	0.38

Table 4.8: *MgS thickness and growth rate determined by 115 XRI from the 'Batch C' samples.*

min, 2 min and 3 min respectively were examined. RHEED patterns indicated that the MgS growth was in zinc-blende phase for all three samples.

The strain between these two II-VI compounds is much larger than that found in the III-V system, resulting the interference fringes repeating more frequently with increasing layer thickness [19]. By using two reflections with different planar spacing such as the 004 (Figure 4.10) and 115 (Figure 4.11) a unique value can be obtained.

The simulation model contained a $Mg_xZn_{1-x}S$ layer to allow for the Zn incorporation. All three samples showed good crystallinity and were in good agreement over growth rate, with $\sim$ 0.36 Å/s obtained. The amount of Zn present in the MgS layers was in the range 0-1.2%, which is similar to that obtained with the larger fluxes. The growth rate of ZnSe was confirmed to be at $\sim$ 0.9 Å/s. Details are given in Table 4.7 (004) and Table 4.8 (115).

From this growth rate measurement, the thickness of the first five 'Batch C' samples, HWC383, HWC382, HWC390, HWC391 and HWC392 grown for examining the effect of varying Mg flux was calculated to be 39 nm for a growth time of 18 minutes.

4.6 Epitaxial Lift Off on MgS

The 'Batch B' MgS samples grown prior to 'Batch C' had problems with the ELO. Large changes in etching time as well as different pieces of a single substrate behaving differently to the etching solution have been noticed during processing 'Batch B' samples. All of those samples were grown with higher Mg flux and recent AFM scans have shown microscopic surface pits on those samples. These pit formations were thought to extend through the ZnSe capping layer. This could ultimately leave the MgS layer in contact with the atmosphere and a resulting oxidation.

After improving the ZB MgS growth and calibrating thickness, it was decided to grow a few more samples for the epitaxial lift off and to study if the recent changes in the growth made any improvements. Four samples HWC384, HWC385, HWC396 and HWC397 were grown with the structure ZnSe(60nm)/ MgS(x nm)/ ZnSe(60nm), where x was 6.5

Sample No.	MgS Thickness (nm)	Lift off Time (min)
HWC384	6.5	4
HWC385	4.3	6
HWC396	4.3	7
HWC397	2.1	Did not lift

Table 4.9: *Results of epitaxial Lift-off performed on 'Batch C' MgS samples.*

nm, 4.3 nm, 4.3 nm and 2.1 nm respectively and a Mg BEP of 13 nA was used. Times to complete the lift off are given in Table 4.9

Previous attempts on 'Batch B' have shown that some samples which lifted immediately after growth, failed to lift if tried again after several weeks. To check if this was caused by oxidation starting at the surface pits, cleaved pieces of HWC384, HWC396 and HWC397 were attempted to etch again after two months. As expected, the first two samples lifted easily in the same time as found previously. HWC397 did not lift again.

4.7 Effect of a smoothing layer on thick MgS layers

Further attempts were made to grow thick layers of ZB MgS directly on a ZnSe layer grown on top of a GaAs(100) substrate. The first samples were deposited on a $\sim$ 60 nm thick ZnSe buffer layer in order to separate the subsequent MgS from the GaAs/ZnSe interface and ensure a smooth starting surface. HWC393 was grown with the structure ZnSe(60nm)/ MgS(64nm)/ ZnSe(2nm), where the growth of the MgS layer was stopped when RHEED started showing spots. AFM images showed a predominantly flat surface but with smaller pits of $\sim$ 15 nm deep. It was not possible to grow thicker MgS beyond 64 nm with this structure as a phase transformation was imminent.

Previously Heriot-Watt MBE group have demonstrated that the critical thickness of ZB MgS for phase conversion to RS can be increased by incorporating a ZnSe/MgS smoothing layer [20], and so the effect of such layers was investigated. HWC394 was grown to study the effects of a smoothing layer with the structure ZnSe(60nm)/ MgS(21nm)/ ZnSe(30nm)/ MgS(130nm)/ ZnSe(4nm). The growth was halted when MgS layer was at 130 nm thick as the integral RHEED patterns began to show spots and diffusion, indicating a rough surface. This addition of the smoothing layer has doubled the ZB MgS thickness. AFM shows a flat surface with cracks beginning to form along [1$\bar{1}$0] and 1 D ridges along [110]. The cracks on this sample were 60 nm deep, but RHEED and XRI analysis shows that the sample remains in ZB phase. Figure 4.12 shows a section analysis of HWC393 and HWC394.

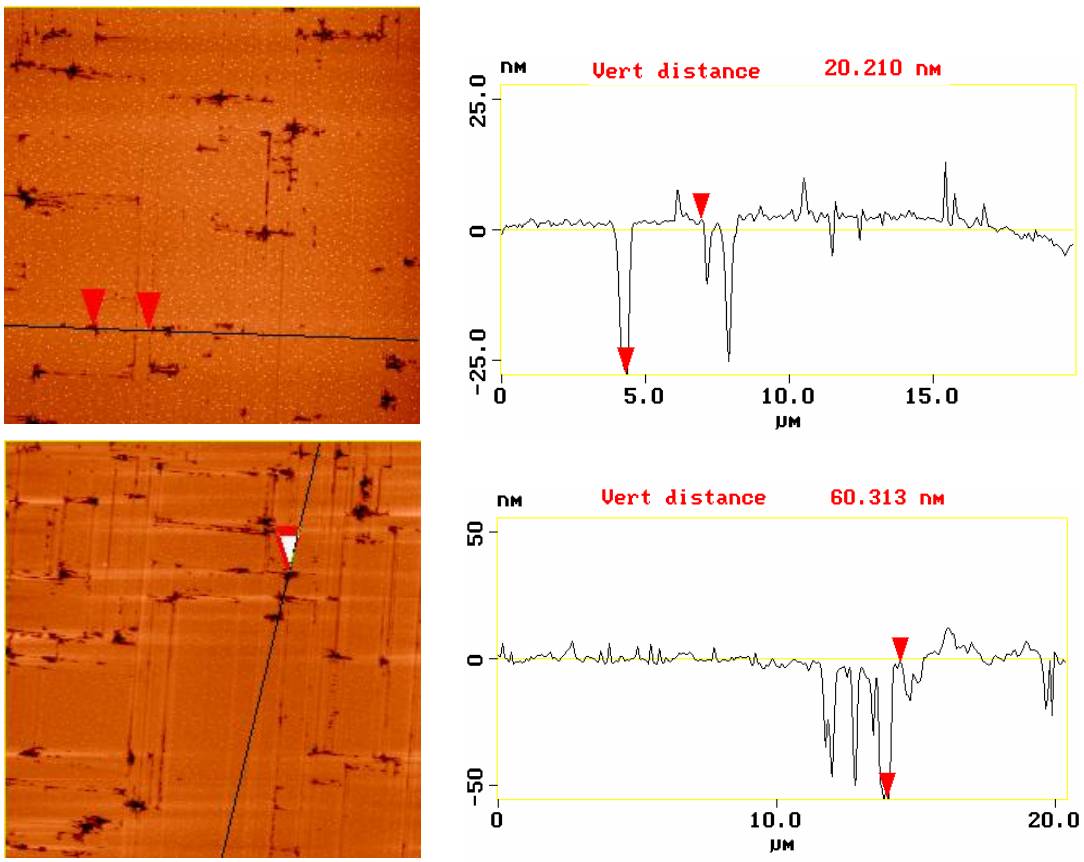

Figure 4.12: *AFM section analysis of HWC393 and HWC394*

Several samples were then grown varying the ZnSe/MgS/ZnSe smoothing layer composition to study the way it affects the morphology of the 130 nm thick MgS layer. HWC395 was grown with structure ZnSe(30nm)/ MgS(7nm)/ ZnSe(30nm)/ MgS(130nm)/ ZnSe-(4nm), where RHEED has showed spots and went diffuse after $\sim$ 80 nm into MgS growth. However the growth was continued till the MgS layer was 130 nm thick and by the end of the growth RHEED showed weak faceted pattern, indicating the phase transition into RS. AFM analysis has shown a surface with cracks up to 75 nm deep, elongated along [1$\bar{1}$0] orientation.

Superlattice buffer structures were also grown to study the changes in the MgS layer. HWC399 was grown with a 10 cycle ZnSe(12nm)/ MgS(3nm) buffer structure before depositing the thick MgS. At the end of the superlattice, RHEED showed strong, streaky patterns indicating a flat surface. However in the last quarter of the MgS growth RHEED started to show spots along [110] azimuth and later by the end of the 130 nm thick MgS growth, it became diffuse. The streaky pattern was still visible meaning the layer retained the ZB crystal structure, confirmed subsequently by XRD. AFM images have shown cracked surface similar to the previous samples. AFM roughness analysis has shown a

Sample No.	Smoothing layer thickness [ZnSe/MgS/ZnSe] (nm)	Thick MgS layer thickness (nm)	Average Pit Depth (nm)	Pit Density ($x10^5 cm^{-2}$)	RMS Roughness (nm)	RHEED observations
HWC394	90/21/30	130	60	50	2.63	Streaky pattern through out
HWC395	30/70/30	130	80	50	16.592	Streaky, but went bit spotty and diffused by the end of growth
HWC399	[12/3] x 10 superlattice	130	65	30	4.568	streaky throughout, but elongated spots by the end of growth
HWC401	12/30/24	130	20	50	1.589	streaky c(2x2) through out the growth, went spotty a bit by the end.

Table 4.10: *AFM and RHEED observations from samples grown with smoothing layers.*

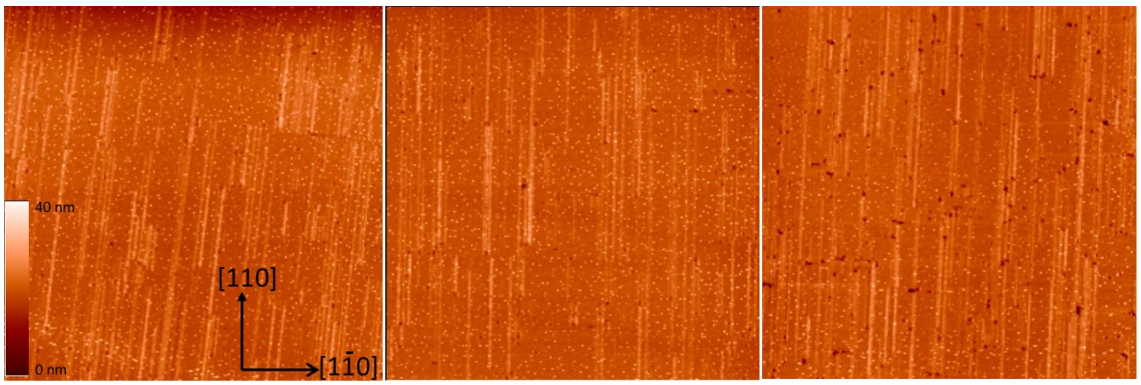

Figure 4.13: $20\mu m \times 20\mu m$ *AFM images from samples (a) HWC403, (b) HWC405 and (c) HWC406.*

slightly larger RMS roughness than HWC394 (See Table 4.10).

These samples were grown using MgS/ZnSe superlattice buffers of the form GaAs / ZnSe (d_1)+ MgS (d_2) / ZnSe/ MgS. In the case of a strain symmetrised superlattice, with $d_1 \sim 4d_2$ there was no obvious improvement seen in the maximum critical thickness before the phase conversion. Also AFM measurements showed that the surface produced by depositing a thin MgS layer on a very thin layer of ZnSe deposited on GaAs substrate produced a much smoother surface than previously thought. So it was decided to incorporate these changes in a smoothing layer structure similar to HWC394.

The next sample, HWC401 was a significant improvement in minimising the surface roughness by reducing cracks. The sample was grown with a structure ZnSe(12nm)/ MgS(30nm)/ ZnSe(24nm)/ MgS(130nm)/ ZnSe(4nm). The RHEED was streaky throughout the growth indicating a 2D growth and spots began to appear only in the final 10 nm of MgS growth.AFM images showed a surface with 1D ridges along [110]. Very shallow pits $\sim$15 nm deep were visible on the surface. This surface had the lowest surface roughness measurements thus far. RMS surface roughness measurements for these samples are given in Table 4.10 .

Subsequently a set of three samples, HWC403, HWC405 and HWC406 were grown with the structure ZnSe (6nm)/ MgS (12nm)/ ZnSe (x nm)/ MgS (130 nm)/ ZnSe (4 nm), where x was 12nm, 6nm, and 18 nm respectively. Growth was halted at 130 nm of MgS to study the surface of samples. Even with a 130 nm thick MgS layer, the surface showed a strong and streaky RHEED pattern along [110] azimuth indicating a ZB surface with no signs of

Sample No.	Smoothing layer thickness [ZnSe/MgS/ZnSe] (nm)	MgS thickness (nm)	RMS roughness (nm)
HWC403	6 / 12 / 12	130	1.89
HWC405	6 / 12 / 6	130	2.07
HWC406	6 / 12 / 18	130	2.29

Table 4.11: *AFM surface roughness values obtained from samples grown with varying smoothing layers.*

phase conversion [18]. The c(2x2) pattern was visible during the growth of MgS layer.

AFM images in Figure 4.13, show that the two samples with central 6 nm or 12 nm thick ZnSe layers generate the flattest thick MgS layers, and that the 12 nm ZnSe layer producing the flattest surface. Residual roughness (Table 4.11) on these two samples arises primarily from patches of 1D oriented ridges unlike the sample with the thicker ZnSe layer where there is a contribution from the small cracks. 1D ridges or nanowires developed on thick MgS layers are believed to be arising from the anisotropic strain in the MgS layer during partial relaxation and are formed well before the onset of the phase transition [21]. These ridges are visible throughout from 130 nm to the maximum thickness achieved so far.

The structure of sample HWC403 was adopted for growing even thicker ZB MgS since this surface had the fewest 1D nanowires and the surface roughness was lower than the other two samples in this series. This study has shown the significance of the smoothing layer structure in growing thick ZB MgS.

4.8 Observation of surface pits

Two different populations of pits are observed on the samples grown for this study, neither of which have been observed previously on samples grown at 270°C. The surface is almost flat and featureless for the samples grown with 13 nA and 15 nA Mg BEP, but the samples grown with higher Mg fluxes contain deep pits (denoted type A pits), with densities increasing rapidly with Mg flux. The type A pits are irregular in shape and vary from

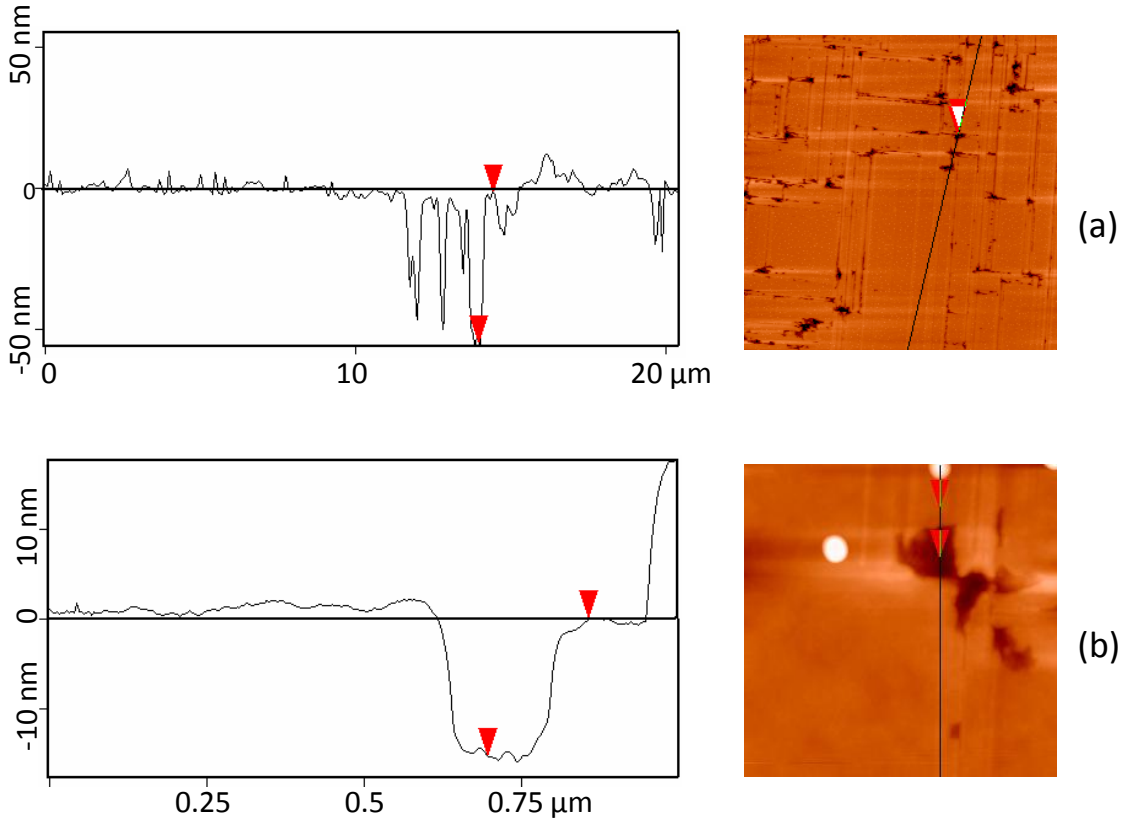

Figure 4.14: *Cross sectional analysis (left) of AFM images (right) of (a) Type A and (b) Type B pits. Note the different horizontal and vertical scales for (a) and (b).*

<1 μm to >2 μm in diameter, although the highest Mg fluxes produce on average larger pits. These pits have shallow side walls without a flat region at the bottom, but within experimental error all pits on a given sample have the same depth, which is close to the MgS layer thickness obtained from X-ray measurements. There is no apparent preferred alignment direction of pits on any of the samples. On samples with lower type A pit densities there are some cracks which run into or between adjacent pits which are possibly associated with local relief of the tensile strain in the MgS layer. The depth of the type A pits and their random distribution is compatible with their origin being a fault in the nucleation at the underlying surface.

AFM scans of subsequent 64 nm thick MgS samples grown with 13nA and 15 nA Mg BEP showed that both of the samples did not have any type A pits, but showed $5-8\times10^6$ cm^{-2} shallower pits (denoted type B pits) together with some [110] oriented ridges which have been observed previously on layers grown at 270 °C [18]. The sample grown with 13 nA BEP had lower densities of both type B pits and ridges

The type B pits are ∼10-15 nm deep and quite different in appearance from the irregular type A pits. A comparison between the two types showing the different profiles in cross-section is given in Figure 4.14. The type B pits have side walls with straight sections that are aligned with $< 110 >$ directions and are more regular, some being approximately square. They also have a large central region which is, within 1-2 nm, approximately flat. As they form during growth with lower Mg fluxes than type A pits, it is unlikely that they are the same pits which have nearly filled with ZB MgS. They could arise from the RS inclusions which have been observed in ZB MgS layers [22] and are bounded by $\{111\}$ stacking faults that originate at the ZnSe/GaAs interface and propagate through the ZnSe layer. The higher density of the RS phase means the layer will be thinner by 13 nm in the pit than the surrounding 64 nm thick ZB layer, assuming no lateral transport of material on the surface, which is in agreement with the observed pit depths. A pyramidal RS inclusion bounded by stacking faults should have a width of ∼90 nm in these layers. The majority of type B pits are much wider, but a small number are 90-100nm wide and significantly none are smaller.

Previous AFM studies of MgS (100) surfaces did not observe either type of pit, but only examined samples grown at the highest temperature (270 °C). At this temperature, the predominant surface features are 1D ridges [18], whereas pit formation appears favored at 240°C.

4.9 Growth of the thickest ZB MgS

It was stated earlier that above a certain critical thickness the ZB MgS layer always reverts to the stable RS structure. The thickest ZB Mgs layer reported thus far was 134 nm thick [12] and attempts to grow above this thickness resulted in the phase transition to RS.

To investigate the growth of thicker ZB MgS layers, three samples were grown by gradually raising the thickness up to where it appears to be starting to undergo phase transition. Samples with different thickness helped to understand the surface formations and relaxation of the thick MgS layer. HWC403, HWC407 and HWC409 were grown with structure ZnSe (6 nm)/ MgS (22nm)/ ZnSe (12 nm)/ MgS (x nm)/ ZnSe (4nm), where x was 130

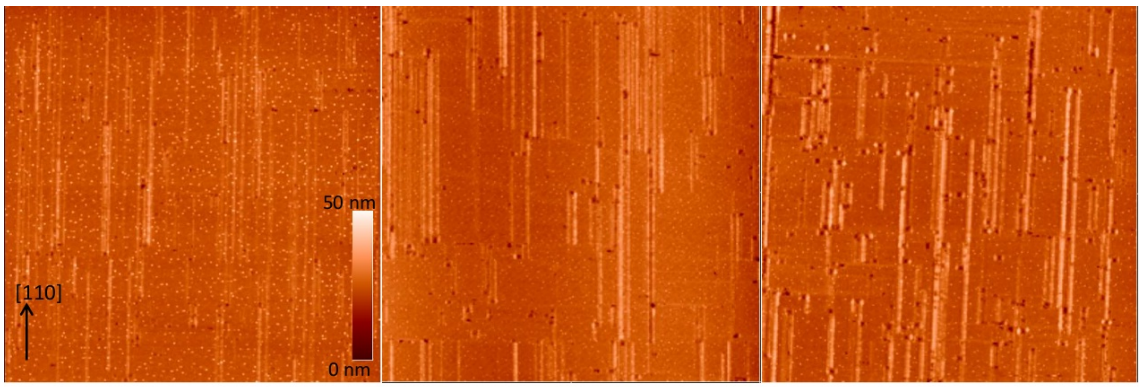

Figure 4.15: *$20\mu m \times 20\mu m$ AFM images from samples with the structure ZnSe(6nm)/MgS(22nm)/ ZnSe(12nm)/MgS(x nm)/ZnSe (4nm) where x is: (a) 130 nm (HWC403), (b) 160nm (HWC407), (c) 200nm (HWC409).*

Sample No.	MgS thickness (nm)	Pit Density (x10^5cm^{-2})	RMS roughness (nm)
HWC403	130	10	1.89
HWC407	160	15	2.4
HWC409	200	50	2.6

Table 4.12: *AFM surface anaysis data obtained from the three thickest MgS samples*

nm, 160 nm and 200 nm respectively. Progress of growth was continuously monitored using RHEED, with streaky patterns indicating ZB phase. The c(2x2) reconstruction was also present for the initial 90 % of the growth time. Soon after reaching 200 nm thick, RHEED started to appear diffuse and spotty which indicates that the layer is starting to undergo a phase transition from ZB to RS and at this stage growth was halted.

AFM was used for studying the surface roughness and crack formations. AFM images showed smooth surfaces for samples with 130 and 160 nm of MgS while, nanoscopic cracks began to form in the 200 nm layer (See Figure 4.15 and Table 4.12). However the 200 nm layer maintained the ZB structure and is the thickest ZB MgS layer grown to date.

XRD analysis on 004 plane, also shed light on the relaxation of the structure at three different thicknesses. ZB MgS peaks become broader as the thickness increases can be seen from Figure 4.16. HWC403 and HWC407 show $\sim$ 92% and $\sim$ 97% relaxation respectively at thicknesses of 130 nm and 162 nm. The 200 nm sample shows the widest peak which corresponds to a 100% relaxed layer.

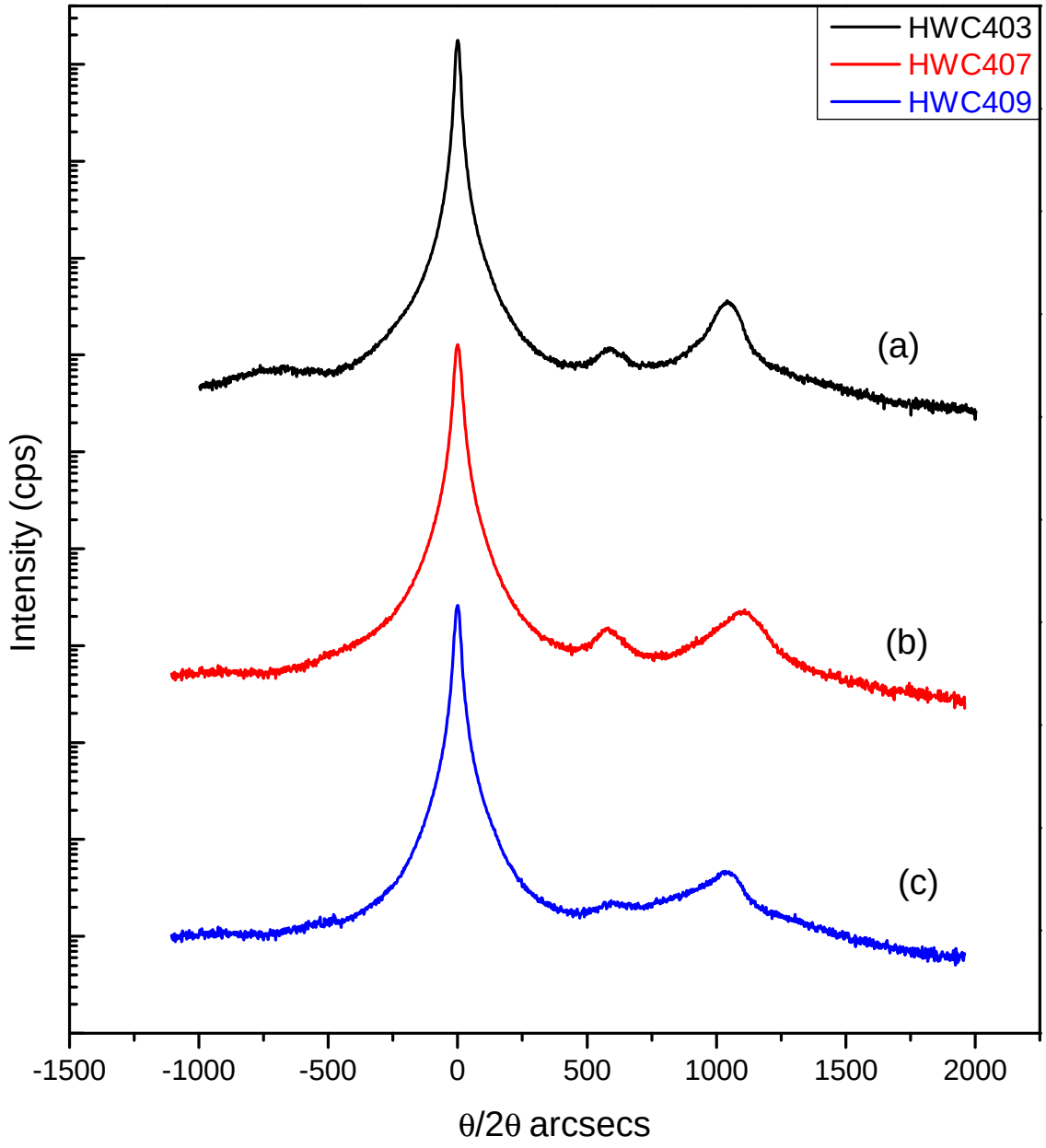

Figure 4.16: *004 double crystal rocking curves from samples with the structure ZnSe(6nm)/ MgS(22nm)/ZnSe(12nm)/MgS(x nm)/ZnSe (4nm) where x is: (a) 130 nm, (b) 162nm, (c) 200nm. The ZB MgS peak is at ∼1000 arcsec, while the smaller peak at 600-700 arcsec is a stray reflection from the GaAs substrate.*

4.10 AFM Topology of the rock salt MgS surface

Figure 4.17 shows images from HWC395 which has the structure ZnSe(30nm)/MgS(70nm)/ ZnSe(30nm)/MgS(130 nm)/ZnSe (2nm). By the end of the growth, RHEED showed diagonal faceted patterns indicating the phase transition from ZB to RS. This AFM scan shows large cracks along both [110] and [1$\bar{1}$0] directions. Section analysis on this sample has shown that the cracks have propagated from the surface, through the MgS layer to the top of the underlying ZnSe buffer layer.

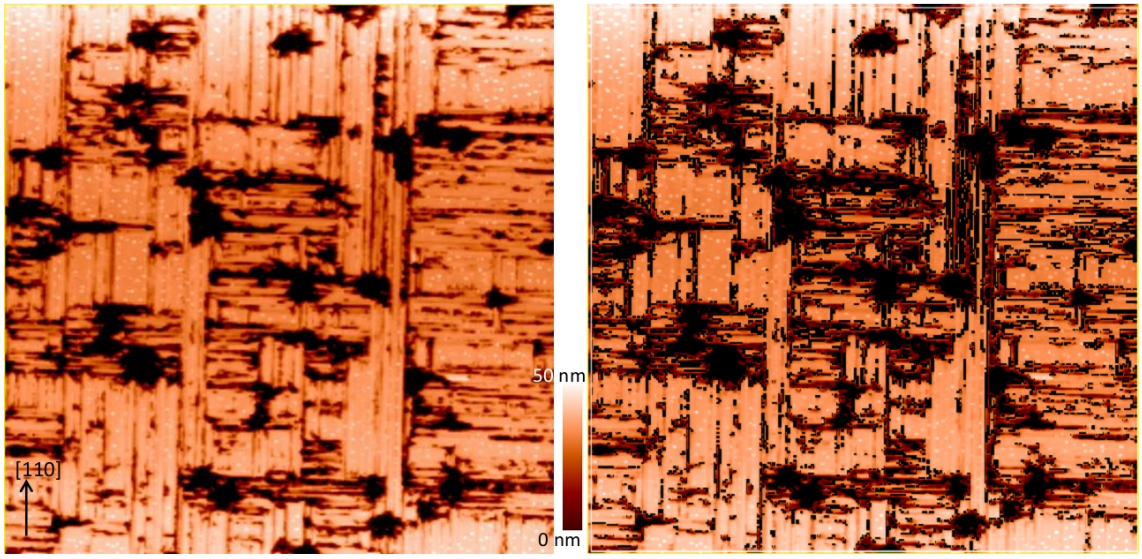

Figure 4.17: *$20\mu m \times 20\mu m$ AFM images of HWC395 with the structure ZnSe(30nm)/MgS(70nm)/ ZnSe(30nm)/MgS(130 nm)/ZnSe (2nm) showing (a) crack formation at the point of rock salt formation. In (b), the roughness measurement plot of the same area, where areas with similar height profile are highlighted. In (b), areas in lighter shade are near atomically flat (RMS roughness = $\sim$ 0.7 nm)*

Other interesting features include perfectly flat surface areas in between the cracks. Such areas are highlighted in Figure 4.17(b). The mainly rectangular areas are nearly atomically flat with a surface roughness of just 0.72 nm compared to the total area roughness of $\sim$ 17 nm. The surface roughness obtained from the flat areas are on par with the surface roughness of smoother thin layers of ZB MgS, especially when allowing for the presence of selenium clusters which slightly increase the roughness. These flat areas are elongated along [110] and all lie at the same height. Some transformation mechanisms generate different height blocks which would have height differences of $\sim$20 nm and be clearly visible. These mechanisms are ruled out by this structure.

4.11 Summary

Challenges faced during the initial attempts to grow thick ZB MgS layers have been studied. Problems with thermocouple temperature measurements and sample loading were rectified by replacing the substrate manipulator. Pyrometers were used to get a more accurate temperature reading.

Lower growth rate and higher Zn incorporation resulting from a series of changes in the growth conditions have been examined. AFM was used for analysing sample surfaces and for roughness measurements. Samples were studied for any changes in the MgS layer quality as a function of ZnS flux and growth temperature. The effect of reducing the Mg flux on the growth of ZB MgS layers has been studied. Reducing the Mg flux was found to produce flatter layers devoid of pits which could then be grown with much greater thicknesses in the ZB structure. Reducing the Mg flux by a factor of three has produced the best MgS surface devoid of all observable defects at 38 nm thick .

Using the reduced Mg flux, samples were grown for growth rate and layer composition calibration. From the three samples grown, the growth rate of MgS was found to be $\sim$ 0.36 Å/s and a Zn incorporation in the MgS layer was estimated to be $\sim$ 0 - 1.2 %.

'Batch B' samples, grown at the beginning of this work behaved abnormally in the etching solution. Three samples were grown for etching with the reduced Mg flux. Sample with thickness above 3 nm were found to etch faster than previously thought and they did not show any difference in etching time when etched two months after growth. Thus the changes in the growth have proved to reduce sample degradation.

Further improvements were made by adding smoothing layers. Using thin layers of ZnSe as buffer layer was found to be more favourable for thick MgS growths. ZnSe/MgS/ZnSe smoothing layers of different composition were used to grow much thicker MgS layers in ZB. ZB MgS was grown up to 200 nm thick using these smoothing layers, which is the thickest ZB MgS layer grown to date.

4.12 Future Work

The thickest ZB MgS layer of 200 nm grown for this study may not be a critical thickness. More samples needs to be grown by varying smoothing layer and it could shed more light into the transformation mechanism. The influence of reducing Mg flux below 13 nA was not studied here (examined later in Chapter 8). The point where the Zn incorporation in MgS increases is an interesting topic as from this study, it has been proved that even after reducing the Mg flux to a third, there was no increase in the amount of Zn present.

One major issue with the RHEED study is that at the moment there is no video capturing devices in use. Post growth RHEED pattern analysis is not possible. During the superlattice growth, it was very difficult to monitor the surface modifications. The changes in RHEED patterns during phase transitions could have been used for analysing surface morphology.

The characterisation techniques used here, AFM and XRI/XRD were of invaluable help. However there are still more characterisation techniques which should be used to investigate this material to further increase our understanding, for example Transmission Electron Microscopy (TEM) which would help to analyse dislocations in detail. As in quantum dots it would also show how the crystals have been modified from the original ZB structure.

More detailed AFM scans can be used to obtain further structural information. Amplitude function in the AFM provides actual deflection measurements as the tip scans the surface compared to the height. Any smoothing caused by the AFM tip dimensions can be eliminated this way. The actual step size of the terraces inside pits can be measured by using amplitude measurement.

4.13 References

[1] A. Navrotsky and J. C. Phillips. “Ionicity and phase transitions at negative pressures”. *Phys. Rev. B* Vol. 11 (1975), pp. 1583–1586 (cited on page: 85).

[2] C. Bradford, C. B. O’Donnell, B. Urbaszek, A. Balocchi, C. Morhain, K. A. Prior and B. C. Cavenett. “Growth of zinc blende MgS/ZnSe single quantum wells by molecular-beam epitaxy using ZnS as a sulphur source”. *Applied Physics Letters* Vol. 76 (2000), pp. 3929–3931 (cited on pages: 86, 87).

[3] C. Kruse, G. Alexe, M. Klude, H. Heinke and D. Hommel. “High reflectivity p-type doped distributed Bragg reflectors using ZnSe/MgS superlattices”. *Phys. Stat. Sol. B* Vol. 229 (2002). 10th International Conference on II-VI Compounds, Bremen, Germany, Sep 09-14, 2001, pp. 111–115 (cited on page: 86).

[4] M. Funato, A. Balocchi, C. Bradford, K. A. Prior and B. C. Cavenett. “Photoluminescence properties of MgS/CdSe quantum wells and quantum dots”. *Appl. Phys. Lett.* Vol. 80 (2002), pp. 443–445 (cited on page: 86).

[5] A. Balocchi, A. Curran, T. C. M. Graham, C. Bradford, K. A. Prior and R. J. Warburton. “Epitaxial liftoff of ZnSe-based heterostructures using a II-VI release layer”. *Appl. Phys. Lett.* Vol. 86 (2005) (cited on page: 86).

[6] O. Fedorych, C. Kruse, A. Ruban, D. Hommel, G. Bacher and T. Kümmell. “Room temperature single photon emission from an epitaxially grown quantum dot”. *Appl. Phys. Lett.* Vol. 100, 061114 (2012), p. 061114 (cited on page: 86).

[7] Y.-H. Lai, W.-Y. Cheung, S.-K. Lok, G. K. L. Wong, S.-K. Ho, K.-W. Tam and I.-K. Sou. “Rocksalt MgS solar blind ultra-violet detectors”. *AIP Advances* Vol. 2, 012149 (2012), p. 012149 (cited on pages: 86, 87).

[8] N. Singh and D. R. Vij. “Luminescence and related properties of magnesium sulphide phosphors”. *Journal of Materials Science* Vol. 29 (1994), pp. 4941–4945 (cited on page: 85).

[9] N. Teraguchi, H. Mouri, Y. Tomomura, A. Suzuki, H. Taniguchi, J. Rorison and G. Duggan. “Growth of ZnSe/MgS strained-layer superlattices by molecular beam epitaxy”. *Applied Physics Letters* Vol. 67 (1995), pp. 2945–2947 (cited on page: 87).

[10] L. Konczewicz, P. Bigenwald, T. Cloitre, M. Chibane, R. Ricou, P. Testud, O. Briot and R. L. Aulombard. “MOVPE growth of zincblende magnesium sulphide”. *Journal of Crystal Growth* Vol. 159 (1996). Proceedings of the seventh international conference on II-VI compouds and devices, pp. 117–120 (cited on page: 87).

[11] H. Nashiki, I. Suemune, H. Kumano, H. Suzuki, T. Obinata, K. Uesugi and J. Nakahara. “Excitonic luminescence up to room temperature in a ZnSe/MgS superlattice”. *Applied Physics Letters* Vol. 70 (1997), pp. 2350–2352 (cited on page: 87).

[12] C. Bradford, C. B. O’Donnell, B. Urbaszek, A. Balocchi, C. Morhain, K. Prior and B. Cavenett. “Growth of zinc blende MgS and MgS/ZnSe quantum wells by MBE using ZnS as a sulphur source”. *Journal of Crystal Growth* Vol. 227–228 (2001). Proceeding of the Eleventh International Conference on Molecular Beam Epitaxy, pp. 634–638 (cited on pages: 87, 95, 115).

[13] S. A. Telfer, C. Morhain, B. Urbaszek, C. O’Donnell, P. Tomasini, A. Balocchi, K. A. Prior and B. C. Cavenett. “MBE growth of ZnS and ZnCdS layers on GaP”. *Journal of Crystal Growth* Vol. 214–215 (2000), pp. 197–201 (cited on page: 88).

[14] J. Massies and J. P. Contour. “Substrate chemical etching prior to molecular-beam epitaxy: An x-ray photoelectron spectroscopy study of GaAs (001) surfaces etched by the $H_2SO_4 - H_2O_2 - H_2O$ solution”. *Journal of Applied Physics* Vol. 58 (1985), pp. 806–810 (cited on page: 89).

[15] L. H. Kuo, L. Salamanca-Riba, B. J. Wu, G. Hofler, J. M. DePuydt and H. Cheng. “Dependence of the density and type of stacking faults on the surface treatment of the substrate and growth mode in ZnS_xSe_{1-x}/ZnSe buffer layer/GaAs heterostructures”. *Applied Physics Letters* Vol. 67 (1995), pp. 3298–3300 (cited on page: 89).

[16] S. V. Ivanov, S. V. Sorokin, P. S. Kop’ev, J. R. Kim, H. D. Jung and H. S. Park. “Composition, stoichiometry and growth rate control in molecular beam epitaxy of ZnSe based ternary and quaternary alloys”. *Journal of Crystal Growth* Vol. 159 (1996). Proceedings of the seventh international conference on II-VI compouds and devices, pp. 16–20 (cited on page: 90).

[17] A. J. SpringThorpe, S. J. Ingrey, B. Emmerstorfer, P. Mandeville and W. T. Moore. “Measurement of GaAs surface oxide desorption temperatures”. *Applied Physics Letters* Vol. 50 (1987), pp. 77–79 (cited on page: 92).

[18] R. T. Moug, C. Bradford and K. A. Prior. “MBE growth of MgS nanowires characterized using AFM”. *J. Crystal Growth* Vol. 301 (2007). 14th International Conference on Molecular Beam Epitaxy (MBE XIV), Waseda Univ, Tokyo, Japan, Sep 03-08, 2006, pp. 289–292 (cited on pages: 105, 113–115).

[19] K. A. Prior, X. Tang, C. O’Donnell, C. Bradford, L. David and B. C. Cavenett. “Characterization of MBE grown II-VI semiconductor thin layers by X-ray interference”. *Journal of Crystal Growth* Vol. 251 (2003), pp. 565–570 (cited on page: 107).

[20] C. Bradford, C. B. O’Donnell, B. Urbaszek, C. Morhain, A. Balocchi, K. A. Prior and B. C. Cavenett. “Highly confined excitons in MgS/ZnSe quantum wells grown by molecular beam epitaxy”. *Phys. Rev. B* Vol. 64 (2001), pages (cited on page: 109).

[21] C. Bradford, K. A. Prior and B. C. Cavenett. “Development of surface structures in MBE grown MgS and the origin of the phase instability”. *physica status solidi (c)* Vol. 1 (2004), pp. 645–648 (cited on page: 113).

[22] C. Bocchi, A. Catellani, F. Germini, L. Nasi, J. K. Morrod, K. A. Prior and G. Calestani. “Metastable zinc-blende MgS structure: Combined experimental and theoretical study”. *Phys. Rev. B* Vol. 79 (2009), p. 235310 (cited on page: 115).

Chapter 5

Growth and stability of ZB MgS grown on GaAs, GaP and InP substrates

5.1 Introduction

It has long been recognized that a thin film can be grown in a crystal structure other than the one it would normally adopt by depositing it on a substrate with that crystal structure. MgS is an example of a compound grown in this manner, as discussed previously, the stable bulk crystal structure is RS but thin epitaxial ZB films can be grown on a (001) ZnSe layer on GaAs substrate.

One early study [1] suggested that a requirement for this metastable growth to occur was a high supersaturation during growth. Low supersaturation (near-equilibrium) growth techniques would only produce the stable phase. In addition, similar lattice constants for the substrate and metastable phase of the epilayer stabilize the metastable phase up to a certain critical size for the material deposit. In this model the high surface area to volume ratio is a key parameter in the stabilization.

Subsequently a different method was used to determine the stability of crystal structures when depositing RS materials on ZB substrates by Froyen, Wei and Zunger [2]. This is referred to here as the FWZ model, and this chapter is an experimental investigation into this model. The model is discussed in Section 5.3, but a key point is that the growth of the metastable layer requires near lattice match of substrate and epitaxial metastable layer to

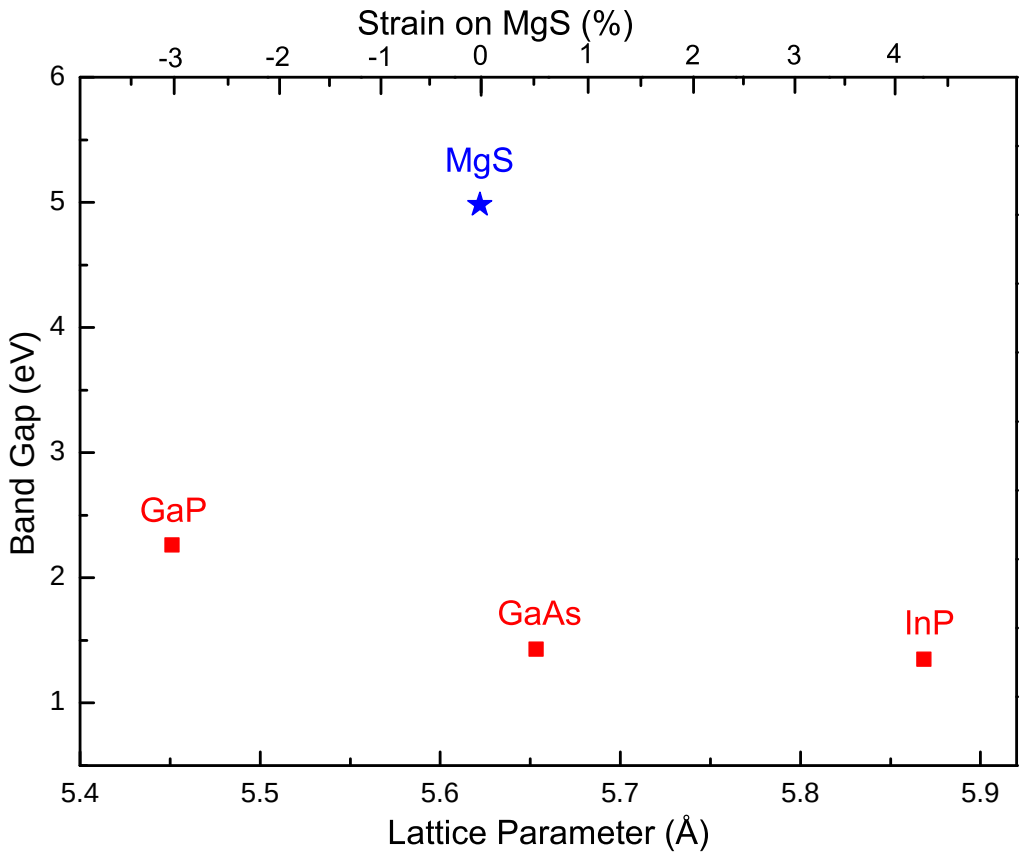

Figure 5.1: *Lattice parameter vs. band gap of ZB MgS and the three substrates GaP, GaAs and InP. The lattice mismatch between MgS and respective substrates are also given. '-' sign denotes compressive strain, whereas '+' denotes tensile strain*

prevent relaxation. As a result the growth of ZB MgS was never attempted previously on any substrates other than GaAs, because of the large lattice mismatch.

This chapter describes the first studies of the growth of ZB MgS on three different substrates with a wide range of lattice mismatches, ranging from InP with 4.4 % tensile strain to GaP with 3.0 % compressive strain. (See Figure 5.1)

5.2 Growth on different substrates

One of the principal problems in the development of II-VI semiconductor compounds is the need to grow on III-V substrates [3]. Large electrostatic fields at the II-VI / III-V heteroepitaxial interface could severely disrupt the growth and lead to rough interfaces with poor electronic properties [4]. Large fields are avoided by tailoring interfaces to eliminate charge imbalances and residual electrical dipoles. This is achieved by growing a graded or

mixed interface containing equal numbers of III-VI and II-V bonds, for example, Ga-Se and Zn-As bonds for the ZnSe/GaAs system. At the same time, mixed compounds such as Ga_2Se_3 must be avoided as they do not have the ZB crystal structure.

The resulting lattice mismatch between the III-V substrate and II-VI epitaxial layer leads to strain between the two materials. Strain relief in the growing layers will invariably lead to the formation of dislocations, resulting in degradation of the material quality. As a result, the substrates for II-VI material growth have always been chosen so that the lattice mismatch is as low as possible. This leads to a default set of III-V substrate/II-VI epilayer combinations, such as GaAs/ZnSe, GaP/ZnS, InP/ZnCdSe, etc, where the respective lattice mismatches are minimal. However, very thin layers of large lattice mismatched epilayers have been grown on III-V substrates for quantum structures, although of similar thicker layers resulted in huge dislocation densities.

Previously, ZB MgS has never been grown on any substrates other than GaAs (on thin ZnSe buffers), where the lattice mismatch is approximately 0.6 %. A detailed MgS growth method is described in Chapter 4, with successful growth of ZB MgS on GaAs substrate up to 200 nm thick demonstrated recently [5]. Similar thickness ZnSe epilayers have also been grown only on GaAs (and ZnSe) substrates [6]. The only high strain systems are the growths of low dimensional ZnSe quantum structures on lattice mismatched substrates [7, 8].

5.3 Predictions of the Froyen-Wei-Zunger (FWZ) model

In the late 1980s, Froyen, Wei and Zunger (FWZ), have described how hydrostatic pressure versus volume data relate to epitaxial structural energies. They suggested a method to determine the stability of crystal structures when depositing metastable layers such as RS materials in ZB structure [2]. For each different substrate and epitaxial film combination, the energy of both phases of the epitaxial layer can be plotted as a function of the lattice parameter. This same model can also be used to determine the stability of other metastable thin film crystal structures including those where the stable structure is not cubic. In particular, it has been used to predict the stability of ZB epitaxial layers where

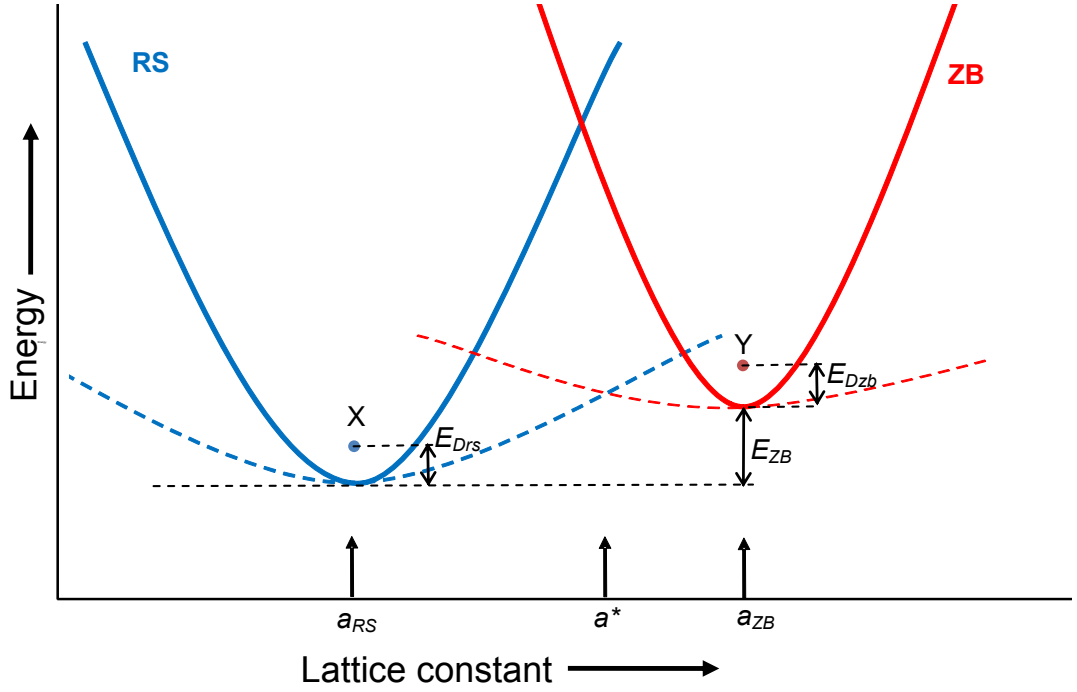

Figure 5.2: *Schematic diagram of crystal energy per formula unit as a function of lattice constant for both the rock salt (RS, blue curves) and zinc blende (ZB, red curves) phases with unstrained lattice constants a_{RS} and a_{ZB} respectively. The solid curves are for bulk material, while thin biaxially strained layers are dashed curves crossing at a^*. The ZB phase is metastable with a minimum energy E_{ZB}. Points X and Y with energies E_{Drs} and E_{Dzb} are RS and ZB layers respectively that have relaxed by the introduction of dislocations.*

the stable structure is nickel arsenide [9]. However, in this case it has been suggested that interfacial energies may dominate in thin film growth [10]. The crystal structure adopted by the interfacial layer is also important.

The FWZ method is shown schematically in Figure 5.2. Here the RS structure has an energy per formula unit (shown in blue) varying parabolically with lattice constant with a minimum at the equilibrium lattice constant a_{RS}. The corresponding ZB (red) curve minimum at a_{ZB} lies at an energy E_{ZB} above the RS minimum, meaning the ZB phase is metastable. Growth of thin films of either phase can occur on a substrate of different lattice constant a_{sub}. Pseudomorphic growth requires the epitaxial layer to be biaxially strained to the substrate lattice constant, and the biaxial strain energy curves have smaller curvatures than for hydrostatic strains (dashed lines in Figure 5.2). The ZB and RS curves intersect at some lattice constant a^*, and if $a_{sub} \geq a^*$ then the biaxially strained ZB phase has the lower energy and is stable. Effectively, the stability of the two phases is reversed due to the greater strain in the RS layer.

As h, the layer thickness increases, relaxation through the formation of strain relieving dislocations becomes possible. The relaxed RS phase with dislocations is shown schematically as point X in Figure 5.2 and has an energy greater than the perfect unstrained crystal of E_{Drs}. In this schematic, E_{Drs} is a function of h, reducing to zero as the layer becomes thicker. When $h = h_{cdrs}$, the energy falls below that for the strained layer, giving the critical thickness for dislocation formation in the RS phase. In contrast, a relaxed ZB phase, without conversion to RS, produces a layer at point Y in Figure 5.2 at a critical thickness $h = h_{cdzb}$.

The FWZ model therefore makes the following predictions about growth. First, the ZB phase grows initially only if $a_{sub} \geq a^*$, otherwise the RS phase forms. Second, as discussed, typically $h = h_{cdrs} < h_{cdzb}$, so conversion from strained ZB to relaxed RS will occur at a minimum layer thickness $h = h_{cdrs}$. All ZB growth at $h < h_{cdrs}$ will be metastable.

A compound originally highlighted by FWZ as an example was MgS, having a_{ZB} close to a_{sub} for GaAs and a small calculated E_{ZB}. The predicted a^* was 5.5Å, so thin layers (≤ 1 nm) of the ZB phase grown on GaAs would be stable.

5.4 Substrate cleaning

All layers used for this study were grown on (100) oriented substrates from three different manufacturers. GaAs (AXT), GaP (ITME) and InP (Wafer technologies) substrates were used. A clean and stoichiometric surface is imperative for the growth of high quality epitaxial films. This require removal of native oxide layers and other contaminations from substrate surfaces. Three different cleaning methods have been used for the three substrates. GaAs and GaP are described together as their cleaning was relatively straightforward. InP required more development and is described separately.

5.4.1 GaAs and GaP substrate cleaning

For cleaning GaAs substrates, the same method detailed in Chapter 4 has been followed, where the substrate is chemically etched in a 2:2:20 solution of $H_2O_2 : H_2O : H_2SO_4$ for 90 seconds.

For GaP substrates, a cleaning method successfully used previously at Heriot-Watt has been adopted. Prior to the growth, GaP (100) substrates were etched in 15:5:5 solution of $HCl : HNO_3 : H_2O$ for 120 seconds at room temperature [11]. Substrates were then quickly rinsed in 18 MΩ deionised water and then dried with oxygen-free nitrogen gas. The substrates were then moved to the growth chamber after mounting on a molybdenum block using indium glue.

5.4.2 InP substrate cleaning

Several methods of cleaning InP(100) surfaces have been widely used [12–21]. Traditional cleaning techniques for thermally stable materials include ion sputtering and annealing but the relatively low decomposition temperature of InP at $\sim 380^oC$ prevents effective annealing of the damage caused by ion sputtering. Sulfur passivation leads to stable surface termination, but the chemisorbed sulphur atoms cannot be removed completely by thermal annealing at temperatures below the decomposition temperature of InP [16–18].

An effective and practical method for cleaning semiconductor surfaces is wet chemical etching [19–21]. As mentioned in previous sections, all the substrates used at Heriot-Watt MBE group have always been chemically cleaned. This required finding a suitable chemical etch for InP substrates. One group of solutions widely used for cleaning InP(100) are based on hydrogen peroxide (H_2O_2). These methods are effective in obtaining a clean GaAs(100) surface as well.

HCl has also been used widely on InP(100) substrates, but mainly for etching rather than as a chemical cleaning agent [22–26]. Furthermore, oxide and carbon contamination were

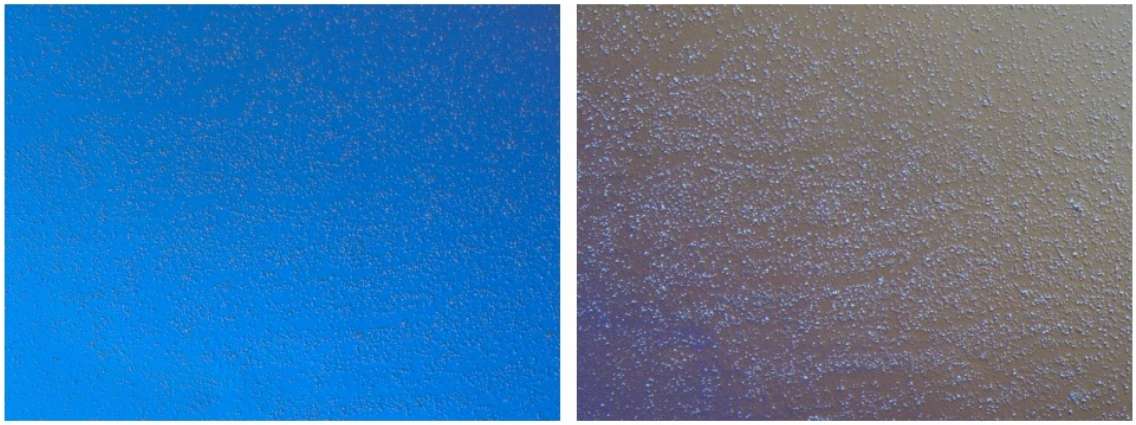

Figure 5.3: *100× UV microscope images from two InP substrates, improperly vacuum annealed at 440°C, showing Indium droplets formation on surface.*

reported on the substrate surface after HCl etching [24]. This result may not be because of the chemical reactions of InP with HCl, but due to the atmosphereic contamination after the etching. Because of the effectiveness in SiO_2 etching due to its unique property of dissolving SiO_2 into soluble SiF_6^{2-}, HF has also been used for InP cleaning, but being a weak acid it is not expected to perform as good as HCl in oxide removal.

5.4.3 One-step chemical etching process previously used at Heriot-Watt

This study first examined a one step chemical cleaning process using a H_2O_2 based solution, which is typically used in the primary chemical etching step in the cleaning of the GaAs surfaces, detailed in section 4.2.2. Although this process, when followed by vacuum annealing will result in a clean and stoichiometric GaAs(100) surface, in the case of InP substrates it was not effective. A 2 × 4 RHEED pattern indicating a clean surface was obtained, always above the congruent evaporation temperature of InP. The initial clean up temperature varied from 400 °C to 430 °C. Interestingly, no surface degradation has been observed in RHEED, as all the patterns were streaky once the surface is cleaned up and the streaks were maintained even at the low growth temperature. However, as soon as the growth started, RHEED became very spotty indicating a 3D growth.

At this stage InP test samples were chemically cleaned, vacuum annealed at temperatures in the range of 400 °C to 430 °C and brought out of the chamber for examining the surface. UV microscope images from these samples show structures like tiny indium droplets all

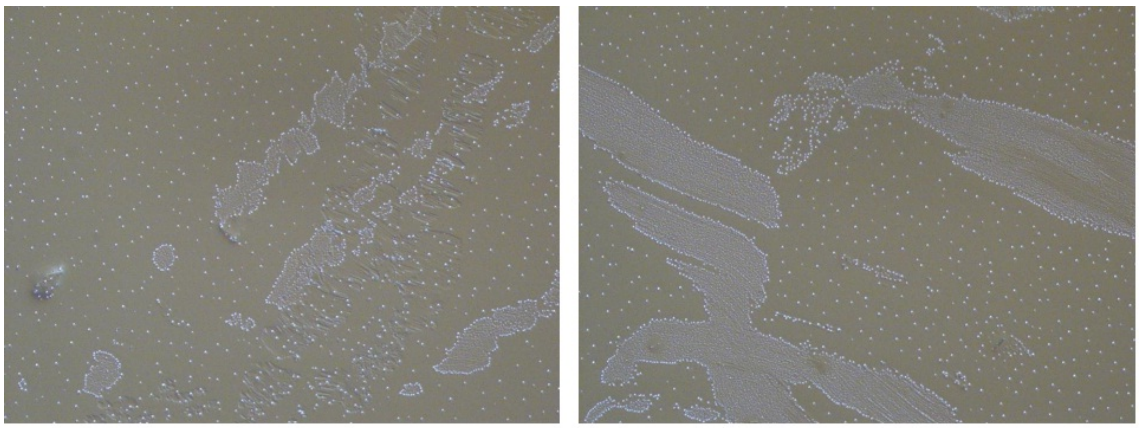

Figure 5.4: *200× UV microscope image from two InP substrate surfaces, vacuum annealed at 400°C, showing the presence of indium droplets.*

over the surface as shown in Figure 5.3 and Figure 5.4. Noticeably these samples have perfectly flat areas in between the indium droplets. During the heating of the substrate, phosphorus is removed above the InP decomposition temperature and the excess indium forms droplets on the surface. This formation is not visible in RHEED as the separation distance of the droplets is orders of magnitude larger than the RHEED coherence length. In III-V systems there is an overpressure of As or P during the heat clean which prevents the In buildup, which is not possible in a II-VI chamber [27].

Previously, two different clean up techniques were examined at Heriot-Watt to find which could best remove the surface oxide while minimising the density of the indium droplets. The first technique involved raising the substrate temperature slowly in 50°C steps every 2 minutes to a peak temperature of $\sim 390^{o}$C , where the 4 $\times$ reconstruction first becomes visible. Increasing the temperature at this low rate limited the possibility of overheating the sample. Once the temperature reached that peak, the substrate was cooled suddenly to the growth temperature. During the cooldown the surface was monitored by RHEED, with the 4 $\times$ reconstruction maintained, indicating a smooth flat surface. However UV microscopy of the surface clearly showed the In droplets on the surface. A reduction in the In droplets density was observed with lowering the peak temperature, but complete oxide layer removal required a higher temperature.

The second method used to remove the oxide from the InP surface involved quickly raising the substrate temperature to 395°C and holding it constant for approximately 40 minutes. This method required the congruent sublimation of InP. Early studies of the

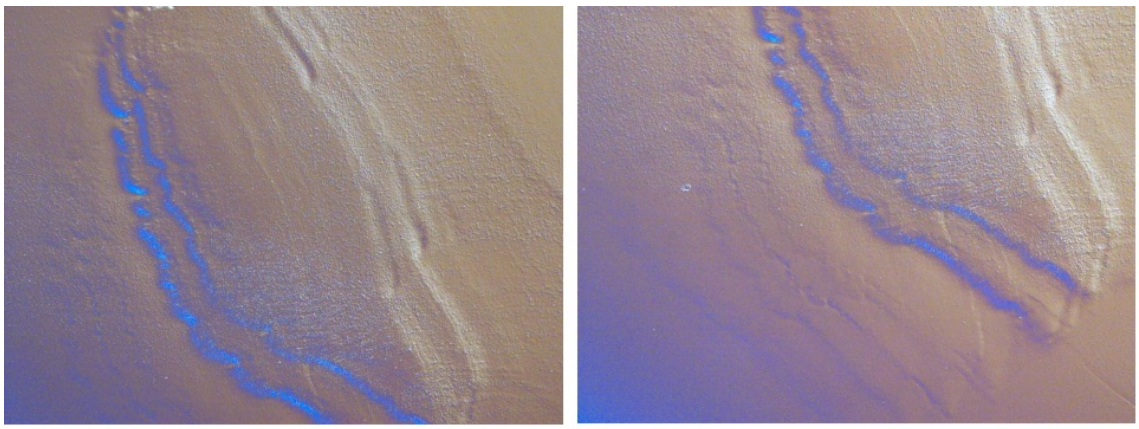

Figure 5.5: *100× UV microscope image of a sample surface, vacuum annealed at 400°C, showing Indium droplets along with linear surface features arised from the use of an improper chemical etch.*

growth of InP by MBE state that the maximum congruent evaporation rate was 10^{-5} monolayers per second, suggesting that cleaning the InP by simply heating it to the congruent evaporation temperature would be inefficient [28]. However, another study has since demonstrated that InP substrate cleaning can be successfully carried out by maintaining a temperature of 380 $\pm$ 50°C for 15 minutes [29]. The cleaning was carried out without any fluxes incident on the surface. The oxide removal was confirmed by X-ray Photoelectron Spectroscopy carried out in a UHV chamber connected to the MBE chamber. The temperature range used corresponds to the congruent evaporation temperature and therefore the oxide layer present on the surface of the InP is removed while still maintaining the congruent evaporation of the InP. This method was tried at Heriot-Watt earlier and proved effective even though the surface was not completely indium droplet free.

This method was repeated on the InP substrates for this study. But the RHEED patterns during growth suggested that it was not reproducible. RHEED spots arising due to the surface roughening during annealing have been noticed throughout. The same problem has been reported in the previous studies at Heriot-Watt, but since the surface was adequate for the growth of lattice matched, thick epitaxial layers, an alternate method was not developed. UV microscopy images of the samples thus treated has shown fewer indium droplets but has shown some linear surface features as given in Figure 5.5. These features would have prevented growth of flat II-VI layers and so this cleaning method was unacceptable. This decision required finding yet another chemical cleaning solution.

5.4.4 A two-step chemical etching process

A surface analysis study, using photoemission electron spectroscopy (PES) on chemical species remaining on InP(100) surface after different chemical cleaning techniques has suggested that a two step chemical cleaning is required for effective oxide removal [30].

For the first cleaning step, a hydrogen peroxide based solution was used. InP(100) substrates were etched in a 4:1:100 solution of $H_2SO_4 : H_2O_2 : H_2O$ for two minutes. The substrate surface is hydrophilic after etching with hydrogen peroxide based solutions. After the cleaning step, the surface has 0.23-0.5 ML of oxide, which most likely takes the form of indium phosphate ($InPO_4$). The vacuum annealing does not completely remove the oxide from the surface [31].

After the sample is etched in the initial etch solution, it is dipped in a 1:1 solution of $H_2SO_4 : H_2O$ for 30 seconds then rinsed in 18 MΩ deionised water and quickly dried using oxygen-free nitrogen gas. The surface is hydrophobic after the second chemical cleaning step, having 0.4 ML of elemental phosphorous terminated surface [31]. At the beginning of the reaction, H atoms bind to the surface phosphorous atoms and hence the surface will have a hydrogen termination on the phosphorous sites after treating with a strong acid solution. A hydrophobic surface created by hydrogen termination is well known for Si surfaces because the H-Si bond is almost non-polarized due to the small difference of their electron-negativity. Thus the excess phosphorous surface component may not be elemental but surface phosphorous atoms bonded to hydrogen instead [30]. However this is different in the case of GaAs surface after the same chemical treatment. A GaAs surface has several layers of elemental As [32]. Hence there is no hydrogen termination for the GaAs surface and it is not as hydrophobic as InP.

The hydrophobic substrate surface created by this two-step chemical cleaning process is not only resistant to oxidation but also results in less carbon contamination from the solution [31]. When the substrate is annealed in vacuum, the elemental phosphorous is removed at a relatively low temperature, 330^{o}C.

This method has been successfully adopted for cleaning the InP(100) substrates used for

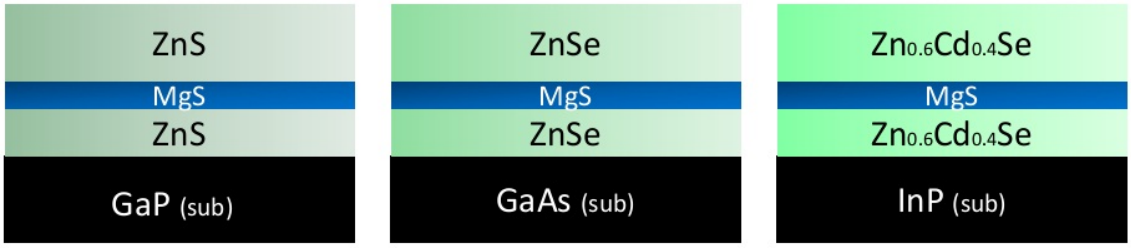

Figure 5.6: *Schematic of the MgS heterostructures grown on the three substrates.*

this study. As a result, the clean up temperature was dropped significantly to $\sim 320^{o}$C. Vacuum annealed samples processed this way were examined using UV microscopy and no evidence of indium droplet formation has been found. RHEED has also shown a flatter surface during subsequent growths.

5.5 Growth

Heriot-Watt MBE group has previously shown that ZB MgS grows on GaAs and under optimum conditions thicknesses over two orders of magnitude greater than h_{cdrs} are easily achievable [33, 34]. In order to determine the influence of the substrate lattice constant on growth mode, in this chapter the growth of MgS on three different substrates (GaP, GaAs and InP) with a wide range of lattice mismatches is compared.

All previous successful growths of ZB MgS by the Heriot-Watt MBE group have occurred on thin ZnSe buffers deposited on GaAs substrates, and recently it was shown that an almost identical growth procedure to the one used at Heriot-Watt forms only RS MgS if deposited directly on GaAs substrates [35]. In this paper it was suggested that intermediate compounds with structures which do not closely resemble ZB are formed (This claim was carefully examined following this work and the results are given in Chapter 8). Accordingly, to ensure that the ZB crystal structure is maintained across the interface, the MgS layers are grown on II-VI buffers that are approximately lattice matched to the three III-V substrates. The combinations chosen and the MgS strains are given in Table 5.1 which are also schematically shown in Figure 5.6. Relaxation of the buffer layer is possible and the table also gives the strains between MgS and a relaxed buffer.

All epilayers were grown using the same growth method and conditions as detailed in the

Heterostructure	Strain to ZB MgS $\varepsilon_{\text{substrate(buffer)}}(\%)$	Strain to RS MgS $\varepsilon_{\text{substrate(buffer)}}(\%)$
GaP/ZnS	- 3.0 (-3.8)	4.8 (4.0)
GaAs/ZnSe	0.6 (0.8)	8.7 (9.0)
InP/$Zn_{0.6}Cd_{0.4}Se$	4.4 (3.7)	12.9 (12.1)

Table 5.1: *Strains of MgS on different substrates and buffer layer combinations.*

previous chapters. All three substrates were chemically etched as described in Section 5.4, prior to loading into the chamber.

After loading, samples were degassed in the preparation chamber, then transferred to the growth chamber where the oxide layers were desorbed. The desorption temperatures were measured with a IRCON IR pyrometer as $\sim 540^{\circ}$C, $\sim 520^{\circ}$C and $\sim 320^{\circ}$C for GaAs, GaP and InP respectively. Before depositing II-VI buffer layers, the substrates were cooled. For GaAs and InP substrates the temperature was reduced to 250 °C under a flux of Zn [36], while GaP was cooled without any added flux to 170 °C. Following oxide removal, and during the 10-15 minutes needed to cool the sample to the growth temperature, sharp 4x2, 2x4 and 2x1 RHEED patterns were always obtained from GaAs, GaP and InP respectively, indicating minimal sulfur contamination of the substrate surface.

ZnSe on GaAs (-0.2% lattice mismatch), ZnS on GaP (0.7% lattice mismatch) and $Zn_{0.6}$-$Cd_{0.4}Se$ on InP (0.9% lattice mismatch) were used as buffer layers for this study. After deposition of the buffer layers the MgS layer was deposited, followed by a capping layer to prevent oxidation. The MgS phase was monitored during growth by RHEED. The transition from ZB to RS has been described previously and is marked by sudden clear changes in the pattern [33, 34]. Confirmation of the phase present was also obtained after growth using X-Ray Diffraction (XRD) with the Bede D200 Diffractometer as demonstrated previously for MgS on GaAs(100) (See Chapter 4). Layer thicknesses and compositions were determined using the Jordan Valley RADS simulation program. The results of the growths are discussed in the sections below.

5.5.1 Growth on GaAs

Due to the near lattice match of MgS on GaAs, and the previous extensive experience at Heriot-Watt with ZB MgS growth, this substrate is used as a reference. On GaAs substrates, growth occurred on a ZnSe buffer layer at 250 °C to produce samples with structure GaAs(sub) /ZnSe(50nm) /MgS(12nm) /ZnSe(320nm). Even though ZB MgS has been previously grown for upto 200 nm thick on GaAs substrate, it was decided to initially set the thickness of MgS epilayer at 12 nm, which equates to $\sim$ 5 minutes of growth at the rate of $\sim$ 0.38 Å/s.

A thicker ZnSe capping layer was grown than in previous studies to obtain a more intense X-ray signal for subsequent analysis. The ZnSe buffer layer RHEED pattern is a very sharp 2x1 indicating a flat surface which becomes a streaky c(2x2) RHEED pattern as soon as the MgS growth starts [37]. The 2x1 pattern reappears during the capping ZnSe layer. Throughout the growth the RHEED patterns were compatible with growth of the ZB phase, and no features which could be assigned to RS growth were observed. X-ray analysis of the structure gave the sample thicknesses and a MgS growth rate of $\sim$ 0.38 Å/s.

5.5.2 Growth on GaP

Samples were grown on GaP substrates with ZnS buffers which were deposited at 170 °C before increasing the substrate temperature to 250 °C for the MgS growth. Within experimental error the growth temperatures and fluxes for the MgS layers were identical with those used for growth on GaAs substrates. The initial structures produced were GaP(sub) /ZnS(60nm) /MgS(12nm) /ZnS(320nm) and for the ZnS capping layer the substrate temperature was reduced to 170 °C. The ZnS buffer layer shows a very faint c(2x2) RHEED pattern, which becomes stronger and streakier during MgS layer growth and does not change in intensity during the growth of the cap. Surprisingly the RHEED patterns indicated that the MgS surface was very smooth and the ZnS capping layer growth was much smoother than the buffer layer. Again, there was no indication of RS conversion during growth.

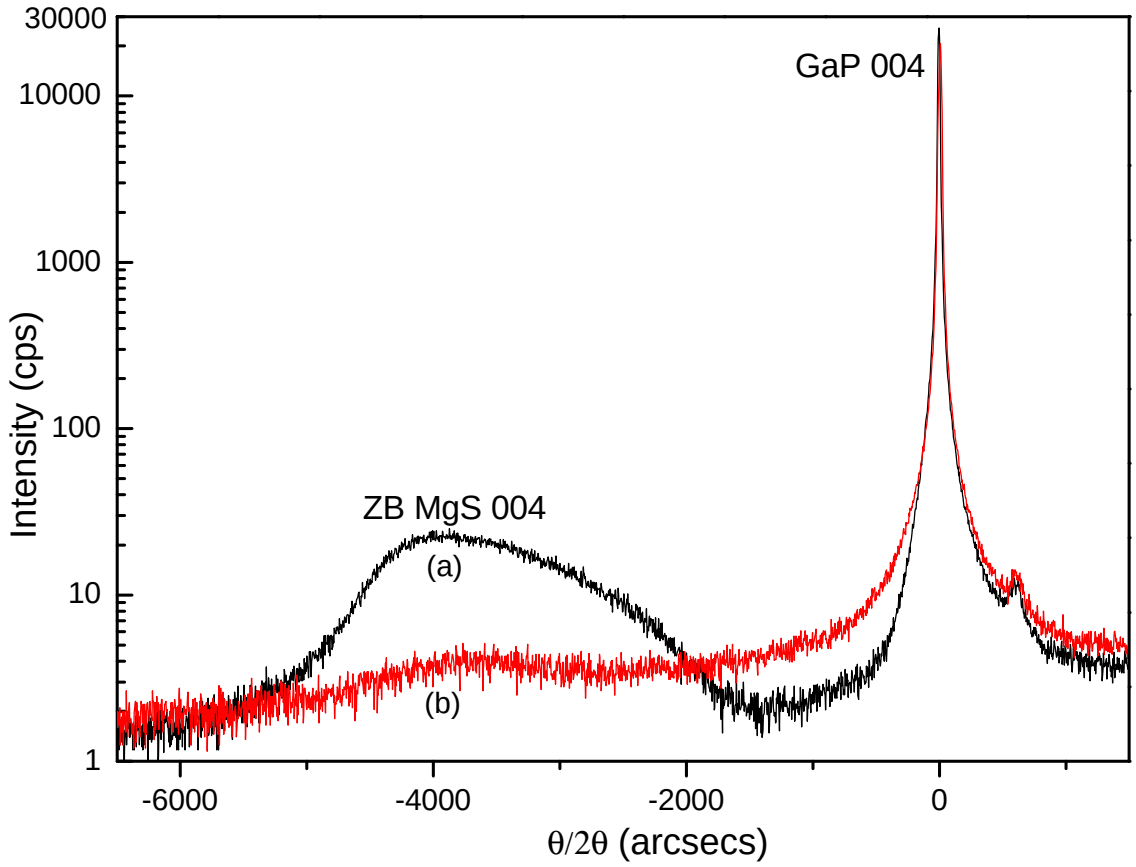

Figure 5.7: *004 x-ray rocking curves from two GaP/ZnS (10 nm)/MgS (x nm)/ZnS (4 nm) structures, where x is: (a) 40 nm, (b) 70 nm. Here (a) shows a broad MgS epilayer peak at the correct position for a fully relaxed ZB layer and a subsidiary weaker peak, which is assigned to ZnMgS mixing layers a few nm thick between the MgS and surrounding ZnS cladding. The overall asymmetric shape of the peak arises from this intermixing.*

5.5.3 Growth of thicker MgS on GaP

Subsequently, samples were grown to determine the maximum ZB MgS thickness possible on a GaP substrate with structure GaP(sub) /ZnS (10nm)/MgS (x nm)/ZnS (4nm). Here the capping layer was only used to prevent oxidation of MgS. For x upto $\sim$ 40 nm, RHEED showed a streaky c(2x2) pattern with no spots or diffuse features, indicating high quality ZB MgS can be grown. With further growth the RHEED streaks became spots and at $x \sim$ 70nm, the pattern became diffuse. Figure 5.7 shows the 004 x-ray rocking curves from (a) the 40 nm and (b) the 70 nm thick layers. In the former the MgS epilayer peak is broad, and at the correct position for a fully relaxed ZB layer, but is very weak or absent from all thicker samples, confirming the phase conversion to RS of the underlying MgS.

5.5.4 Growth on InP

Samples were also grown on InP substrates with the structure, InP (sub)/$Zn_{0.6}Cd_{0.4}Se$ (80 nm)/MgS (12 nm)/$Zn_{0.6}Cd_{0.4}Se$ (320 nm). In this case, at the start of the buffer layer growth the RHEED patterns were spotty, but gradually improved to give a streaky 2x1 pattern and therefore a thicker buffer layer was used to produce a smoother ZnCdSe surface. The MgS layer again grew smoothly, giving a sharp and streaky c(2x2) RHEED pattern and the $Zn_{0.6}Cd_{0.4}Se$ capping layer also showed a streaky RHEED pattern throughout the growth.

These results show that ZB MgS can be grown on substrates over a wide range of strain, including large compressive strain. The deposited layers appear very similar on all three substrates and during growth it was noticed that it was impossible to tell from the RHEED patterns alone which substrate was being used. This result was completely unexpected as all previous experience by at least four different growers has found that growth of ZB MgS is very sensitive to growth conditions, in particular substrate temperature and fluxes. However if the growth conditions are optimized for good ZB growth, then the choice of substrate appears far less critical.

Irrespective of the strain state in the epitaxial layers at the start of growth, relaxation occurs through mismatch dislocations. The capping layers grown on top of the MgS clearly relax and modeling of the X-ray data from the thickest ZB MgS layers indicates these are also relaxed. This behavior had previously been seen for layers grown on GaAs substrates [34], [38] and has now been confirmed for GaP and InP.

5.6 Dislocation density calculations

For the epilayers grown on GaAs, GaP and InP substrates, rocking curves were obtained with the incident beams aligned along [110] and [1$\bar{1}$0]. Symmetric 004 double crystal x-ray rocking curves were obtained using Cu $K\alpha_1$ radiation and a Bede diffractometer. The [110] and [1$\bar{1}$0] directions were identified from the individual substrate manufactures' notes. Subsequently, the crystal orientations were confirmed by etching the substrates

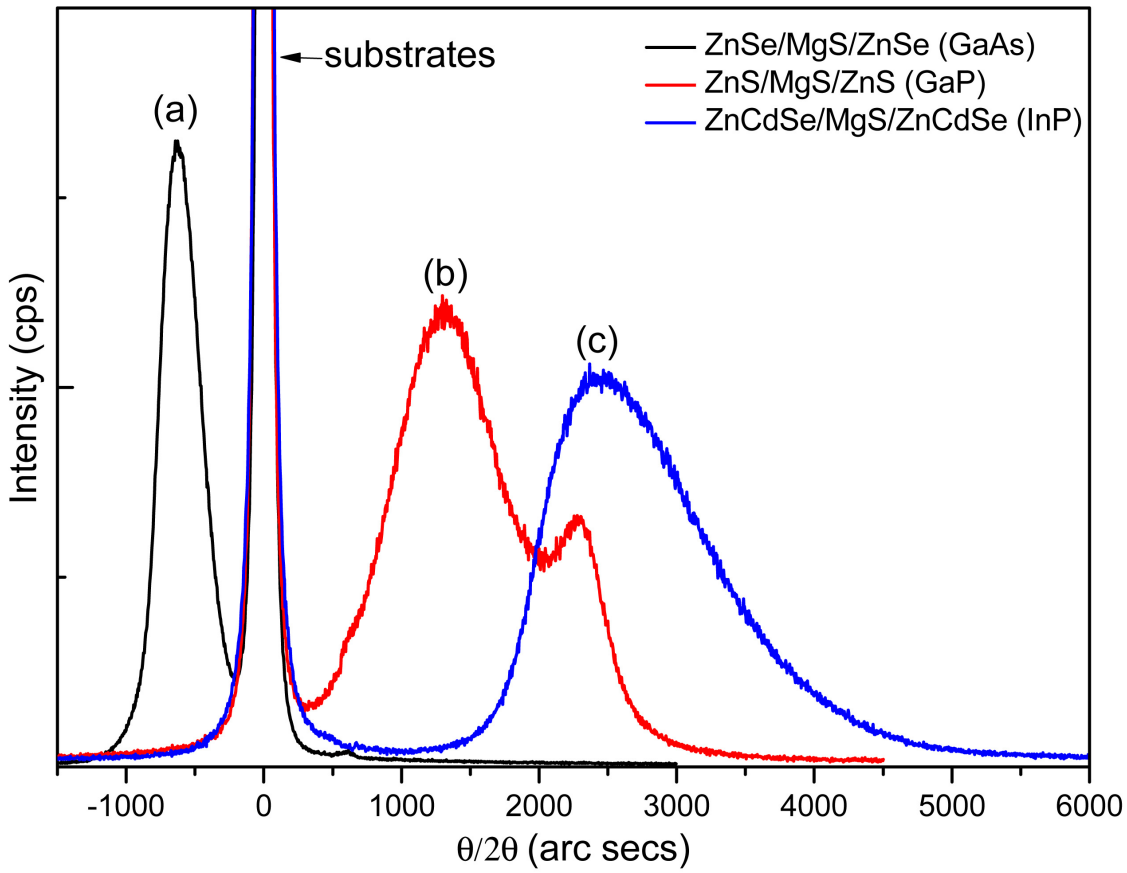

Figure 5.8: *004 x-ray rocking curves from samples with structures (a) GaAs (sub)/ZnSe (50nm)/ MgS (12nm)/ZnSe (320nm), (b) GaP (sub)/ZnS (60nm)/MgS (12nm)/ZnS (320nm), (c) InP (sub)/*$Zn_{0.6}Cd_{0.4}Se$ *(80nm)/MgS (12nm)/*$Zn_{0.6}Cd_{0.4}Se$ *(320nm). The curves are shown with the substrate peaks aligned at the origin. The broad peaks are from the capping layer. In (b) the subsidiary peak at larger angle arises from the strained ZnS buffer layer.*

in a 1:400 solution of bromine:methanol for 16 sec at 0 ^{o}C. This crystallographic etch reveals pyramidal pits which elongate along the [110] direction [39]. These pits can be observed through an optical microscope at 1000×.

The obtained DCXRD scans from samples grown on all three substrates and representative examples are shown in Figure 5.8. Strong epilayer peaks from the capping layers are visible in all these samples, confirming the ZB structure is maintained throughout. Because of the thick capping layers, all the heterostructures are relaxed, giving broad peaks with no thickness fringes.

In thick relaxed semiconductor layers, the dislocation density can be measured and its anisotropy determined by measuring the FWHM of the relevant layer peak at different azimuthal angles [40] (Figure 5.9). Dislocations exist on two types of slip systems with

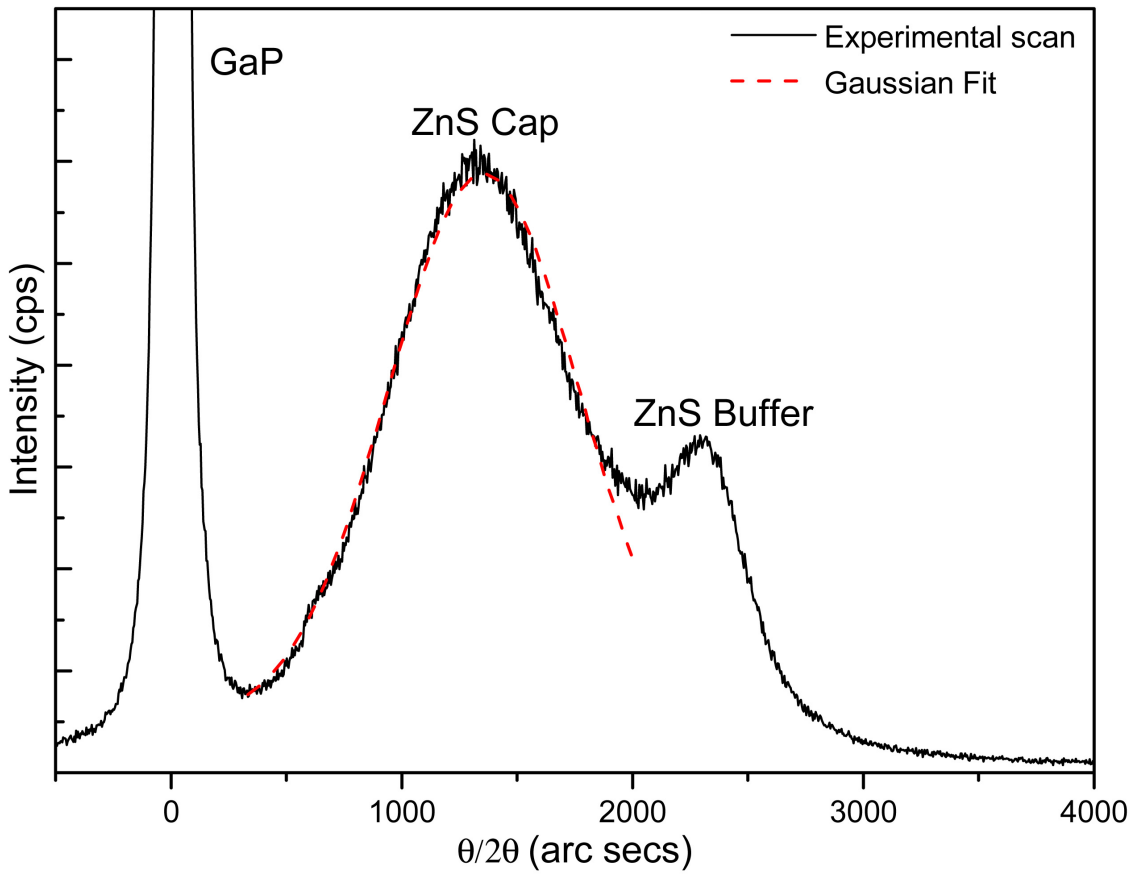

Figure 5.9: *004 x-ray rocking curve for a GaP/ZnS/MgS/ZnS (001) structure at [110] direction. Also shown is the Gaussian fit for the ZnS capping layer diffraction peak. The subsidiary peak at larger angle arises from the strained ZnS buffer layer.*

their misfit dislocation line segments oriented along either [110] (D_A) or [1$\bar{1}$0] (D_B). An imbalance in the densities of dislocations on these slip systems produces an observable azimuthal variation in the rocking curve width for symmetric x-ray reflections (see Figure 5.10).

If symmetric x-ray rocking curves are measured at a Bragg angle θ_B such that $tan^2\theta_B <$ 5 (for example, 004 rocking curves measured with Cu $K\alpha_1$ radiation) and the dislocation density is greater than about 10^6 cm^{-2}, then the rocking curve width is dominated by the angular mosaic spread introduced by dislocations [41]. The type A and type B dislocations will broaden the symmetric rocking curve when the azimuth is such that the projection of the incident beam is normal to the misfit dislocation line vector but not when these directions are parallel [40]. The individual dislocation densities on the two azimuths can be estimated from Eq. 5.1 and 5.2.

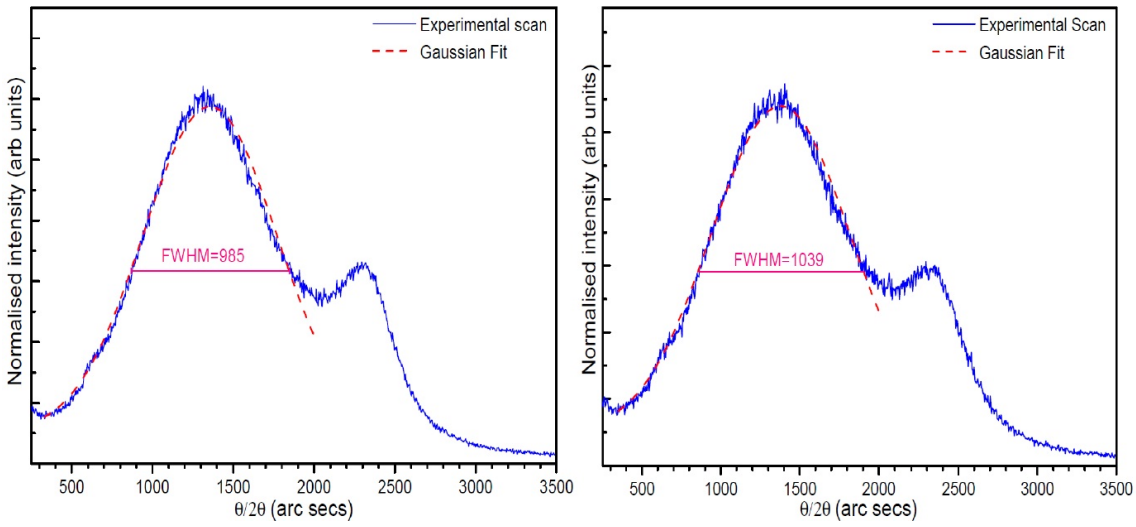

Figure 5.10: *Gaussian fit of 004 X-ray rocking curves from a GaP/ZnS/MgS/ZnS heterostructure. Scans along [110] (left) and* $[1\bar{1}0]$ *(right) directions along with the respective calculated FWHM are given. A difference of 54 arc secs (0.118 Rad) in FWHM has been found on rotating the sample 90º.*

$$\mathrm{D}_{[110]} \approx \frac{\beta^2(\psi=0)}{8\pi\ln(2)b^2\cos^2\gamma_{\mathrm{A}}} = \frac{\beta^2(\psi=0)}{8.7b^2} \tag{5.1}$$

$$\mathrm{D}_{[1\bar{1}0]} \approx \frac{\beta^2(\psi=90^\circ)}{8\pi\ln(2)b^2\cos^2\gamma_{\mathrm{B}}} = \frac{\beta^2(\psi=90^\circ)}{8.7b^2} \tag{5.2}$$

where the zero azimuth $(\psi = 0)$ is when the projection of the incident x-ray beam is aligned with the [110] direction in the surface of the sample and $(\psi = 90^\circ)$ is when the projection of X-ray beam is aligned with the $[1\bar{1}0]$ direction in the surface of the sample. γ_A and γ_B are the angles between the Burgers vectors and the diffraction vectors for the dislocation on the two azimuths. β is the rocking curve width, obtained from the full width at half maximum (FWHM) and the length of the burgers vector b has been calculated using Eq. 5.3, where a is the lattice constant of the substrate.

$$b = a\frac{\sqrt{2}}{2} \tag{5.3}$$

Origin Pro data analysis software has been used to calculate the FWHM from epilayer peaks. A linear peak fitting function has been used to separate epilayer peaks in case both the buffer layer and capping layer occur at the same angle and a Gaussian fit function was

				FWHM (Rad) x10^{-3}		Dislocation density cm^{-2}	
Substrate	Epilayers	Capping layer thickness (nm)	Burgers vector b (nm)	$\beta_{[110]}$	$\beta_{[1\bar{1}0]}$	$D_{[110]}$	$D_{[1\bar{1}0]}$
GaAs	MgS/ZnSe	360	0.4	1.674	1.709	2.02 x10^{8}	2.10 x10^{8}
GaP	MgS/ZnS	360	0.385	4.780	5.040	1.77 x10^{9}	1.96 x10^{9}
InP	MgS/ZnCdSe	360	0.415	6.015	6.040	2.42 x10^{9}	2.43 x10^{9}

Table 5.2: *Dislocation densities calculated from two azimuths from capping layer FWHM.*

used for deriving the FWHM from individual capping layers.

Epitaxial layers thicker than 300 nm have been used for this study. Care was taken to adjust the sample tilt to bring the diffraction vector exactly into the plane of the diffractometer at each azimuth, in order to avoid any alignment errors which could account for any observed azimuthal variation. In addition, sufficiently high dislocation densities have been observed from the rocking curve widths that any dynamical diffraction effects may be neglected and may be ruled out as the cause of azimuthal rocking curve variation. The calculated dislocation densities are given in Table 5.2.

From these calculations, it is evident that the GaAs/ZnSe/MgS/ZnSe, GaP/ZnS/MgS/ZnS and InP/ZnCdSe/MgS/ZnCdSe samples have unequal dislocation densities on the two types of azimuths with fewer dislocations along [110] than $[1\bar{1}0]$ direction. In all cases, dislocations are anisotropic and presumably in at least one of the orthogonal <110> directions, relaxation is not complete. It also suggests that the mismatch dislocations in ZB MgS are probably the same type as those in the surrounding layers, despite MgS having very different elastic constants [2, 38, 42]. On comparison, the previously published results for epitaxial ZnSe layers on GaAs show almost identical dislocation densities to the GaAs / ZnSe/ MgS/ ZnSe samples studied here [40].

5.7 Experimental results vs. FWZ prediction

On the energy schematic in Figure 5.2, MgS evolves from a point on the strained ZB (red, dashed) curve to point Y before transferring subsequently to point X. This is true for all three substrates, particularly including GaP. The lattice constant of GaP is 5.451 Å, which is smaller than the original value a^* of 5.5 Å estimated by FWZ. The energy diagram for the MgS ZB and RS phases has recently been recalculated [38], giving a value of a_{MgS} much closer to the experimental value than the one obtained by FWZ and additionally re-evaluating a^*. The new value is $a^* \approx 5.465$ Å, which is still larger than a_{GaP}.

There are potentially two major sources of error in calculating a^*. The first is the residual zinc level in the MgS, which is typically in the range 0.5-3%. At the higher levels this

causes a significant increase in the MgS elastic constants which increases a^* by ≈ 0.02 Å. The second source of error is the value of E_{ZB} used. There is no experimental value for this quantity, and both calculations (FWZ and the recent re-evaluation) [2, 38] used a value of 170 meV per formula unit. In order to obtain $a^* < a_{GaP}$, then E_{ZB} must be decreased by 80-100 meV, a significant reduction. It therefore appears that according to the FWZ model growth of ZB MgS on GaP is impossible, in direct contrast to these observations.

Growth of ZB MgS on GaAs and InP is allowed under the FWZ model, but the pathway from strained ZB (red curve) to relaxed ZB (point Y) to relaxed RS (point X) is not. FWZ estimated h_{cdrs} for RS MgS was 5 Å when the in-plane lattice constant was equal to the ZB MgS lattice constant. The critical thickness can be recalculated using different versions of Matthew's formula to allow for the anisotropy of the elastic constants [43], but similar results are obtained.

Using Matthew's theory to calculate the critical thickness suggests that the phase transition is initiated by or linked in some way to the formation of the first mismatch dislocation. It is possible that instead the transformation requires a much larger minimum dislocation density, associated with significant relaxation. An upper bound for this can be found by determining the critical thickness for the formation of a complete dislocation network for relaxation, but this still gives very similar thicknesses of only a few Å. These small values of the various critical thicknesses arise from the elastic constants of RS MgS where c_{11} is large and c_{44} is small. Hence any strain produces a large amount of strain energy as this depends on c_{11}, while dislocations need little energy to form as this is a distortion which scales with c_{44}.

This gives confidence that the implication that relaxation in RS MgS should be much easier than in ZB MgS is correct, even though the exact values obtained are undoubtedly very inaccurate as the predicted values are all of similar magnitude as the Burgers vector. There are two key points confirmed by these rough estimates. First, strained ZB MgS should always relax to RS MgS before relaxed ZB MgS can form, and second, any layer of ZB MgS over 5 Å thick is unstable with respect to the RS phase. These conclusions are completely different to the observed behavior of MgS which indicate that the growth of MgS in the ZB form is truly metastable, as it can be grown with a wide range of strains,

both tensile and compressive and then relaxes through the normal misfit mechanism back to its unstrained ZB lattice constant. Under ideal conditions it can grow very thick relaxed layers, and as shown in Chapter 4, thicknesses of up to 200nm are possible. To date, the thickest ZB layers deposited on GaAs and the majority of this growth were completely relaxed.

One final point is that, in the case of ZnSe epitaxy on GaAs, there has been much effort by many groups over a long period of time to ensure the lowest possible dislocation density. One possibility, (although unlikely) is that with GaAs/ZnSe(50 nm) buffer layers the threading dislocation density from the substrate is so low that the MgS layer is unable to relax and growth remains pseudomorphic. In this case relaxation will only occur after growth of the MgS layer due to the introduction of dislocations from the relaxed capping layer. To test this idea the dislocation density in the MgS can be increased substantially by growing a relaxed 300 nm ZnSe buffer layer. Comparison of MgS layers deposited on 50 nm thick strained layers and 300 nm thick relaxed layers with different dislocation densities shows no change in RHEED or X-ray diffraction peaks indicating that threading dislocation densities are not important.

5.8 Summary

The growth of ZB MgS layers on GaP, GaAs and InP substrates under both tensile and compressive strain has been successfully demonstrated. Both RHEED and X-ray diffraction measurements indicate that the ZB phase can be grown in layers up to 40 nm thick on all substrates. Conversion of the ZB phase to RS MgS occurs only after the ZB phase has relaxed. Theoretical predictions suggest that growth should not produce the relaxed ZB phase and that stable growth on GaP substrates is highly unlikely. The results suggest that epitaxial strain is unlikely to be important in stabilizing the ZB phase and that the growth is truly metastable. Upto 40 nm thick ZB MgS has been grown on GaP substrates without using a smoothing layer.

Thicker capping layers grown on top of the MgS layers have been used to study dislocation density asymmetries. These dislocations exist on two types of slip systems with

their misfit dislocation line segments oriented along either a [110] or a $[1\bar{1}0]$ direction. A difference in the densities of dislocations on these two systems produces an observable azimuthal variation in rocking curve width for symmetric x-ray reflections.

5.9 Future Work

Although the quantitative analysis is approximate, these dislocations density calculations have good relative accuracy. The difference in the dislocation densities calculated from different azimuths may be due to the difference in the mobilities for α and β dislocations in the zinc blende lattice, but further research is necessary to clarify this. TEM can be used to study the higher dislocation density in detail.

Although up to 40nm of ZB MgS has been grown on GaP substrates, no attempts were made to improve the maximum thickness possible using a smoothing layer, which was successful on GaAs substrates. Previously, it has been shown that on a GaAs substrate, by replacing the ZnSe buffer layer with a ZnSe/MgS/ZnSe smoothing layer, the possible ZB MgS thickness can be significantly improved [34]. One possible structure is GaP/ ZnS (a quick low temperature buffer followed by a thin, 20-30 nm buffer layer)/ MgS(10 nm)/ ZnS (20-30 nm)/ MgS (thicker layer).

No attempts were made to grow ZB MgS thicker than 12 nm on InP substrates. A smoothing layer similar to the one mentioned above can be tried for growing thicker layers.

5.10 References

[1] W. A. Jesser. “A theory of pseudomophism in thin films”. *Mater. Sci. Eng.* Vol. 4 (1969), pp. 279–286 (cited on page: 124).

[2] S. Froyen, S. H. Wei and A. Zunger. “Epitaxy-induced structural phase transformations”. *Phys. Rev. B* Vol. 38 (1988), pp. 10124–10127 (cited on pages: 124, 126, 143, 144).

[3] H. H. Farrell, M. C. Tamargo and J. L. de Miguel. “Optimal GaAs(100) substrate terminations for heteroepitaxy”. *Applied Physics Letters* Vol. 58 (1991), pp. 355–357 (cited on page: 125).

[4] M. C. Tamargo, J. L. de Miguel, D. M. Hwang and H. H. Farrell. “Structural characterization of GaAs/ZnSe interfaces”. *Journal of Vacuum Science and Technology B: Microelectronics and Nanometer Structures* Vol. 6 (1988), pp. 784–787 (cited on page: 125).

[5] A. Rajan, R. T. Moug and K. A. Prior. “Control of surface defects in zinc blende MgS grown by MBE”. *Journal of Crystal Growth* Vol. 368 (2013), pp. 62–66 (cited on page: 126).

[6] H. Wenisch, K. Schüll, D. Hommel, G. Landwehr, D. Siche and H. Hartmann. “Molecular beam epitaxial growth and characterization of ZnSe on (001) ZnSe substrates and its application in light-emitting diodes”. *Semiconductor Science and Technology* Vol. 11 (1996), p. 107 (cited on page: 126).

[7] Y. F. Chan, X. F. Duan, S. K. Chan, I. K. Sou, X. X. Zhang and N. Wang. “ZnSe nanowires epitaxially grown on GaP(111) substrates by molecular-beam epitaxy”. *Applied Physics Letters* Vol. 83 (2003), pp. 2665–2667 (cited on page: 126).

[8] C. H. Hsiao, S. J. Chang, S. B. Wang, S. C. Hung, S. P. Chang, T. C. Li, W. J. Lin and B. R. Huang. “MBE growth of ZnSe nanowires on oxidized silicon substrate”. *Superlattices and Microstructures* Vol. 46 (2009), pp. 572–577 (cited on page: 126).

[9] Y. J. Zhao and A. Zunger. “Zinc-blende half-metallic ferromagnets are rarely stabilized by coherent epitaxy”. *Phys. Rev. B* Vol. 71 (2005) (cited on page: 127).

[10] M. S. Miao and W. R. L. Lambrecht. “Effects of biaxial strain on stability and half-metallicity of Cr and Mn pnictides and chalcogenides in the zinc-blende structure”. *Physical Review B* Vol. 72 (2005) (cited on page: 127).

[11] S. A. Telfer, C. Morhain, B. Urbaszek, C. O’Donnell, P. Tomasini, A. Balocchi, K. A. Prior and B. C. Cavenett. “MBE growth of ZnS and ZnCdS layers on GaP”. *Journal of Crystal Growth* Vol. 214–215 (2000), pp. 197–201 (cited on page: 129).

[12] T. Kikawa, I. Ochiai and S. Takatani. “Atomic-hydrogen cleaning of GaAs and InP surfaces studied by photoemission spectroscopy.” *Surface Science* Vol. 316 (1994), 238–246 (cited on page: 129).

[13] S. Ritchie, S. R. Johnson, C. Lavoie, J. A. Mackenzie, T. Tiedje and R. Streater. “Semiconductor substrate cleaning and surface morphology in molecular beam epitaxy”. *Surface Science* Vol. 374 (1997), pp. 418–426 (cited on page: 129).

[14] K. A. Elamrawi, M. A. Hafez and H. E. Elsayed-Ali. “Atomic hydrogen cleaning of InP(100) for preparation of a negative electron affinity photocathode”. *Journal of Applied Physics* Vol. 84 (1998), pp. 4568–4572 (cited on page: 129).

[15] R. K. Gebhardt, A. B. Preobrajenski and T. Chassé. “Core and valence-level photoemission study of the $\mathrm{InP}(001) - (2 \times 1)\mathrm{S}$ surface: Surface structure and electronic states”. *Phys. Rev. B* Vol. 61 (2000), pp. 9997–10000 (cited on page: 129).

[16] V. Chab, L. Pekarek, I. Ulrych, J. Suchy, K. C. Prince, M. Peloi, M. Evans, C. Comicioli, M. Zacchigna and C. Crotti. “Soft X-ray photoemission studies of SInP(100)”. *Surface Science* Vol. 377 - 379 (1997). European Conference on Surface Science, pp. 261–265 (cited on page: 129).

[17] G. W. Anderson, M. C. Hanf, P. R. Norton, Z. H. Lu and M. J. Graham. “Thermal stability of sulfur passivated InP(100)-(1 x 1)”. *Applied Physics Letters* Vol. 65 (1994), pp. 171–173 (cited on page: 129).

[18] T. Chassé, H. Peisert, P. Streubel and R. Szargan. “Sulfurization of InP(001) surfaces studied by X-ray photoelectron and X-ray induced Auger electron spectroscopies (XPS/XAES)”. *Surface Science* Vol. 331 - 333, Part A (1995). Proceedings of the 14th European Conference on Surface Science, pp. 434–440 (cited on page: 129).

[19] J. Massies, F. Turco and J.-P. Contour. “A Chemical Etching Process to Obtain Clean InP {001} Surfaces”. *Japanese Journal of Applied Physics* Vol. 25 (1986), pp. L664–L667 (cited on page: 129).

[20] D. Kikuchi and S. Adachi. “Chemically cleaned InP(100) surfaces in aqueous HF solutions”. *Materials Science and Engineering: B* Vol. 76 (2000), pp. 133–138 (cited on page: 129).

[21] A. Guivarc’h, H. L’Haridon, G. Pelous, G. Hollinger and P. Pertosa. “Chemical cleaning of InP surfaces: Oxide composition and electrical properties”. *Journal of Applied Physics* Vol. 55 (1984), pp. 1139–1148 (cited on page: 129).

[22] H. Yao and K. Itaya. “Atomically resolved scanning tunneling microscopy images of InP(001), (111)A, and (111)B surfaces in sulfuric acid solution”. *Journal of the electrochemical society* Vol. 145 (1998), 3090–3094 (cited on page: 129).

[23] D. T. C. Huo, M. F. Yan, J. D. Wynn and D. P. Wilt. “Chemical etching of (001) InP by HBr-H2O2-H2O-HCl Solution”. *Journal of the electrochemical society* Vol. 136 (1989), 3094–3097 (cited on page: 129).

[24] P. Segar, C. Koval, B. Koel and S. Gebhard. “A comprehensive investigation of HCl and Br2/NH3(aq) etched p-InP interfaces”. *Journal of the electrochemical society* Vol. 137 (1990), 544–552 (cited on pages: 129, 130).

[25] S. Dasneves and M. Depaoli. “A quantitative study of chemical etching of InP”. *Journal of the electrochemical society* Vol. 140 (1993), 2599–2603 (cited on page: 129).

[26] S. Uekusa, K. Oigawa and M. Tacano. “Preferential etching of InP for sub-micron fabrication with HCl/H3PO4 solution”. *Journal of the electrochemical society* Vol. 132 (1985), 671–673 (cited on page: 129).

[27] G. J. Davies, R. Heckingbottom, H. Ohno, C. E. C. Wood and A. R. Calawa. “Arsenic stabilization of InP substrates for growth of Ga[sub x]In[sub 1 - x]As layers by molecular beam epitaxy”. *Applied Physics Letters* Vol. 37 (1980), pp. 290–292 (cited on page: 131).

[28] R. F. C. Farrow. “Growth of indium phosphide films from In and P_2 beams in ultra-high vacuum”. *J. Phys. D: Appl. Phys.* Vol. 7 (1974), p. L121 (cited on page: 132).

[29] H. Bando, H. Yoshino, H. Okamoto and K. Iizuka. “Phosphorous-beam free InP substrate cleaning for MBE”. *Journal of Crystal Growth* Vol. 278 (2005). 13th International Conference on Molecular Beam Epitaxy, pp. 464–467 (cited on page: 132).

[30] Y. Sun, Z. Liu, F. Machuca, P. Pianetta and W. E. Spicer. “Optimized cleaning method for producing device quality InP(100) surfaces”. *Journal of Applied Physics* Vol. 97, 124902 (2005), p. 124902 (cited on page: 133).

[31] Y. Sun, Z. Liu, F. Machuca, P. Pianetta and W. E. Spicer. “Preparation of clean InP(100) surfaces studied by synchrotron radiation photoemission”. *Journal of Vacuum Science and Technology A: Vacuum, Surfaces, and Films* Vol. 21 (2003), pp. 219–225 (cited on page: 133).

[32] Z. Liu, Y. Sun, F. Machuca, P. Pianetta, W. E. Spicer and R. F. W. Pease. “Preparation of clean GaAs(100) studied by synchrotron radiation photoemission”. *Journal of Vacuum Science and Technology A: Vacuum, Surfaces, and Films* Vol. 21 (2003), pp. 212–218 (cited on page: 133).

[33] C. Bradford, C. B. O’Donnell, B. Urbaszek, A. Balocchi, C. Morhain, K. A. Prior and B. C. Cavenett. “Growth of zinc blende MgS/ZnSe single quantum wells by molecular-beam epitaxy using ZnS as a sulphur source”. *Appl. Phys. Lett.* Vol. 76 (2000), pp. 3929–3931 (cited on pages: 134, 135).

[34] C. Bradford, C. B. O’Donnell, B. Urbaszek, C. Morhain, A. Balocchi, K. A. Prior and B. C. Cavenett. “Highly confined excitons in MgS/ZnSe quantum wells grown by molecular beam epitaxy”. *Phys. Rev. B* Vol. 64 (2001), p. 195309 (cited on pages: 134, 135, 138, 146).

[35] Y.-H. Lai, W.-Y. Cheung, S.-K. Lok, G. K. L. Wong, S.-K. Ho, K.-W. Tam and I.-K. Sou. “Rocksalt MgS solar blind ultra-violet detectors”. *AIP Advances* Vol. 2, 012149 (2012), p. 012149 (cited on page: 134).

[36] L. H. Kuo, K. Kimura, S. Miwa, T. Yasuda and T. Yao. “Dependence of generation and structures of stacking faults on growing surface stoichiometries in ZnSe/GaAs”. *Appl. Phys. Lett.* Vol. 69 (1996), pp. 1408–1410 (cited on page: 135).

[37] R. T. Moug, C. Bradford and K. A. Prior. “Surface Reconstructions of Zincblende MgS (100) Observed by Using RHEED”. *J. Korean Phys. Soc.* Vol. 53 (2008), pp. 2996–2999 (cited on page: 136).

[38] C. Bocchi, A. Catellani, F. Germini, L. Nasi, J. K. Morrod, K. A. Prior and G. Calestani. “Metastable zinc-blende MgS structure: Combined experimental and theoretical study”. *Phys. Rev. B* Vol. 79 (2009), p. 235310 (cited on pages: 138, 143, 144).

[39] G. D. U’Ren, M. S. Goorsky, G. Meis-Haugen, K. K. Law, T. J. Miller and K. W. Haberern. “Defect characterization of etch pits in ZnSe based epitaxial layers”. *Applied Physics Letters* Vol. 69 (1996), pp. 1089–1091 (cited on page: 139).

[40] B. Yarlagadda, A. Rodriguez, P. Li, R. Velampati, J. F. Ocampo, E. N. Suarez, P. B. Rago, D. Shah, J. E. Ayers and F. C. Jain. “X-ray characterization of dislocation density asymmetries in heteroepitaxial semiconductors”. *Applied Physics Letters* Vol. 92, 202103 (2008), p. 202103 (cited on pages: 139, 140, 143).

[41] J. E. Ayers. “The measurement of threading dislocation densities in semiconductor crystals by X-ray diffraction”. *Journal of Crystal Growth* Vol. 135 (1994), pp. 71–77 (cited on page: 140).

[42] D. Wolverson, D. M. Bird, C. Bradford, K. A. Prior and B. C. Cavenett. “Lattice dynamics and elastic properties of zinc-blende MgS”. *Physical Review B* Vol. 64 (2001) (cited on page: 143).

[43] E. A. Fitzgerald. “Dislocations in strained-layer epitaxy - Theory, experiment, and applications”. *Materials Science Reports* Vol. 7 (1991), pp. 91–142 (cited on page: 144).

Chapter 6

Epitaxial lift-off of II-VI heterostructures from III-V substrates

6.1 Introduction

The integration of different semiconductor materials on a single substrate has been an important research area for many years. Successful MBE fabrication of these heterostructures requires the growth of semiconductor layers with excellent crystal quality on single crystal substrates. Unfortunately, limitations in this technique are encountered due to lattice mismatch of the different materials used, resulting in the introduction of large dislocation densities, which results in degradation of device quality. The limited availability of the range of substrates is one of the main challenges in semiconductor growth. The lattice parameter of a substrate is the most important factor in determining the suitability for epitaxial growth.

The main limitation in the II-VI semiconductor material development is the need to grow II-VI materials on III-V substrates [1] such as GaAs, GaP, InP, etc as these are readily available, of high quality and cheaper than any II-VI substrates. However, most of these II-VI semiconductors, with the exception of some tellurides, have relatively large band gaps. This means any light emitted by the II-VI epilayers incident on the III-V substrates will be absorbed and transmission measurements of bandgaps are not possible. This is a serious issue at times and it would be very beneficial to be able to remove the epitaxial layer after growth.

Additionally, normally the most expensive item in epitaxial growth is the substrate and Epitaxial Lift-off (ELO) offers possibilities for reusing substrates. In certain technologies, i.e. solar cells, a single crystal substrate is simply too expensive and it is currently seen as a critical issue in increasing device usage. Similarly, the mechanical or thermal properties of a substrate may also inhibit efficient post growth device performance, for example in a device which experiences a large heat load during operation. The thermal conductivity of the substrate may be too low in this case and depositing the epilayers on another suitable substrate would be highly advantageous.

ELO is a technique that introduces flexibility to the fabrication and integration of semiconductor devices. It is a post growth process, first reported in 1978 [2], which enables the active part of a semiconductor heterostructure to be etched from its original substrate and deposited onto a new substrate.

6.1.1 ELO alternatives

The term epitaxial lift-off is widely used in literature to describe the process that etches away a release layer grown into a structure, such as AlAs or here, MgS. However there are other techniques to separate epitaxial layers from their substrates.

Chemically and mechanically etching away the whole substrate is one option. This method has been developed for a number of materials systems, but has disadvantages including, the substrates cannot be re-used and the etching will often damage the epilayers [3–5].

Thermal lift-off is a process where the substrate is chosen to have a very different thermal expansion coefficient with respect to the epilayers. When cooling, the differential contraction induces a large stress field which is released by the initiation and the propagation of a crack parallel to the surface and thus results in delamination [6]. Although this method has an advantage that it does not require any post growth processing, it however require patterning of the substrate before growth to control or assist the delamination process and typically causes damage to the epitaxial layers.

Laser lift-off (LLO) is another successfully developed technique in which the thin epitaxial layers are etched using pulsed-excimer laser processing [7–9]. Here the entire structure is exposed to short, high intensity pulses of laser light that are preferentially absorbed by either the epilayers or substrate resulting a small volume to decompose. This method allows layers to be etched faster, but is likely to induce damage.

6.2 Epitaxial Lift-off (ELO): An overview

ELO has been initially performed with III-V materials by exploiting the huge contrast in the etch rates of GaAs and $Al_xGa_{1-x}As$ in HF [2, 10]. For values of $x \geq 0.5$, the etch rate of the Al-containing alloy is many orders of magnitude faster than that of GaAs and so ELO can be achieved in these materials by growing a thin release layer of AlAs between the substrate and the active layer. After growth, the wafer is etched in HF, which selectively etches through the AlAs but has negligible effect on GaAs, InGaAs and low Al-content AlGaAs alloys.

In addition to the importance of the etch selectivity, another crucial factor is to stress the epitaxial layer thus causing it to bow up slightly maintaining an open channel for the etch to proceed [10]. Although the stress can be applied by several methods, the simplest method is achieved by applying a layer of black Apiezon W wax to the top of the structure, which also helps support it after the etch. The wax, when cooled to room temperature, is under tension and the substrate under compression, so, as the release layer is etched away, the thin film curls up slightly, thus aiding the lift-off process.

The use of a release layer for separating an epilayers from its substrate was first demonstrated by Konagai et al. [2]. They successfully showed the lift-off of a 30 μm thick GaAs layer using a 5 μm thick $Al_{0.7}Ga_{0.3}As$ release layer by exploiting the difference in etch speeds of AlAs and GaAs in HF. A metal layer had been evaporated onto the surface to support the epitaxial layers and then coated with Apiezon W wax to protect it. Epilayer pieces up to a few millimetres wide were found to be etching, but larger pieces did not etch. This was explained by the etchant and reaction products no longer being efficiently exchanged through the narrow etch channel.

Further modifications including the annealing of Apiezon wax to form a domed shape, straining the epilayers underneath have significantly improved the etch rate as well the maximum etchable area [10]. Subsequent works examined the handling and van der Waals bonding of the lifted layers, which helps lifted epilayers to be attached to a new substrate without an adhesive [11, 12].

ELO technology has already been applied successfully to transfer various III-V semiconductor devices from one substrate to another. For instance: GaAs light emitting diodes (LED) [13], GaAs/AlGaAs laser diodes [14, 15], GaAs metal-semiconductor field-effect transistors (MESFETs) [16], strained single quantum well in InGaAs/GaAs high electron mobility transistors (HEMTs) [17], InGaAs/InP p-i-n photodetectors [18], rib waveguides [19] and solar cells [20] have all been transferred on to a variety of foreign substrates including silicon, sapphire and glass.

Subsequently, several attempts have been made to speed up the lift-off process and to make it compatible with industrial scale semiconductor processing so that ELO also becomes a commercially viable technology [21, 22]. Furthermore attempts have been made to develop techniques to strain the epilayers without cracking them to allow larger areas to be lifted. This resulted in the demonstration of many modifications including, weight induced epitaxial lift-off process (WI-ELO) [23] and the use of a flexible plastic carrier to aid the lift-off of a whole $2^{"}$ wafer [24]. These are discussed in detail in Chapter 7.

Special care has to be given while handling lifted epilayers as, using strain to increase the liftable area and etch rate, has however been shown to induce cleavage cracks in some cases [25]. In electrical devices, these cracks could break a circuit, increasing its resistance. Later it has been reported that after ELO, the epilayers have little mechanical strength and as a result strains as low as 0.1% can introduce cracks. A switch from using Apiezon wax to a very thin ($<1\mu$m thick) photo-resist layers for support has proved to be advantageous in producing crack-free films. Such a thin layer can tolerate much smaller stresses, meaning there is less stretching of the lifted-off film [26].

6.3 Epitaxial Lift-off: II-VI materials

Despite the success of ELO method when applied to III-Vs, it initially required both III-V and II-VI MBE when applied to II-VI semiconductors [27], due to the unavailability of a suitable sacrificial material. Although it was possible to grow II-VI layers on a wafer with an AlAs layer to use with the III-V ELO method, this is very inconvenient as it not only increases the thickness of the epilayers which can be lifted off but it also requires both III-V and II-VI growth chambers.

The Heriot-Watt MBE group pioneered II-VI ELO by substituting AlAs with highly reactive MgS as the sacrificial layer. It was discovered that a thin layer of MgS in a ZnSe based heterostructure acts in an analogous way to AlAs in a GaAs based heterostructure. By exploiting the pronounced difference in chemical properties between MgS and ZnSe in 30% HCl solution, successful ELO has been demonstrated. The etch rate of MgS layer has been found to be $\sim 10^8$ times larger than the etch rate of a ZnSe layer [28].

6.3.1 Release layer thickness

From previous experimental work, the minimum MgS release layer thickness necessary for lift-off was found to be $\sim$ 3nm [29]. This minimum thickness arises from the van der Waals interaction between two adjacent unetched layers. This force is very short ranged, typically just a few nanometres, varying with the layer separation cubed. Here, the layer separation is simply the thickness of the MgS release layer.

By considering the van der Waals potentials calculated for GaAs and silicon, the amount of force resulting from the van der Waals interaction can be estimated [30]. These show a force per unit area equivalent to a pressure $>$18 atm when the layers are separated by 2nm, decreasing to $\sim$5 atm. at 3nm. Although the total force acting to separate the epilayers from the substrate is unknown, the wax coating produces an upward pressure of the order of 10s of atmospheres arising from its surface tension ($0.065 \pm 0.003 \mathrm{Nm}^{-1}$). This explains that for any thickness below 3nm, the Van der Waals force will match or overcome the upward force of the wax and thus stop the epilayers from lifting.

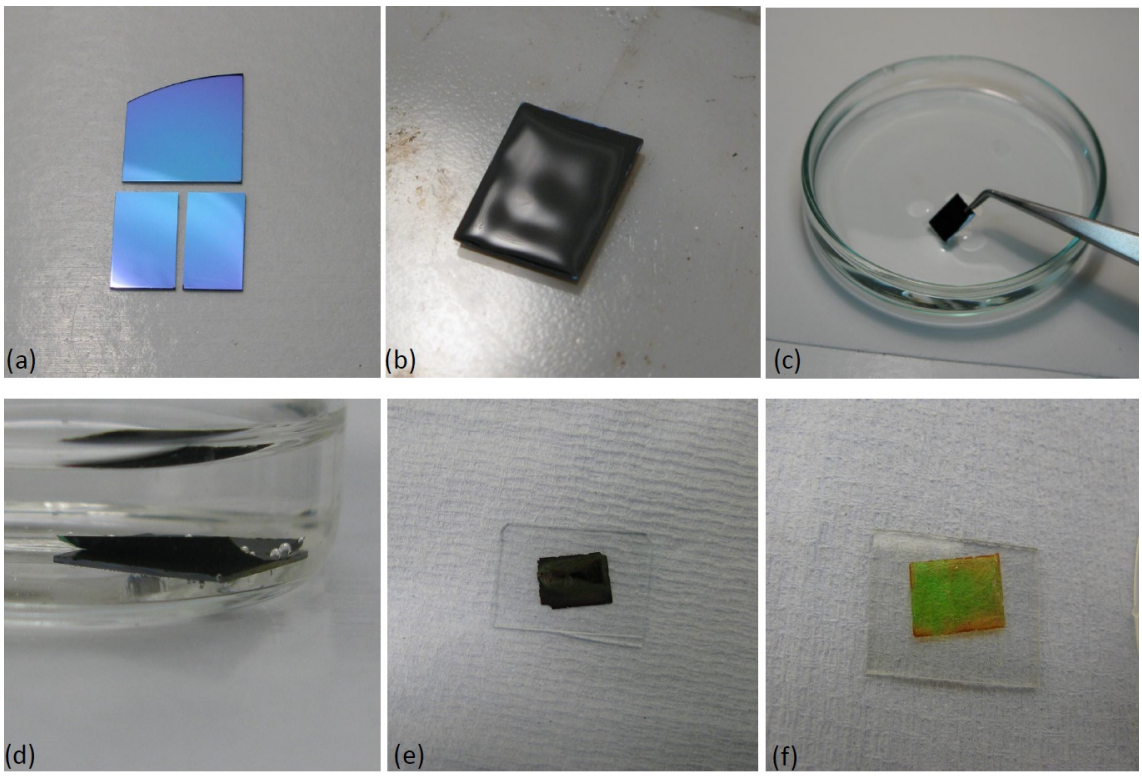

Figure 6.1: *Photographic representation of various stages involved in Apiezon wax based ELO; (a) cleaved sample, (b) wax applied on the surface, (c) immersing in HCl etch solution, (d) ELO in progress, (e) separated epilayer deposited on glass substrate and (f) wax removed from the epilayer using 1-bromopropane.*

6.4 Epitaxial Lift-off: MgS based method

The MgS based II-VI epitaxial lift-off involves several stages, shown pictorially in Figure 6.1.

1. Cleaving: Samples are first cleaved into pieces typically $\sim 3 \times 3\text{mm}^2$ in size from the wafer material, taking considerable care to get perfect cleaves. Further into this project, the size of a cleaved sample has been scaled up to $\sim 10 \times 10\text{mm}^2$ for successful lift-off.

2. Applying wax: The cleaved sample is then heated to $\sim 125^{\text{o}}$C and small pieces of wax placed on the sample surface. At this temperature, the wax melts and forms a smooth dome.

3. Chemical etch: The wax coated sample is placed face up in a solution of 30% HCl at room temperature. The etch rate primarily depends on the thickness of the MgS

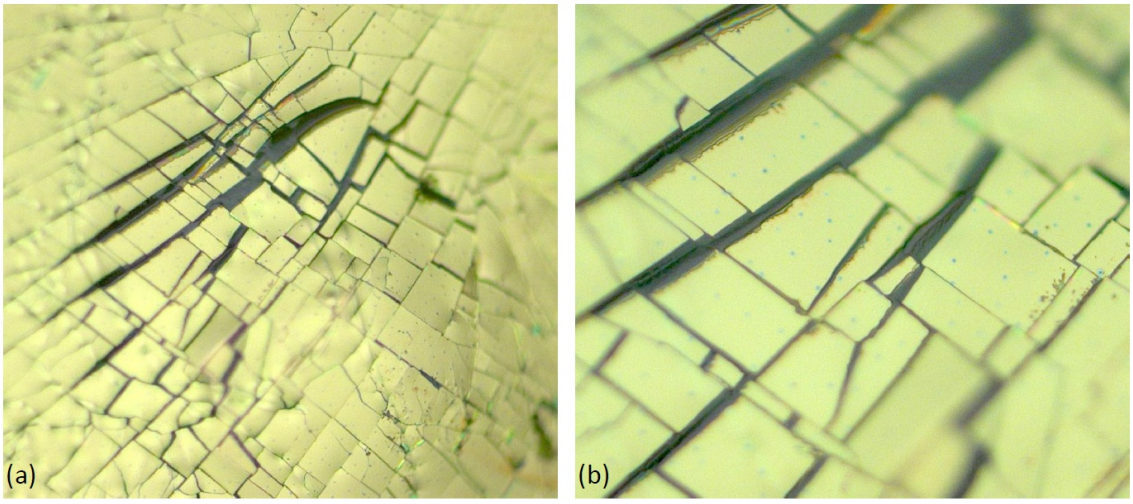

Figure 6.2: *(a) 50× and (b) 200× UVM images showing the crack formations on the surface of a lifted epitaxial layer, resulting from applying excessive pressure during depositing on a glass substrate.*

layer, dimensions of the sample, and in certain cases, the MgS/epilayer interface. Cleave edges accidently coated with wax will prevent etching from that side and ultimately slow down the process. The estimated etch rate of MgS release layer is $\sim 3\text{mm/h}$. After etching the waxed epilayer separates from the substrate and floats to the surface of the solution.

4. Deposition: The lifted epilayer is then carefully removed from the etch solution and rinsed in deionised water prior to depositing on to a new substrate while under water. The sample is then partially dried by removing from the water and applying a small pressure on top. No glue is used in the deposition as the van der Waals force is strong enough to form a bond between the epilayer and new substrate. Typically a pressure of $\sim 500\text{Nm}^{-2}$ is applied on top of the sample to initiate the bonding as well as to drain any water trapped in between the epilayer and substrate. However samples have also been bonded without any force being applied.

5. Wax removal: After overnight drying, the wax is removed by dissolving it in 1-Bromopropane solution. The wax will completely dissolve in less than a minute. The sample is then cleaned in acetone or IPA and water.

While depositing onto a new substrate, considerable care should be given as the epilayer/wax structure is very fragile and easily damaged if handled roughly. This is very important when the pressure is being applied, as too much pressure is found to crack the samples.

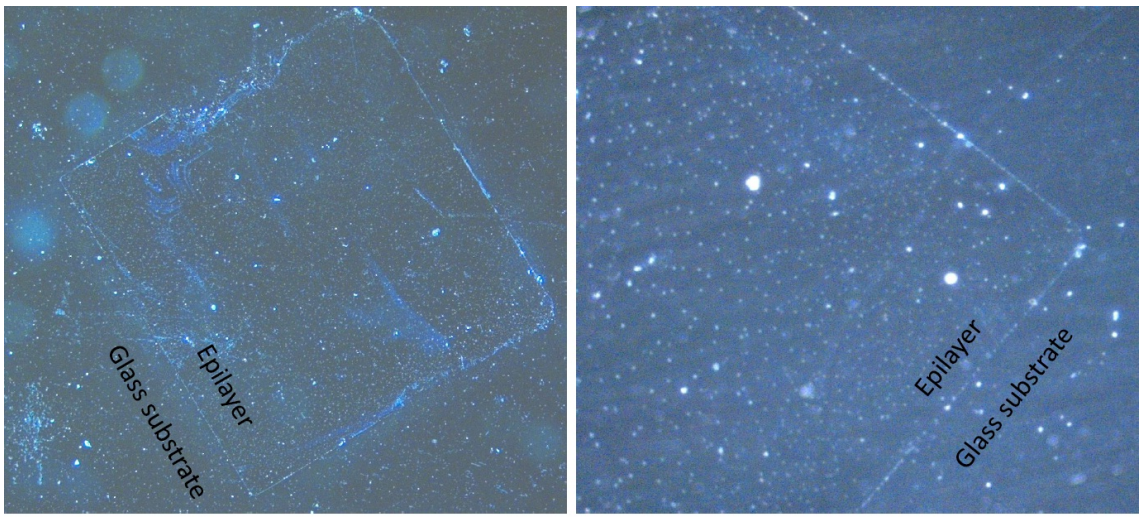

Figure 6.3: *UVM images showing the effect of dust particles present on the glass substrate, on deposited epilayer.*

Figure 6.2 shows cracks formed on a lifted ZnSe epilayer primarily due to the excessive force applied during deposition.

The presence of dust particles in between the epilayer and the new substrate can cause cracks, and also leaves an area of epilayer not bonded to the substrate. Even though the surface of the glass substrates used here are optically flat (surface roughness less than a quarter wavelength at 633 nm), the lifted off layers are not completely crack free. The quality of the samples can be improved by carrying out the ELO in a clean room (HW ELO lab does not have a filtered air supply).

After cleaving larger glass substrates into smaller pieces using a diamond scribe for suitable handling before depositing the lifted layer, microscopic glass particles are often found to be sticking to the substrate surface, even after the deposition stage, which occurs underwater (See Figure 6.3). Carefully rinsing the substrate pieces thoroughly prior to the deposition has been found to completely eliminate any contamination from the surface.

6.4.1 MgS chemical etch mechanism

The etch solution used for all the liftoff detailed in this thesis is 30% ($\sim$12 mol) HCl. MgS reacts with HCl to form Mg^{2+} and Cl^{-} ions along with hydrogen sulphide. The

reaction is given in Equation 6.1.

$$MgS + 2HCl \Rightarrow Mg^{2+} + 2Cl^{-} + 2H_2S \tag{6.1}$$

Both the Mg^{2+} and Cl^{-} ions formed are highly soluble in water up to high concentrations. However H_2S has a limited diffusion rate and could form bubbles if the concentration exceeds its solubility limit. This could in turn effect the etch reaction by blocking the exchange of the reactants and fresh H^{+} ions. Nevertheless this was at this stage thought very unlikely as the amount of H_2S produced is negligible being only $\sim 15 \times 10^{-6}$ moles for a 5 mm^2 MgS layer of 5 nm thick. This point is returned to in Chapter 7.

6.5 Growth of MgS based liftoff structures

The successful growth of heterostructures containing ZB MgS on three different III-V substrates: GaP, GaAs and InP [31] is detailed in Chapter 5. In the following sections, the use of ZB MgS as a sacrificial layer in ELO for II-VI heterostructures deposited on all three substrates is examined in detail. This is the first time that ELO has been successfully performed using the same sacrificial layer over a range of different substrates.

All three substrates were chemically cleaned using the methods detailed in Section 5.4 and were grown by MBE on GaP, GaAs and InP substrates using the procedures given previously in Chapter 5 [31]. A sample with the structure: GaAs/ ZnSe(50nm)/ MgS(7nm)/ ZnSe(300nm) was grown first, as successful ELO has been performed on similar structures earlier [32]. In this structure ZB MgS is lattice matched to both GaAs and ZnSe and this structure was taken as a reference to compare the ELO from other substrates.

On GaP and InP substrates two different sets of samples were grown. In the first set the II-VI layers, apart from the MgS were lattice matched to the III-V substrates. In the second set the epitaxial layers to be lifted were all ZnSe, which is lattice matched to ZB MgS and GaAs but not to the other substrates. The two sets of samples deposited on GaP had structures: GaP/ ZnS(40nm)/ MgS(7nm)/ X, where X is either a ZnS (200nm) or ZnSe (300nm) layer. Similarly, the samples grown on InP had structures InP/

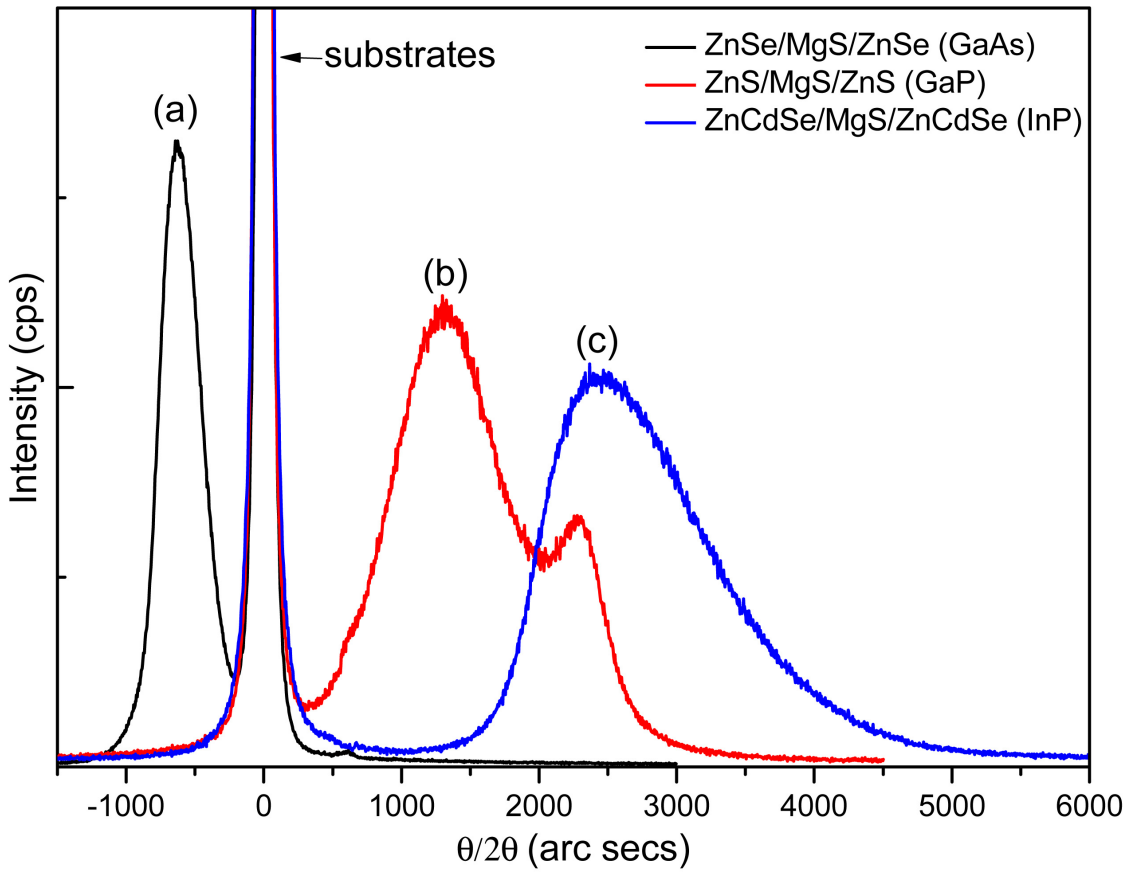

Figure 6.4: *004 XRD rocking curves from (a) ZnSe/MgS/ZnSe, (b) ZnS/MgS/ZnS and (c) ZnCdSe/MgS/ZnCdSe epitaxial layers on GaAs, GaP and InP substrates respectively (substrate peaks are superimposed).*

$Zn_{0.6}Cd_{0.4}Se$(60nm)/ MgS(7nm)/ X, where X is either $Zn_{0.6}Cd_{0.4}Se$ (300nm) or ZnSe (300nm). On these two substrates some relaxation of the MgS layers will occur during growth, meaning that in both the GaP/ZnS/MgS/ZnS and InP/ZnCdSe/MgS/ZnCdSe structures the strain states of the top and bottom layers will not be identical.

6.6 X-Ray Diffraction of structures before ELO

Before ELO, symmetric 004 double crystal XRD rocking curves were obtained from all structures grown and are shown in Figure 6.4 and Figure 6.5 for the first and second sets of samples respectively. In each figure, the positions of all substrate peaks are superimposed and centred at the origin. The curves show peaks from only the thicker buffer and top layers, as the central MgS layer is too thin to show a resolvable peak. In these structures, the strain between the substrate and epitaxial layers results in some relaxation. This is most obvious in the GaP/ZnS/MgS/ZnS structure, where the different strains in top and bottom

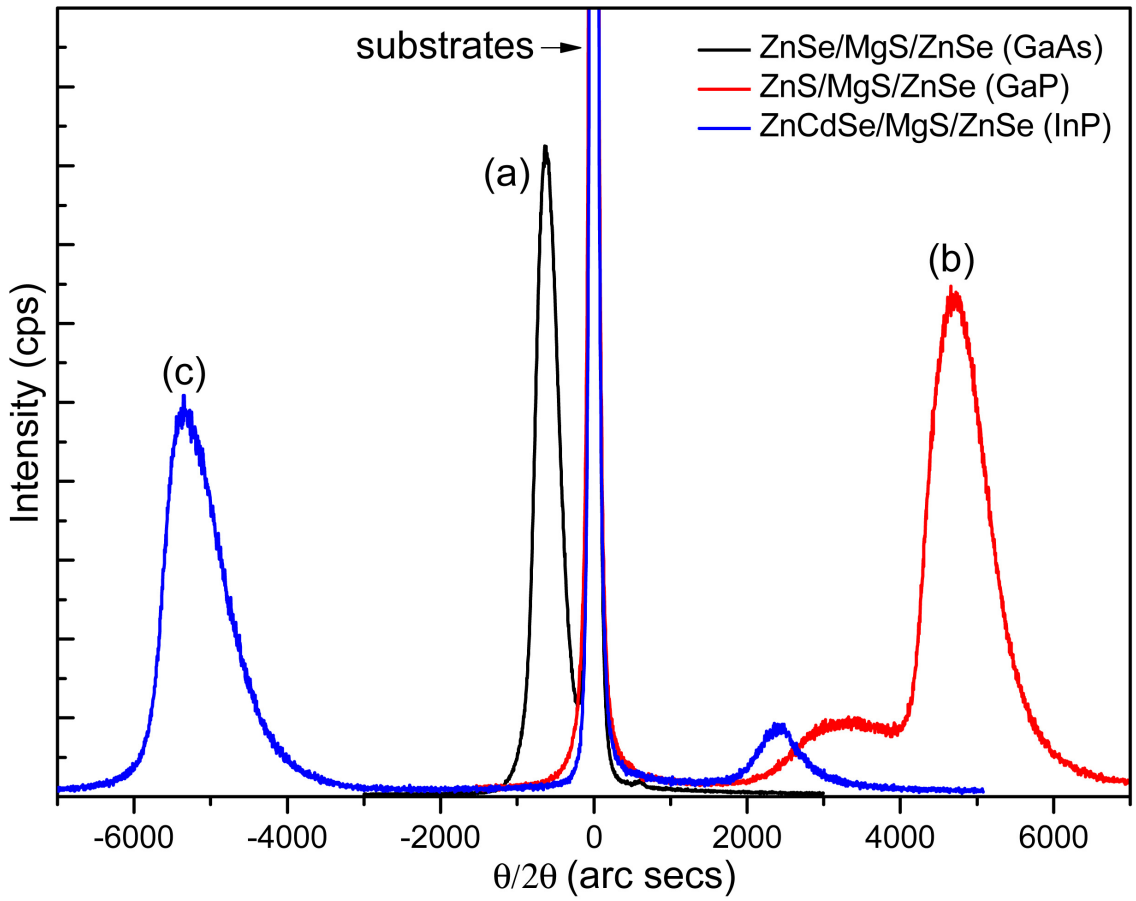

Figure 6.5: *004 XRD rocking curves from (a) ZnSe/MgS/ZnSe, (b) ZnS/MgS/ZnSe and (c) ZnCdSe/MgS/ZnSe epitaxial layers on GaAs, GaP and InP substrates respectively (substrate peaks are superimposed).*

layers produce two clearly resolvable peaks. In the InP/ZnCdSe/MgS/ZnCdSe structure there is only one overall peak but it is asymmetric and resolvable into two Gaussian components.

The peaks attributable to the ZnSe layers in set 2 have been identified and from them the residual strain and layer relaxation are calculated. In these structures the residual strains are small and are comparable in magnitude to the thermal strains introduced on cooling the samples. Removing these thermal expansion induced strains allows the strains and sample relaxation at the growth temperature to be calculated. Although small, the thermal strain is large enough to change the residual strain in the layer grown on GaP from compressive to tensile (Table 6.1).

	GaP	GaAs	InP
a_{sub} (nm)	0.5451	0.5653	0.586
Lattice mismatch to ZnSe	-3.8%	-0.3%	3.4%
X-ray measured values			
Strain at 300K	0.1%	-0.2%	0.1%
Calculated strain at growth temperature	0.0%	-0.2%	0.1%

Table 6.1: *Lattice constants of the three substrates and lattice mismatch of ZnSe layers, together with the minimum plane strain measured by X-ray diffraction at 300K and the calculated strain at the growth temperature.*

6.7 Epitaxial Lift-off on GaP, GaAs and InP substrates based structures

Lift-off was performed on samples, $\sim 4\times4$ mm^2 cleaved from the wafer material, taking considerable care to get perfect cleaves. A detailed explanation on the whole ELO process is given in section 6.4.

Previously, the maximum etch rate of the MgS release layer from a GaAs/ ZnSe/ MgS/ ZnSe sample was found to be about 3 mm/hr [33], which is approximately thirty times faster than the etch rate of AlAs release layers in GaAs based lift-off [10] and typically ZnSe/MgS/ZnSe samples are released from the buffer layer within about 30 min. However samples grown on InP etched much faster, with InP/ ZnCdSe(60nm)/ MgS(7nm)/ ZnCdSe(300nm) sample etching in only 2 mins, while the corresponding sample in the second set with a ZnSe capping layer etched in 4 mins.

In contrast to the GaAs and InP substrates based structures, layers grown on GaP substrates etched very slowly, taking about 24 hours to lift the ZnSe epilayer from GaP/ ZnS/ MgS(7nm)/ ZnSe structure. However, the set 1 samples, with a thick ZnS capping layer did not etch even after 48 hours.

A possible cause of the slow and inconsistent etch rate in structures grown on GaP could be the growth of an etch resistant ZnMgS alloy containing a high mole fraction of zinc [33]. This could be produced by the temperature changes during the growth of the

MgS/ZnS heterostructure, as ZnS was grown at 170^{o}C and MgS at 250^{o}C. Based on the estimation there is potentially a $\sim$ 4-8 ^{o}C temperature error if insufficient time is allowed for the substrate to equilibrate, but during these growths care was taken to ensure stable substrate temperatures by monitoring using both the sample manipulator thermocouple and IR pyrometers. The ZnS compound source which supplies the sulfur introduces a residual zinc incorporation in the MgS layers of $\sim$ 0.5-3% [34] in the normal growth temperature range of 240-270^{o}C, which increases at lower temperatures [35]. However changes introduced by the largest conceivable temperature offset are unlikely to increase the zinc concentration to the critical 20-25% mole fraction which is arguably high enough to prevent etching [33].

Problems with temperature stability during growth are unlikely to be the origin of the low etch rate in the layers grown on GaP, and in addition can not explain the significantly increased etch rate in layers deposited on InP. The model of ELO etching proposed by Yablonovich [10], suggests that the maximum possible etch rate should be limited by the solubility of the gaseous reaction product. A comparison of the solubilities of hydrogen (produced during the etching of AlAs) and hydrogen sulphide (in the present case), gives an estimate of the maximum etch rate for MgS as $\sim$300 times higher than for AlAs layers of comparable thickness [33]. This is approximately the rate observed in the fastest etching structures which are grown on InP.

In II-VI structures grown on GaAs, the etch rate is almost zero for $d < 3$ nm, thought to be due to the strong dispersion forces holding the layers on either side of the MgS together which prevents the free transport of reagents and products, thereby stopping etching [33] (see Section 6.3.1). In the present set of samples all MgS layers had the same nominal thickness, but this will be reduced by any interdiffusion. In the case of ZnSe/MgS structures, previous X-ray interference studies have shown that a limited amount of intermixing does occur, with ZnMgSSe layers a few monolayers thick forming at each interface [34] [36]. The ZnMgSSe phase diagram is known to have a moderate region of imiscibility [37], and the observed degree of intermixing of ZnSe/MgS is in line with this. Significantly, there is no miscibility gap in the ternary ZnMgS system and in this case much larger interdiffusion would be expected leading to a substantially smaller d. Previous observations of MgS/ZnS intermixing in double crystal X-ray spectra from thin ZnS/MgS/ZnS heterostructures were reported [31].

A full calculated phase diagram for CdMgSSe has not been published, but using the same model as used previously for ZnMgSSe [37] it is found that the region of miscibility is drastically reduced to the percent level. Consequently, intermixing will not occur, giving sharp boundaries between layers and a larger d. For the three substrates for the same nominal thickness of MgS, the actual layer thicknesses are $d_{GaP} < d_{GaAs} < d_{InP}$ which gives etch rates in the correct order for $d < 10$ nm.

To confirm this, a new set of samples were grown on GaP with a nominal $d = 15$ nm using identical growth conditions and ELO procedure as before. This time the ZnS/MgS/ZnSe sample was lifted in ~ 1 hour. However the ZnS/MgS/ZnS sample still did not lift even after 24 hours in the etch solution. However, surprisingly the wax layer was found to be separated from the sample and floating. No signs of epitaxial layer was found on the wax layer. This strange behaviour was never observed previously here or reported else where.

Further investigation into the chemical reactions between ZnS and HCl revealed that ZnS dissolves in HCl slowly, releasing H_2S. The chemical reaction is given below (Equation 6.2).

$$\mathrm{ZnS(s)} + 2\mathrm{HCl(aq)} \Rightarrow \mathrm{ZnCl_2(aq)} + 2\mathrm{H_2S(g)} \tag{6.2}$$

This reaction uses HCl and competes with the MgS etching and although slower than the reaction between MgS and HCl, completely etches away the ZnS layer in most cases, eventually separating a plain wax layer. This finding made it necessary to investigate the use of another etch solution (initial attempts using two new etch solutions are detailed in future works section). Although the ZnS lifting has failed, it is important to note that the ZnSe cap layer lifted easily, confirming the idea of enhanced intermixing in ZnS/MgS barrier in the first batch of samples grown with a thinner MgS release layer.

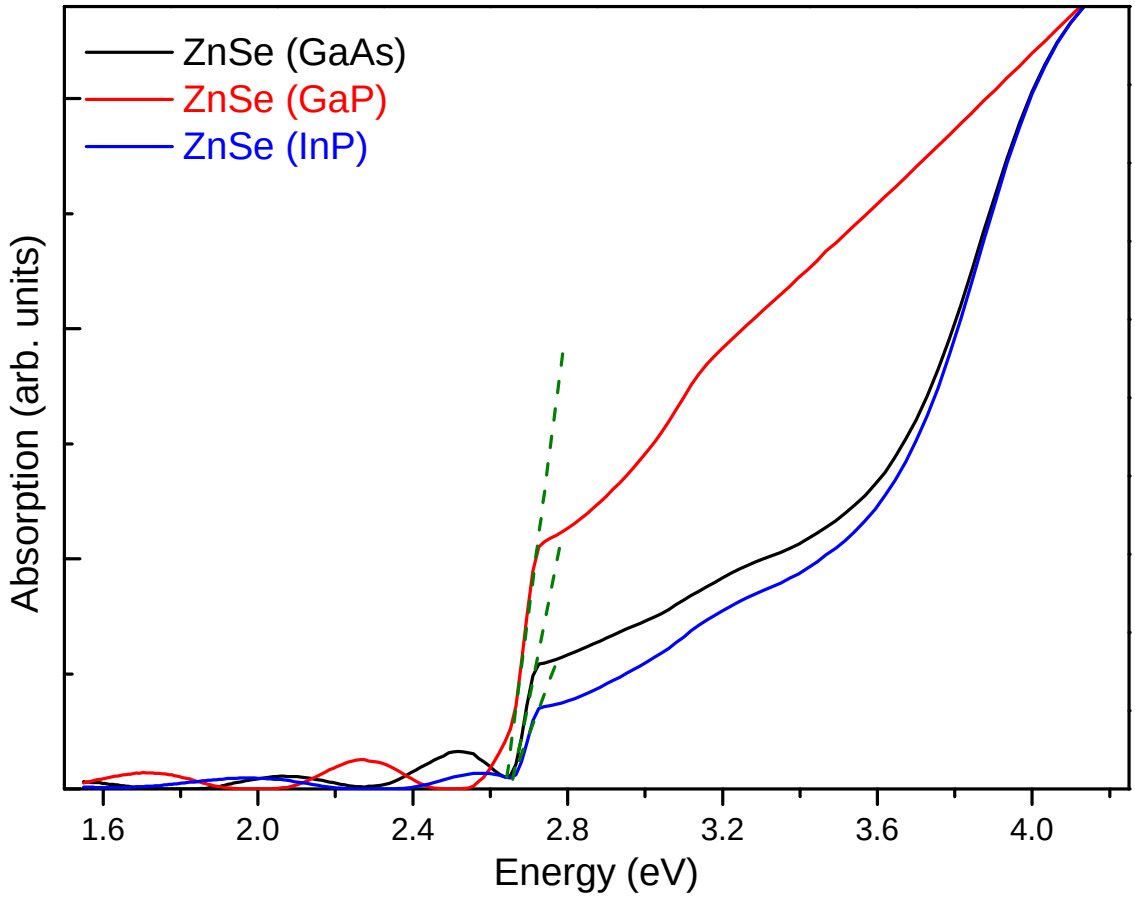

Figure 6.6: *Absorption spectra of ZnSe epitaxial layers lifted-off from GaP (red), GaAs (black) and InP (blue). Band edge is marked by green dotted line.*

6.8 Optical analysis of the structures

After ELO, the released layers were placed on glass substrates and bonded by applying light pressure. Images taken using an optical microscope at 1000× magnification ($280 \times 210 \mu m^2$ area) show that, under ideal lift-off conditions, the surface of the lifted material after deposition on glass is virtually identical to the material prior to the lift-off. Although only 200-300 nm thick, the epitaxial layers were crack-free over square millimeter areas. Any defects are mostly related to the presence of small dust particles at the glass/semiconductor interface, as this work was carried out in a laboratory with an unfiltered air supply.

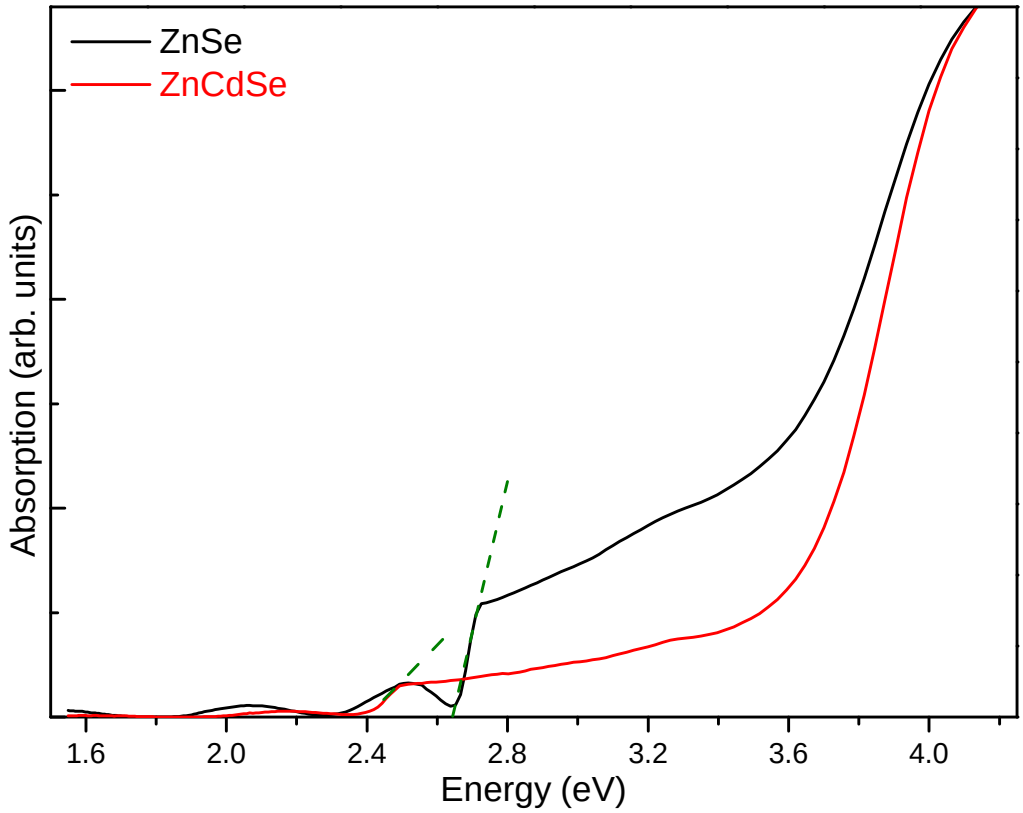

Figure 6.7: *Comparison of absorption spectra of ZnSe and ZnCdSe epitaxial layers after ELO and transfer to glass substrates. Band edge is marked by green dotted line.*

6.8.1 Analysis of absorption spectra

Absorption spectra were obtained using a vertical-VASE ellipsometer system covering the spectral range of 190-1700 nm. Figure 6.6 shows the absorption spectra from the three ZnSe layers after ELO which were grown on GaAs, GaP and InP substrates. These spectra all exhibit a sharp increase in absorption at the band edge, which confirms that the lifted layers have remained crystalline, with well resolved fringes below the bandgap showing that the layers are optically flat. A ZnSe band gap of approximately 2.7 eV is obtained from all the three ZnSe layer spectra.

Similarly Figure 6.7 shows a comparison of absorption spectra from a ZnSe layer lifted from GaAs and a ZnCdSe layer lifted from InP substrate and transferred to glass. Band gaps of 2.4 eV and 2.7 eV were obtained from ZnCdSe and ZnSe epilayers respectively and again the crystalline nature of the films is preserved after ELO.

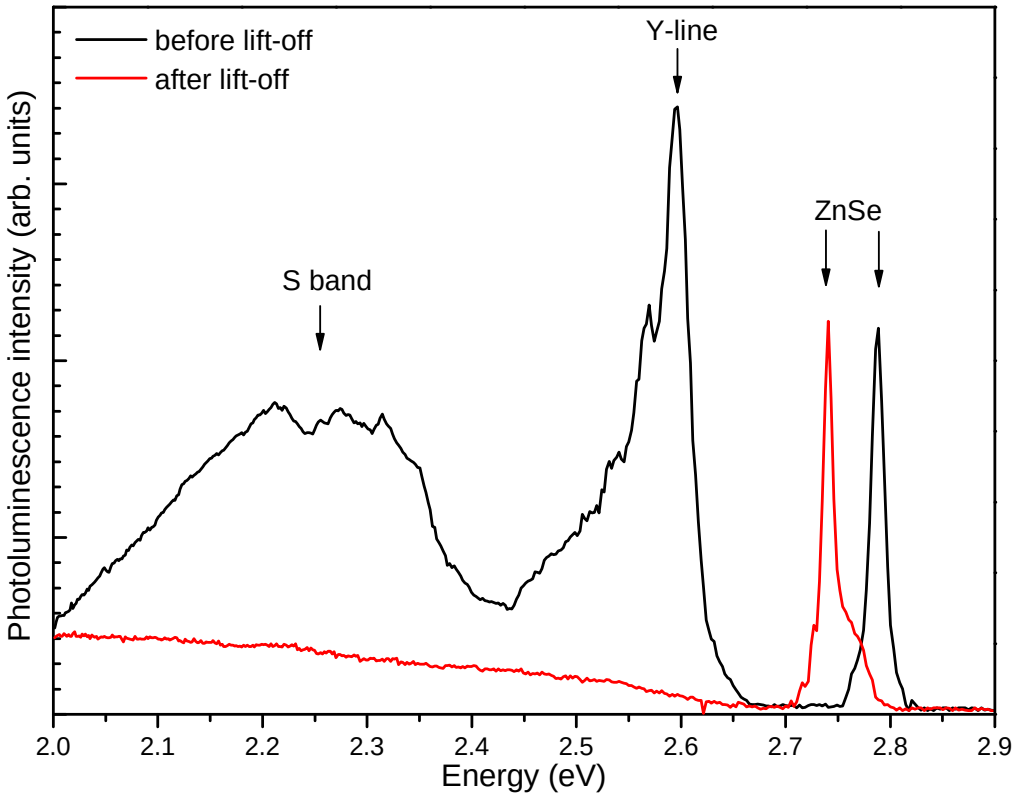

Figure 6.8: *Photoluminescence at 77K from a GaP/ZnS/MgS/ZnSe heterostructure before ELO and from the top ZnSe layer after ELO and deposition on glass. The intensities of the ZnSe peaks have been normalized for comparison.*

6.8.2 Analysis of PL spectra

77K PL Spectra from ZnSe epilayers grown on GaP before ELO and from the ZnSe layer after ELO and transfer to a glass substrate are compared in Figure 6.8. In the ZnS/MgS/ZnSe heterostructure before ELO, only the top ZnSe layer has a bandgap smaller than the irradiating photon energy and the observable features in the spectrum correspond to those previously found in epitaxial ZnSe layers deposited on GaAs substrates. These features include the broad peak around 2.2-2.3 eV, denoted the S band, previously assigned to either impurity or defect related luminescence [38]. There is also the more intense, sharper Y-line at 2.6 eV together with its LO phonon replicas arising from misfit dislocations [39]. The prominent peak observed before ELO at $\sim$ 2.75 eV arises from near band edge emission from the ZnSe epilayers. In the sample shown the Y line is more intense than the near band edge emission, suggesting the structure has a high density of misfit dislocations, as confirmed by almost complete relaxation found by the X-ray double crystal measurements given in Table 6.3.

	GaP	GaAs	InP
PL from epitaxial layer			
ZnSe peak sposition (eV)	2.7879	2.7889	2.7795
FWHM (meV)	15.31	18.56	16.47
Strain (PL) at 77K	$-1.0\text{x}10^{-2}$	$-1.1\text{x}10^{-2}$	$-1.6\text{x}10^{-3}$
Calculated strain at growth temperature	$-1.3\text{x}10^{-3}$	$-1.7\text{x}10^{-3}$	$1.4\text{x}10^{-5}$
+/- strain	$1.6\text{x}10^{-2}$	$1.9\text{x}10^{-2}$	$1.7\text{x}10^{-2}$
PL from lifted layer			
ZnSe peak sposition (eV)	2.7428	2.7496	2.7668
FWHM (meV)	36.19	33.36	22.6
Strain (PL) at 77K	$5.7\text{x}10^{-3}$	$4.6\text{x}10^{-3}$	$1.8\text{x}10^{-3}$
+/- strain	$5.8\text{x}10^{-3}$	$5.4\text{x}10^{-3}$	$3.6\text{x}10^{-3}$

Table 6.2: *Table of PL peak positions, and FWHM for ZnSe layers before and after ELO. Strains are given both at room temperature and at the growth temperature for the layer before ELO. PL transitions are assigned to light holes for tensile (positive) strains and heavy holes for compressive (negative) strains.*

After ELO, the spectrum from the ZnSe layer is very different with a noticeable shift in the energy of the near band edge emission of approximately ~ 50 meV that is clearly visible in Figure 6.8. In this figure the two peaks have been normalised to the same intensity. It is difficult to compare the absolute emission intensities before and after ELO as slight differences in focusing and the different reflectivities of glass and semiconductor substrate change the detected signal. A comparison of the signal strengths from lifted and unlifted layers shows that the excitonic region peaks were weaker in the lifted layer, typically by an order of magnitude but occasionally by only 50%. There are various obvious causes for the reduction in signal strength. One is that unlike the as-grown layer, the lifted layer has two free surfaces at which surface recombination can occur. There are also likely two large depletion regions in the lifted layer. In undoped samples these could easily reach over 50% of the sample volume meaning that the volume of the emitting region is substantially reduced.

It is also noticeable that the other spectral features have almost disappeared from the lifted layer. The Y line arises from the large density of mismatch dislocations in the sample. If the dislocations were not located within the ZnSe layer, but immediately below it, either in the thin MgS or the ZnS layer, then after ELO they would be removed from the

	GaP	GaAs	InP
Relaxation (X-ray, unlifted layer)	99%	30%	98%
Relaxation (PL, unlifted layer)	97%	37%	100%
Relaxation (PL, lifted layer)	115%	273%	95%

Table 6.3: *Relaxations in the ZnSe epitaxial layers determined from the strains and mismatches given in Table 6.1 and 6.2.*

sample. However, both these layers have smaller strain thickness products than the ZnSe and it is more likely that the dislocations are located in the ZnSe layer. An alternative explanation is that the mismatch dislocations are present in the lifted layer but are no longer optically active. In the original structure the lower surface of the ZnSe originally formed a heterojunction with MgS. After ELO it is effectively a free surface complete with a depletion region where any optical signature from the mismatch dislocations would be significantly reduced.

The resolution of the PL system is such that an exact assignment for the peaks can not be given. However the samples are doped and in the Heriot-Watt system these are dominated by free carrier transitions rather than donor bound transitions. Nevertheless, the overall peak envelope could contain contributions from more than one peak. It is noticeable that the individual peaks occur at different energies in different layers and that these peaks shift after ELO. As the relative contribution of free carrier and donor bound peaks within the low resolution peak envelope is not changed, any shift must be due to a change in strain. If there are more than one peak present they will all shift together with lattice change in relative position.

The positions of the main PL peaks for the ZnSe layers both before and after ELO are given in Table 6.2 together with their FWHM. All the PL peaks are very broad, with FWHM between 15-18 meV for the as grown samples, increasing to 22-35 meV after ELO. Table 6.2 gives the strain distributions for samples before and after ELO which were calculated assuming tetragonal strain within the layer. In the case of samples before ELO the strain can be recalculated to allow for the strain introduced on cooling to 77K by the difference in thermal expansion coefficients of ZnSe and the III-V substrates. The PL strains given in Table 6.2 are in reasonable agreement with the strains determined from X-ray diffraction given in Table 6.1. This can be seen by comparing the relaxations in the

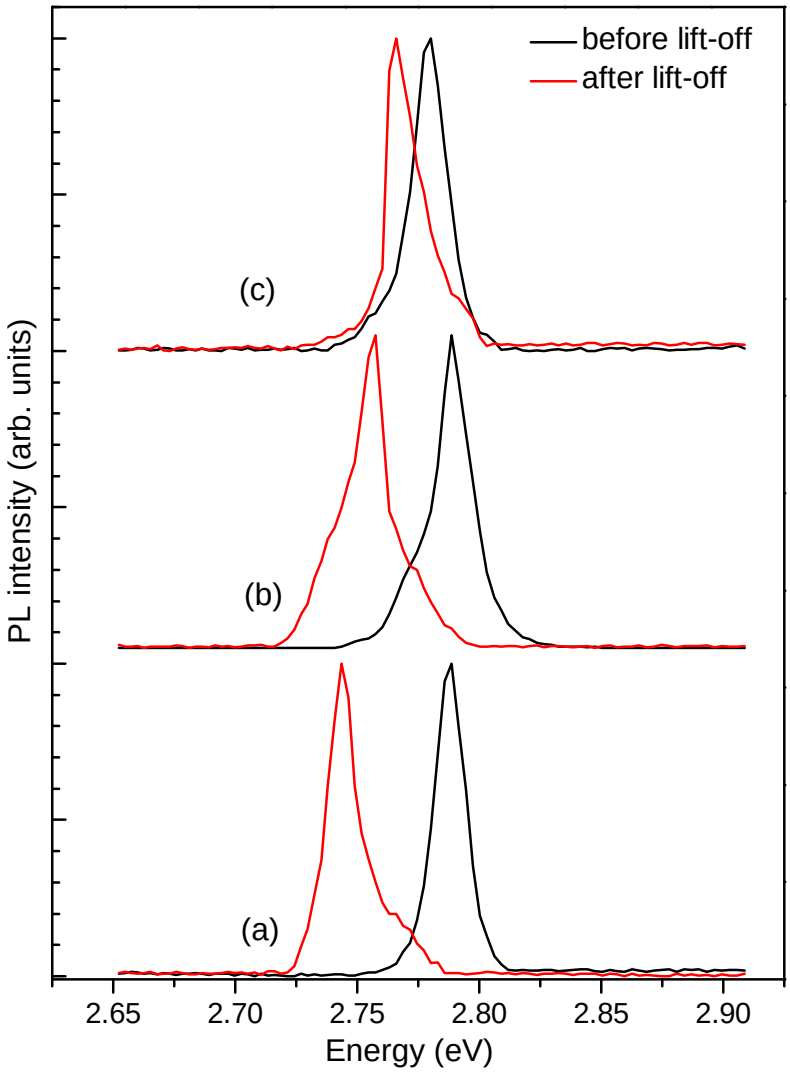

Figure 6.9: *Photoluminescence at 77K from ZnSe epitaxial layers grown on (a) GaP, (b) GaAs and (c) InP substrates, both before (black) and after ELO and transferring to a glass substrate (red). The spectra were normalized in intensity for comparison.*

layers determined from the strains measured by X-ray diffraction and PL which are given in Table 6.3.

After ELO, in addition to being significantly broadened, the peaks from all layers are shifted to lower emission energies (see Figure 6.9 and Figure 6.10). The shift arises from small tensile strains in the lifted layers. The change in strain state from compressive to tensile is accompanied by a change in the lowest energy transition from e-hh (compressive strain) to e-lh (tensile strain). The rate of change of PL emission energy as a function of strain is very different for these two transitions, and is much larger for tensile strain. Thus the observed increase in FWHM of the PL peaks after ELO is not associated with a significant change in the strain distribution.

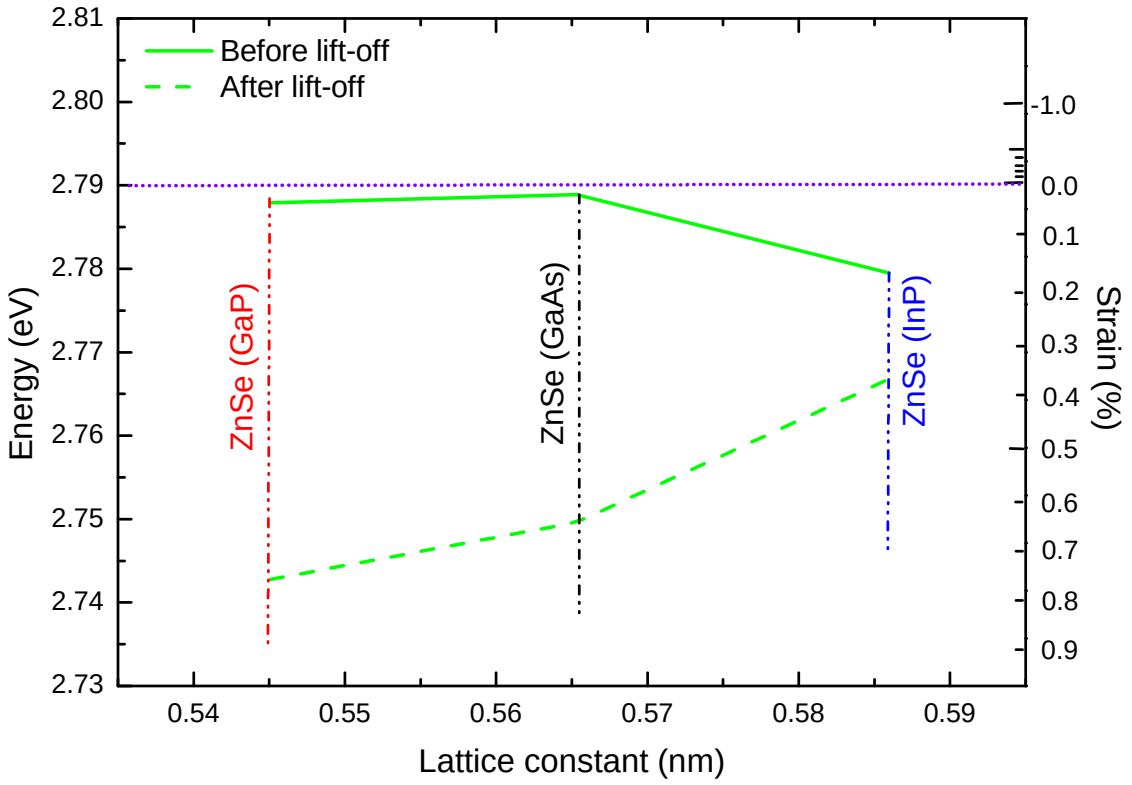

Figure 6.10: *Schematic showing the shift of epilayer peak emission energy before (green solid) and after (green dotted) the lift-off, obtained from photoluminescence at 77K from ZnSe epitaxial layers grown on GaP, GaAs and InP substrates. The violet dotted line separates compressive (above the line) and tensile (below the line) strain areas.*

One possible origin of the tensile strain might be the difference in thermal expansion coefficients of ZnSe and glass substrates used. However previous work on ZnMgSSe/ZnSe ELO structures which were also transferred to glass did not observe a PL peak shift which could be attributed to the glass [40] which was thought due to the weak adhesion between the semiconductor and the new substrate. It is also significant that the PL peak positions, and hence average strains are different in samples grown on different substrates. This means that after ELO the three ZnSe layers which are of identical thickness and were grown under identical conditions have different strain states.

The ZnSe samples are clearly not identical, and the differences arise from the types of dislocation they contain and their distribution within the samples. It should be emphasized that these layer thicknesses were chosen to optimize the X-ray signal strength and the relaxation observed is an inevitable consequence of that choice. The samples grown on GaAs are only partially relaxed, and the dislocation distribution in the ZnSe epilayers is higher at the ZnSe/GaAs interface [41] [42]. This means that before ELO the upper part of the ZnSe layer is still compressively strained. After removing the substrate, the layer

lowers its total strain energy by reducing the compressive strain in the top of the layer while placing the lower part of the layer in tension. This balancing of the strain states in unrelaxed multilayers with much smaller compressive and tensile strains has previously been seen in ELO samples grown on GaAs substrates [40]. For the samples used in the present study the average residual strain in the ZnSe layer after ELO is now tensile. This is shown by the calculated sample relaxations given in Table 6.3 being greater than 100%.

In contrast, the samples grown on GaP and InP substrates relaxed almost completely during growth, but from initial compressive and tensile strain states respectively. There will, however, still be small residual strains due to work hardening. As the relaxation mechanisms for tensile and compressive strains in III-V semiconductors utilise different dislocation types [43] [44], after relaxation the samples presumably contain completely different populations of dislocations and residual strain states. In all three cases it should be noted that the average strain is small and the range of strains is large enough that the unstrained state occurs within the distribution.

6.9 Summary

The use of thin ZB MgS epilayers as an effective sacrificial layer for epitaxial lift-off for layers deposited on GaP, GaAs and InP is studied and successfully demonstrated. Different II-VI semiconductors either lattice matched to the substrates or the ZB MgS were successfully lifted-off all three substrates. For layers deposited on GaAs and InP substrates ELO can be performed in a few hours with high yield on large areas of material using ZB MgS layers only 7 nm thick. In the case of GaP substrates a fast reproducible process is obtained by increasing the MgS layer thickness to 15 nm. However the attempts to lift-off ZnS layers have failed as it dissolves in HCl, the etch solution used here.

The lifted epilayers have been structurally and optically characterized and no damage has been introduced to the lifted layer by the ELO process. Changes in the PL peak positions are observed which are due to small changes in the strain state of the samples after ELO.

6.10 Future Work

Although ELO has been successfully demonstrated on three different substrates, the inability to lift-off ZnS epilayers shows the need to develop an alternate etch solution. During the final stages of this work, attempts were made to test two different etch solutions, citric acid ($C_6H_8O_7$) and NaOH. A test sample with the structure, GaAs/MgS/ZnSe was successfully lifted off on both the above mentioned etches and this further shows that any weak acid or alkali can be used for etching away the MgS release layer. 99% and 40% of aqueous citric acid solutions have proved equally effective in this case. However, due to time constraints none of these etches were attempted on ZnS containing structures.

High resolution PL is necessary for a detailed study of the lifted epilayers mentioned here as the present PL setup at Heriot-Watt is not adequate. The samples used in this study were designed to be thick enough that good signals could be clearly distinguished in XRD. However this meant that the layers were either partially or nearly completely relaxed, as indicated in Table 6.3, and the measurements were made with a low resolution system with an estimated peak FWHM of 6meV. Growing quantum well structures between ZnMgSSe barriers will provide more information about the lifted layers as in this case the quaternary alloy is resistant to the etch solution.

6.11 References

[1] H. H. Farrell, M. C. Tamargo and J. L. de Miguel. “Optimal GaAs(100) substrate terminations for heteroepitaxy”. *Applied Physics Letters* Vol. 58 (1991), pp. 355–357 (cited on page: 152).

[2] M. Konagai, M. Sugimoto and K. Takahashi. “High efficiency GaAs thin film solar cells by peeled film technology”. *Journal of Crystal Growth* Vol. 45 (1978), pp. 277–280 (cited on pages: 153, 154).

[3] L.-M. Liu, G. Lindauer, W. B. Alexander and P. H. Holloway. “Surface preparation of ZnSe by chemical methods”. *Journal of Vacuum Science and Technology B: Microelectronics and Nanometer Structures* Vol. 13 (1995), pp. 2238–2244 (cited on page: 153).

[4] M. Rei Vilar, J. El Beghdadi, F. Debontridder, R. Artzi, R. Naaman, A. M. Ferraria and A. M. Botelho do Rego. “Characterization of wet-etched GaAs (100) surfaces”. *Surface and Interface Analysis* Vol. 37 (2005), pp. 673–682 (cited on page: 153).

[5] S. Pinel, J. Tasselli, J. P. Bailbé, A. Marty, P. Puech and D. Estève. “Mechanical lapping, handling and transfer of ultra-thin wafers”. *Journal of Micromechanics and Microengineering* Vol. 8 (1998), p. 338 (cited on page: 153).

[6] F. Dross, J. Robbelein, B. Vandevelde, E. Van Kerschaver, I. Gordon, G. Beaucarne and J. Poortmans. “Stress-induced large-area lift-off of crystalline Si films”. *Applied Physics A* Vol. 89 (2007), pp. 149–152 (cited on page: 153).

[7] W. S. Wong, T. Sands, N. W. Cheung, M. Kneissl, D. P. Bour, P. Mei, L. T. Romano and N. M. Johnson. “Fabrication of thin-film InGaN light-emitting diode membranes by laser lift-off”. *Applied Physics Letters* Vol. 75 (1999), pp. 1360–1362 (cited on page: 154).

[8] M. K. Kelly, O. Ambacher, R. Dimitrov, R. Handschuh and M. Stutzmann. “Optical Process for Liftoff of Group III-Nitride Films”. *physica status solidi (a)* Vol. 159 (1997), R3–R4 (cited on page: 154).

[9] W. S. Wong, T. Sands and N. W. Cheung. “Damage-free separation of GaN thin films from sapphire substrates”. *Applied Physics Letters* Vol. 72 (1998), pp. 599–601 (cited on page: 154).

[10] E. Yablonovitch, T. Gmitter, J. P. Harbison and R. Bhat. “Extreme selectivity in the lift-off of epitaxial GaAs films”. *Applied Physics Letters* Vol. 51 (1987), pp. 2222–2224 (cited on pages: 154, 155, 163, 164).

[11] E. Yablonovitch, D. M. Hwang, T. J. Gmitter, L. T. Florez and J. P. Harbison. “Van der Waals bonding of GaAs epitaxial liftoff films onto arbitrary substrates”. *Applied Physics Letters* Vol. 56 (1990), pp. 2419–2421 (cited on page: 155).

[12] E. Yablonovitch, T. Sands, D. M. Hwang, I. Schnitzer, T. J. Gmitter, S. K. Shastry, D. S. Hill and J. C. C. Fan. “Van der Waals bonding of GaAs on Pd leads to a permanent, solid-phase-topotaxial, metallurgical bond”. *Applied Physics Letters* Vol. 59 (1991), pp. 3159–3161 (cited on page: 155).

[13] I. Pollentier, P. Demeester, A. Ackaert, L. Buydens, P. Van Daele and R. Baets. “Epitaxial lift-off GaAs LEDs to Si for fabrication of opto-electronic integrated circuits”. *Electronics Letters* Vol. 26 (1990), pp. 193–194 (cited on page: 155).

[14] E. Yablonovitch, E. Kapon, T. J. Gmitter, C. P. Yun and R. Bhat. “Double heterostructure GaAs/AlGaAs thin film diode lasers on glass substrates”. *Photonics Technology Letters, IEEE* Vol. 1 (1989), pp. 41–42 (cited on page: 155).

[15] I. Pollentier, P. Demeester, A. Ackaert, L. Buydens, P. Vandaele and R. Baets. “Epitaxial Lift-off GaAs LEDs to Si for fabrication of opto-electronic integrated-circuits”. *Electronic Letters* Vol. 26 (1990), 193–194 (cited on page: 155).

[16] C. van Hoof, W. de Raedt, M. van Rossum and G. Borghs. “MESFET lift-off from GaAs substrate to glass host”. *Electronics Letters* Vol. 25 (1989), pp. 136–137 (cited on page: 155).

[17] J. F. Klem, E. D. Jones, D. R. Myers and J. A. Lott. “Characterization of thin AlGaAs/InGaAs/GaAs quantum-well structures bonded directly to SiO_2/Si and glass substrates”. *Journal of Applied Physics* Vol. 66 (1989), pp. 459–462 (cited on page: 155).

[18] H. Schumacher, T. J. Gmitter, H. P. LeBlanc, R. Bhat, E. Yablonovitch and M. A. Koza. “High-speed InP/InGaAs photodiode on sapphire substrate prepared by epitaxial lift-off”. *Electron Devices, IEEE Transactions on* Vol. 36 (1989), p. 2625 (cited on page: 155).

[19] A. Yiyan, W. K. Chan, T. S. Ravi, T. J. Gmitter, R. Bhat and K. H. Yoo. “Grafted InGaAsP Light Emitting Diodes on glass channel wave-guides”. *Electronic Letters* Vol. 28 (1992), 341–342 (cited on page: 155).

[20] K. J. Weber, A. W. Blakers and K. R. Catchpole. “The Epilift technique for Si solar cells”. *Applied Physics A* Vol. 69 (1999), pp. 195–199 (cited on page: 155).

[21] J. J. Schermer, G. J. Bauhuis, P. Mulder, W. J. Meulemeesters, E. Haverkamp, M. M. A. J. Voncken and P. K. Larsen. “High rate epitaxial lift-off of InGaP films from GaAs substrates”. *Applied Physics Letters* Vol. 76 (2000), pp. 2131–2133 (cited on page: 155).

[22] P. Demeester, I. Pollentieer, P. Dedobbelaere, C. Brys and P. Vandaele. “Epitaxial Lift-off and its applications”. *Semiconductor Science and Technology* Vol. 8 (1993), 1124–1135 (cited on page: 155).

[23] M. M. A. Voncken, J. J. Schermer, G. Maduro, G. J. Bauhuis, P. Mulder and P. K. Larsen. “Influence of radius of curvature on the lateral etch rate of the weight induced epitaxial lift-off process”. *Materials Science and Engineering: B* Vol. 95 (2002), pp. 242–248 (cited on page: 155).

[24] J. J. Schermer, P. Mulder, G. J. Bauhuis, M. M. A. J. Voncken, J. van Deelen, E. Haverkamp and P. K. Larsen. “Epitaxial Lift-Off for large area thin film III/V devices”. *physica status solidi (a)* Vol. 202 (2005), pp. 501–508 (cited on page: 155).

[25] W. Chang, C. P. Kao, G. A. Pike, J. A. Slone and E. Yablonovitch. “Vapor phase epitaxial liftoff of GaAs and silicon single crystal films”. *Solar Energy Materials and Solar Cells* Vol. 58 (1999), pp. 141–146 (cited on page: 155).

[26] E. Yablonovitch. *Ultra-efficient Epitaxial Liftoff Solar Cells Exploiting Optical Confinement in the Wave Limit: 19 July 1994 - 18 July 1998*. National Renewable Energy Laboratory, 1999 (cited on page: 155).

[27] C. Brys, F. Vermaerke, P. Demeester, P. V. Daele, K. Rakennus, A. Salokatve, P. Uusimaa, M. Pessa, A. L. Bradley, J. P. Doran, J. O’Gorman and J. Hegarty. “Epitaxial lift-off of ZnSe based II–VI structures”. *Applied Physics Letters* Vol. 66 (1995), pp. 1086–1088 (cited on page: 156).

[28] A. Balocchi, A. Curran, T. C. M. Graham, C. Bradford, K. A. Prior and R. J. Warburton. “Epitaxial liftoff of ZnSe-based heterostructures using a II-VI release layer”. *Appl. Phys. Lett.* Vol. 86 (2005) (cited on page: 156).

[29] A. Curran, S. Brown, R. J. Warburton and K. A. Prior. “Determination of the etching mechanism in MgS and ZnMgSSe epitaxial lift-off layers”. *physica status solidi (b)* Vol. 247 (2010), pp. 1399–1401 (cited on page: 156).

[30] A. Gusso and G. J. Delben. “Dispersion force for materials relevant for micro- and nanodevices fabrication”. *Journal of Physics D: Applied Physics* Vol. 41 (2008), p. 175405 (cited on page: 156).

[31] A. Rajan, R. T. Moug and K. A. Prior. “Growth and stability of zinc blende MgS on GaAs, GaP, and InP substrates”. *Applied Physics Letters* Vol. 102, 032102 (2013), p. 032102 (cited on pages: 160, 164).

[32] A. Balocchi, A. Curran, T. C. M. Graham, C. Bradford, K. A. Prior and R. J. Warburton. “Epitaxial liftoff of ZnSe-based heterostructures using a II-VI release layer”. *Applied Physics Letters* Vol. 86, 011915 (2005), p. 011915 (cited on page: 160).

[33] A. Curran, S. Brown, R. J. Warburton and K. A. Prior. “Determination of the etching mechanism in MgS and ZnMgSSe epitaxial lift-off layers”. *Physica Status Solidi B* Vol. 247 (2010), pp. 1399–1401 (cited on pages: 163, 164).

[34] C. Bradford, C. B. O’Donnell, B. Urbaszek, A. Balocchi, C. Morhain, K. A. Prior and B. C. Cavenett. “Growth of zinc blende MgS/ZnSe single quantum wells by molecular-beam epitaxy using ZnS as a sulphur source”. *Appl. Phys. Lett.* Vol. 76 (2000), pp. 3929–3931 (cited on page: 164).

[35] C. Bradford, R. T. Moug, A. Curran, D. Thuau, R. J. Warburton and K. A. Prior. “Growth and Characterization of ZnMgS and ZnMgS/ZnSe Quantum Wells grown on GaAs (100) by Using MBE”. *Journal of the Korean Physical Society* Vol. 53 (2008), pp. 3000–3003 (cited on page: 164).

[36] K. A. Prior, X. Tang, C. O’Donnell, C. Bradford, L. David and B. C. Cavenett. “Characterization of MBE grown II-VI semiconductor thin layers by X-ray interference”. *J. Crystal Growth* Vol. 251 (2003), pp. 565–570 (cited on page: 164).

[37] V. S. Sorokin, S. V. Sorokin, V. A. Kaygorodov and S. V. Ivanov. “Instability and immiscibility regions in $Mg_xZn_{1-x}S_ySe_{1-y}$ alloys”. *Journal of Crystal Growth* Vol. 214 (2000), pp. 130–134 (cited on pages: 164, 165).

[38] J. Gutowski, N. Presser and G. Kudlek. *Phys. Status Solidi A* Vol. 120 (1990), p. 11 (cited on page: 168).

[39] S. Myhajlenko, J. L. Batstone, H. J. Hutchinson and J. W. Steeds. “Luminescence studies of individual dislocations in II-VI (ZnSe) and III-V (InP) semiconductors”. *Journal of Physics C: Solid State Physics* Vol. 17 (1984), p. 6477 (cited on page: 168).

[40] R. Moug, C. Bradford, A. Curran, F. Izdebski, I. Davidson, K. A. Prior and R. J. Warburton. “Development of an epitaxial lift-off technology for II-VI nanostructures using ZnMgSSe alloys”. *Microelectronics Journal* Vol. 40 (2009), pp. 530–532 (cited on pages: 172, 173).

[41] J. E. Ayers. “New model for the thickness and mismatch dependencies of threading dislocation densities in mismatched heteroepitaxial layers”. *J. Appl. Phys.* Vol. 78 (1995), pp. 3724–3726 (cited on page: 172).

[42] S. Kalisetty, M. Gokhale, K. Bao, J. E. Ayers and F. C. Jain. “The influence of impurities on the dislocation behavior in heteroepitaxial ZnSe on GaAs”. *Appl. Phys. Lett.* Vol. 68 (1996), pp. 1693–1695 (cited on page: 172).

[43] P. M. J. Maree, J. C. Barbour, J. F. van der Veen, K. L. Kavanagh, C. W. T. Bulle-Lieuwma and M. P. A. Viegers. “Generation of misfit dislocations in semiconductors”. *J. Appl. Phys.* Vol. 62 (1987), pp. 4413–4420 (cited on page: 173).

[44] G. Salviati, C. Ferrari, L. Lazzarini, L. Nasi, A. V. Drigo, M. Berti, D. D. Salvador, M. Natali and M. Mazzer. “Structural characterization of InGaAs/InP heterostructures grown under compressive and tensile stress”. *Appl. Surface Sci.* Vol. 188 (2002), pp. 36–48 (cited on page: 173).

Chapter 7

Epitaxial Lift-off and Surface passivation; A new perspective

7.1 Introduction

In this chapter, two of the important processing techniques in II-VI MBE growth, namely Epitaxial Lift-off (ELO) and sample passivation are examined and modifications to the procedures currently used are explained in order to eliminate the various limitations associated with the existing methods.

Although ELO has been well demonstrated as a successful technique, the existing technology has several limitations. A simple and effective modification to the existing ELO process is detailed in this chapter. A new method for passivating sample surfaces over very long period under atmospheric exposure is explained in the next section.

7.2 Limitations of existing II-VI ELO technique

A detailed description on the existing ELO technology is given in Chapter 6. Although ELO is a widely used method for separating epilayers from substrates, it has several disadvantages which seriously compromise the quality of both the lifted layer and substrate.

7.2.1 Application of wax cap

The existing ELO technique involves applying a layer of Apiezon wax to the sample surface. This wax layer provides mechanical support to the epilayer once it is lifted from the substrate. The slightly dome shaped wax layer also provides sufficient tensile stress to cause the epitaxial layer to curl during lift off and thus helps clear the etch channel in the sacrificial layer and so increases the etch rate. However, applying the wax layer on sample surface has some disadvantages.

Special care has to be taken while applying wax on the sample surface. Samples are normally cleaved into rectangular pieces and wax after melting form a circular shape due to its surface tension. This requires spreading the wax evenly on the sample surface. A non-uniform layer of wax generates regions of high and low stress in the epilayer, which results in an increase in the density of cracks formed.

If cleaved pieces of an ELO sample are added to the etch solution, they are etched irrespective of the presence of a wax supportive layer. However in the case of an unwaxed sample, the epilayer breaks up into minute fragments instead of remaining as a single layer because of the absence of a support structure. While applying the wax layer, it is possible to introduce micrometer square areas with no wax cover. These areas when exposed to etch solution detach from the epilayer, leaving holes. It is suggested that this can relieve the stress.

Another disadvantage is that if some of the molten wax extends down onto the side face and covers the MgS, then it prevents the etch solution from accessing the sacrificial layer on that side. This is a serious issue as at times this can prevent the etching altogether. Even if the etch solution manages to completely dissolve the sacrificial layer from other sides, this wax deposition on the side could act as a bond between the epitaxial layer and the substrate, thus effectively preventing the separation of the layers.

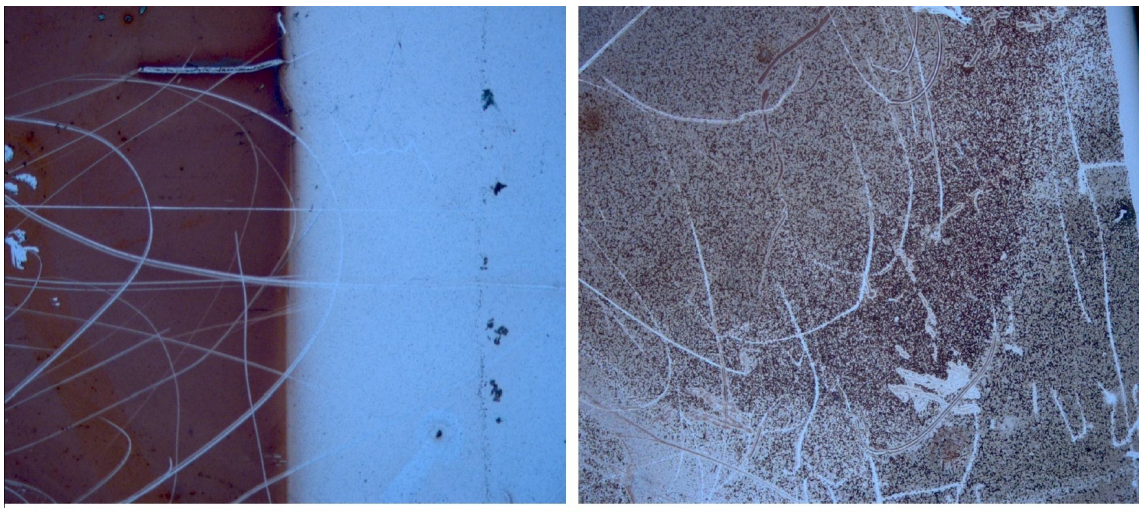

Figure 7.1: *100× UVM images of two different substrates after ELO showing surface damages. Two contrasting halves can be seen in (a), where the darker left half is where the epitaxial film has curled up initially and the clear right half has the epitaxial layer separated but still resting on the substrate.*

7.2.2 Use of solvents and solvent-related contamination

Normally the Apiezon wax layer is removed by dissolving it in a solvent which can cause some difficulties in the ELO processing. Trichloroethylene (C_2HCl_3) was originally used but this substance is highly toxic and requires working in a properly ventilated fume cupboard. This is also an ozone layer depleting substance (ODS) and hence restricted under the Montreal Protocol. 1-Bromopropane ($CH_3CH_2CH_2Br$) has been newly introduced as an alternative to trichloroethylene and used extensively here. However 1-Bromopropane is also a hazardous solvent as it can harm both the nervous system and the reproductive system.

Another disadvantage in using a solvent to remove the wax in the ELO process is the likeliness of impurity deposition on both the epilayer and substrate surface after lift off. Leaving the samples in etch solution (here, HCl) for prolonged period introduces deposition of impurities onto the substrate surface. This is an important issue if the substrate is to be used for a regrowth. Although these depositions can be rinsed off to a certain extent, this involves an additional substrate cleaning process. As the corners of a sample tend to lift first, these areas are exposed to the etch solution longer than the middle of the sample. As a result different areas of the substrate get different amount of materials deposition. This is seen in Figure 7.1(a). In this extreme case, This substrate was in the

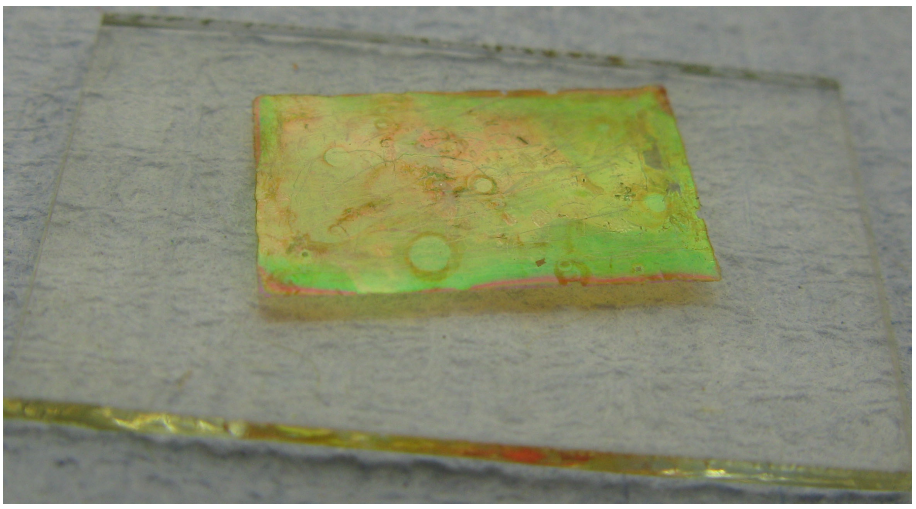

Figure 7.2: *Photograph of an epitaxial layer deposited on a glass substrate after lifting off from the substrate, showing residual deposition from the solvent, 1-Bromopropane.*

etch solution for two days because although the epilayer was completely separated, there was no way of knowing as the right half was still resting on the substrate after separation. In the mean time, the left half which has been curled up initially has been deposited with a dark dusty residue. These particles could possibly be formed from the interaction of the etch solution with the wax. Another substrate surface, damaged from residual deposit is shown in Figure 7.1(b). These dusty deposits are on the separated substrate surface and not on the epilayer, and can be completely wiped off the substrate if required.

Considerable care must be given to prevent any material deposition on the epilayer surface after removing the wax using the solvent solution. Most of the time, tiny particles from wax and fragments of the epilayer get deposited on the surface. Similarly when the lifted epilayer is dried, the solvent leaves a residue on the surface. Since 1-Bromopropane has a very low miscibility in water, ethanol is used as an additional solvent in the next step to dissolve any bromopropane from the epilayer. Although this method provides a very good quality epilayer over square millimetres, it becomes very difficult to completely eliminate impurities from the entire surface (See Figure 7.2).

7.2.3 Curling of epilayer

As the ELO process progresses, the epitaxial layer experiences stresses due to the wax and curls up, forcing open the small crevice between substrate and epilayer, thereby clearing

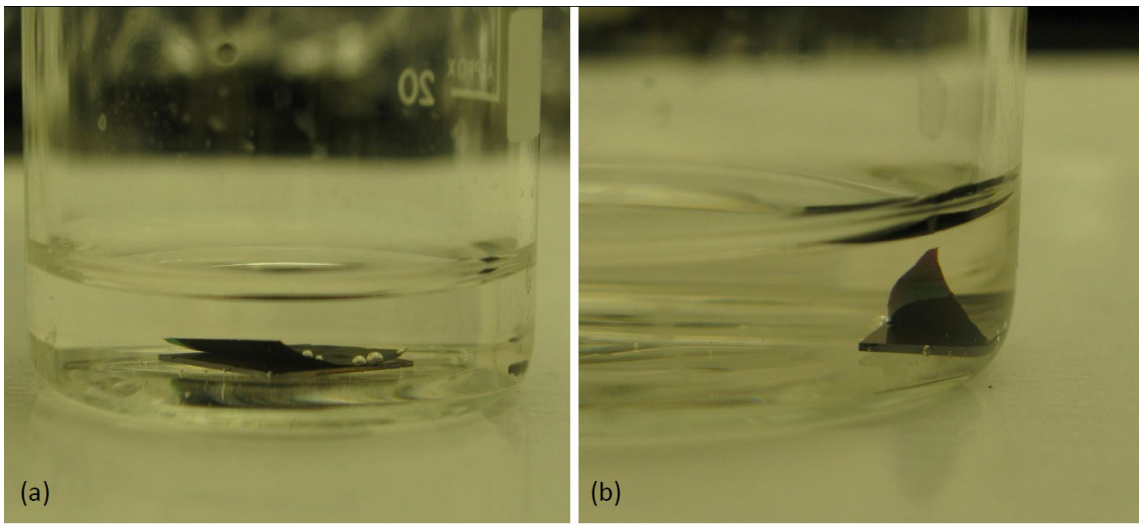

Figure 7.3: *Photographs of (a) uniform, reasonably curled and (b) overly curled epitaxial layers in etch solution. In the latter, there is very high probability for the curled up part to be snapped off from the rest during the deposition stage or subsequent wax removal process.*

the etch channels. As a result of this upwards curling effect, the etching is no longer stopped at a certain depth but speeds up the ELO process by helping the H_2S gas escape into the etching solution [1]. However for larger areas, sometimes the thin epilayers curl upwards too much and when trying to deposit onto a new substrate the curled corner of the epilayer will not bond under the Van der Waals forces. As a result most of the time these overly curled portions will be broken off the epilayer. Figure 7.3 shows a comparison between two different amounts of curling observed during ELO.

7.2.4 Scalable area

Although the estimated initial MgS etch rate of 3mm/hr is an order of magnitude faster than the etch rate of AlAs release layers in GaAs-based lift-off [1, 2], the etch process becomes much slower for larger areas. As the etching channels approach the centre of a sacrificial layer, there is a good chance for the entire process to stop as the curvature induced by the wax is minimal at the centre. At times this requires pushing the epilayer slightly to free the attached material in the centre. This forcible separation leads to crack formation around the centre areas (See Figure 7.4). As a result, the demonstrated devices are typically in the range of several millimetres in size.

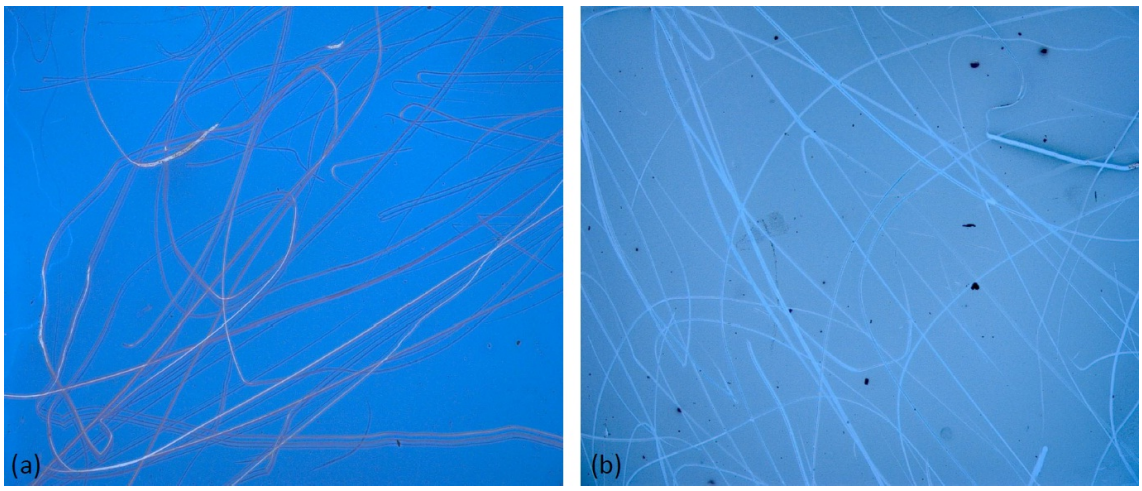

Figure 7.4: *UVM images of two different substrate surfaces after ELO, showing continuous scratches arising possibly due to the small manual force applied on the wax layer at times to separate the epitaxial layer from substrate. Sometimes a small applied force is necessary to determine if the etch has completed as sometimes the etched off epilayers stick to the substrate using capillary forces.*

7.2.5 Damage to substrate

Ideally one of the most important advantages of the ELO process is the ability to separate the substrate without introducing any cracks or impurity depositions. But the substrate surface damage arising from the current ELO treatment is primarily due to the use of a wax layer and the longer period of time in etch solution limits the use of a substrate for regrowth.

7.2.6 Inability to control and monitor the etch process

The tension induced by the surface wax layer cannot be controlled well and as a result it has proven difficult to investigate the details of the etch mechanism and optimise the process control parameters. Due to the black wax layer on top, the progress of etch cannot be monitored *in situ*.

For industrial applications it is necessary to obtain better control over the ELO technique so that the process can be optimised to allow for the separation of much large area devices at sufficiently high etch rates without compromising the device quality. In this chapter a modification to the existing ELO technique is demonstrated through which the above

mentioned limitations can be avoided.

7.3 Recent developments in III-V ELO

Several changes have been suggested and demonstrated to improve the basic ELO technique. Notably all of these modifications were designed for the III-V based ELO structures.

To eliminate most of the limitations described in Section 7.2, the major focus has been on finding an alternative to the wax based lift-off system. Since it is very difficult to control such fragile thin film structures, it is necessary to mount the epilayers on a carrier which is resistant to etch solution and acts as a frame on which the epilayer sticks to after lift off is completed. A thin sheet of flexible polymer was initially tried as a replacement to the wax layer [3]. A flexible carrier was required as the epilayer needed to curl up in the etching. In this case, rather than using the tension in the wax layer to open the crevice during the lift off process, a controllable external force is applied to the thin film through the polymer carrier. This carrier provided continuous support and allowed for the manipulation of the thin film during and after the lift off process.

7.3.1 Weight Induced Epitaxial Lift-Off (WIELO)

Several techniques were tried based on the flexible plastic carrier lift-off. A successful method was demonstrated by applying a variable weight to the plastic carrier which provides the required external force [3]. In this model, the sample with the plastic carrier attached is mounted upside down above the etch solution in a closed container [4, 5]. Due to the saturated vapour of the HF solution used in the container, one droplet of etch solution positioned on the plastic foil against the edge of the sample on the side of the weight is normally enough to separate the epilayer from the substrate. The schematic representation of this configuration is given in Figure 7.5(a) and is generally referred to as Weight Induced Epitaxial Lift-Off (WIELO).

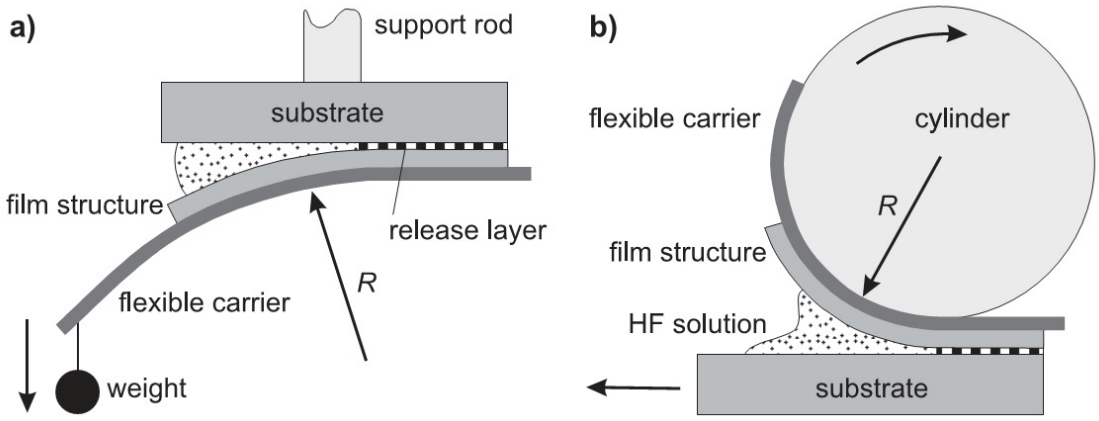

Figure 7.5: *Schematic of two recent advancements in ELO technique. (a) The weight induced ELO process and (b) ELO with a stabilized radius of curvature by guiding the temporary flexible carrier over a cylinder surface. [3]*

The main limitation of this setup is that the flexible carrier bends too easily especially if a new droplet of HF solution has to be applied during the lift-off process. This normally induces crack formation in epitaxial layer structures. Developments were made further in this system in which the slit is forced open with a constant radius of curvature by guiding the foil and the part of the epitaxial layer being separated over a curved surface (Figure 7.5(b)).

Although this technique has proven successful in lifting off III-V based material systems, it has never been attempted in II-VI systems. One of the important working principles of the WIELO is the use of a closed container system utilising the saturated vapour of HF. This method is not practical in the case of the 30% aqueous solution of HCl, used for MgS. Moreover the setup required for the above mentioned WIELO is complex and requires precise control throughout the lift-off process.

7.4 Polyurethane based carriers for II-VI ELO

Irrespective of the configuration used, the application of the flexible plastic carrier has proved successful for handling the thin epitaxial layers and releasing larger areas. Similarly there seems to be no fundamental limitations to scale up the process towards even larger films as long as a slight curling is provided for the etching to proceed.

A very simple method to lift epitaxial layers using a flexible polymer carrier that simply replaces the wax layer is demonstrated here. To avoid too much bending of the plastic layer and thus damaging the epilayer, a more rigid grade of flexible polymer carrier layer is used here. Plastic layers of different thicknesses were initially tried and after considering the availability, cost, durability and flexibility, polyurethane sheets were chosen. Polyurethane is a polymer composed of a chain of organic units joined by carbamate (urethane) links and is commonly recycled. It is resistive to HCl etch solution and is also used as a substrate in several thin film structures. Additionally most polyurethanes are thermosetting polymers that do not melt when heated.

Polyurethane sheets are easily available in the form of electronic screen protectors, which have one side coated with silicone glue that helps them to bond easily to smooth surfaces.

7.4.1 Steps of the improved ELO process

The ELO method involves several stages which are shown in Figure 7.6.

1. Cleaving: As explained in Chapter 6, samples are initially cleaved, but into $\sim 15 \times 15\text{mm}^2$ pieces which is five times larger than the area normally lifted with the wax layer technique. Although epilayers up to $\sim 10 \times 10\text{mm}^2$ in size were occasionally separated using the wax technique, the film layers were not in good shape with residual deposition from the solvent, imperfectly etched sides and corners, etc. In most cases an external force was required to completely separate the epilayer from substrate.

2. Applying polyurethane carrier layer: Polyurethane sheets were cut in the required shape and size and then carefully applied to the surface of the sample, making sure no air bubbles or dust particles were trapped. The polyurethane sheets instantly attached to the sample surface using electrostatic force. It is important to cut these sheets into pieces slightly larger than the sample as no external force, but the uniform stress induced by the carrier is used to separate the epilayers. If the structure

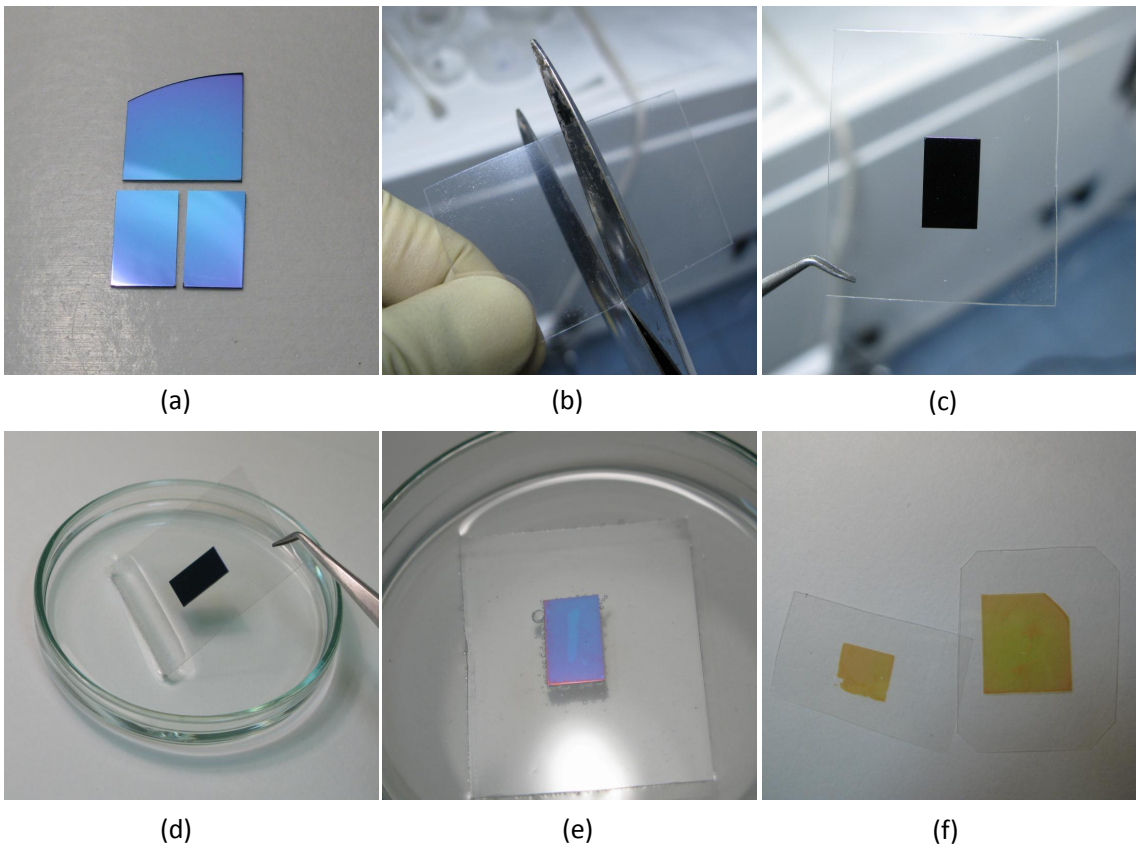

Figure 7.6: *Various stages involved in polyurethane based ELO. (a) Cleaved sample, (b) cutting plastic carriers in appropriate size, (c) plastic carrier applied to the sample surface, (d) placing in HCl solution, (e) etch in progress and (f) lifted layers on polyurethane carrier.*

is left at the bottom of the etch solution (as opposed to floating), a small buoyancy force is also present.

3. Chemical etching: The samples attached to the polyurethane carrier layer are then placed in a 30% aqueous solution of HCl. The MgS sacrificial layer is etched away, while the etch resistant polyurethane film supports the separated epilayer. Once the etch is completed, the released epitaxial layer along with the plastic layer floats to the surface of etch solution.

4. Examination: The lifted epilayer is then removed from the etch solution and rinsed in deionised water. The polyurethane layer itself can be used as a substrate for some applications (discussed later). Material characterisation including photoluminescence and transmission spectra, etc. can be obtained while the epilayer is attached to the polyurethane film.

5. Removal of the polyurethane carrier layer: The polyurethane layer can be easily removed to allow transferring onto other substrates. The epilayer on polyurethane is first attached to a wet substrate (here, glass) by utilising the van der Waals forces and then left to dry for few hours. The whole block is then immersed into a beaker of butanone ($CH_3C(O)CH_2CH_3$), which completely dissolves polyurethane leaving the epilayer bonded to the glass substrate. The substrate and epilayer assembly is finally washed in deionised water.

7.4.2 Advantages of polyurethane based ELO

Most of the limitations associated with the wax layer based lift off process originated from the use of the wax itself. From the deposition to the removal, wax has proved problematic when it comes to handling and processing the lifted epitaxial layer. The use of polyurethane sheet as a substitute for wax has dramatically improved the handling and quality of the epilayers.

The polyurethane film exerts a uniform stress on the epitaxial layer unlike a wax layer, where due to the non uniform spreading, different stresses are experienced by different areas of the thin film. Similarly over-curling of the epilayer is avoided by using a plastic carrier. In a wax layer based process, the corners of the epilayer curls up significantly depending on the size and shape of the epilayer as well as the amount of wax applied. The right amount of wax required for a particular size or shape of an epilayer is critical and very difficult to control unless an automated system is developed. Over-curled corners of large epilayers tend to break off after removing from the etch solution. Equally, the smaller portions of the epilayers, similarly separated from the edges and corners further disintegrate and stays in the etch solution unnoticed. These fine particles can stick to the separated epilayer and the substrate, degrading the quality.

Handling the samples becomes much easier when using a polyurethane sheet as the carrier. The flexible nature of the carrier makes it easy to transfer the film to a range of surfaces. On the other hand, the epilayer/wax combination is very brittle and very careful handling is required. Another advantage of the polyurethane based lift-off is that the flex-

ible carrier itself can be used as a substrate for a range of applications including flexible solar cells. Likewise the scalable area makes this technique even more favourable. Epitaxial layers up to $\sim 30 \times 30\text{mm}^2$ have been successfully separated from the substrates free of major defects such as cracks.

Using polyurethane sheets as an alternative to wax layers does not require hazardous solvents such as trichloroethylene or 1-bromopropane, which have been replaced by butanone. The issues related to the residual solvent deposits on the substrate and epilayer surfaces during wax based ELO (Section 7.2.2) has been completely eliminated.

The transparent polyurethane sheets also provide valuable information about the etch channels (See section 7.4.3). The etch progress can be easily monitored and the characteristics of the reaction can be studied this way.

Finally, the low cost, easy availability and ease of application to the existing technology also make the polyurethane based carriers attractive. This method also does not require any mechanical equipments. Compared to the WIELO technology, no additional weight is required to induce stress. Instead, the polyurethane immersed in the etch solution exerts a force upwards which stresses the epitaxial layer.

7.4.3 Observation of the etch process

One of the advantages in using a polyurethane carrier is that, through the transparent layer, the whole etch process can be observed. This way, the progression of etch channels through the sacrificial layer and any obstructions can be monitored and the reaction kinetics studied. In this section the first ever visual study of an epitaxial lift off process is detailed.

A sample was prepared in the same way as described in Section 7.4.1. A polyurethane sheet was attached to the sample surface and placed in a glass petri dish, which was then placed under the microscope that was focused on the sample surface. The etch solution was then poured into the petri dish.

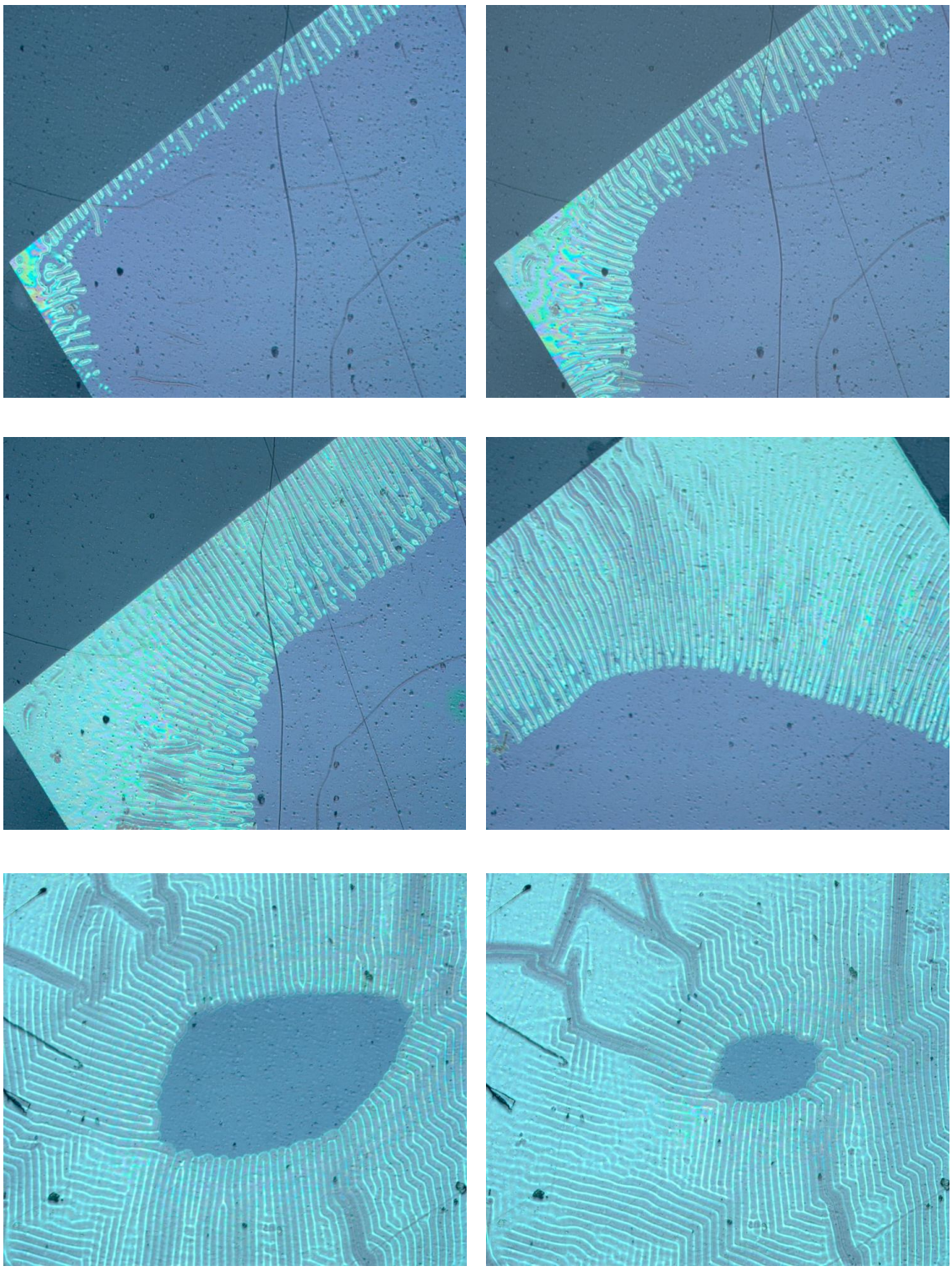

Figure 7.7: *UVM images from various stages of a transparent polyurethane carrier based ELO. Any black marks appearing in the images are on the outer surface of the carrier layer used and have no effect on the epilayer or etching process.*

The etch can be performed in two ways; by completely immersing the sample and placing it at the bottom of the petri dish by adhering the edges of the polyurethane film to the dish edges or by allowing the sample to float on the surface. Both ways are effective as in the first case the buoyancy of the polyurethane film provides the stress whereas in the second

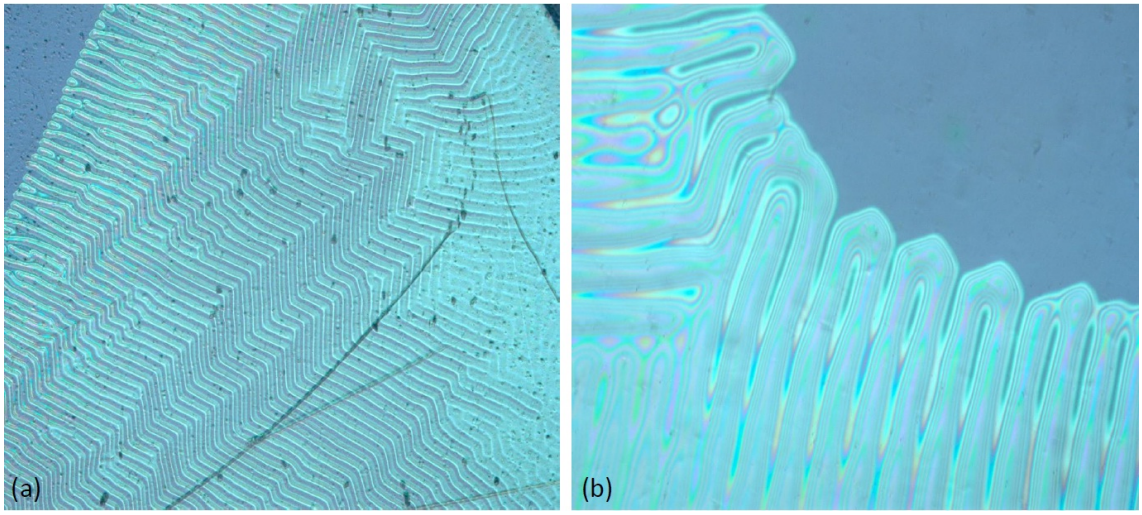

Figure 7.8: *UVM images showing (a) 100× and (b) 500× magnified view of the progression of etch channels in polyurethane carrier based ELO. (Note: The black mark on (a) is a scratch on the outer surface of the carrier and has no effect on etching)*

case, the weight of the substrate provides the stress. For larger samples an additional supportive film is attached to the substrate to minimise the stress. To make focussing easier, in this case the sample was immersed.

Initially the etch starts from all sides and rapidly moves inwards. Figure 7.7 shows various stages of the ELO. The progression of the etch channel forward and H_2S gas transfer (as bubbles moving towards the edges through the channels) can be seen through an optical microscope. These H_2S bubbles completely dissolves into the HCl solution, as soon as coming out of the etch channels. This finding is against the Yablonovitch model [1], where it suggested that the bubbles are formed when the concentration exceeds the solubility limit of H_2S and the etch rate drops. But here, the bubble formation and transfer through the etch channels were noticed from the beginning and no change in etch rate was noticed. This shows that H_2S gas is not dissolving inside the etch channel and as a result the concentration of etch solution inside etch channels remain stable resulting in a constant etch rate.

Although the etch channels initially appear to be aligned, there is clearly no particular crystallographic directions involved. Interestingly the distances between individual etch channels are the same. However a few larger channels formed as a result of merging smaller etch channels can also be seen. As these channels move inwards the outer ends join together and this initiates the separation of the epilayer from the substrate. Finally the etch channels from all directions meet at the centre and the epilayer completely separates

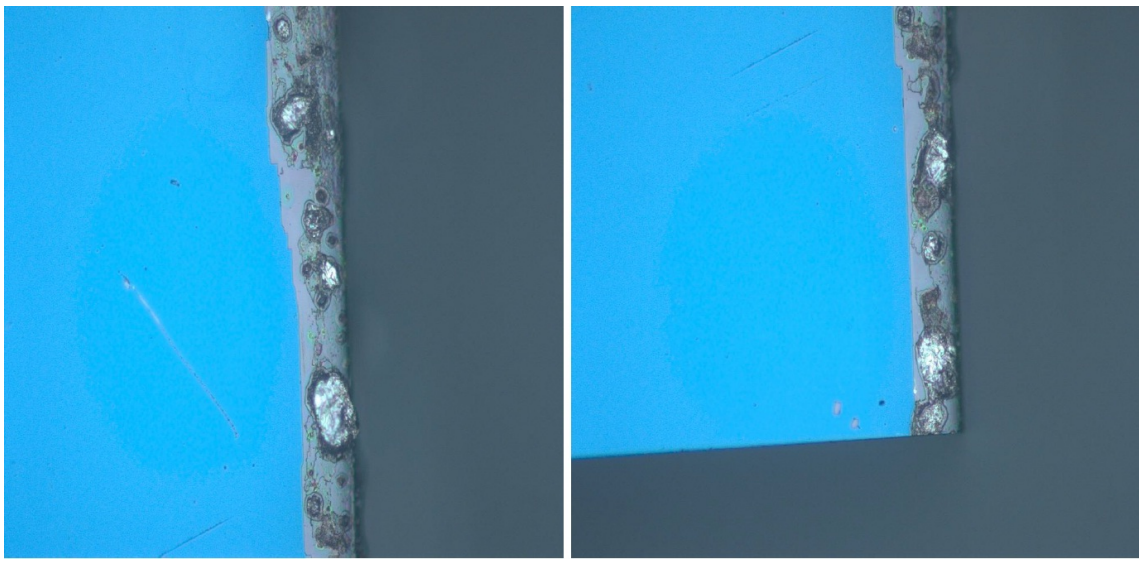

Figure 7.9: *50× UVM images showing a narrow, unetched strip of material along one edge. The large area in blue colour is the substrate where the etch was successful.*

from the substrate. Figure 7.8 shows a magnified view of the etch channels.

The rate at which etch channels from different edges progress is different. One significant (and unexpected) finding is that the etch channels originate from freshly cleaved edges move much faster than the channels originating from non-cleaved edges (as-grown edges). This could be due to the deposition of a very thin layer of ZnSe on the sides of the sample during the growth of the ZnSe top layer.

Similarly, occasionally it was noticed that certain edges will not initiate any etch channels throughout the process resulting in a thin strip of unetched layer along that particular edge. Figure 7.9 shows UVM images from such a sample. One possible cause is a thin indium layer on that edge resulting from the bonding process. It is a common practice during bonding on the molybdenum block, to move the substrate around on the melted indium to ensure it is properly glued. If excess indium is used, this movement results in a thin film of indium sticking to the edges.

7.5 Stabilisation of semiconductor surfaces

One of the major difficulties in handling the materials grown in the MBE chamber at Heriot-Watt is the lack of techniques to preserve the sample. Growth takes place in ultra

high vacuum, where there are minimal surface contaminants. When the sample is brought outside the chamber into the atmosphere, various factors affect the stability of the surface layers. The scale of the effects varies according to the surface epilayer. In this section a surface passivation method is tested on various samples and its effect on the stability of different compounds is studied.

Control over the stability of an as-grown sample is an integral part of the MBE growth process. In many cases, transporting samples between various laboratories across the globe requires considerable care, especially in the case of certain highly reactive materials such as MgS. Exposing an as-grown sample to atmosphere, in most cases restricts the possibility to reintroduce it into the chamber and perform growth of another layer on top of it due to various factors described below.

7.5.1 Surface reactions

Passivating a sample depends entirely on its reactivity in atmosphere and different materials react very differently. There are two cases where these reactions could degrade a sample beyond usability. First, the material oxidises which completely degrades the surface. In certain materials the whole capping layer could react. Second, for less reactive materials, the exposure to atmosphere results in a thin surface layer formation. In most cases this thin layer will be formed as a result of the reaction between the surface layer and oxygen in atmosphere. These oxide layers are typically up to a few monolayers thick, and for many applications can be ignored as they do not influence the structure or stability of the material on which they are formed. However these layers prevent any additional epitaxial depositions, rendering the sample unusable for further growth.

7.5.2 Case study: MgS

MgS is a highly reactive material grown extensively at Heriot-Watt. This very reactivity has made it an impressive candidate for the sacrificial layer in II-VI ELO. However MgS also reacts with oxygen when exposed to atmosphere, forming magnesium oxide and

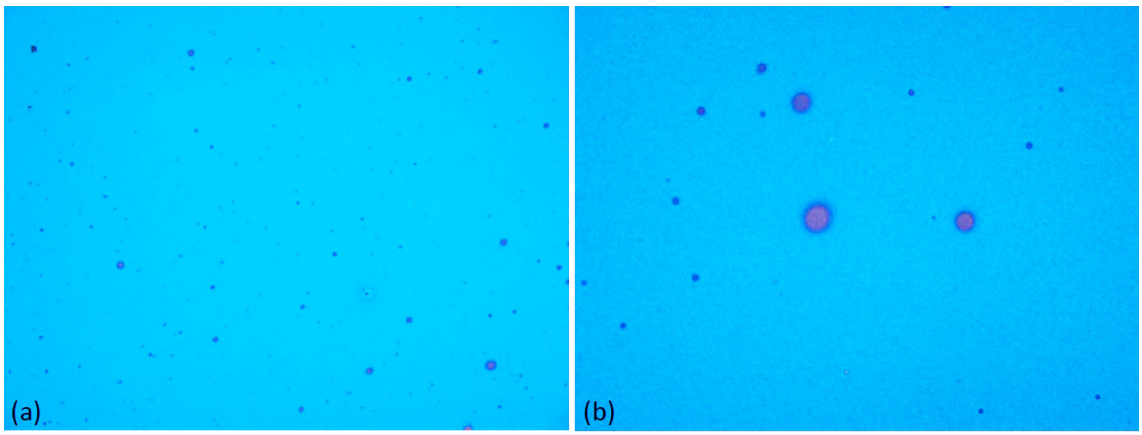

Figure 7.10: *(a) 100× and (b) 200× UVM images of an MgS layer with a 2 ML ZnSe cap showing surface degradation, two weeks from the growth.*

critically this reaction is not limited to the surface layer, but extends through the whole MgS layer. This reaction makes it impossible to grow a sample terminating in MgS.

For surface characterisation studies of MgS, it is essential to grow a very thin capping layer of a stable material on top of MgS to prevent the oxidation. Typically 2-4 nm thick layers of ZnSe are grown on the MgS layers, and these capping layers, being so thin do not normally change the surface morphology. This capping layer method is not ideal in many cases where direct contact to the MgS layer is required and could mask any nanoscopic surface features present on MgS surface during surface topography using AFM. To avoid such difficulties, even thinner ZnSe layers just a few ML thick (generally 2-4 ML) have been tried. However the degradation of such extremely thinner layers has been noted over time. (See Figure 7.10)

7.5.3 Case study: ZnSe

ZnSe is a very stable compound compared to MgS. However the formation of a very thin oxide layer on ZnSe has been observed when exposed to atmosphere. This thin layer is only a few ML thick and has no significant effect on the structural or optical characterisation.

The only major disadvantage of this thin oxide (ZnO) is when attempting a regrowth on an as-grown ZnSe layer. Once removed from the vacuum chamber, it is very difficult

to re-initiate the growth on the surface. There is no effective chemical etchant available which completely removes the zinc oxide layer without damaging the underlying ZnSe. ZnO is also thermally stable and cannot be removed in vacuum by heat treatment, unlike for example gallium oxide. RHEED shows that the normal 2×1 (Se rich) streaky pattern visible during ZnSe growth, starts as a completely spotty pattern during a regrowth of ZnSe on this oxide layer. Although the integral streaks return in 2 minutes ($\sim$ 10nm), the interface will still be rough and oxide patches will introduce more dislocations and stacking faults.

The results of further attempts of ZnSe regrowth on ZnSe layers exposed to atmosphere are detailed in Section 8.4.1.

7.5.4 Case study: CdSe quantum dots deposited on MgS

Due to its ultra wide band gap ($\sim$ 5eV), MgS is used as a barrier for CdSe QD structures. Because of the reactive nature of MgS, such quantum structures always require a thick ZnSe capping layer. For surface characterisation studies, dots are generally grown on MgS layers and capped with a few ML ZnSe. As explained above, this thin cap is effective only for few hours and then degrades and so any measurements have to be taken within this period. Growing a stable and thicker cap up to 2-3 nm has been found to be alter the morphology and can even bury really small features.

The method of growing a cap only a few ML thick is effective only for samples which will be characterised within few hours from growth. There were many instances where the structures must be examined extensively over a longer period or sent to another laboratory, and in such cases the lack of a suitable sample preservation method is a significant problem. For analysis using techniques such as AFM, SERS (Surface enhanced Raman spectroscopy), etc. it is preferable to have a cap free surface if possible.

7.6 Existing surface passivation techniques

There are a range of methods for storing samples over a longer period and the following are some of the most important techniques used for transport or storage.

7.6.1 Vacuum desiccators

Vacuum desiccators are sealable enclosures containing desiccants (usually an otherwise inert solid such as silica gel) used for preserving moisture sensitive items for later use. A stopcock is included to permit the desiccator to be evacuated using a vacuum pump. A common use for desiccators is to protect chemicals which are hygroscopic or which react with water from humidity.

Although a vacuum desiccator is an ideal solution for storing samples over a longer time, the contents of desiccators are exposed to atmospheric moisture whenever the desiccators are opened. Similarly laboratory grade desiccators are made of heavy glass and comparatively larger in size, preventing easy transportation.

7.6.2 Vacuum transfer devices

There are different methods of sample transfer under vacuum, each transfer device having its own particular advantages and disadvantages. The methods vary from simple vacuum sealed, disposable glass tubes to high end, reusable vacuum boxes. All these devices involve either extensive preparation or higher costs and hence are not widely used for sample transportation.

7.6.3 Arsenic passivation layer in III-V semiconductors

Clean surfaces of MBE grown III-V epitaxial layers may be passivated against atmospheric contamination such as oxide layer formation by the *in situ* condensation of the

higher vapour pressure element of the compound. The passivating layer can be removed by gentle heating. This has been reported for GaAs [6–8] and AlAs [6, 9]. Further research has demonstrated significant improvements in interfaces formed by regrowth of GaAs surfaces exposed to air and deionised water which had previously been passivated using thin arsenic layers condensed *in situ* [10]. It was found that As passivation provided a large reduction in the carrier loss normally seen in carrier concentration depth profiles of regrown interfaces in lightly doped n-type material.

Arsenic deposition is now widely used in III-V MBE as As layers can be easily applied post growth in the growth chamber and later removed by gently heating.

7.7 Selenium protection layer in II-VI materials

The chemical and electronic properties of selenium passivated GaAs (001) surfaces were investigated previously by a combination of theoretical calculations and core level photoemission experiments [11] and it was found that the surfaces were very unreactive and could be considered as chemically passivated. Subsequently the stability of a Se passivation layer on a Si (001) surface was investigated using a non-destructive surface sensitive technique: time-of-flight positron annihilation induced Auger electron spectroscopy. After 10 days of exposure in the air, the Se passivation layer surface was observed to incorporate some oxygen but to remain largely intact [12].

The application of a selenium protective capping layer in II-VI semiconductors is investigated in this section. Samples grown for this study are characterised using RHEED, AFM and XRD. The effect of the Se layer on the regrowth on ZnSe and MgS layers is also examined.

7.7.1 Deposition method

The Se protective layer is applied to structures using a very simple method. Once the growth is finished, the sample is first cooled to below $\sim 120\ ^{o}$C. Se is deposited directly

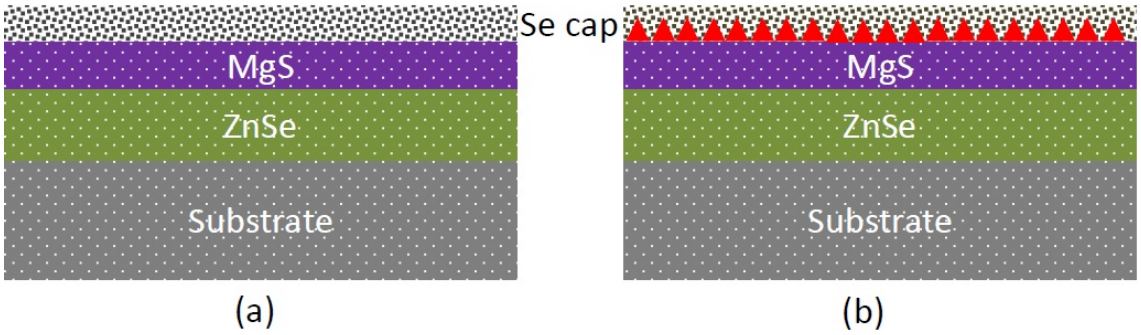

Figure 7.11: *Schematic of the structure of Se capped (a) MgS structure and (b) CdSe quantum dot structure.*

on the sample surface by opening the Se cell. Within 5 sec of starting the Se deposition, all the RHEED features disappear, indicating the formation of an amorphous Se surface layer. The structure of a typical Se capping layer applied sample is given in Figure 7.11.

The thickness of Se deposition depends on both the sample temperature and the Se flux. Initially samples were grown with a 5 min Se deposition while sample temperature was lowered from 120 to 100 ^{o}C. Different deposition times were later examined for different materials.

7.7.2 Selenium on ZnSe surface

At first, Se deposition was attempted on ZnSe layers. Samples were cooled immediately after the growth to the Se deposition temperature of $\leq$ 120 ^{o}C while maintaining a sharp and streaky 2$\times$1 RHEED pattern indicating flat Se rich ZnSe surface. As soon as the Se deposition is started, the RHEED patterns disappeared.

A set of samples were grown with varying Se cap thicknesses using deposition times varying from 5 min to 40 min. Samples were then removed from the growth chamber and carefully removed from the molybdenum block. Indium, which is used as a glue to fix the sample to molybdenum block has a melting point of 156 ^{o}C. Special care must be given while separating the sample from the molybdenum block as if the temperature used rises above $\sim$ 175 ^{o}C, Se starts to evaporate and ultimately exposes the underlying surface to atmosphere. Se vapour is also toxic, if inhaled.

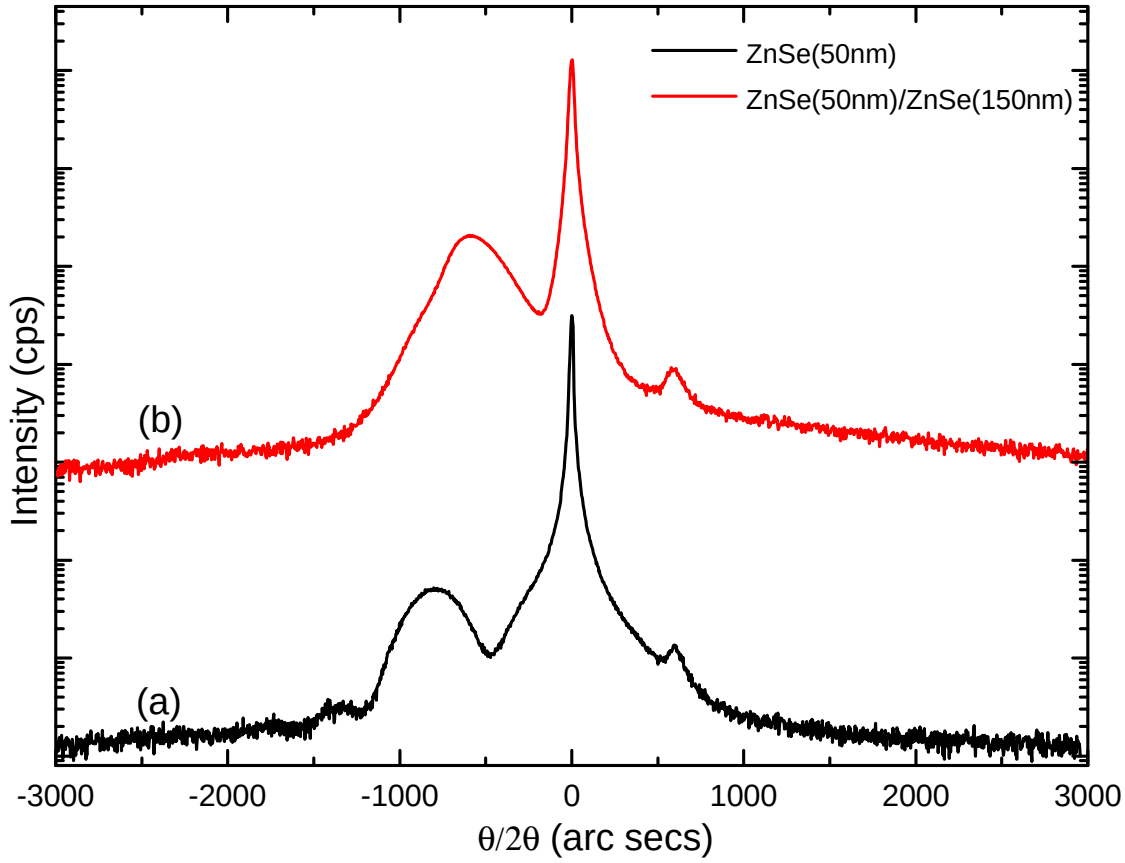

Figure 7.12: *A comparison of 004 XRD scans from samples with structure (a) ZnSe(60nm) and (b) a 150nm ZnSe grown on top of the first structure, after preserving three months using a Se coating.*

Samples were then examined using XRD and AFM over the next few weeks. No difference in surface morphology was observed between samples grown with 5 min, 20 min and 40 min of Se deposition. After two weeks samples were glued back to the molybdenum block and re-introduced to the growth chamber. No sample treatment was used at this stage. Any dust particles stuck to the sample surface were simply removed by using a jet of oxygen free nitrogen gas.

Once returned to the growth chamber, RHEED from the sample surface initially shows the blank screen confirming the presence of an amorphous Se surface layer. The sample is then slowly heated to above 200 ^{o}C. A sudden change in the RHEED pattern can be seen at this temperature as, at first the integral streaks and then the half order streaks reappears. The sample is then further heated to the growth temperature and a regrowth is performed. RHEED shows a sharp and streaky 2×1 pattern throughout the growth indicating a smooth 2D growth. No RHEED spots were visible to indicate signs of 3D nucleation.

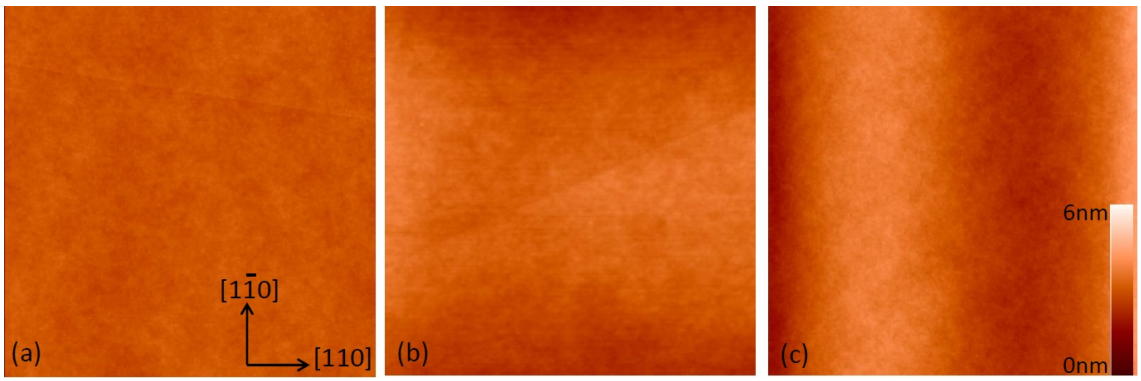

Figure 7.13: $10\mu m \times 10\mu m$ *AFM images showing representative areas from samples (a) HWC462, (b) HWC486 and (c) HWC467 on the day of growth.*

After the regrowth, samples were re-examined using AFM and XRD. AFM images showed a near atomically flat surface with a roughness of $\sim$ 0.6 nm and this value is well within the surface roughness range of a normal GaAs/ZnSe structure grown here. To investigate the structural stability of the structures after Se desorption, a ZnSe(150nm) layer was grown on top an already grown structure which was left outside the chamber for three months. The original sample had a 60nm ZnSe structure with a Se coating. 004 XRD scans were obtained before and after the regrowth. A comparison of the XRD scans are given in Figure 7.12. The original structure shows a strained 60nm ZnSe layer whereas the regrown structure has shown a $\sim$ 50% relaxed 150 nm thick ZnSe cap layer peak and an un-relaxed shoulder peak indicating the original structure.

7.7.3 Selenium on MgS surface

MgS samples grown on a ZnSe buffer layer were processed in the same way as in the previous ZnSe section. The only difference is the change in the RHEED pattern, which in this case is from a c(2×2) pattern to amorphous. Three samples HWC462, HWC486 and HWC467 were grown with 5 min, 20 min and 40 min of Se deposition. Samples were initially measured using AFM and XRD. AFM images again showed very flat surfaces for all the samples. All the sample surfaces were near atomically flat with an RMS roughness in the range of 0.5-0.6 nm. Figure 7.13 shows AFM images obtained after growth, from all three samples.

Sample surfaces were continuously monitored using AFM every day to study the stability

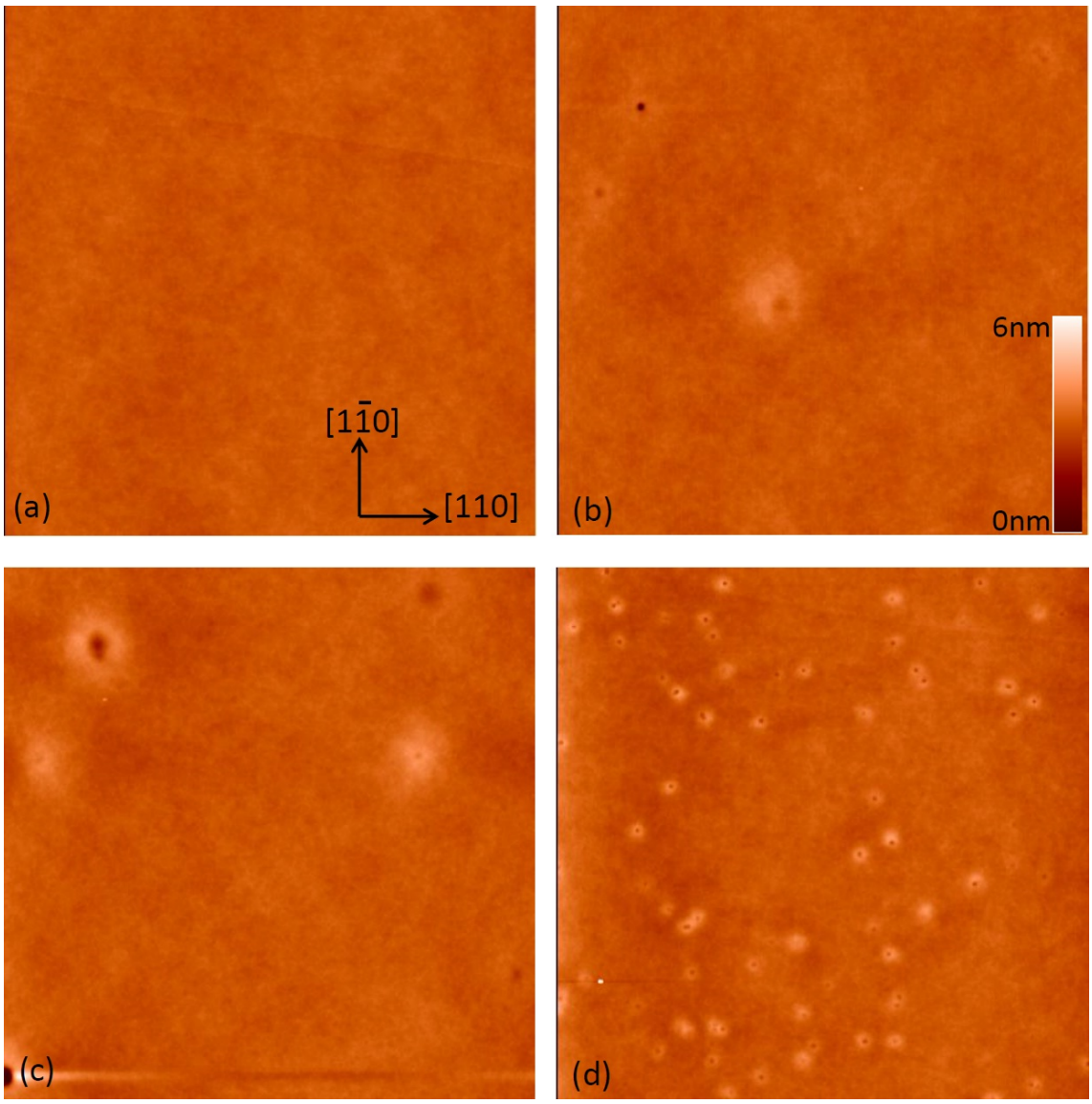

Figure 7.14: $10\mu m \times 10\mu m$ *AFM images showing representative areas from HWC462 on (a) Day 1, (b) Day 3, (c) Day 5 and (d) Day 10.*

of the MgS layer underneath. After two days HWC462, the sample grown with 5 mins of Se deposition developed some surface features. The density of such surface spots increased over the next few days. Figure 7.14 shows the AFM topography of sample HWC462, measured over several days. The other two samples still showed a flat surface. Samples were further monitored for another four weeks and still no surface features were observed on the other two samples.

After 4 weeks, HWC462 was reintroduced into the growth chamber and attempted re-growth. The sample showed a spotty RHEED pattern as soon as the Se layer was desorbed, as expected. The surface features which appeared on the AFM images are possibly from areas where the thickness of Se layer was not adequate to protect the MgS layer

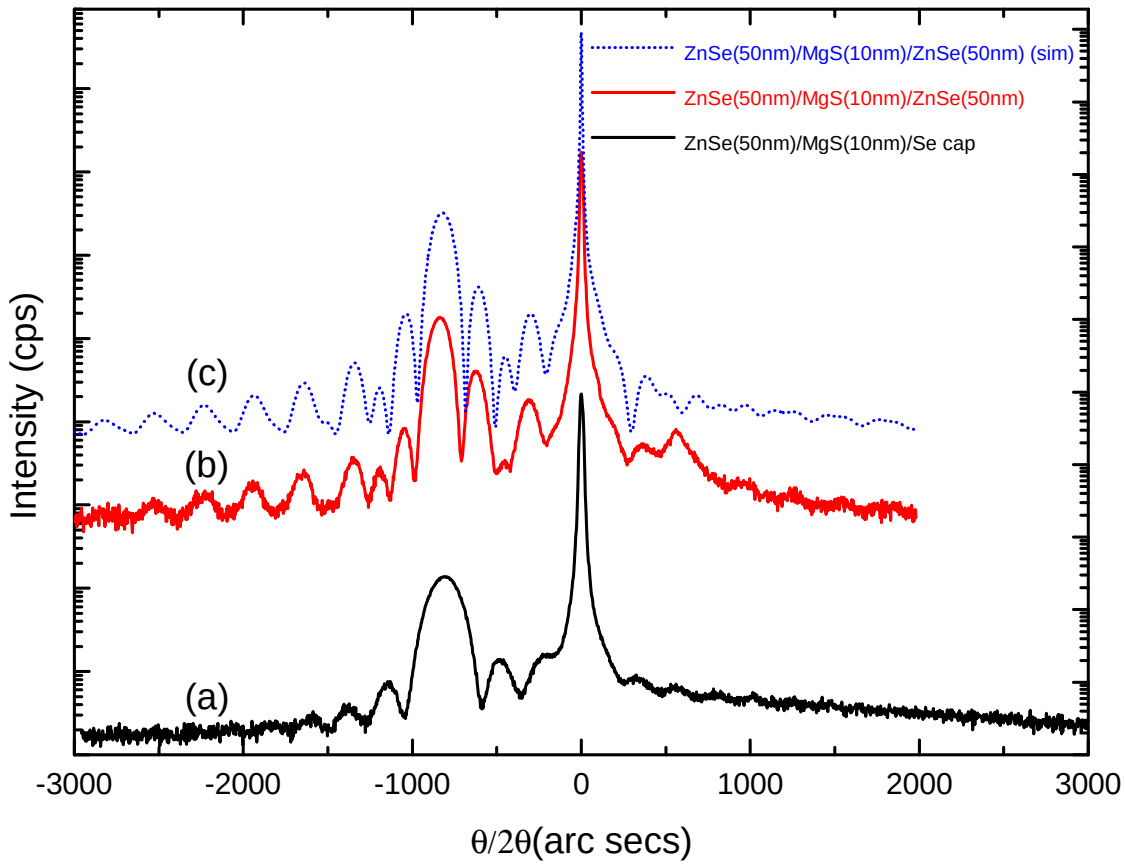

Figure 7.15: *004 XRD experimental scans from HWC467 with (a) an initial structure ZnSe(50nm)/ MgS(10nm)/ Se cap, (b) a final structure ZnSe(50nm, initial growth)/ MgS(10nm, initial growth)/ ZnSe(50nm, regrown after three months by removing the Se protective cap) and (c) a simulated fitting of (b). During the three months between the growths, the initial structure was left on an office table, uncovered and exposed to atmospheric conditions.*

from reacting with atmosphere. This could be due to the desorption of Se during removal of the sample from the molybdenum block (higher temperature) or simply that not enough Se deposition took place in the 5 min. The regrowth of a ZnSe layer on top of the MgS surface layer was again showed spotty streaks in RHEED, indicating the presence of a rough 3D surface.

The other two samples HWC486 and HWC467 were reintroduced into the chamber after 12 weeks and were noticeably unaffected by such prolonged atmospheric exposure. After the Se desorption, sharp and streaky c(2×2) patterns reappeared in RHEED indicating a good crystalline quality surface devoid of any 3D nucleation. Successful ZnSe re-growth were performed on both HWC486 and HWC467. A sharp 2×1 RHEED pattern replaced the c(2×2) indicating a Se rich ZnSe growth. Figure 7.15 shows a comparison of 004 XRD scans obtained from HWC467 with an initial structure GaAs(substrate)/ ZnSe(50nm)/ MgS(10nm)/ Se cap and a final structure, GaAs(substrate)/ ZnSe(50nm

initial growth)/ MgS(10nm initial growth)/ ZnSe (50nm, regrowth after desorbing Se cap). The experimental scan from the latter showed the two distinctive ZnSe layers and Pendellösung fringes indicating the high crystalline quality of the grown layer. AFM scans on the same samples again showed flat surfaces with roughness values in the range of 0.5-0.6 nm.

From the above observations, a Se deposition time of at least 20 min has been fixed for all the future growths. The Se deposition time also depends on the sample temperature. For HWC462 the Se layer was deposited when the sample temperature was between 120 and 100 ^{o}C. An even lower temperature could speed up the Se deposition and thus the deposition time could be reduced.

7.7.4 Transportation and surface characterisation

Previous sections focussed on the regrowth aspect of amorphous Se deposition on ZnSe and MgS. For transportation, Se capped samples can be easily transported simply in a sample storage box.

In this case ZnSe does not require any Se capping at all, as the very thin oxide layer formed is a passive layer and does not interfere during additional surface analysis. However, structures containing MgS have to have a protective layer until just before the surface analysis to avoid any surface degradation. Just before the analysis the sample may be heated to $\sim$ 200 ^{o}C to desorb the amorphous Se protective layer. Vacuum conditions are not necessary as no difference has been observed between two cleaved pieces of the same sample heat treated under vacuum and at atmospheric pressure. In atmosphere the changes to the sample surface can be witnessed by naked eye. Figure 7.16 shows various stages of Se desorption performed under atmospheric conditions, in a clean room at 200 ^{o}C. In roughly 30 sec, all the Se is evaporated and a flat surface was visible.

Any surface characterisation can be thus performed when needed by keeping the sample surface buried under an amorphous Se layer. However the surface MgS layer will oxidise rapidly within a few hours from the removal of the Se protective layer.

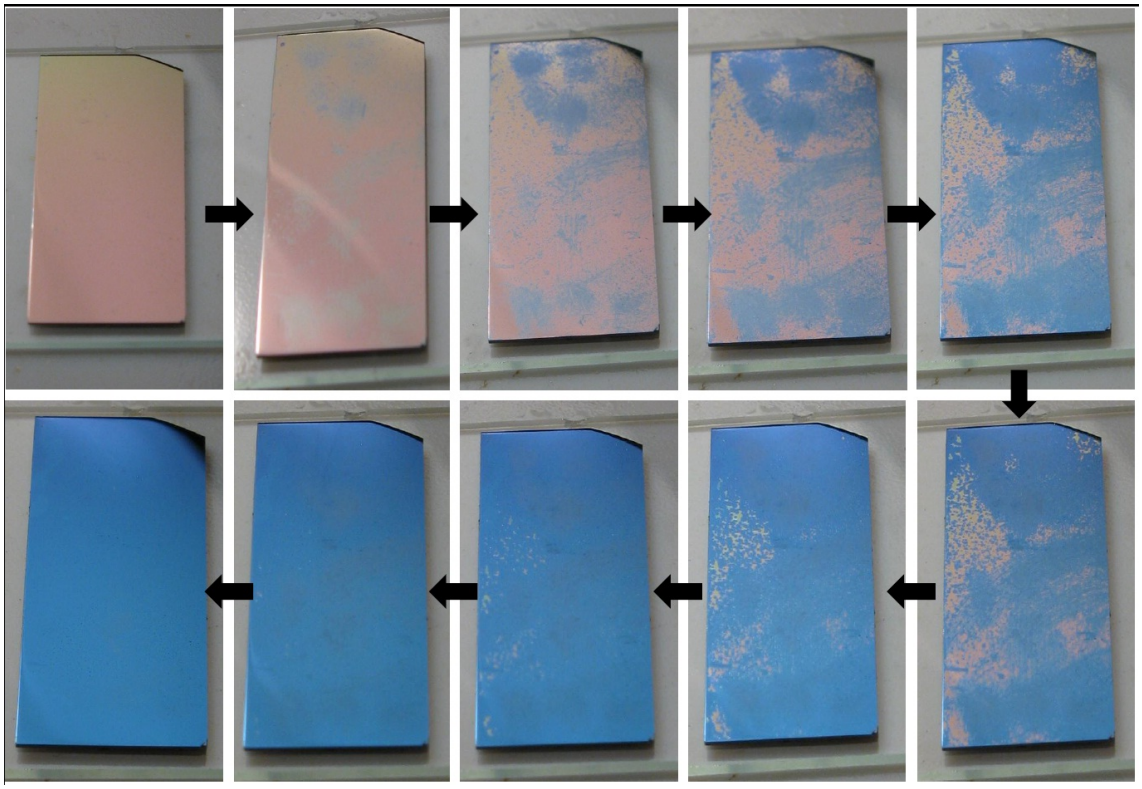

Figure 7.16: *A photographic representation of various stages of Se desorption under atmospheric conditions. The first image is a sample coated with amorphous Se and the final image shows a completely Se desorbed MgS surface. The whole process took under 30 sec at 200^{o}C. (Pictures taken at $\sim$ 3 sec interval)*

7.8 Summary

An existing MBE processing technique ELO, has been modified by replacing the traditional wax application with a silicone coated polyurethane carrier. This flexible carrier enables fast and easy lift off of large area epitaxial layers with reduced defects and surface contaminations. Epitaxial layers up to 30×30 mm^2 area were successfully lifted-off and transferred to foreign substrates. The residues from wax and solvents can be completely avoided using this technique.

Characterisation can be performed while the epilayers are attached to the carrier. Epilayer damages arising from over curling of corners can be completely avoided. The whole etching process, including the formation and progression of etch channels and the transfer of H_2S gas can be clearly observed under a microscope through the transparent carrier.

A new processing technique for preserving as-grown II-VI material surfaces from atmospheric contaminants has been demonstrated. By depositing a layer of amorphous Se

protects the semiconductor surfaces from the formation of oxide layers and other reactions. Later this Se protective layer can be easily desorbed by heating to $\sim$ 200 ^{o}C. No differences were observed between samples undergone Se desorption under vacuum condition and at atmospheric pressure. AFM was used for monitoring the sample surfaces over time whereas *in situ* observations were carried out using RHEED.

By using the Se protective layer, samples can be stored in normal atmospheric conditions for longer periods for either a regrowth or surface characterisation on a later time. Regrowth were performed on both ZnSe and MgS layers and 004 XRD scans were used to ensure the structure and crystallinity of samples before and after regrowth. Sample processed this way can be easily transported anywhere without worrying about surface contaminants. Any dust can be easily removed by using a jet of nitrogen gas or even air.

7.9 Future Work

The material deposition on the substrate under prolonged exposure in etch solution is not well understood. Apiezon wax used was thought to be resistant to HCl solution. However the only other materials to be found in the solution when the layer is etched away are Mg ions and H_2S gas. The fact that these deposits can be washed off the surface (and hence are loosely adhering) makes it difficult to examine using any of the characterisation methods available here. SIMS or Auger spectroscopy could be used to determine the nature and origin of these materials. It was also noticed that such deposits were absent when the wax layer was replaced by a polymer carrier, pointing strongly towards a reaction of etch solution with the wax layer.

Very little has been done to study the evolution and properties of the etch channels despite the fact that arguably this is the first time the etch channels were observed or recorded. Previous models of etching of III-V and II-VI semiconductors have all assumed (1) the liquid-solid interface is straight and (2) the maximum H_2S concentration is limited by saturation. This is possibly not true as bubble formation is seen and therefore some supersaturation is possible. The rate at which channels from different edges progress forward

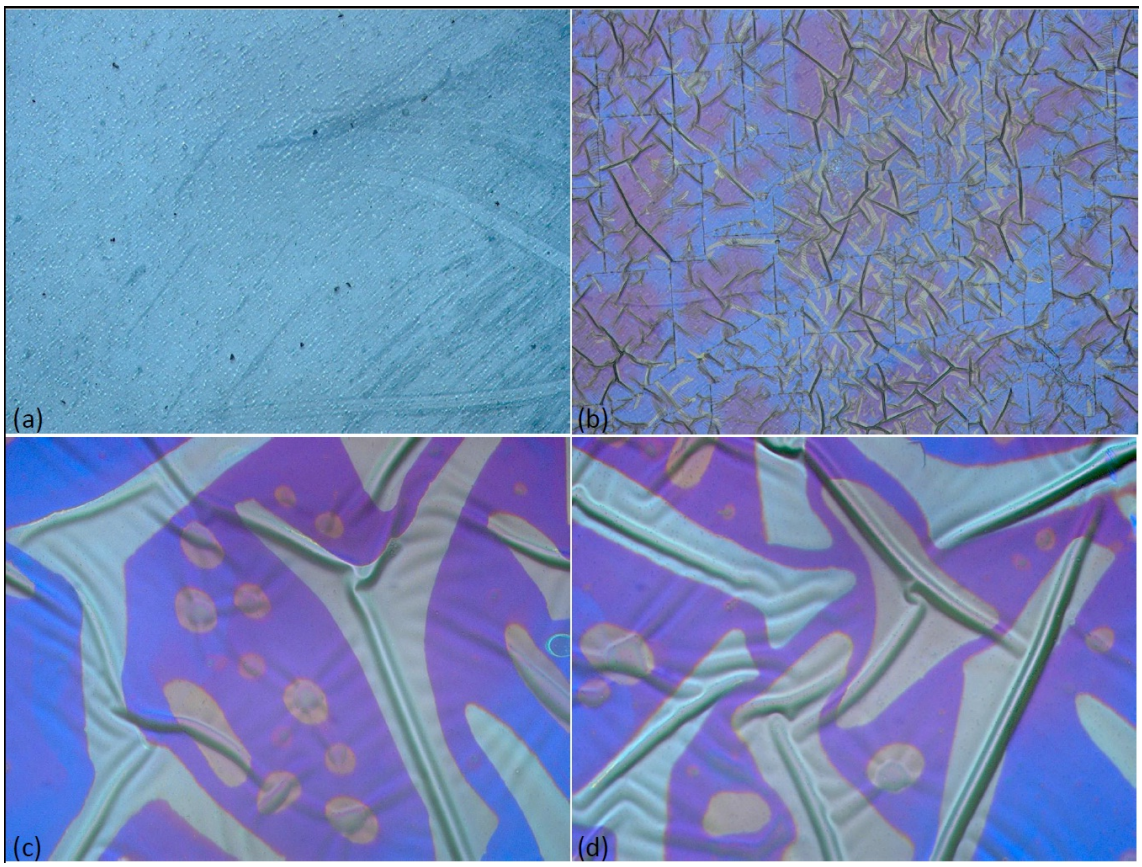

Figure 7.17: *UVM images showing (a) the surface of a polyurethane carrier (50×), (b) cracks formed along [110] and [1$\bar{1}$0] as a result of bending the flexible carrier (50×) and (c) & (d) an epilayer deposited on polyurethane carrier showing rippled surface formations due to the compressive strain exerted by the carrier (500×).*

is different. Although a few of the possible reasons have been considered, more study need to be carried out to investigate this phenomenon. The effect of the 'stepped' pattern in which the etch channels progress on etch rate (if any) has not been studied.

Although proved very effective over the existing wax based ELO, the use of a flexible carrier does raise certain challenges. The polyurethane material used here, is of lower quality and not optically flat (Figure 7.17(a)). In certain cases crack formations along [110] and [1$\bar{1}$0] directions were observed as a result of slight bending of the carrier layer during handling (Figure 7.17(b)). Similarly, the compressive strain exerted by the plastic carrier is greater than that of the substrate in which the epilayer was initially deposited. This ultimately results in rippled surface formations as seen in Figure 7.17(c) and 7.17(d). These issues can be eliminated by using high quality polyurethane or polyethylene terephthalate carriers.

7.10 References

[1] E. Yablonovitch, T. Gmitter, J. P. Harbison and R. Bhat. “Extreme selectivity in the lift-off of epitaxial GaAs films”. *Applied Physics Letters* Vol. 51 (1987), pp. 2222–2224 (cited on pages: 184, 193).

[2] C. Bradford, A. Currran, A. Balocchi, B. C. Cavenett, K. A. Prior and R. J. Warburton. “Epitaxial lift-off of MBE grown II - VI heterostructures using a novel MgS release layer”. *Journal of Crystal Growth* Vol. 278 (2005). 13th International Conference on Molecular Beam Epitaxy, pp. 325–328 (cited on page: 184).

[3] J. J. Schermer, P. Mulder, G. J. Bauhuis, M. M. A. J. Voncken, J. van Deelen, E. Haverkamp and P. K. Larsen. “Epitaxial Lift-Off for large area thin film III/V devices”. *physica status solidi (a)* Vol. 202 (2005), pp. 501–508 (cited on pages: 186, 187).

[4] J. J. Schermer, G. J. Bauhuis, P. Mulder, W. J. Meulemeesters, E. Haverkamp, M. M. A. J. Voncken and P. K. Larsen. “High rate epitaxial lift-off of InGaP films from GaAs substrates”. *Applied Physics Letters* Vol. 76 (2000), pp. 2131–2133 (cited on page: 186).

[5] M. M. A. Voncken, J. J. Schermer, G. Maduro, G. J. Bauhuis, P. Mulder and P. K. Larsen. “Influence of radius of curvature on the lateral etch rate of the weight induced epitaxial lift-off process”. *Materials Science and Engineering: B* Vol. 95 (2002), pp. 242–248 (cited on page: 186).

[6] S. P. Kowalczyk, D. L. Miller, J. R. Waldrop, P. G. Newman and R. W. Grant. “Protection of molecular beam epitaxy grown $Al_xGa_{1-x}As$ epilayers during ambient transfer”. *Journal of Vacuum Science and Technology* Vol. 19 (1981), pp. 255–256 (cited on page: 199).

[7] J. M. Woodall, P. Oelhafen, T. N. Jackson, J. L. Freeouf and G. D. Pettit. “Photoelectrochemical passivation of GaAs surfaces”. *Journal of Vacuum Science & Technology B: Microelectronics and Nanometer Structures* Vol. 1 (1983), pp. 795–798 (cited on page: 199).

[8] S. J. Eglash, M. D. Williams, P. H. Mahowald, N. Newman, I. Lindau and W. E. Spicer. “Aluminum Schottky barrier formation on arsenic capped and heat cleaned

MBE GaAs(100)". *Journal of Vacuum Science & Technology B: Microelectronics and Nanometer Structures* Vol. 2 (1984), pp. 481–485 (cited on page: 199).

[9] A. Kahn, J. Carelli, D. L. Miller and S. P. Kowalczyk. "Comparative LEED studies of $Al_xGa_{1-x}As(110)$ and GaAs(110)–Al(theta)". *Journal of Vacuum Science and Technology* Vol. 21 (1982), pp. 380–383 (cited on page: 199).

[10] D. L. Miller, R. T. Chen, K. Elliott and S. P. Kowalczyk. "Molecular-beam-epitaxy GaAs regrowth with clean interfaces by arsenic passivation". *Journal of Applied Physics* Vol. 57 (1985), pp. 1922–1927 (cited on page: 199).

[11] C. González, I. Benito, J. Ortega, L. Jurczyszyn, J. M. Blanco, R. Pérez, F. Flores, T. U. Kampen, D. R. T. Zahn and W. Braun. "Selenium passivation of GaAs(001): a combined experimental and theoretical study". *Journal of Physics: Condensed Matter* Vol. 16 (2004), p. 2187 (cited on page: 199).

[12] J. G. Zhu, M. P. Nadesalingam, A. H. Weiss and M. Tao. "Stability of Se passivation layers on Si(001) surfaces characterized by time-of-flight positron annihilation induced Auger electron spectroscopy". *Journal of Applied Physics* Vol. 97 (2005), p. 103510 (cited on page: 199).

Chapter 8

Direct epitaxial growth of zinc blende MgS on GaAs and the development of reusable substrates

8.1 Introduction

Single crystal substrate wafers determine a significant part of the costs associated with both III-V and II-VI semiconductor manufacturing. As a result, for a variety of industrial applications including solar cells, the reuse of the wafer is economically beneficial. There exist several established techniques for substrate reuse in III-V material growth [1–4]. Due to a variety of reasons such as higher cost and poorer quality of commercially available II-VI wafers, II-VI materials are generally grown on latticed matched III-V substrates. However, currently there are no existing methods which enable the reuse of a substrate for II-VI regrowth.

The ELO technique in principle offers the most viable route of substrate reuse after separation of the deposited epitaxial layer and transfer to another carrier. In GaAs substrates (III-V growth), ELO is based on the etching away of a sacrificial layer of AlAs in an aqueous solution of HF. After ELO the substrate can be reused for further growth, but only after processing the surface. In II-VI materials, MgS is used as a replacement for AlAs (See Chapter 6) and etched in an aqueous solution of HCl. So far, MgS based ELO has never been used for recycling a substrate for II-VI material growth, primarily due to the inability to grow ZB MgS directly on a substrate. The ZB MgS has always required a buffer layer lattice matched to the substrate to initiate the growth. Despite several at-

tempts by various research groups described below, MgS has always undergone a phase change to RS when attempted growing directly on a substrate.

The first experimental demonstration of the growth of ZB MgS on a GaAs (100) substrate is demonstrated in this chapter. The layers are characterised using RHEED, XRD, PL, SIMS and SEM. ELO is then performed on these samples. Finally the first successful demonstration of substrate reuse for II-VI materials growth is detailed.

8.2 Direct growth of ZB MgS on GaAs

In this section, the first direct epitaxial growth of ZB MgS is detailed with various methods of layer characterisations. Growth rate as well as the Zn incorporation in MgS layers is determined and finally the dislocation densities of various MgS containing layers are compared to ensure the quality of structures.

8.2.1 History of direct MgS growth

The stable bulk crystal structure of MgS is RS and the ZB structure is metastable when grown epitaxially on a (001) GaAs substrate by using a growth technique such as MBE. This has severely limited the initial attempts to grow MgS layers of reasonable thickness in the metastable ZB phase. Teraguchi et al. were the first to grow ZnSe/MgS superlattices on GaAs substrates by MBE using elemental sources of Mg and S and a clear transition from two dimensional growth (2D) to three dimensional (3D) was observed from RHEED as the layer thickness increased [5]. This was attributed to the conversion of the ZB MgS to the RS phase and they estimated that the thickest MgS layer that could be grown without phase conversion was 0.96 nm.

Using ZnSe buffer layers, much thicker ZB MgS layers can be deposited before critical thickness is reached above which the structure reverts to RS [6]. Single ZB MgS layers of up to 67 nm thick were grown on a ZnSe buffer layer, increased in this thesis (see Chapter

4) to 200 nm by growing on top of an additional ZnSe/MgS/ZnSe smoothing layer at 240 ^{o}C.

Other attempts to grow thicker ZB MgS directly on GaAs substrate have always resulted in an apparent phase conversion as soon as the growth starts. A very thorough study recently confirmed that MgS only grows in the RS structure when deposited directly on GaAs under normal growth conditions [7]. Although ZB MgS grown on ZnSe buffer layers has found various applications, many potentially important applications such as reusable substrates requires the growth of ZB MgS directly on the substrate.

8.2.2 Growth procedures

During this work, GaAs (100) substrates from both AXT and Wafer Technologies were used. Minor changes were made to the existing pre growth preparations detailed in Section 4.2.2. After degassing in the preparation chamber, samples were transferred to the growth chamber where the oxide layer was desorbed at $\sim$580 °C and then cooled to the growth temperature 240 °C. No Zn flux was applied to the substrate during cooling down. After oxide removal, and during the 10-15 minutes needed to cool the sample to the growth temperature a sharp 4x2 RHEED pattern was always obtained indicating minimal surface contamination. No changes were noticed from RHEED at this stage compared to a sample cooled down under impinging Zn flux.

8.3 Direct growth of ZB MgS

Following the successful growth of ZB MgS on GaAs, GaP and InP substrates using buffer layers lattice matched to the substrates (see Chapter 5), it was evident that the key parameters in the stability of ZB MgS were the Mg flux followed by substrate temperature. Under optimised conditions the above mentioned work demonstrated the ZB MgS growth over a wide range of lattice mismatches ranging from -3.1% (GaP) to +4.4% (InP).

The most important factor in those growths was the use of a very low Mg:ZnS flux ratio

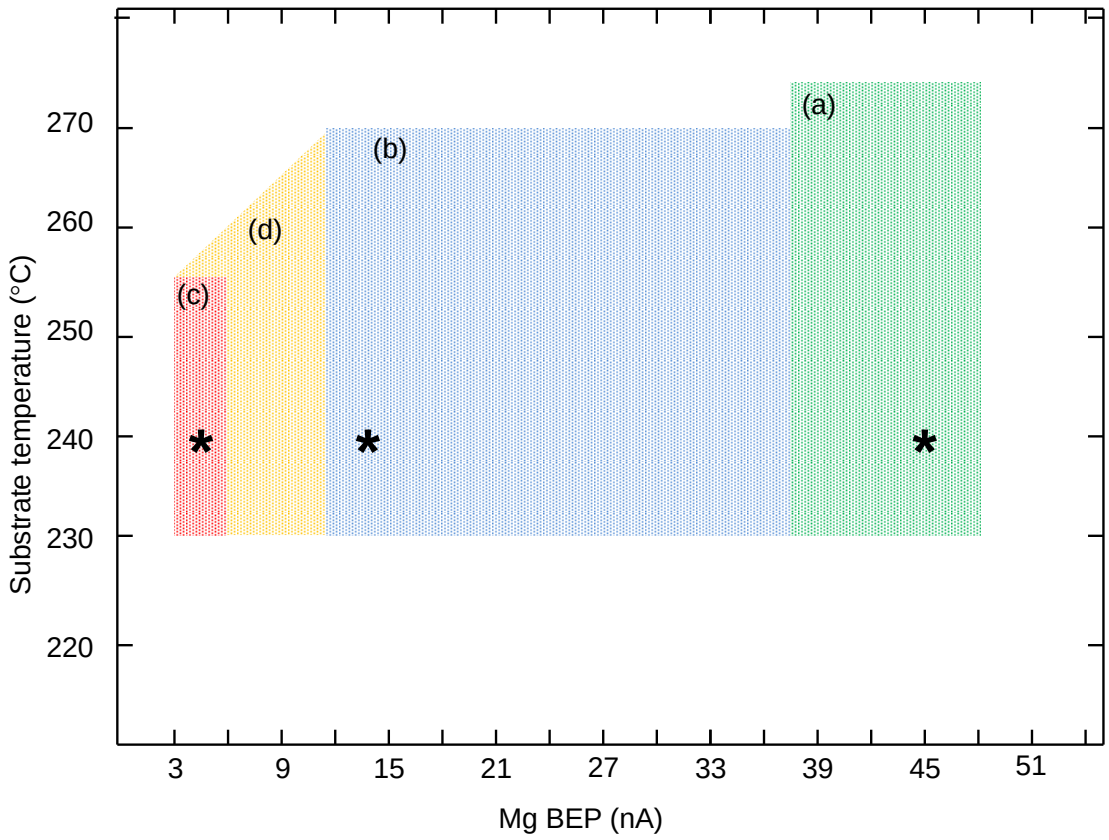

Figure 8.1: *Schematic of the different ZB MgS growth regions plotted in a phase diagram of Mg flux vs substrate temperature. (a) the region in green is where MgS was previously grown at Heriot-Watt, (b) the defect controlled growth of MgS on ZnSe buffer layers, detailed in Chapter 4 was performed in the area shaded in blue, whereas (c) the red box is the only area where ZB MgS can be grown directly on GaAs substrate. Note, the very narrow, 3 nA range of Mg flux. (d) Later it was found that MgS can be grown on a ZnSe buffer layer in the yellow shaded area as well, without compromising layer quality (however, the high temperature slope in this region is an estimate). $*$ denotes the optimal growth area where the thickest layers were grown within the corresponding regions, (a) 134 nm (on ZnSe buffer), (b) 200 nm (on ZnSe buffer) and (c) 35 nm (on GaAs substrate).*

of $\sim$ 1:42 as any increase in the Mg flux was noticed to significantly reducing the ZB thickness. Above a flux ratio of 1:35 it was almost impossible to grow ZB MgS on such widely lattice mismatched substrates.

The same method of controlling the Mg flux within a favourable growth temperature range was adopted to investigate the growth of ZB MgS directly on GaAs substrate. Initially a set of samples were grown by directly depositing MgS on the substrate at 240 ^{o}C. Fluxes of BEP 14 nA and 550 nA were used for Mg and ZnS (flux ratio of 1:40), based on the previous work on the effect of varying Mg flux on initial layer nucleation detailed in chapters 4 and 5 [8, 9]. However, as soon as the growth started, the sharp 4x2 RHEED pattern became diffuse and spottier. Within the first two monolayers growth, the RHEED became

completely spotty with elongated diffraction spots along <111> directions, indicating an abrupt transition from 2D to 3D growth as had seen previously [5].

Further growths were attempted by subsequently lowering the Mg flux and improvements in RHEED patterns were noticed. At a Mg BEP of 7.5 nA, the RHEED pattern showed streaky ZB growth for up to 2 minutes before indicating the reversion to rocksalt structure by showing chevrons as reported earlier [5].

Several samples with the structure MgS (5 min)/ZnSe (10 sec) were then grown by gradually lowering the Mg flux. Here a very thin ZnSe capping layer was grown to prevent the oxidation of MgS layer when in contact with atmosphere. In the region between 3 nA and 6 nA of Mg BEP, a narrow growth range was found, where MgS can be grown directly on GaAs in ZB up to 35 nm (20 min growth time) thick. Interestingly, the Mg:ZnS flux ratio within this growth range is $\sim$ 1:180. A schematic of the growth ranges used in this study compared to the normal MgS growth on ZnSe is shown in Figure 8.1.

A detailed analysis of the as-grown MgS layers directly deposited on GaAs substrate is given in the following section.

8.3.1 Analysis of MgS layers

RHEED was extensively used to observe the growth of MgS. The Mg flux dependence of the ZB phase of MgS was constantly monitored and was significant in locating the very narrow growth regime. The ZB phase of layers up to 35 nm has been confirmed by RHEED observations during the growth of the MgS layer, which showed clear and sharp integral streaks with faint c(2x2) patterns throughout, which is normal for good quality MgS growth.

After the initial successful growths, several samples were grown for X-ray characterisation. Although direct diffraction from thinner MgS layers is extremely difficult, a sample with the thickest MgS layer was examined with XRD. Figure 8.2 shows the 004 XRD from this sample grown at 240 ^{o}C with the structure GaAs (sub)/ MgS (35 nm)/ZnSe(3

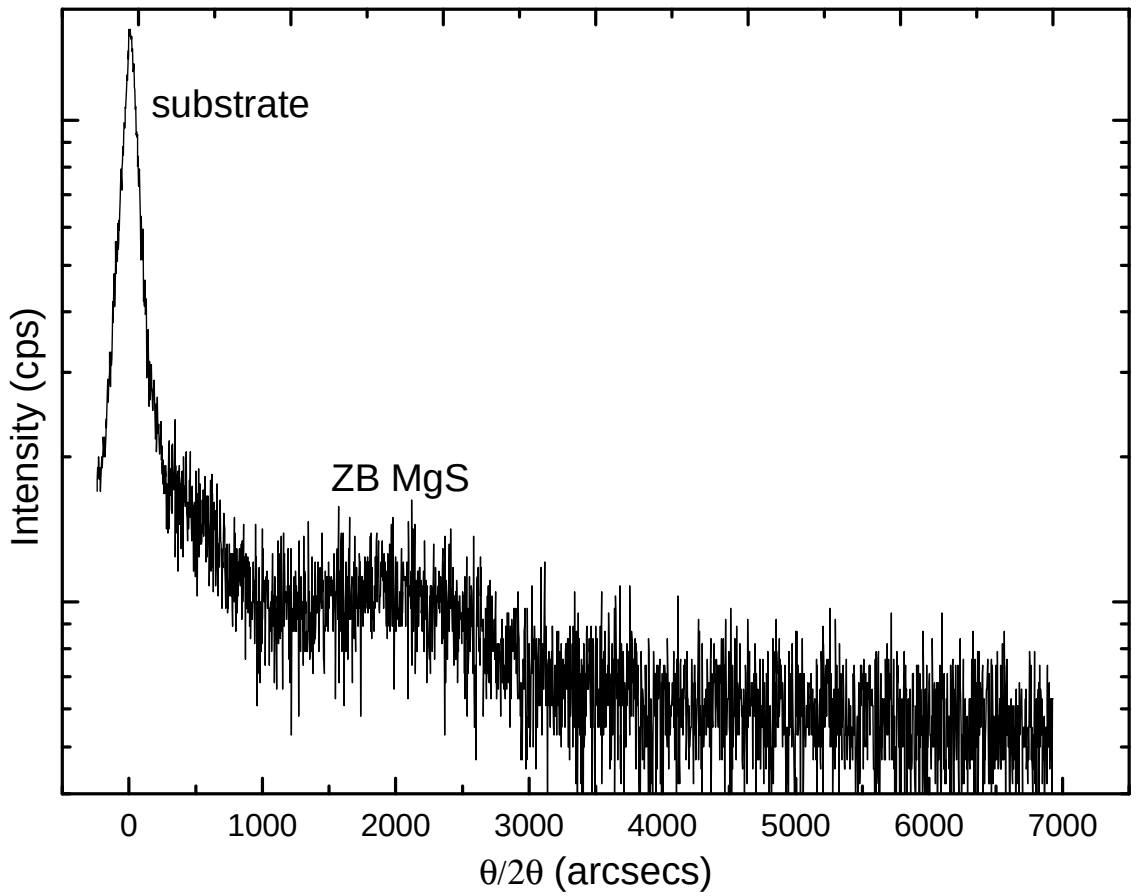

Figure 8.2: *004 XRD scan of the structure GaAs(sub)/ MgS(35 nm)/ ZnSe(3 ML), showing the ZB MgS peak at $\sim$ 2000 arc secs. The noise on the scan is the result of using a wider detector slit as it is difficult to get a well resolved XRD peak from such a thin MgS layer.*

ML). A diffraction signal from the MgS layer was observed at $\sim$ 2000 arc secs showing that the layer retained the ZB crystal structure.

Subsequently a sample with the structure GaAs (sub)/ MgS (12nm)/ ZnSe (300nm) was grown and characterised using X-rays. Here thicker ZnSe capping layers are used primarily to calculate the dislocation densities and probe the layer quality (results are given in Section 8.3.5). Figure 8.3 shows the 004 XRD experimental scan data from this sample which shows a well defined ZnSe peak. The observation of the ZnSe epilayer peak on 004 reflection further confirms that the structure was indeed ZB.

A ZnCdSe quantum well structure was also grown in the form MgS (buffer, 20nm)/ ZnCdSe (quantum well, 4.5nm)/ MgS (barrier, 20nm)/ ZnSe (cap, 3ML). Photoluminescence from this sample is given in Figure 8.4. The QW emission can be seen at 2.37 eV, whereas the emission from the MgS barriers could not be observed as the laser excitation

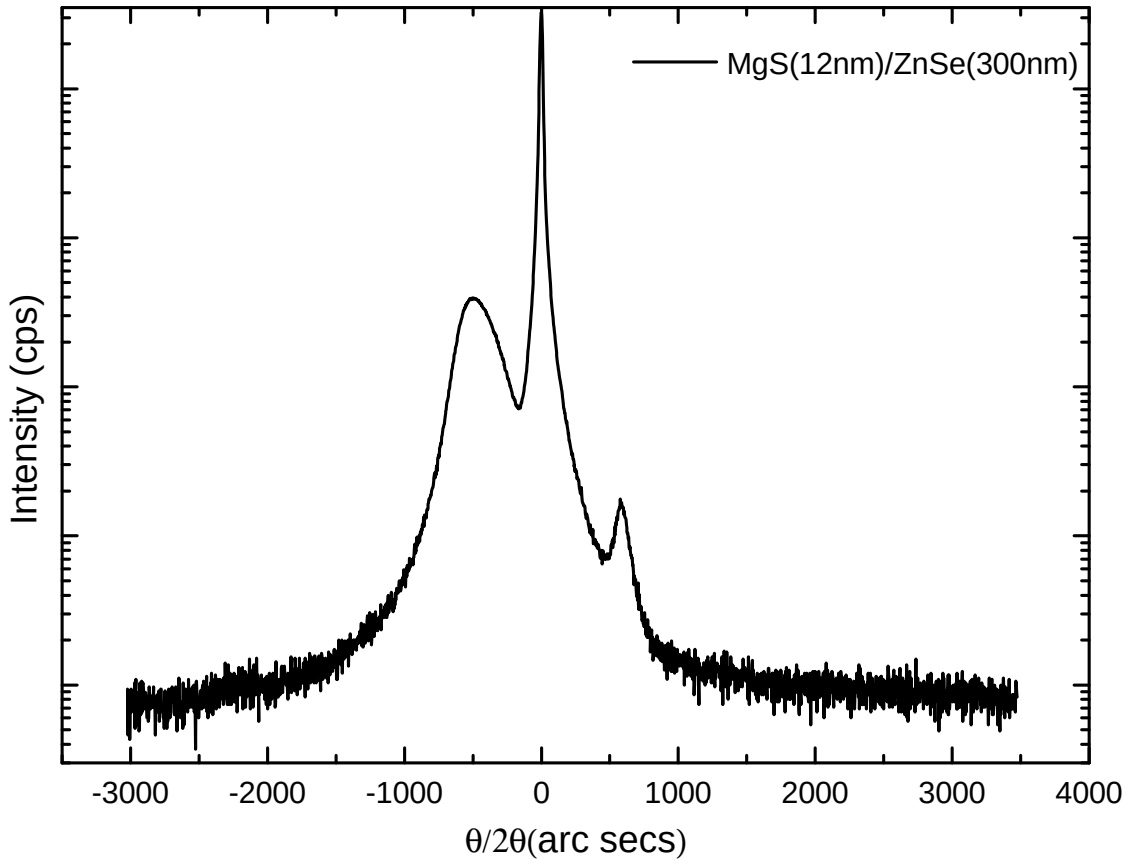

Figure 8.3: *004 XRD scan of the structure GaAs(sub)/ MgS(12 nm)/ ZnSe(300 nm), showing the ZnSe peak at -500 arc secs. The smaller peak at +580 arc secs is a stray reflection from CuKα_2 radiation. MgS at this thickness will not generate an XRD peak.*

energy of 3 eV was lower than the band gap of MgS. The PL excitation is not efficient, as pumping is directly into the well. However the fact that there is any emission at all means that the structure is reasonably free of non-radiative defects and that the MgS barrier is continuous.

The sample shown in Figure 8.3 was also examined by SIMS (Loughborough Surface Analysis). Sharp interfaces were observed between the GaAs, MgS and ZnSe layers and as expected a small residual Zn signal was found in the MgS layer as seen in Figure 8.5. The Zn concentration estimated from SIMS measurements is a maximum of 2 %, assuming that the sputtering rates for Zn in both the ZnSe and MgS matrices are similar. The Zn incorporation was further confirmed during the XRI growth rate measurements detailed in the following section. A comparison of the 004 and 115 reflections showed that this sample was sufficiently thick to be $\sim$ 90% relaxed.

Finally, the sample mentioned above was studied using SEM. As shown in Figure 8.6 the

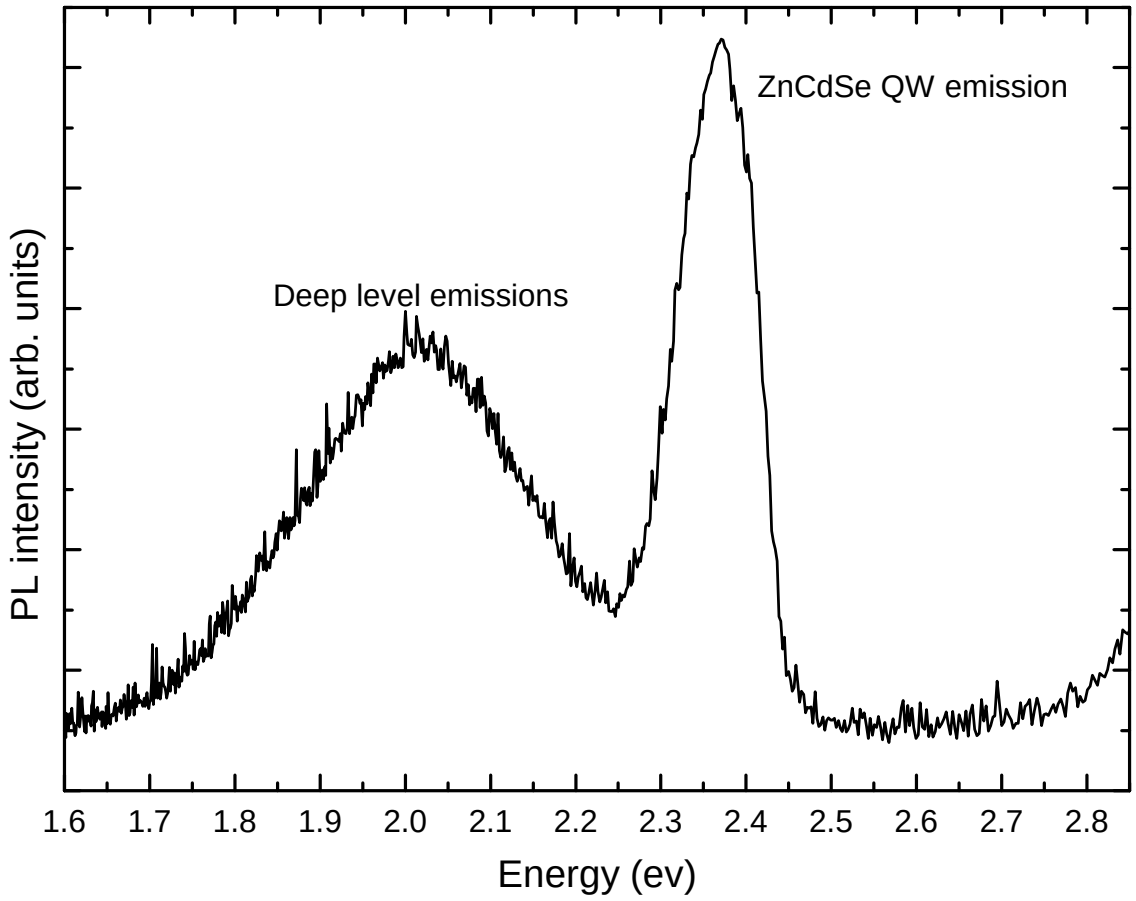

Figure 8.4: *77K Ensemble PL from the structure MgS(20nm)/ ZnCdSe(4.5nm)/ MgS(20nm)*

MgS layers can be seen, sandwiched between GaAs and ZnSe layers.

8.3.2 Growth rate calibration

Initially, growth rate was estimated from the samples grown previously with a Mg BEP of 13 nA. To study the effect of the lower Mg flux on growth rate, composition and crystal quality, three X-Ray Interference (XRI) samples were further grown with the structure ZnSe(40 nm)/MgS/ZnSe(40 nm) where the MgS layer was grown for 1, 2 and 3 min. BEP of 3.5 nA and 500 nA were used for Mg and ZnS respectively. Both 004 and 115 reflections were used to obtain an unique layer thickness and composition [10]. A growth rate of $\sim$0.34 Å/s was obtained from XRI. All samples had well resolved XRI diffraction fringes, which is indicative of good crystallinity throughout the entire structure. The Zn mole fraction in the MgS layers was 0-2.2%, which is in the same range as previously obtained with Mg fluxes 15 times larger [6] and is in good agreement with the value estimated from SIMS analysis.

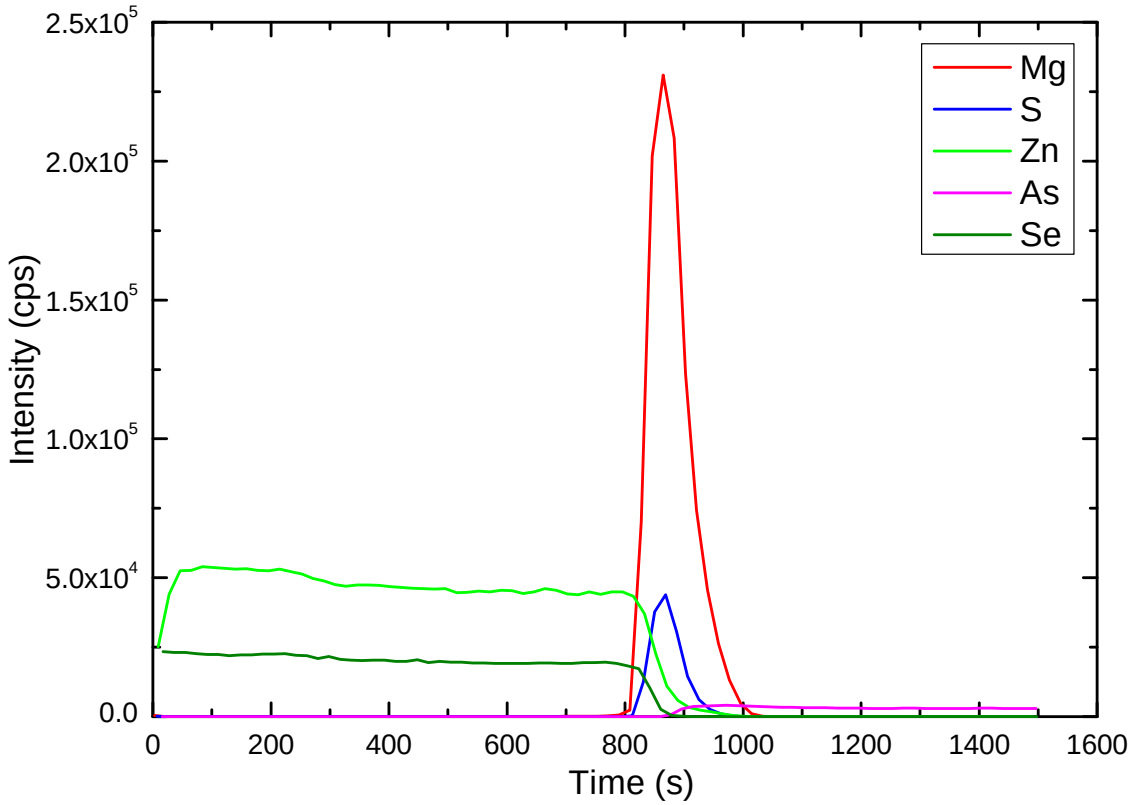

Figure 8.5: *SIMS analysis of the structure GaAs(sub)/ MgS(12 nm)/ ZnSe(300 nm).*

8.3.3 Re-evaluation of the Mg sticking coefficient

The sticking coefficient of an element is the fraction of the arriving atoms that incorporate into the epitaxial layer. Changes in growth temperature and II-VI flux ratio can affect the sticking coefficient so the values determined here are specific to the growth conditions at Heriot-Watt. Earlier studies at Heriot-Watt on MgS grown with higher Mg fluxes has estimated a sticking coefficient of 0.4 and this value is used here for comparison [11].

The flux of magnesium atoms arriving at the surface, J_{Mg} is proportional to the ion gauge current, I_{Mg},

$$J_{Mg} = KI_{Mg} \tag{8.1}$$

where, K is the constant of proportionality. However, not all atoms incorporate in the surface, but only an amount J_{Mg}^{Inc},

$$J_{Mg}^{\text{Inc}} = J_{Mg} \times S \tag{8.2}$$

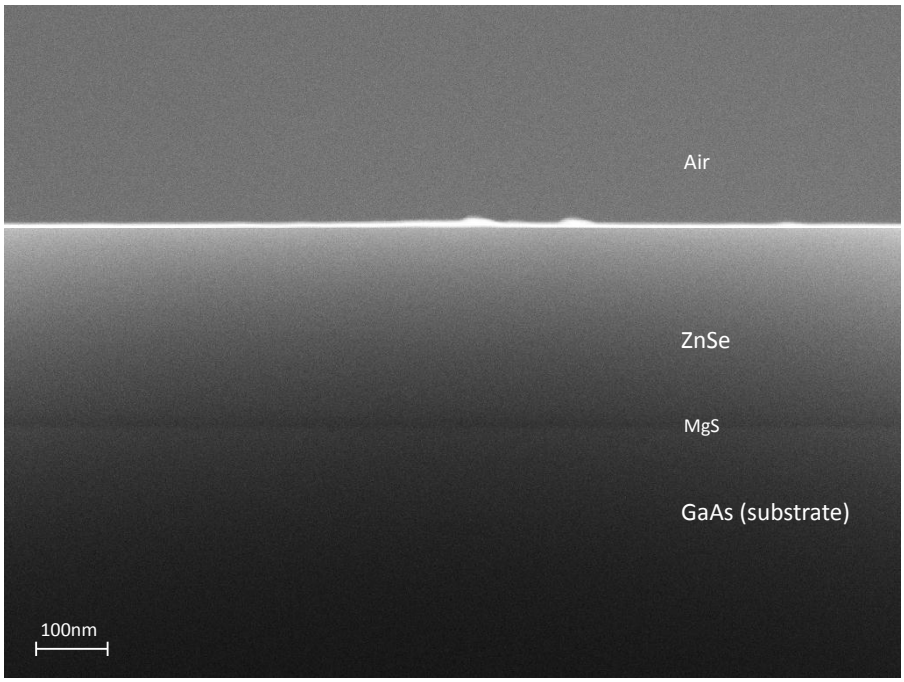

Figure 8.6: *SEM image of the structure GaAs(sub)/ MgS(12 nm)/ ZnSe(300 nm).*

where, S is the sticking coefficient. Similarly, J_{Mg}^{Inc} is proportional to the growth rate, g,

$$g = A \times J_{Mg}^{\text{Inc}} \tag{8.3}$$

where, A is the constant of proportionality. There are two slightly different growth rates, g_1 and g_2 on the two corresponding growth regimes, (1) older higher Mg flux growth and (2) the recent low Mg flux growth. Importantly, here K is a constant and S is a variable.

Combining Equations 8.1, 8.2 and 8.3,

$$g = AJ_{Mg}^{\text{Inc}} = ASJ_{Mg} = ASKI_{Mg} \tag{8.4}$$

$$\frac{g_2}{g_1} = \frac{AS_2KI_{Mg_2}}{AS_1KI_{Mg_1}} \tag{8.5}$$

or

$$\frac{g_2}{g_1} = \left(\frac{S_2}{S_1}\right)\left(\frac{I_{Mg_2}}{I_{Mg_1}}\right) \tag{8.6}$$

Here, g_1 and g_2 are 0.45 Ås^{-1} and 0.34 Ås^{-1} respectively, whereas assuming S_1, is 0.4 (as estimated earlier at Heriot-Watt, using the MgS samples grown with higher Mg flux [11]) and I_{Mg_1} and I_{Mg_2}, 45nA and 5nA respectively, the sticking coefficient, S_2 is found

to be in the region of 0.2, under the growth conditions used previously.

8.3.4 Stability of the growth range

Subsequently samples were grown by changing the growth temperature. The stability of ZB phase was found to be maintained between a growth temperature of 235-250 ^{o}C. For any temperature above this range, the maximum ZB MgS thickness dropped significantly. At a growth temperature of 255 ^{o}C, phase conversion was observed at 3.2 nm. Similarly, any lower temperature was found to increase the Zn mole fraction. Samples grown at 220^{o}C showed $\sim$ 10 % Zn incorporation. No changes were made in the ZnS flux, as in Chapter 4 it was shown that the growth of MgS is not affected by any variation in a large ZnS flux range between 450 nA and 750 nA [8].

A comparison of the growth ranges where ZB MgS can be grown directly on GaAs substrate and also on ZnSe buffer layers is schematically shown in Figure 8.1. All the samples grown within region C in the Figure 8.1 had a usable growth rate and low Zn incorporation. No growths on ZnSe buffer layer were attempted in region D. However from the growth rate and layer composition determination in region C (Section 8.3.2), it is evident that even at a lower Mg BEP of 3 nA, the Zn mole fraction has not increased within this temperature range. This shows that there is every possibility for successful ZB MgS growth on ZnSe buffer layers in region D.

8.3.5 Comparison of dislocation densities

In thick relaxed semiconductor layers, the dislocation density can be measured and its anisotropy determined by measuring the FWHM of the layer peak at different azimuthal angles (Detailed in Section 5.6) [12].

To compare the dislocation densities, two samples were grown where the first had the conventional ZnSe (40 nm)/MgS (10 nm)/ZnSe (300 nm) structure whereas the second sample contained the new MgS (10 nm)/ZnSe (300 nm) structures. 004 rocking curves

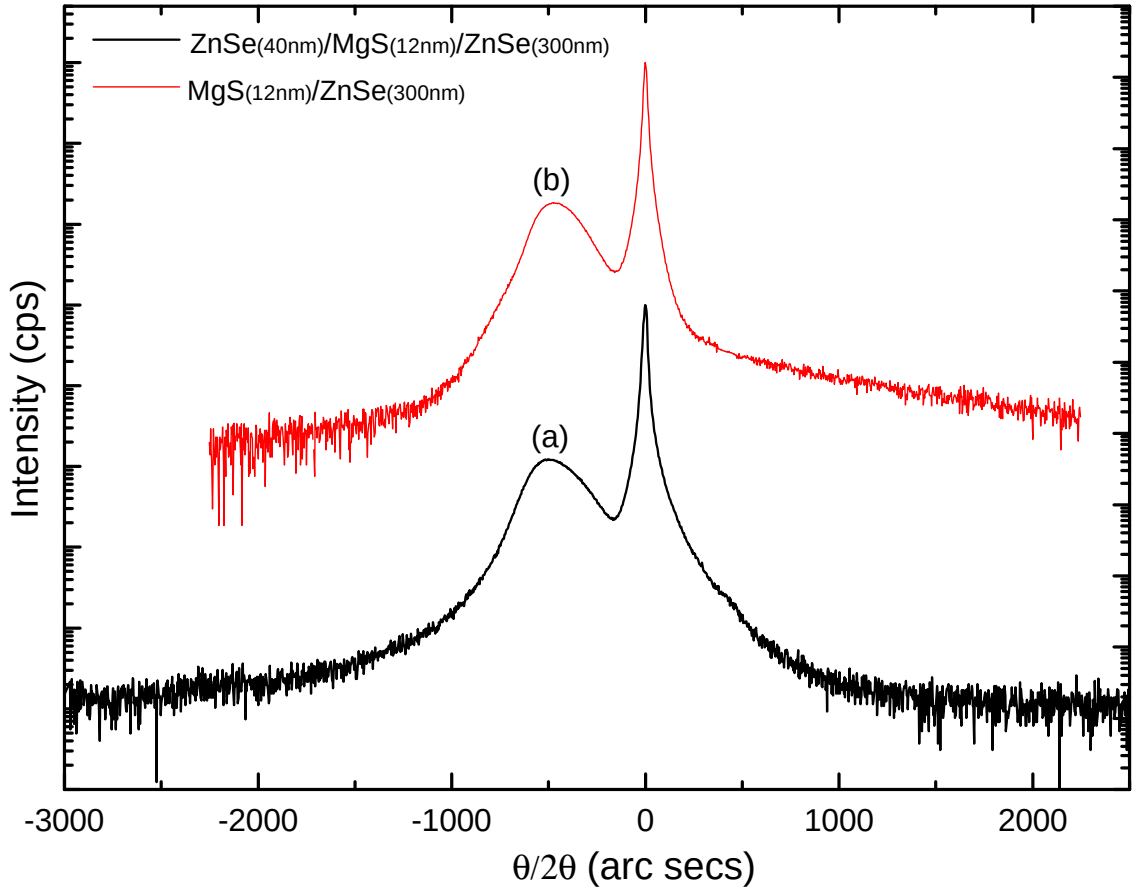

Figure 8.7: *A comparison of 004 XRD scans from structures (a) ZnSe(40nm)/ MgS(12nm)/ ZnSe(300nm) and (b) MgS(12nm)/ ZnSe(300nm). The dislocation densities calculated from the ZnSe epilayer peaks are given in Table 8.1*

were obtained (Figure 8.7) from the epitaxial layers and their dislocation densities estimated for [110] and [1$\bar{1}$0] directions are listed in Table 8.1. All are anisotropic with fewer dislocations along [110] than [1$\bar{1}$0]. Previously published results for epitaxial ZnSe layers grown on GaAs [12] show almost identical dislocation densities to the GaAs/ZnSe/MgS/ZnSe structures examined here. Surprisingly the GaAs/MgS/ZnSe (second set) structures on the other hand, show fewer dislocations than the first set. This reduction in dislocations can be attributed to the absence of the slightly compressive strained (0.3 %), 40 nm thick ZnSe buffer layer. The lower dislocation density on a GaAs/MgS system is interesting and can be used in a wide range of applications, as all of the present day MgS based structures and devices require the growth of a ZnSe barrier.

Heterostructure	Dislocation density (cm^{-2}) $D_{[110]}$	$D_{[1\bar{1}0]}$
ZnSe/MgS/ZnSe	2.02 x10^8	2.10 x10^8
MgS/ZnSe	1.52 x10^8	1.58 x10^8
GaAs/ZnSe [12]	2.0 x10^8	2.50 x10^8

Table 8.1: *Comparison of dislocation densities calculated from two azimuths from 300 nm thick ZnSe capping layer FWHM.*

8.4 Reusable substrates

One of the most important challenges faced by the semiconductor growth industry is high production costs, for a significant part associated with the price of the substrates which are necessary to obtain the generally desired single crystal layer structures. Once the structure is grown, the substrate may not have any functions other than being an expensive carrier for the structure.

In order to reuse a substrate, the first step involves the successful removal and subsequent deposition of the epilayers. Probably the most successful method for GaAs has been ELO. In III-V material systems, ELO utilizes the etching away of a very thin, $\sim$ 10 nm sacrificial AlAs layer in HF. In II-VI materials, a similar thin MgS layer is removed in HCl to separate the epilayers from the substrate. Due to the extreme selectivity of HCl (the contrast in etch rates between MgS and ZnSe in HCl is $\sim 10^8$ [13]), the substrate is left unaffected and can in principle be reused for regrowth.

The viability of the ELO based substrate reuse in III-V materials is well demonstrated by the different III-V devices which have been integrated with foreign substrates such as LEDs on silicon [14, 15], lasers on glass and silicon [16, 17], photo detectors on glass and silicon [18, 19], optical modulators on glass [20, 21], and GaAs MESFETs on an InP directional coupler and a lithium niobate optical switch [22].

One major disadvantage on III-V ELO is that the exposure to the HF solution increases the surface roughness of the wafer on a nanometer scale which prevents its direct reuse. This requires extensive cleaning of the substrate before a regrowth can be commenced.

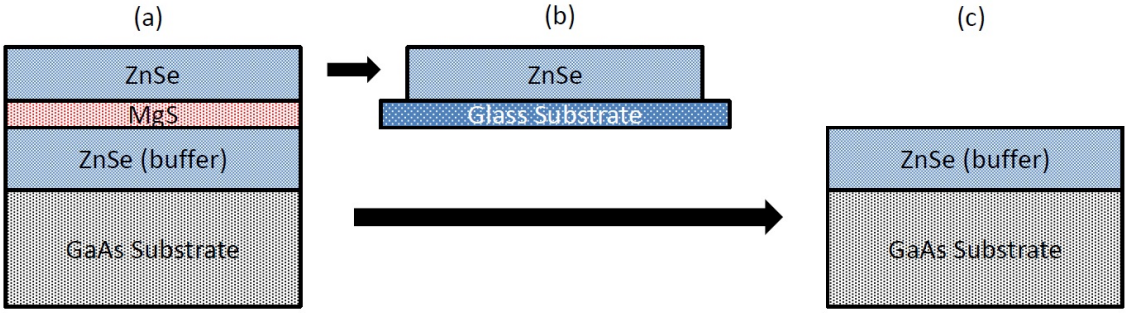

Figure 8.8: *Schematic representation of the GaAs/ZnSe heterostructure based reusable substrate technique.*

There are many re-preparation methods including chemical polishing and mechanical polishing. In chemical polishing, various polishing etch solutions are used to smoothen the substrate surface, but as a result a few microns of substrate is lost every time. In mechanical polishing (also used for the fabrication of epi-ready GaAs substrates), any surface contamination is removed firstly, followed by a chemo-mechanical planarization process to polish the surface. The minimum thickness loss is $\sim 10\ \mu$m in this case and considering the average thickness of a $2^{"}$ substrate being 350 μm, there is limit in the maximum number of times a substrate can be reused. All these processes require additional processing and are costly (but, still up to 80 % cheaper than the cost of new substrates).

The 30% aqueous solution of HCl used in MgS based II-VI ELO, on the other hand is less reactive compared to HF. However the concept of reusable substrates has never been tried in II-VI growth primarily due to the fact that MgS, in ZB phase has never been grown directly on a substrate before. Following the successful demonstration of the direct epitaxial growth of ZB MgS on GaAs (Section 8.2), the substrate reuse is studied in detail in the following sections.

8.4.1 Initial attempts on ZnSe buffer layers

Initially, the possibility of ZB MgS growth directly on a substrate was not considered as a number of reports, mentioned in the previous sections had proved it not possible. During the early stages of this project, the idea of substrate reuse was focussed around the growth of MgS on a ZnSe buffer layer, etching away the MgS layer thus releasing the epilayer and performing regrowth on the ZnSe layer.

Figure 8.8 shows a schematic representation of the MgS based regrowth on a ZnSe buffer layer. A buffer layer up to 50 nm thick is first grown on a GaAs substrate, followed by a 10 nm layer of MgS and a further 50 nm ZnSe cap layer. ELO is then performed on these samples, resulting in the separation of the ZnSe cap layer. The lifted ZnSe epilayer is then transferred and deposited onto a glass substrate. The remaining substrate structure (GaAs/ZnSe(50 nm)) is taken out of the etch solution as soon as the lift-off is complete and rinsed with DI water. The substrate and ZnSe buffer is then chemically etched before transferring to the growth chamber for regrowth.

8.4.2 Surface preparation of ZnSe

The main challenge faced during the regrowth on ZnSe buffer layer was the surface preparation. RHEED images from a ZnSe surface reintroduced into the growth chamber for regrowth showed diffuse streaks indicative of a smooth surface with some oxidation. Although the oxide layer formation on a ZnSe surface is regarded as a slow reaction, few monolayers thick ZnO could be formed by the time, the GaAs/ZnSe structure is back in the growth chamber after ELO.

Previously, hydrogen plasma assisted oxide layer removal was successfully performed on ZnSe substrates [23]. Here, oxygen, chlorine and carbon contamination was removed from the surface of a ZnSe layer by exposure to hydrogen containing plasma. The same group also demonstrated the use of reactive ion etching using BCl_3 for removing a few nanometers of the defective ZnSe surface layer, thus exposing a flat, new layer of ZnSe. However both of these facilities were not available at Heriot-Watt, which required investigating other techniques.

One method of removing the oxide layer is the sulphidisation of the surface. This method has been shown to improve heteroepitaxial growth rates when used on GaAs substrates [24]. The ZnSe surface is etched in a solution of ammonium sulphide $(NH_4)_2S$ to strip away the oxide layer and terminate the surface with sulphur. This was tried, but no significant improvements were visible in RHEED compared to an unetched surface and hence this method was abandoned.

Subsequently GaAs/ZnSe samples were grown and treated with the HCl etch solution to simulate the ZnSe surface after ELO. These samples were then chemically etched using the standard GaAs cleaning solution and transferred to the growth chamber. Initially RHEED showed diffuse streaks, so vacuum annealing was performed on these samples before growth. Heating to $\sim 580^{o}$C lead to slight improvements in the RHEED pattern. When cooled down to the growth temperature of 240^{o}C the RHEED showed sharper streaks indicating a much smoother surface.

8.4.3 Regrowth on ZnSe

Growths were initiated on the vacuum annealed GaAs/ZnSe structures by first depositing a layer of ZnSe. As soon as the regrowth started, the RHEED pattern went very spotty for the first two minutes, indicating 3D growth. RHEED started to improve after two minutes and after three minutes of growth, the 2×1 pattern re-appeared showing very streaky integral streaks which remained throughout the rest of the growth.

It was evident from the RHEED patterns that the first two to three minutes of the ZnSe regrowth was 3D, which corresponds to the growth of approximately 10 nm of ZnSe. Although the remaining growth was smooth, the possibility of dislocations introduced by the nucleation on the ZnSe-ZnSe interface cannot be ignored. Likewise, another disadvantage of this method is that every regrowth requires the deposition of at least 10 nm of excess ZnSe in order to smoothen the interface. This eventually leads to a much thicker substrate structure (GaAs/ZnSe) and as the thickness increases, the critical thickness for relaxation of ZnSe buffer layer become closer, resulting in more dislocations.

One of the samples, initially grown for this work was HWC485 with a structure GaAs(sub)/ ZnSe(40nm)/ MgS(10nm)/ ZnSe(300nm). Here a thick ZnSe capping layer was grown to compare the dislocation densities from x-ray diffraction peaks. After growth, 004 XRD scans from both [110] and $[1\bar{1}0]$ azimuths were obtained. A 50% relaxed single ZnSe epilayer was observed from XRD. Upon simulating, a fully strained buffer layer peak was found to be superimposed in the 50% relaxed epilayer peak. ELO was performed on the sample and the 300 nm thick ZnSe epilayer was released from the substrate structure

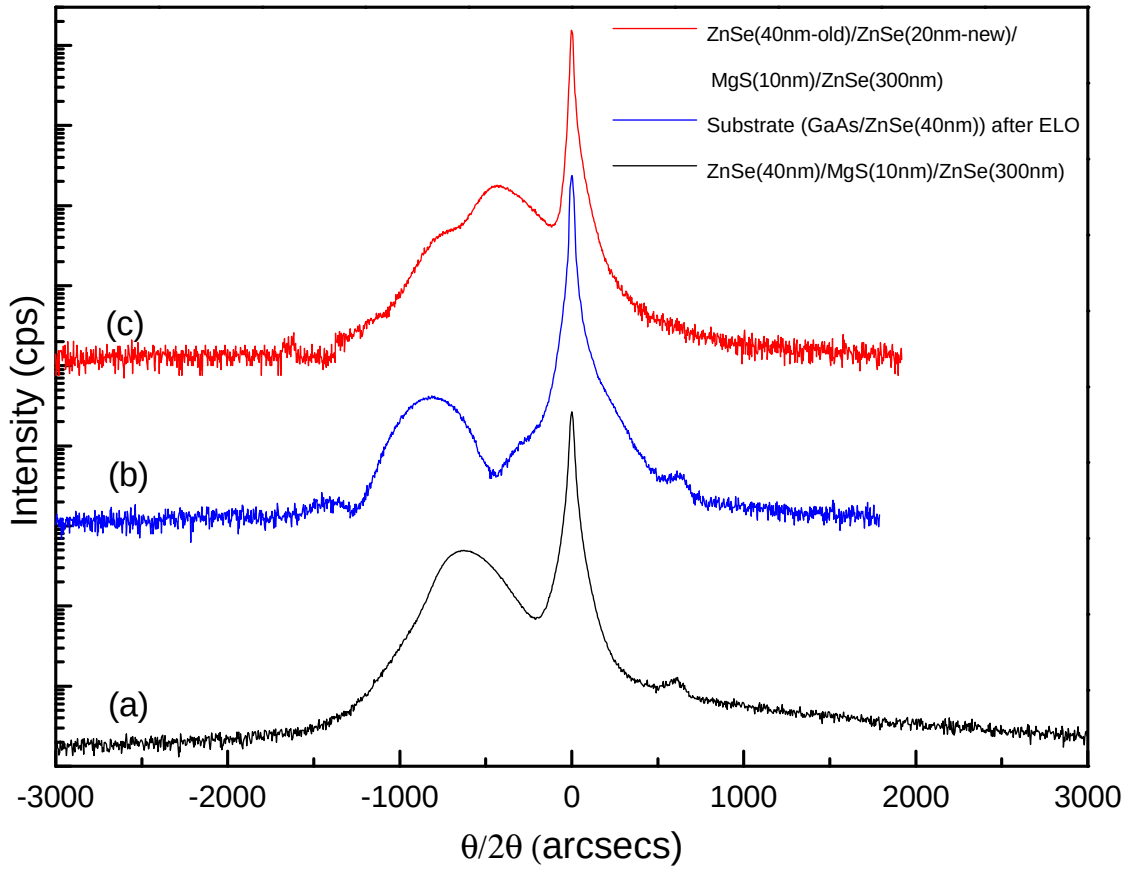

Figure 8.9: *004 XRD scans from (a) HWC485 with the structures GaAs(sub)/ ZnSe(40nm)/ MgS(10nm)/ ZnSe(300nm), (b) after ELO with a structure GaAs(sub)/ ZnSe(40nm) and (c) HWC512 which has a structure ZnSe(20nm)/ MgS(10nm)/ ZnSe(300nm) grown over (b)*

(GaAs/ZnSe). This structure was then examined using XRD and a completely strained, 40 nm thick ZnSe layer was found. A comparison of the XRD of HWC485 before and after ELO is given in Figure 8.9(scans (a) and (b) respectively).

The GaAs/ZnSe substrate structure was then chemically etched, vacuum annealed and a regrowth was performed. The initial spotty RHEED patterns became streaky and showed a 2×1 pattern after two minutes of ZnSe regrowth. This new sample denoted HWC512, has a structure GaAs(sub)/ ZnSe(40nm-old)/ ZnSe(20nm-new)/ MgS(10nm)/ ZnSe(300nm). By the end of the ZnSe buffer growth a very strong and streaky 2×1 pattern was visible which transformed to a c(2×2) pattern during the MgS growth and reverted to a 2×1 pattern during the ZnSe cap layer growth.

004 XRD scans from [110] and [1$\bar{1}$0] azimuths were obtained again. An asymmetric ZnSe epilayer peak, clearly showing at least two ZnSe layers with different strain states can be seen from Figure 8.9(c). The most intense peak, from the 300 nm ZnSe was 100%

Heterostructure	Dislocation density cm^{-2} $D_{[110]}$	$D_{[1\bar{1}0]}$
HWC485	2.02 x10^8	2.10 x10^8
HWC512	5.19 x10^8	5.32 x10^8

Table 8.2: *Comparison of dislocation densities calculated from two azimuths from 300 nm thick ZnSe capping layer FWHM (shown in Figure 8.9).*

relaxed whereas the smaller buffer layer peak showed a 10% relaxation.

When comparing the 300 nm thick ZnSe layer on both HWC485 and HWC512, an increase of relaxation from 50% to 100% can be seen. One of the reasons for the increase in capping layer relaxation is the presence of an additional 20 nm ZnSe buffer layer. But such a thin layer cannot possibly contribute such an increase in the layer relaxation. The presumable cause is the origin of the dislocations at the ZnSe-ZnSe interface as a result of the 3D growth evidenced by RHEED. A comparison of XRD scans from samples HWC485 and HWC512 is given in Figure 8.9(scans (a) and (c) respectively). Upon comparing the dislocation densities of the 300 nm ZnSe epilayers of both HWC485 and HWC512, a considerable increase in dislocations were found in HWC512 (Table 8.2).

8.5 First successful demonstration of completely reusable substrates for II-VI growth

In this section, the first successful demonstration of reusing a III-V substrate for continuous II-VI material regrowth is detailed. Reusable substrates were not tried before in II-VI materials as previously it was not possible to grow an ELO release layer directly on a substrate. With increased confidence from the successful growth of ZB MgS layers directly on GaAs substrate as detailed in Section 8.3, the next obvious step was an attempt at reusable substrates.

A GaAs(substrate)/ MgS(10nm)/ ZnSe(300nm) structure was grown to demonstrate the process. A schematic representation of this method is given in Figure 8.10. A quarter of a 2" GaAs wafer from AXT was used for the regrowth. The first structure was grown

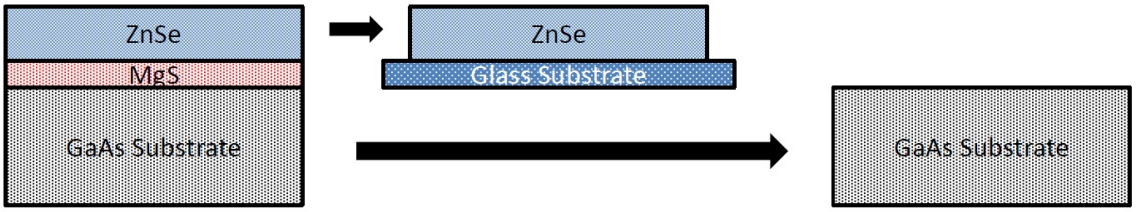

Figure 8.10: *Schematic representation of the directly deposited MgS based reusable substrate technique.*

using the standard growth procedure. XRD scans from [110] and [1$\bar{1}$0] azimuths were obtained.

The 300nm thick epilayer was then carefully lifted off the substrate using ELO. The substrate was then taken out of the etch solution, rinsed using DI water, dried using OFN and 004 XRD scans obtained. The surface of the substrate was examined using AFM and UVM and was devoid of any nanoscale surface formations or defects. AFM analysis over a 20μm $\times$ 20μm area showed a near atomically flat area with an RMS surface roughness of 0.5 nm.

Before commencing the second growth on the substrate, a chemical etch was performed to remove any surface contaminations. This time a different etch solution replaced the standard 20:2:2 H_2SO_4:H_2O_2:H_2O etch solution. Earlier in this study it was noted that upon contact with the standard etch solution, the indium glue on the back of the previously used substrate, reacts and forms a white residue. This eventually leaves a thin layer of white contamination on the substrate surface and it is very difficult to clean afterwards, making the substrate unusable. One possibility is the formation of indium sulphate ($In_2(SO_4)_3$) as a result of the reaction between indium and the concentrated sulphuric acid containing etch solution.

After various tests a less acidic etch solution, 4:1:100 solution of H_2SO_4 : H_2O_2 : H_2O was found to be effective with two minutes of etching. This solution was used for all the chemical etches afterwards. The substrate was always rinsed thoroughly after the chemical etch in DI water to make sure no impurities are left on the surface before finally loading into the growth chamber. No changes were made to the substrate bonding stage, where the standard indium glue was used.

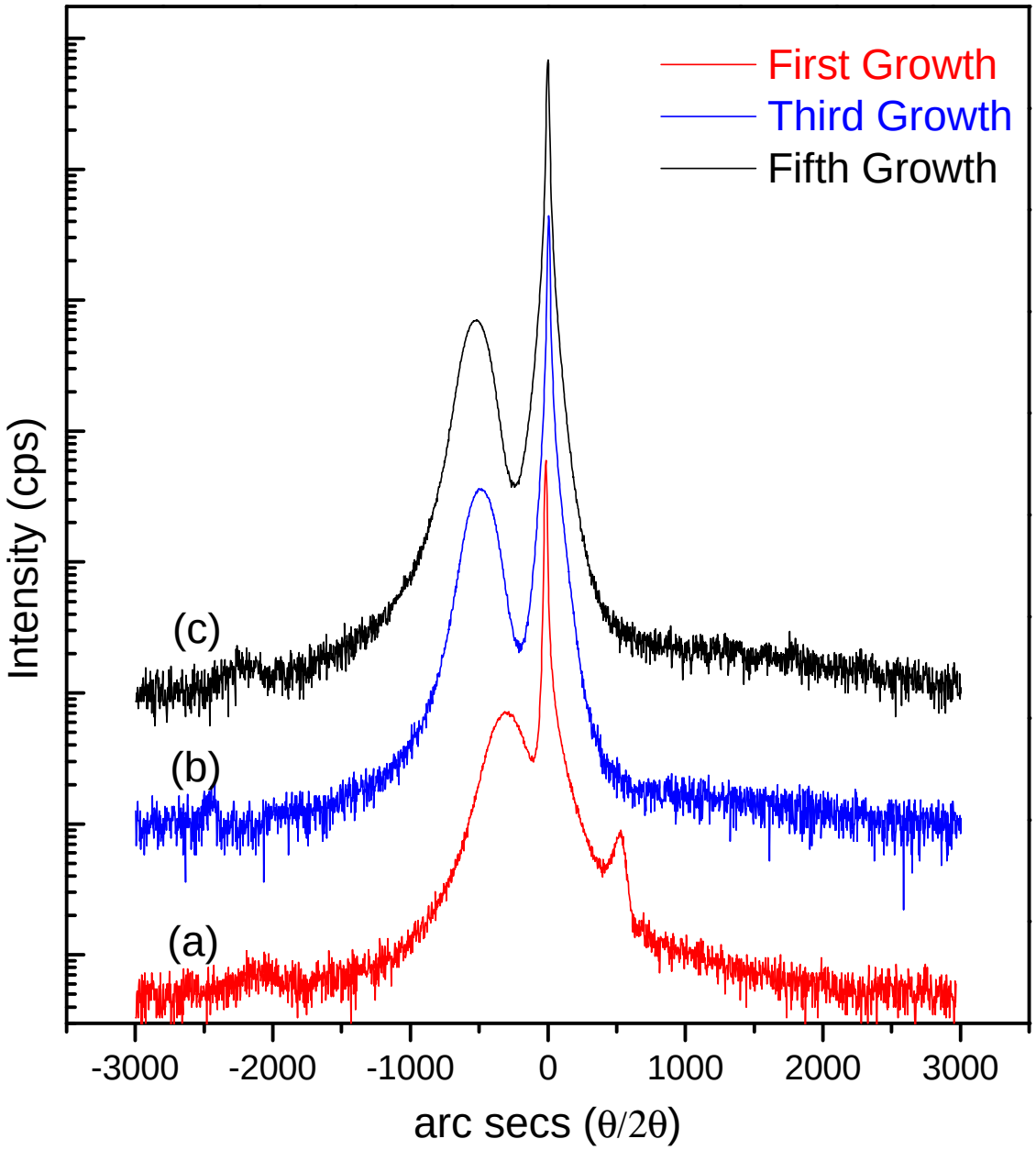

Figure 8.11: *004 XRD scans from the structure GaAs(sub)/ MgS(10nm)/ ZnSe(300nm) grown on a single GaAs wafer, (a) first growth, (b) third regrowth and (c) fifth regrowth. ELO was performed every time to remove the 300nm ZnSe epilayer. 004 scans from the respective substrates after ELO can be seen in Figure 8.12*

.

The substrate was heated and the oxide layer was removed. No change in the RHEED pattern sequence was observed. Upon oxide removal a 4×2 pattern was observed which remained through to the growth temperature. MgS was first deposited on the substrate, with a faint c(2×2) appearing initially after 20 sec which became sharper in 2 minutes. The growth afterwards was steady with no indication of spots in the RHEED pattern. Remarkably the interface seemed to be similar to that of a new substrate with absolutely no signs of surface nucleation seen in the RHEED pattern. The 2×1 RHEED pattern visible during the ZnSe deposition was sharp and streaky throughout.

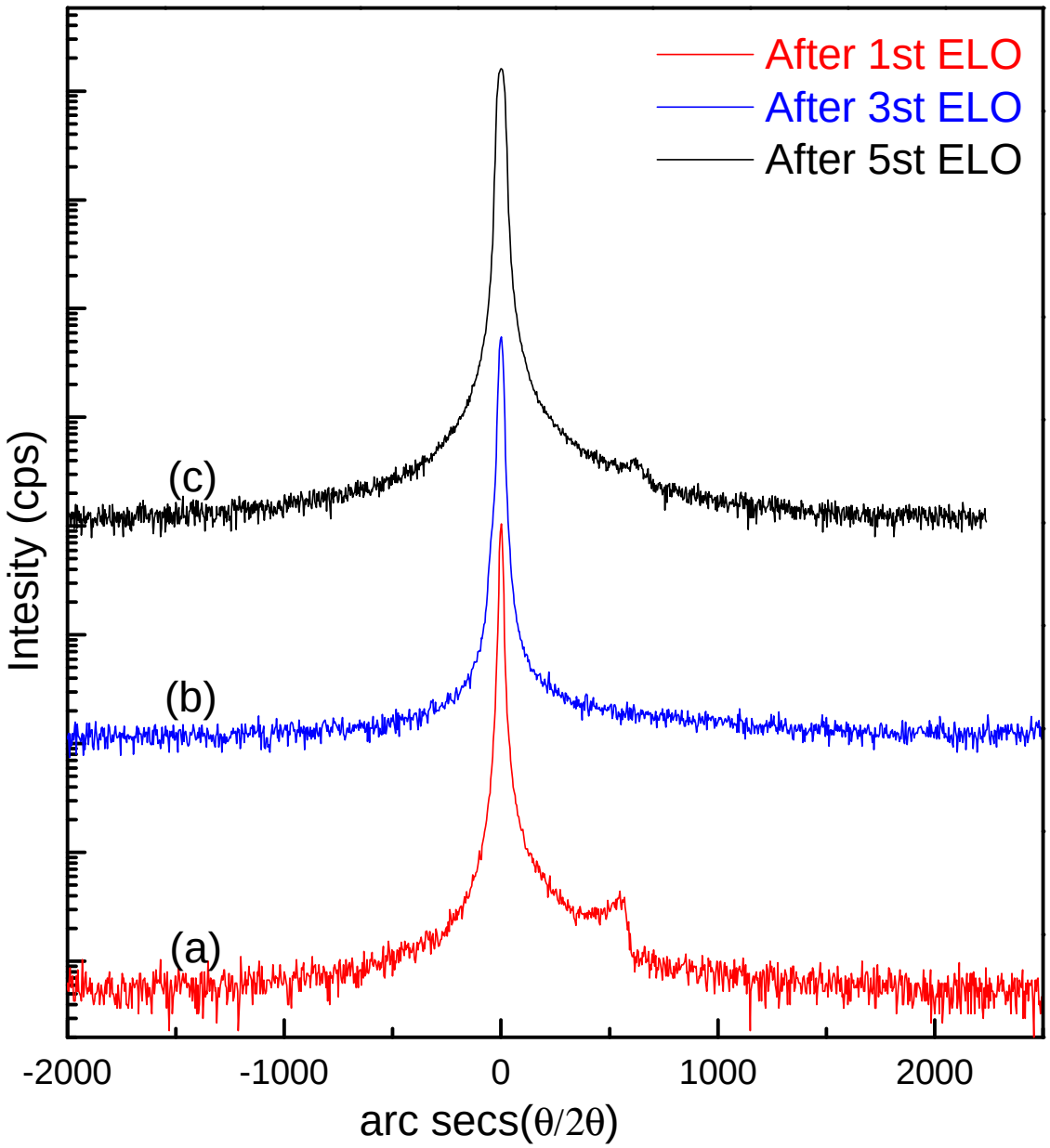

Figure 8.12: *004 XRD scans from the GaAs substrate after performing ELO on the GaAs(sub)/ MgS(10nm)/ ZnSe(300nm) structure. (a) Substrate after first ELO, (b) third ELO and (c) fifth ELO. 004 scans from the respective structures before ELO can be seen in Figure 8.11*

The as-grown sample was initially examined using XRD before performing ELO, which was repeated for the next regrowths. In total, the same substrate was used to grow five times. 004 XRD scans obtained from sequential growths and the corresponding substrates after ELO are shown in Figure 8.11 and 8.12 respectively. All the five growths were identical with no significant difference in terms of RHEED observations during growth or XRD scans detected.

The number of regrowth attempted on this particular substrate was five. However this is

Heterostructure	Dislocation density (cm^{-2}) $D_{[110]}$	$D_{[1\bar{1}0]}$
MgS/ZnSe (First growth)	2.0 x10^8	2.1 x10^8
MgS/ZnSe (Third regrowth)	1.9 x10^8	2.0 x10^8
MgS/ZnSe (Fifth regrowth)	2.0 x10^8	2.2 x10^8

Table 8.3: *Comparison of dislocation densities calculated from two azimuths from 300 nm thick ZnSe capping layer FWHM (shown in Figure 8.11).*

not a maximum as from the XRD scan it can be seen that the substrate is unchanged after five regrowths. A Dektak surface analysis on the substrate has also shown a flat surface.

The dislocation densities were calculated from the 300nm ZnSe layers on three regrown structures (first, third and fifth regrowth) and the results are given in Table 8.3. The number of dislocations from all three epilayers was found to be well within a constant range and denotes the fact that the dislocation density does not increase every time the substrate is reused. This supports the idea that substrate surface was indeed defect free as any increase in interface roughness would have increased the dislocations.

8.5.1 Advantages compared to III-V ELO system

The MgS based reusable substrate method demonstrated here has effectively avoided all the limitations associated with the currently existing III-V ELO based reusable substrate technique. Most of the problems in III-V ELO arise as a result of the use of HF as the etch solution. Although the etch rate of AlAs in HF is much faster than that of the surrounding layers, the highly corrosive acid still reacts with the barrier layers, causing nanometer scale surface roughness on substrate surface. Extensive chemical and mechanical polishing cost time and up to 20% the of price of a new substrate.

By replacing HF with HCl as the etch solution in this method, all of the problems related to surface roughness are avoided as evidenced from AFM scans. No significant changes in surface roughness were observed in AFM scans obtained from a GaAs substrate surface pre-growth and after 5 regrowths. This way, all of the thickness losses and costs associated

with the re-preparation of a substrate for regrowth are avoided. Similarly the faster etch rate of MgS in HCl also helps in lifting off larger areas much quicker.

8.6 Summary

The first experimental demonstration of the direct epitaxial growth of ZB MgS on GaAs substrate has been performed. ZB MgS layers up to 5 to 10 nm, directly deposited on a substrate is necessary in performing ELO and thus reusing substrates. Both RHEED and XRD measurements indicate that the ZB phase can be grown in layers up to 35 nm thick on GaAs substrate. A very narrow growth range has been found for this growth, where the Mg flux has a range of only 3 nA BEP. The Mg:ZnS flux ratio in this growth range was found to be 1:180. XRI samples grown within this range, on ZnSe buffer layers were used to confirm the layer composition and growth rate measurements.

The presence of MgS layer was further confirmed with SIMS and SEM. Dislocation densities were calculated and compared on 300 nm ZnSe cap layers grown on top of a conventional ZnSe/MgS layer and the new directly deposited MgS structure. Surprisingly the new structure has the least number of dislocations.

Initial attempts to use a GaAs(substrate)/ZnSe(buffer) heterostructure as a base for substrate reuse is also described. The absence of an effective technique to remove the oxide formation from the ZnSe surface and the increasing thickness of the substrate base with every reuse has ultimately led to abandoning this method.

The successful reuse of a substrate for the regrowth of II-VI materials has been demonstrated for the first time. In order to avoid the possible formation of $In_2(SO_4)_3$ as a result of the reaction between H_2SO_4 in initial substrate cleaning solution and In on the back of the substrate, a new etch solution has been used.

A MgS(10 nm)/ ZnSe(300 nm) structure was grown and lifted off five times from a single GaAs wafer. XRD was used to examine and ensure the quality of epilayers after growth and the substrates after ELO. Even after the fifth ELO, the substrate remained free from

any surface roughness as evidenced from AFM scans. Dislocation densities were calculated from all the five structures and were stable, meaning the dislocations does not increase with the number of reuses. This method was found to be free from all the limitations associated with the AlAs/HF ELO based III-V substrate reuse method.

8.7 Future Work

Since, both the direct growth of MgS and the reusable substrates are an entirely new area of research in II-VI materials, a very large number of things can be learned from continuing the works demonstrated in this chapter. The time constrains at the end of this project has severely limited, the continuation of the works mentions below.

As evidenced from the XRD and AFM data, the reused substrate was free from any kind of surface formations even after the fifth regrowth, and it means there is infinite possibility in reusing the substrate. However, it will be interesting to study the surface of the substrate in detail after certain number of regrowths. Resonance Raman study of the surface would be ideal to understand the particles on the surface. Similarly a cross sectional TEM study would certainly shed light into the effects of dislocations on the interface. More complex structures containing the directly grown MgS layers can be well studied using PL and electrical measurements.

One of the many areas left unexplored in this chapter is the possible conversion of MgS into ZnS below the 3nA flux range. An area with a sudden drop of Mg sticking coefficient, resulting in the growth of ZnS with a very slow growth rate (possibly negligible at 240^{o}C) is expected to find somewhere below 3nA, Mg BEP.

The modified etch solution for wafer cleaning may not be ideal in long term as it still contains H_2SO_4 and reaction with In cannot be completely ruled out, however small it is. This reaction has been observed rarely during this study. Subsequently, one wafer was used for regrowth without a chemical etch and no significant difficulties were faced during the growth other than a bit longer oxide desorption during vacuum annealing. Considering the time, the substrate was left under atmospheric conditions outside the chamber, this

could also mean that a better result could be obtained by loading the substrate straight into the chamber after ELO.

A comparison surface study of an etched and un-etched substrate would be interesting to see if the HCl solution used for ELO has any effect on the reused substrate surface. Although never tried previously at Heriot-Watt, there are reports of the use of HCl containing solutions for GaAs substrate cleaning [25–27]. If tried successful, HCl based etching could be more effective in substrate reusing as the ELO etch solution already contains HCl. The possibility of loading the substrate straight into the growth chamber after ELO, has to be examined.

As a continuation to the work detailed in Chapter 5, it is interesting to examine the direct growth of ZB MgS on GaP and InP substrates. There is great interest in reusing InP substrates for various applications. Similarly reusing a whole 2" wafer can also be tried. To speed up the etching process, minutely punched plastic carriers can be tried. This way, the rate of gas transport through the etch channels can be increased.

8.8 References

[1] K. Lee, J. D. Zimmerman, X. Xiao, K. Sun and S. R. Forrest. “Reuse of GaAs substrates for epitaxial lift-off by employing protection layers”. *Journal of Applied Physics* Vol. 111, 033527 (2012), p. 033527 (cited on page: 211).

[2] A. van Geelen, P. R. Hageman, G. J. Bauhuis, P. C. van Rijsingen, P. Schmidt and L. J. Giling. “Epitaxial lift-off GaAs solar cell from a reusable GaAs substrate”. *Materials Science and Engineering: B* Vol. 45 (1997), pp. 162–171 (cited on page: 211).

[3] R. P. Gale, R. W. McClelland, B. D. King and J. C. C. Fan. “Thin-film solar cells with over 21% conversion efficiency”. *Solar Cells* Vol. 27 (1989), pp. 99–106 (cited on page: 211).

[4] R. W. McClelland, C. O. Bozler and J. C. C. Fan. “A technique for producing epitaxial films on reuseable substrates”. *Applied Physics Letters* Vol. 37 (1980), pp. 560–562 (cited on page: 211).

[5] N. Teraguchi, H. Mouri, Y. Tomomura, A. Suzuki, H. Taniguchi, J. Rorison and G. Duggan. “Growth of ZnSe/MgS strained-layer superlattices by molecular beam epitaxy”. *Applied Physics Letters* Vol. 67 (1995), pp. 2945–2947 (cited on pages: 212, 215).

[6] C. Bradford, C. B. O’Donnell, B. Urbaszek, A. Balocchi, C. Morhain, K. A. Prior and B. C. Cavenett. “Growth of zinc blende MgS/ZnSe single quantum wells by molecular-beam epitaxy using ZnS as a sulphur source”. *Appl. Phys. Lett.* Vol. 76 (2000), pp. 3929–3931 (cited on pages: 212, 218).

[7] Y.-H. Lai, W.-Y. Cheung, S.-K. Lok, G. K. L. Wong, S.-K. Ho, K.-W. Tam and I.-K. Sou. “Rocksalt MgS solar blind ultra-violet detectors”. *AIP Advances* Vol. 2, 012149 (2012), p. 012149 (cited on page: 213).

[8] A. Rajan, R. T. Moug and K. A. Prior. “Control of surface defects in zinc blende MgS grown by MBE”. *Journal of Crystal Growth* Vol. 368 (2013), pp. 62–66 (cited on pages: 214, 221).

[9] A. Rajan, R. T. Moug and K. A. Prior. “Growth and stability of zinc blende MgS on GaAs, GaP, and InP substrates”. *Applied Physics Letters* Vol. 102, 032102 (2013), p. 032102 (cited on page: 214).

[10] K. A. Prior, X. Tang, C. O’Donnell, C. Bradford, L. David and B. C. Cavenett. “Characterization of MBE grown II-VI semiconductor thin layers by X-ray interference”. *J. Crystal Growth* Vol. 251 (2003), pp. 565–570 (cited on page: 218).

[11] K. A. Prior, C. Bradford, I. A. Davidson and R. T. Moug. “Metastable II-VI sulphides: Growth, characterization and stability”. *Journal of Crystal Growth* Vol. 323 (2011). Proceedings of the 16th International Conference on Molecular Beam Epitaxy (ICMBE), pp. 114–121 (cited on pages: 219, 220).

[12] B. Yarlagadda, A. Rodriguez, P. Li, R. Velampati, J. F. Ocampo, E. N. Suarez, P. B. Rago, D. Shah, J. E. Ayers and F. C. Jain. “X-ray characterization of dislocation density asymmetries in heteroepitaxial semiconductors”. *Applied Physics Letters* Vol. 92, 202103 (2008), p. 202103 (cited on pages: 221–223).

[13] A. Balocchi, A. Curran, T. C. M. Graham, C. Bradford, K. A. Prior and R. J. Warburton. “Epitaxial liftoff of ZnSe-based heterostructures using a II-VI release layer”. *Appl. Phys. Lett.* Vol. 86 (2005) (cited on page: 223).

[14] I. Schnitzer, E. Yablonovitch, C. Caneau, T. J. Gmitter and A. Scherer. “30% external quantum efficiency from surface textured, thin-film light-emitting diodes”. *Applied Physics Letters* Vol. 63 (1993), pp. 2174–2176 (cited on page: 223).

[15] A. Yi-Yan, W. K. Chan, T. S. Ravi, T. J. Gmitter, R. Bhat and K. H. Yoo. “Grafted InGaAsP light emitting diodes on glass channel waveguides”. *Electronics Letters* Vol. 28 (1992), pp. 341–342 (cited on page: 223).

[16] E. Yablonovitch, E. Kapon, T. J. Gmitter, C. P. Yun and R. Bhat. “Double heterostructure GaAs/AlGaAs thin film diode lasers on glass substrates”. *Photonics Technology Letters, IEEE* Vol. 1 (1989), pp. 41–42 (cited on page: 223).

[17] I. Pollentier, L. Buydens, P. Van Daele and P. Demeester. “Fabrication of a GaAs-AlGaAs GRIN-SCH SQW laser diode on silicon by epitaxial lift-off”. *Photonics Technology Letters, IEEE* Vol. 3 (1991), pp. 115–117 (cited on page: 223).

[18] A. Yi-Yan, W. K. Chan, C. K. Nguyen, T. J. Gmitter, R. Bhat and J. L. Jackel. "GaInAs/InP pin photodetectors integrated with glass waveguides". *Electronics Letters* Vol. 27 (1991), pp. 87–89 (cited on page: 223).

[19] M. C. Hargis, R. E. Carnahan, J. S. Brown and N. M. Jokerst. "Epitaxial lift-off GaAs/AlGaAs metal-semiconductor-metal photodetectors with back passivation". *Photonics Technology Letters, IEEE* Vol. 5 (1993), pp. 1210–1212 (cited on page: 223).

[20] L. Buydens, P. D. Dobbelaere, P. Demeester, I. Pollentier and P. V. Daele. "GaAs/AlGaAs multiple-quantum-well vertical optical modulators on glass using the epitaxial lift-off technique". *Opt. Lett.* Vol. 16 (1991), pp. 916–918 (cited on page: 223).

[21] K. H. Calhoun and N. M. Jokerst. "AlGaAs/GaAs/AlGaAs thin-film Fabry—Perot modulator on a glass substrate by using alignable epitaxial lift-off". *Opt. Lett.* Vol. 18 (1993), pp. 882–884 (cited on page: 223).

[22] E. Yablonovitch, K. Kash, T. J. Gmitter, L. T. Florez, J. P. Harbison and E. Colas. "Regrowth of GaAs quantum wells on GaAs liftoff films 'van der Waals bonded' to silicon substrates". *Electronics Letters* Vol. 25 (1989), p. 171 (cited on page: 223).

[23] W. C. Hughes, C. Boney, M. A. L. Johnson, J. W. C. Jr. and J. F. Schetzina. "Surface preparation of ZnSe substrates for MBE growth of II - VI light emitters". *Journal of Crystal Growth* Vol. 175 - 176, Part 1 (1997). Molecular Beam Epitaxy 1996, pp. 546–551 (cited on page: 225).

[24] Y.-h. Wu, Y. Kawakami, S. Fujita and S. Fujita. "Growth and characterization of ZnSe on (NH4) 2Sx-treated GaAs substrates: effect of GaAs surface microstructure on the growth rate of ZnSe". *Journal of Crystal Growth* Vol. 111 (1991), pp. 757–761 (cited on page: 225).

[25] M. V. Lebedev, E. Mankel, T. Mayer and W. Jaegermann. "Wet Etching of GaAs(100) in Acidic and Basic Solutions: A Synchrotron-Photoemission Spectroscopy Study". *The Journal of Physical Chemistry C* Vol. 112 (2008), pp. 18510–18515 (cited on page: 235).

[26] R. P. Vasquez, B. F. Lewis and F. J. Grunthaner. "Cleaning chemistry of GaAs(100) and InSb(100) substrates for molecular beam epitaxy". *Journal of Vacuum Sci-*

ence & Technology B: Microelectronics and Nanometer Structures Vol. 1 (1983), pp. 791–794 (cited on page: 235).

[27] O. E. Tereshchenko, S. I. Chikichev and A. S. Terekhov. "Composition and structure of HCl-isopropanol treated and vacuum annealed GaAs(100) surfaces". *Journal of Vacuum Science & Technology A: Vacuum, Surfaces, and Films* Vol. 17 (1999), pp. 2655–2662 (cited on page: 235).

Chapter 9

Conclusions and outlook

In the previous chapters, details of the growth, stability and processing of ZB MgS based structures has been presented. Each chapter ended with a summary and detailed future work section. In this chapter, the collective results will be summarised and discussed. Despite having some very interesting properties such as the ultra wide bandgap and the lattice match to GaAs, the metastable ZB MgS has not found any attention-grabbing applications. Although the use of MgS as an efficient release layer in ELO has been demonstrated previously, this application is also limited largely within the fundamental research community. The main limiting factor for MgS not being used widely for ELO in real life structures was the inability to grow the ZB phase of MgS directly on a substrate. Similarly the growth was limited to GaAs substrate based structures because of the lattice match.

The main motivation for the experimental work detailed in this thesis was the potential advantages of ZB MgS in ELO. As explained earlier the main limiting factor was the restricted range of growth parameters. Most of this growth range has been exploited by various research groups resulting in failed attempts to grow the ZB phase either directly on GaAs substrate or on any buffer layer other than ZnSe. Accordingly, growth of MgS was never attempted on lattice mismatched substrates, which was mainly due to the impression that the metastable phase is very sensitive to growth conditions.

The initial work which started this project was not focussed on the ZB MgS growth, but CdSe QDs grown on MgS barriers, which was essentially carried out alongside working on improving the growth conditions of MgS. The density control of QDs is a real challenge when it comes to self assembly, as the parameters for control of dot formation are

limited in MBE growth on non-patterned substrates. The focus in this work was on finding a method to control the number density to the low 10^9 cm^{-2}, as this region was particularly difficult in MBE growth. Although there is a relation to the number of dots formed to the amount of material deposited, it is not reproducible. A new method is explained in this thesis where, by introducing appropriate time delays after layer deposition and during annealing, the dot formation can be effectively controlled. No changes were made to any other growth parameters including the amount of the material deposited (4ML). These time delays were proved to be effective in bringing the number of QDs down to as low as $3.8 \times 10^9 cm^{-2}$ and more importantly this is reproducible. At least three samples were grown at every point in the introduced time delays to confirm the reproducibility of this method. This is the lowest reproducible number of CdSe QDs reported to date grown using a self assembly growth method like MBE. The most interesting finding in this work was the suppression of island formation during the initial 1 min time delay soon after the QD material deposition. During this time alone, at least half of the adatoms initially available for the island formation were found to be lost beyond recovery. Various time regimes, where the number of dots formed were saturated was also noted and this effect certainly makes the control of density easier and effective.

Alongside the investigation of the density control of QDs, work was progressing on the analysis of the ZB MgS growth conditions. Earlier on from this project, it was obvious that any advance in the use of MgS in new applications required optimisation of the growth by eliminating existing growth related problems such as oxidation and surface defect formation. In fact, all of these problems associated with growth can be ultimately traced back to the formation of surface defects. It is through the surface pits that the rapid oxidation of MgS starts. However, in thin MgS layers these pits are nanometer sized and hence cannot be easily detected. A high Mg flux was found to be the reason behind these surface formations. By gradually reducing the Mg BEP from $\sim$ 45 nA to less than 15 nA, pit formation can be effectively avoided and the samples grown using this method were resistant to oxidation. Surprisingly a huge drop in Mg flux from 45 nA to 15 nA, reducing the Mg:ZnS flux ratio to 1:36 has not affected the layer quality and composition in any way as evidenced from the X-ray measurements. Subsequently, after optimising the growth conditions by narrowing down the growth temperature range, the thickest ZB MgS layer grown to date, at 200nm thick was produced on ZnSe/MgS/ZnSe smoothing layers.

Upon optimising the MgS growth the next obvious step was to attempt growth on lattice mismatched substrates. ZB MgS growth was successfully performed on GaP and InP substrates where the lattice mismatches were -3.1% and 4.4% respectively. Here the MgS layers were grown on ZnS and $Zn_{0.6}Cd_{0.4}Se$ buffer layers lattice matched to the respective substrates. The growth on GaP is particularly interesting, as theoretical predictions forbid the growth of ZB MgS on GaP due to the compressive strain. This shows that the epitaxial strain is unlikely to be important in stabilising the ZB phase and the growth is truly metastable. Up to 40nm thick layers of ZB MgS has been grown on GaP substrate before the phase conversion to RS. This is the first time that a metastable compound has been successfully grown over such a wide range of lattice mismatches. Dislocation density asymmetry was studied from the thicker capping layers grown on top of MgS layers. All the examined layers have shown unequal dislocation densities on the two different azimuths, with fewer dislocations along [110].

Following this work, the application of MgS based ELO was examined on GaP and InP substrates for the first time. Structures were grown with a 7nm thick ZB MgS release layer and lift-off performed successfully on both substrates, except where a ZnS cap layer was used on GaP. Epitaxial layers lattice matched to both the substrates (except ZnS) and further to the MgS layer were successfully separated from the original structure and transferred to a glass substrate. As-grown structures were characterised structurally using X-rays and the lifted epitaxial layers were optically examined using PL and absorption spectroscopy. Differences in etch times were observed on different substrates where InP based structures lifted much faster than standard GaAs based structures. Initially, difficulties were faced during ELO on GaP based structures. Various etch related issues such as intermixing at the MgS/ZnS interface and higher Zn incorporation in MgS layer due to substrate temperature changes were examined. Zn incorporation was found to be not affecting the etch whereas a thicker ($>$10nm) MgS layer was used to overcome the intermixing related issues. Finally it was found that the ZnS layer dissolves in the etch solution over time and a replacement for the standard etch solution was investigated. The growth of a thicker ($\sim$15nm) MgS release layer is suggested in the future works to attempt ELO using NaOH or citric acid ($C_6H_8O_7$). The ability to lift-off epitaxial layers using a MgS release layer irrespective of the lattice mismatches opens up a whole new range of flexibility in II-VI based ELO.

Some of the limitations of a traditional wax based ELO surfaced during working on the lift-off on different substrates. Over curling of the epitaxial layer, uneven stress induced by non uniform wax deposition, inability to observe the etch progress and the difficulty in handling the brittle, waxed structure are few of the drawbacks of the existing Apiezon wax based ELO. A possible reaction between the etch solution and wax was found to be leaving a dusty deposit on the separated substrate over time which makes it unusable for recycling. Similarly the solvent, used for the removal of wax layer can leave a residual deposit on lifted epilayer and required further cleaning. The application of a flexible polyurethane carrier instead of the wax layer has been demonstrated in this thesis. This new method is very easy to apply and effectively eliminates all the limiting factors associated with the wax based ELO. Moreover this flexible carrier can act as a substrate in certain applications such as solar panels. Equally, the use of transparent polyurethane carriers helps to study the etch channels and H_2S gas transport through these channels. Although not studied in detail here, the etch rate and formation of etch channels could easily be observed and studied using a basic optical microscope setup.

MgS has always been grown with a thin ZnSe capping layer to prevent the oxidation. This has proved difficult at times, especially when the surface features on a bare MgS sample have to be studied. During this project, AFM and SEARS studies of surface dot formation on MgS required a cap free surface and it was observed that after a few hours exposure to atmosphere, the surface MgS layer oxidised, distorting the surface dot structures. Transportation of the samples to other laboratories also lacks an easy and coast effective protective method. Even in the case of less reactive materials like ZnSe, surface oxide layer formation is unavoidable. This was a difficult situation as it severely limited the possibility of growing an additional epitaxial layer on top of an already existing II-VI structure, grown in another lab. Deposition of an additional amorphous Se layer on top of the structure at the end of the growth has proved very effective in tackling the surface oxidation. This amorphous Se can be deposited at a low substrate temperature, typically $<100^{o}$C and can be easily removed prior to the next regrowth or characterisation stage. The Se removal can be performed by heating the sample at $\sim 200^{o}$C for 2 minutes either under vacuum or even at atmosphere and will not affect the structure in any way.

The main obstacle in reusing a III-V substrate for II-VI growth was the inability to grow a release layer directly on a substrate. Initially attempts were made to use a GaAs/ZnSe

heterostructure for regrowth as MgS can be easily grown on ZnSe. But a range of problems such as ZnSe surface oxidation and increasing thickness of the substrate structure (GaAs/ZnSe) with every regrowth to smoothen the interface has resulted in abandoning this method. This made it necessary to investigate the epitaxial growth of ZB MgS directly on GaAs. From the previous work on controlling the surface defects, it was evident that Mg flux and substrate temperature were the key parameters to investigate. As a result a new ZB MgS growth region, well outside the normal growth range was found. Within a Mg flux range of 3-6 nA and substrate temperature of 230-255 ^{o}C, ZB MgS can be grown directly on GaAs substrate. X-rays, SIMS, PL and SEM were used to confirm the ZB MgS growth on GaAs. Layers up to 35nm thick were grown on GaAs before the phase conversion to RS has observed. Despite several previous attempts by various research groups, this is the first time ZB MgS has ever been grown directly on a substrate.

With increased confidence from the direct growth of MgS on GaAs, the next obvious objective was the development of reusable substrates. ELO has been successfully performed on MgS layers grown directly on the substrate. A MgS(10nm)/ZnSe(300nm) structure was then grown on a GaAs quarter wafer and successfully separated by etching the MgS. The separated substrate was used for regrowth and another four structures were grown on the same substrate by performing ELO after every growth. The dislocation densities were calculated from all the five ZnSe capping layers and found to be similar, which means the dislocations do not increase with substrate reuse. The substrate after five regrowths has shown no structural defects upon examining using X-rays and AFM. The maximum number of regrowths attempted was limited only by time constraints of this project. This is the first time, the recycling of substrates has successfully been performed in II-VI materials. Significantly, this method does not result in any of the numerous limitations currently associated with the HF based III-V substrate reuse. This is a potentially important technique for reusing expensive substrates especially in wide ranges of industrially produced, large area semiconductor structures.

This thesis looked into several problems faced in the growth and processing stages of ZB MgS based structures and effective techniques were developed. A number of significant future work ideas are detailed at the end of each chapter.